L-Università ta' Malta
Faculty of Engineering

MASTER OF SCIENCE IN ENGINEERING DISSERTATION

Investigating Thermal Performance Characteristics of Subsea Compressed Gas Energy Storage Systems With Gas-Liquid Phase Change

Luke Jurgen Briffa

Supervised by:

Prof. Inġ. Tonio Sant

A dissertation submitted in partial fulfilment of the requirements for the degree of Master of Science in Engineering

by the

Faculty of Engineering

November 2022

Copyright Notice

1) Copyright in text of this dissertation rests with the Author. Copies (by any process) either in full, or of extracts may be made only in accordance with regulations held by the Library of the University of Malta. Details may be obtained from the Librarian. This page must form part of any such copies made. Further copies (by any process) made in accordance with such instruction may not be made without the permission (in writing) of the Author.

2) Ownership of the right over any original intellectual property which may be combined in or derived from this dissertation is vested in the University of Malta and may not be made available for use by third parties without the written permission of the University, which will prescribe the terms and conditions of any such agreement.

3) Publication rights over the academic and/or research results presented in this dissertation are vested jointly in both the Author and his/her academic Supervisors(s), and unless such rights are explicitly waived in writing, both parties must be listed among the authors in any academic publication that is derived substantially from this work. Furthermore, any other public communication/disclosure of any other form the focuses on the project must acknowledge that this work has been carried out by the Author and the Supervisor(s) (named explicitly) through the University of Malta.

Dedication

Dedicate this dissertation to all those
who wished to continue their studies,
however were not able to do so due to life's injustice

Abstract

One of the main sustainable development goals for the United Nations is the reduction of greenhouse gases from fossil fuel combustion. Reduction of fossil fuels is possible by shifting the electricity energy market towards renewable energy sources (RES). Although RES technologies such as wind and solar power are now mature enough to effectively combat climate change, the intermittency in supply presents severe engineering challenges when large RES farms are interconnected to electricity grids. Such challenges of RES could be mitigated through the integration of energy storage systems (ESS). Due to the ocean covering the vast majority of Earth's surface while a considerable amount of Earth's population lives within the vicinity of the sea it is logical to invest in offshore ESSs.

The study presented throughout this dissertation deals with a novel concept of a subsea hydro-pneumatic energy storage (HPES) system utilising carbon dioxide (CO_2) as the compressible fluid. Carbon dioxide was studied since it is able to experience a phase change (gas-liquid-gas) during the storage cycle in typical subsea temperatures when limiting the peak operating pressure below the critical value. The influence of integrating a piston and an inner liner within the accumulator, to mitigate issues related to gas dissolution in sea water and corrosion were explored.

A preliminary thermal analysis of the novel concept was carried out through in-house developed codes using *Python*® V3.8. The proposed accumulator was initially studied when utilising air as the compressible fluid, thus providing an initial understanding of the thermal behaviour of the accumulator in the presence of the integrated piston and inner liner. Air was then substituted with CO_2 to study its behaviour within the proposed accumulator. Conclusions for this study were drawn for the separate accumulators and through a comparison between the results of the two gases.

Based on the results obtained, it has firstly been established that the diameter-to-length ratio influences the accumulator thermal behaviour irrespective of the fluid utilised for compression. The introduction of the piston in the accumulator only resulted in a marginally influence on the round-trip thermal efficiency of the system. On the other hand, the introduction of the inner liner was found to have a considerable influence on the thermal efficiency, especially when CO_2 was used. This study concluded that a CO_2-based accumulator manages to store more energy per unit accumulator volume and per unit mass of steel than one working with air.

Acknowledgements

First and foremost, I wish to show my sincere gratitude towards my supervisor, Prof. Inġ. Tonio Sant for his constant support, mentoring and guidance throughout this study. His words of wisdom and continuous feedback kept me motivated throughout this journey. Moreover, I am grateful for the opportunities and experiences he has given me through the years as it is an honour to be one of his students.

This research formed part of the SEA2F project (Investigating the Thermal Performance of Subsea Energy Storage Accumulators with a 2-Phase Fluid transition). The project was financed by the FUSION R&I Research Excellence Programme funded by the Malta Council for Science and Technology (Grant number REP-2021-008).

I am grateful for the technical support that Mr. Roberto Bonello managed to provide and for all the help in setting up specific software.

Also, I would like to thank Dr. Inġ. Daniel Buhagiar and Charise Cutajar for providing a helping hand where possible while sharing his expertise.

A special thanks goes to the researchers in the Postgraduate Research Suite Room 217 for the endless enjoyable conversations and all the unforgettable memories which I will cherish for life.

Finally, I would like to express my sincere gratitude towards my family members, especially my parents, Andrew and Dorianne, for their continuous impeccable support and moral help. Nonetheless, I am grateful for my fiancée, Maria, who managed to comfort me through her words in the toughest moments of this journey.

Table of Contents

List of Figures

List of Tables

List of Abbreviations

A-CAES	Adiabatic Compressed Air Energy Storage
BES	Battery Energy Storage
CAES	Compressed Air Energy Storage
CAIR	Code for the air based hydro pneumatic energy storage system
CCES	Compressed CO_2 Energy Storage
CEF	Cycle Energy Factor
CNESA	China Energy Storage Alliance
CO_2	Carbon Dioxide
C^2O_2	Code for the carbon dioxide based hydro pneumatic energy storage system
CPU	Central Processing Unit
D-CAES	Diabatic Compressed Air Energy Storage
ESS	Energy Storage System
FE	Finite Element
FEA	Finite Element Analysis
FLASC	Liquid-piston Accumulator using Seawater under Compression
GHG	Greenhouse Gases
GLIDES	Ground Level Diverse Energy Storage
HDD	Hard Disk Drive
HDPE	High Density Polyethylene
HP	High Pressure
HPES	Hydro Pneumatic Energy Storage
I-CAES	Isothermal Compressed Air Energy Storage
IDE	Integrated Development Environment

LAES	Liquid Air Energy Storage
Li	Lithium
LP	Low Pressure
MS	Microsoft
N_2	Nitrogen
ORNL	Oak Ridge National Laboratory
OS	Operating System
PET	Polyethylene Terephthalate
PIG	Pipeline Inspection Gauge
PP	Polypropylene
PU	Polyurethane
PSH	Pumped Storage Hydropower
R&D	Research and Development
Ra	Rayleigh Number
RAM	Random Access Memory
Re	Reynolds Number
RES	Renewable Energy Sources
RMS	Root Mean Square
SDG	Sustainable Development Goals
SSD	Solid State Drive
TES	Thermal Energy Storage
UPS	Uninterrupted Power Supply
USA	United States of America
UWCAES	Underwater Compressed Air Energy Storage

Nomenclature

Symbol	Description	Units
Small Letters		
a	The number of increments for the hold stage	-
c_{inl}	Specific heat capacity of the inner liner material	$J.kg^{-1}K^{-1}$
c_{osp}	Specific heat capacity of the outer steel pipeline	$J.kg^{-1}K^{-1}$
$c_{\text{p (sw)}}$	Specific heat capacity of sea water	$J.kg^{-1}K^{-1}$
$c_{\text{p (g)}}$	Specific heat at constant pressure of the gas	$J.kg^{-1}K^{-1}$
c_{v}	Specific heat at constant volume of the gas	$J.kg^{-1}K^{-1}$
d_{i}	Internal diameter of the accumulator	m
d_{m}	Internal diameter of the pipeline and outer diameter of the inner liner	m
d_{o}	Outer diameter of the accumulator	m
d_{p}	Pipeline inspection gauge clamping disc diameter	m
d_{s}	Diameter of the pipeline inspection gauge disc	m
f_{fr}	Friction factor of the pipe	-
f_{i}	Interfacial roughness factor	-
g	Acceleration due to gravity	$m^2.s^{-1}$
h	Specific enthalpy / Combined internal and external convective heat transfer coefficient	$J.kg^{-1}K^{-1}$/ $W.m^{-2}K^{-1}$
h_{c}	Convective condensation heat transfer coefficient	$W.m^{-2}K^{-1}$
h_{f}	Nusselt film condensing coefficient on top perimeter of the inner part of the accumulator	$W.m^{-2}K^{-1}$
h_{in}	Internal convective heat transfer coefficient	$W.m^{-2}K^{-1}$
h_{out}	External convective heat transfer coefficient	$W.m^{-2}K^{-1}$
h_{depth}	Hydrostatic head acting on the system	m
h_{L}	Specific enthalpy of the saturated liquid of the gas for the current temperature	$J.kg^{-1}K^{-1}$

h_{V}	Specific enthalpy of the saturated vapour of the gas for the current temperature	$J.kg^{-1}K^{-1}$
h_{LV}	Enthalpy of vaporisation	$J.kg^{-1}$
hld_{t}	Hold stage duration	hrs
k	Chamfer dimension ratio/ Number of the current increment for a that specific stage, specifically for hold stages	-
k_{inl}	Inner liner thermal conductivity	$W.m^{-1}K^{-1}$
k_{g}	Thermal conductivity of the gas	$W.m^{-1}K^{-1}$
k_{l}	Thermal conductivity of the liquid portion	$W.m^{-1}K^{-1}$
k_{osp}	Outer steel pipeline thermal conductivity	$W.m^{-1}K^{-1}$
k_{sw}	Thermal conductivity of the surrounding sea water	$W.m^{-1}K^{-1}$
m	Mass of the gas within the pressure chamber	kg
n	Polytropic index	-
Δp	Pressure difference between the two surfaces of the pipeline inspection gauge disc	Pa
p_{ch}	Pressure of the pressure chamber	Pa
p_{cr}	Critical pressure of the gas	Pa
p_{f}	Final pressure of the pressure chamber stated by the user	Pa
p_{h}	Hydrostatic pressure acting on the system	Pa
p_{i}	Initial pressure of the pressure chamber stated by the user	Pa
p_{ref}	Reference pressure	Pa
p_{sw}	Injected sea water pressure into or out of the system	Pa
q	Total heat flux	$W.m^{-2}$
r_{c}	Pipeline inspection gauge disc chamfer dimension	m
r_{i}	Internal radius of the accumulator	m
r_{o}	Outer radius of the accumulator	m
r_{x}	Radius of the midpoint within the inner liner	m

r_{y}	Radius of the midpoint within the outer steel pipeline	m
Δt	The size of the incremental time step	s
t	Elapsed time of the whole simulation	hrs
$t_{\mathrm{c-d}}$	Charging/Discharging duration	s
th	Thickness of disc	m
u	Specific internal energy of the system	$J.kg^{-1}$
u_{dif}	The minimal acceptable value for the difference of the specific enthalpy	(%)
u_{L}	Velocity of the liquid in the liquid-vapour phase	$m.s^{-1}$
u_{v}	Velocity of the vapour in the liquid-vapour phase	$m.s^{-1}$
v	Kinematic viscosity of surrounding sea water	$m^2.s^{-1}$
$\bar{v}$	Unit mole of the compressible gas	$m^3.kmol^{-1}$
v_{L}	Specific volume of the saturated liquid	$m^3.kg^{-1}$
v_{V}	Specific volume of the saturated gas	$m^3.kg^{-1}$
v_{spec}	Specific volume of the gas at the current time increment	$m^3.kg^{-1}$
x	Dryness fraction	-

Symbol	Description	Units
Capital Letters		
A	Inner cross-sectional area of the accumulator	m^2
A_{i}	Accumulator circumferential area of the inner wall	m^2
A_{L}	Cross-sectional area occupied by the liquified gas during the two-phase flow	m^2
A_{Ld}	Dimension less cross-sectional area occupied by the liquified gas during the two-phase flow	-
A_{o}	Accumulator circumferential area of the outer wall	m^2
A_{PIG}	Area of the pipeline inspection gauge	m^2
A_{V}	Area occupied by the vapour gas during the two-phase flow	m^2
A_{Vd}	Dimension less cross-sectional area occupied by the vapour gas during the two-phase flow	-
Bo	Boiling number	-
C_{f}	Pipeline inspection gauge contact force due to the interference between the disc and the accumulator diameter	N
C_{fr}	Contact force ratio as a result of the thickness to diameter ratio equal to 0.03 and a pressure difference on a PIG disc of 0.1 MPa	-
D	Thermal diffusivity	$m^2.s^{-1}$
D_{h}	Hydraulic diameter of the liquefied gas	m
$E_{\mathrm{c-d}}$	Energy for charging or discharging	Whr
E_{dis}	Energy extracted during discharging	Whr
E_{ch}	Energy stored during charging	Whr
F	Modification factor	-
F_{f}	Pipeline inspection gauge disc friction force	N
Fa	New dimensionless number	-
G	Total mass flux of liquid and vapour	$kg.m^{-2}s^{-1}$
G_{sw}	Sea water Grashof number	-

G_{strat}	Stratified mass flux	$kg.m^{-2}s^{-1}$
L_{ch}	Length of the pressure chamber	m
L_{tr}	Transitional length	m
N_{dis}	Number of increments for the discharging stage	-
N_{st}	Number of increments for the storage stage	-
Nu	Nusselt number	-
Pr	Prandtl number	-
Q	Heat transfer to/from the surrounding wall	J
R	Universal gas constant (8.3145)	$J.mol^{-1}K^{-1}$
$R_{(2-1),(3-2),(4-3)}$	Resistances between nodes 2-1, 3-2 and 4-3	$K.W^{-1}$
R_{conv}	Convective resistance	$K.W^{-1}$
R_{cond}	Conductive resistance	$K.W^{-1}$
Ra	Rayleigh number	-
Re	Reynolds number	-
S	Saturation Factor	-
$T_{1,2,3,4}$	Temperature of nodes 1, 2, 3 and 4	K
T_{calc}	Temperature of the current increment for the two-phase flow	K
T_{cr}	Critical temperature of the gas	K
T_{inc}	Incremental temperature size	K
ΔU	Change in internal energy	J
U_{PIG}	Pipeline inspection gauge velocity	$m.s^{-1}$
$\dot{V}$	Pump flow rate	$m^3.s^{-1}$
V	Pressure chamber volume	m^3
ΔV	Change in volume within the pressure chamber	m^3
V_{inl}	Volume occupied by the inner liner	m^3
V_{osp}	Volume occupied by the outer steel pipeline	m^3
V_{t}	New volume of the current time step	m^3
W	Work done on/by the gas (air or CO_2)	J
Z	Compressibility factor	-

Symbol	Description	Units
Greek Letters		
α	Local vapour void fraction	-
β	Coefficient of Thermal Expansions	K^{-1}
δ	Percentage interference ratio of the piston to the inside of the pipeline/ Liquid film thickness	-/ m
ϵ	Wall roughness of inner accumulator	m
ε	The difference between the temperature of air within the accumulator to that of the surrounding sea water	K
ζ	Pipeline inspection gauge clamping rate ratio	-
η	Dynamic viscosity	$kg.m^{-1}s^{-1}$
η_{L}	Dynamic viscosity of liquefied gas	$kg.m^{-1}s^{-1}$
$\eta_{\mathrm{L,f}}$	Dynamic viscosity of the liquefied saturated gas at fluid temperature	$kg.m^{-1}s^{-1}$
$\eta_{\mathrm{L,w}}$	Dynamic viscosity of the liquefied saturated gas at wall temperature	$kg.m^{-1}s^{-1}$
η_{sw}	Dynamic viscosity of the surrounding sea water	$kg.m^{-1}s^{-1}$
η_{g}	Dynamic viscosity of the gas	$kg.m^{-1}s^{-1}$
θ	Falling film angle	rad
θ_{strat}	Stratified angle	rad
μ_{k}	Kinetic friction coefficient	-
μ_{s}	Static friction coefficient	-
ν	Momentum diffusivity of sea water	-
ξ	Pipeline inspection gauge thickness to accumulator internal diameter ratio	-
ρ_{ch}	Density of the gas within the pressure chamber	$kg.m^{-3}$
ρ_{cr}	Gas critical density	$kg.m^{-3}$
ρ_{g}	Density of gas	$kg.m^{-3}$
ρ_{inl}	Density of inner liner	$kg.m^{-3}$
ρ_{L}	Density of liquid phase	$kg.m^{-3}$

ρ_{osp}	Density of outer steel pipeline	kg.m^{-3}
ρ_{sw}	Density of seawater	kg.m^{-3}
ρ_{V}	Density of the vapour phase	kg.m^{-3}
σ	Surface Tension	N.m^{-1}
τ_{iso}	The root mean square of the gas temperature with respect to that of the surrounding sea water	
ϕ_l	Two-phase multiplier for liquid phase	-

Subscripts

Abbreviation	Description
$c-d$	Charging and discharging
i	Indicating the absolute current increment, unless stated otherwise
$i-1$	Indicating the results of the previous increment
in	Inner side (such as for the internal convective heat transfer coefficient)
g	Gas
lam	Laminar flow
out	Outer side (such for the external convective heat transfer coefficient)
sw	Sea water
$turb$	Turbulent flow
L	Liquid
V	Vapour

1 Introduction

The United Nations established the Sustainable Development Goals (SDGs) in 2015, dividing them into 17 main goals as shown in Figure 1.1 [1]. The 13th goal is to take action towards climate change and its impact by mitigating greenhouse gases (GHG). One of the main greenhouse gases contributors is carbon dioxide (CO_2), which is a bi-product of combustion of fossil fuels [2]. Reduction of fossil fuels is possible by shifting the electricity energy market towards renewable energy sources (RES).

Figure 1.1- 17 Sustainable Development Goals [1]

Renewable energy sources are continuously increasing in their popularity on a day-to-day basis, providing hope in addressing climate change reducing GHG. Back in 2010, RES such as wind and solar only contributed to 1.7 % of the global electricity generation. To the contrary, in 2020 the mentioned RES contributed to 8.7 % of the global electricity generation, much greater than what have been predicted. Renewable energy sources are increasing in their popularity due to the reduction in their cost, making them more competitive with fossil fuel electricity [3].

Although RES aid in reducing the GHG emissions, some issues still arise, such as the daily or seasonal intermittency and randomness of RES. In certain cases, the generation from RES is greater than the demand, causing the extra generated electricity to be curtailed. It is typically agreed that approximately around 20% penetration for intermittent RES can destabilise the electricity grid [4]. The imbalance between energy supply and demand causes instability in the quality of the power supply. It also increases the emissions of CO_2 and pollutants from gas turbines operating as spinning reserves as the fluctuating load leads to lower thermal efficiency. The increase penetration of large-scale wind and solar farms into the electricity supply networks is rendering both short and long-term energy storage systems (ESSs) essential in addressing such challenges faced by utilities [4, 5, 6].

1.1 Energy Storage Systems

An energy storage system utilises electrical energy to be stored in different forms, which could be extracted in the future to perform useful work. One of the main issues of ESSs are their initial capital required and the cost of operation, but grid-scale ESSs are increasing in their development and deployment due to technology advancements and policy actions. The ultimate goal of researchers when developing ESSs is to ensure that the environment is not negatively impacted. Irrespective of the researchers work none of the ESSs will excel on all characteristics [4, 6, 7].

Apart from reducing the environmental impact, ESSs could aid in two other instances 1) saving money and 2) improving system reliability. The introduction of ESS saves money by storing energy during periods of low energy demand and extracting energy during peak hours, enhancing the system load factor. This also reduces the necessity of expensive peak generators. Reliability of the electricity grid increases with an ESS since electricity is always available even in the event of a black out [4, 8].

By the end of 2020, the global installed capacity of energy storage has reached 191.1 GW, as stated by the CNESA [4]. Mainly, ESS are classified as follows: mechanical storage system, electrochemical systems, chemical storage and thermal storage systems, as discussed in Chapter 2. It is also discussed that the greatest share of stationary energy storage is covered by pumped storage hydropower (PSH). Although the effort to integrate ESS into the electrical system is a global action, the greatest contributor to it is China, followed by USA while Europe being at the third place [4].

Due to geographical problems, it is not always possible to install PSH systems but an alternative to this is compressed air energy storage (CAES) systems. Compressed air energy storage systems are not something of the last decade but they have been around since the 1940s. Its popularity has been around for such a long period due to offering one of the best alternatives for storing energy with the highest economic feasibility while having a long-expected life time [9].

One of the ESSs benefiting from recent technological advancements is the Li-ion battery. Some of their main advantages over other ESSs are their high round-trip efficiency, high specific energy and power, along with others. Although their continuous development and advantages they still suffer from a number of drawbacks

such as; high capital cost, material limitation, weak recycling and safety issues due to fire hazards [10].

For a sustainable society, the integration of RESs with a mixture ESSs to the electricity grid are a must. As will be highlighted in Chapter 2, some of ESSs offer greater advantages over others but most will suffer the same geographical limitations, unless offshore is considered. The ocean covers the vast majority of the Earth surface, up to 72%, while 40% of the world's population lives within 100 km of the coast making it suitable to invest in offshore ESSs [11]. Numerous countries and cities similar to Malta exist, where abundant territorial sea is present but have geographical limitations. Hence, offshore RES and ESS technologies aid such countries to be sustainable.

1.2 Research Objectives

Acknowledging the importance of energy storage and its relevance to reduce the greenhouse gases emitted sets the motivation for this work. The overall aim of this study is to compare, through numerical investigations, the thermal behaviour of subsea hydro pneumatic energy storage (HPES) systems operating with two different fluids: (1) air in gaseous state and (2) CO_2 undergoing a phase change (gas-liquid-gas) during the storage cycle. Specific objectives were to:

1. conduct a literature review to obtain a better understanding of the problem understudy and clearly identify the knowledge in relevant areas of study;
2. conduct a theoretical analysis of the proposed subsea HPES system;
3. develop a numerical code using *Python*® to simulate the transient thermal behaviour of the proposed HPES system operating in a subsea environment;
4. carry out numerical simulations to compare the thermal performance of subsea air-based and CO_2-based HPES systems.

1.3 Organisation of Work

This section describes briefly how the undertaken research work is documented in this thesis (Figure 1.2). The following chapter reviews literature to obtain a better understanding in relevant areas of study. It focuses on the different types of energy storage systems, especially on CAES. Chapter 2 discusses the different variations of CAES while also focusing on HPES systems for both onshore and offshore applications. Moreover, it discusses the use of air and carbon dioxide in HPES systems. This chapter further discusses technical challenges arising in subsea HPES systems

utilising carbon dioxide as the compressible fluid. Finally, the research gaps for this dissertation are highlighted. Based on the knowledge gained through Chapter 2, Chapter 3 proposes a new subsea HPES accumulator to utilise either air or carbon dioxide as the compressible fluid. The thermo-fluid theory behind the proposed system is described, both for air and carbon dioxide.

Having defined the new system and its theory, Chapter 4 delves into the modelling of the system in *Python*® and the respective flow of the code. This chapter further describes the difference between the two developed codes for air and carbon dioxide. Chapter 5 describes the main parameters of the baseline system for both the air and carbon dioxide HPES systems with and without the anti-corrosion inner polymeric liner and the piston (introduced in Chapter 2). Chapter 6 initially presents the numerical simulation results for the air-based HPES accumulator when varying a set of parameters. This is followed by the results obtained for the CO_2-based HPES accumulator (Chapter 7). Moreover, Chapter 8 compares the results of the air-based and carbon dioxide-based HPES with one another while drawing important conclusions. Chapter 9 summarises the conclusions drawn from the analysis, highlight the limitations of the work and suggestions for further research.

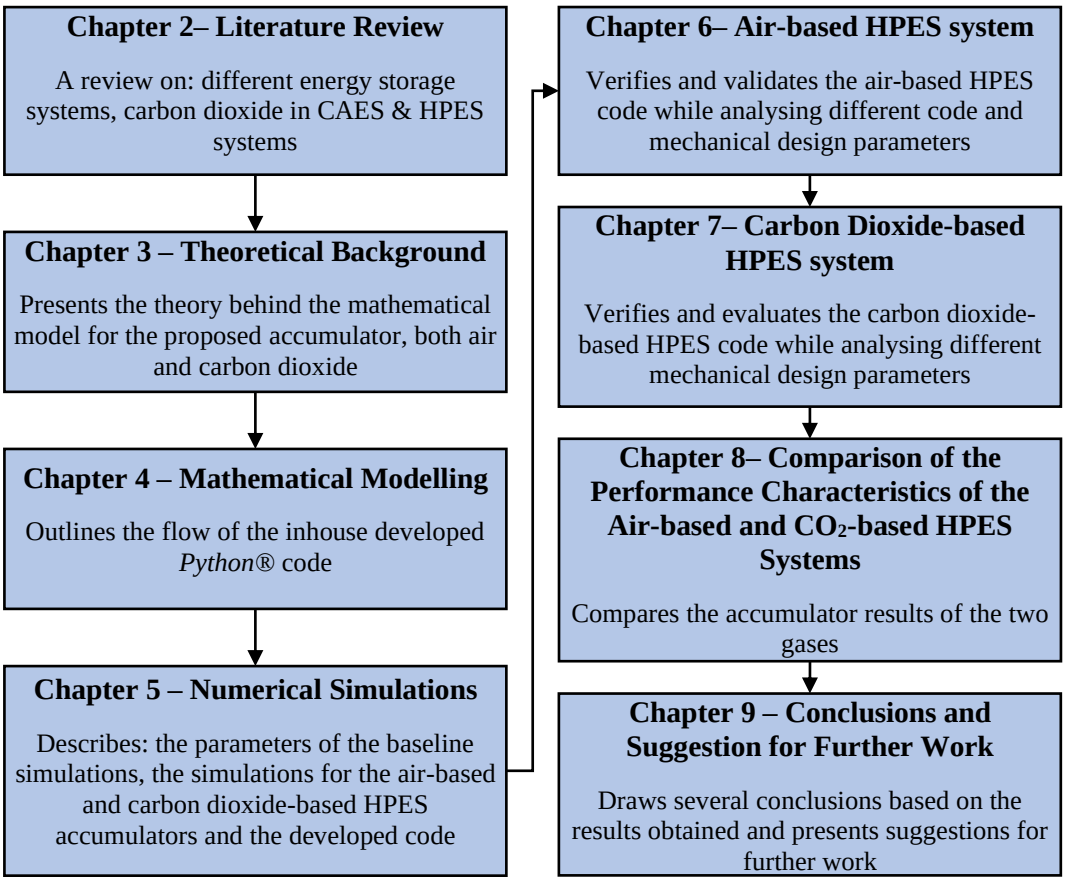

Figure 1.2- Organisation of dissertation

2 Literature Review

This chapter presents an in-depth literature review regarding the following topics relevant to this project: different energy storage systems, compressed air energy storage, hydro pneumatic energy storage and the application of carbon dioxide for energy storage.

2.1 Energy and the Relevance of Energy Storage

Energy plays an important role in our everyday life and it is an essential need globally. Energy comes in several forms but it can be classified into two categories; primary and secondary. The primary forms are those energy sources that only require to be harvested with or without the need to be separated from a contiguous material before the energy can be extracted, as heat or mechanical work. Meanwhile, secondary form includes all forms which occur as the transformation of primary energy using an energy conversion process. Through the years the energy consumption demand has been growing with a rapid pace leading to several unforeseen issues [12, 13].

Energy consumption levels are expected to continue to rise in the near future. Between 2009 and 2019 the global energy consumption has grown by 21% while it is expected to grow by 50% by the year 2050. By 2018, 81% of the energy produced was from fossil fuels, including natural gases, coal and oil. A bi-product of combusting fossil fuels lead to GHG emission which consequently cause global warming and climate change. The effect of global warming and climate change could be mitigated by increasing the contribution of RESs to the global energy market [14]. However, the inclusion of renewable energy to the global energy market introduces new challenges such as the intermittent characteristics of renewable resources [14, 15].

The intermittency of RES, such as wind and solar energy, limits their integration with the electrical grids. Energy storage systems are crucial to address this problem and the mismatch between supply and demand of energy [16]. The industry of ESS is currently dominated by pumped storage hydropower (PSH) as it makes up around 99.5% of the energy storage industry. They are followed by compressed air energy storage systems and lithium-ion batteries [17, 18].

2.2 Different Energy Storage Technologies

The ESS sector is a rapidly growing industry, with a range of different technologies currently under development. Research and development (R & D) efforts are focused

on improving the lifetime, reducing costs and minimising environmental and safety hazards of ESSs. Energy storage technology could be divided into 5 main categories, as depicted by Figure 2.1 [19, 20].

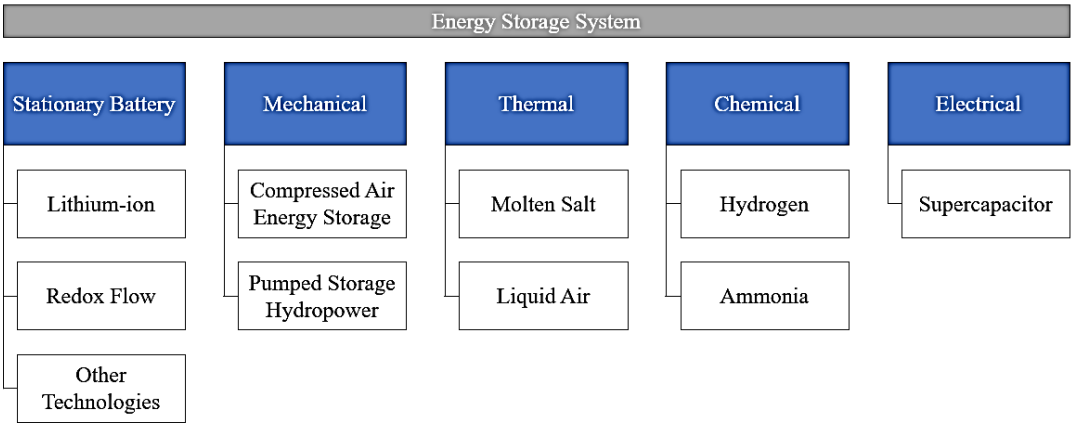

Figure 2.1- Selected few of energy storage technologies [19, 20]

2.2.1 Stationary Battery Energy Storage

Stationary battery energy storage (BES) could be integrated within the main electrical grid as a contributor in different applications. A typical application of stationary BES is uninterrupted power supply (UPS), which could be integrated to either grid nodes, small island grids or off-grid systems. An UPS could be further utilised to buffer frequency flickers and disturbances or provide emergency power in the case of a blackout. Another application for stationary BES is providing a black start capacity following a complete loss of electricity in a grid. Moreover, it could be incorporated into the electrical grid as a control reserve to keep a balance between the electricity generated from the power station and that from renewable source [19, 21].

Examples of stationary BES technologies are lithium-ion BES and redox flow BES. Both technologies have their benefits and limitations, which restrict their integration to the grid. Some benefits of lithium-ion (Li-ion) BES include; 1) relatively low cost, 2) high efficiency as it ranges from 85% to 95% and 3) high energy density. The main limitation of lithium-ion BES is their limited lifetime, ranging between 5 to 10 years. Other limitations are related to the raw materials required. They often include cobalt, whose supply is geographically limited and in certain cases, extracted from mines through child labour. Moreover, another limitation is that they are expensive to recycle due to the hazardous elements composing the Li-ion battery [19, 22]. One of their prevailing issues is that they possess a fire hazard. In certain instances, the aforesaid hazard led to uncontrollable fire accidents such as the Arizona BES systems fires (2012 and 2019) and reoccurring fires on shipping vessels due to Li-ion batteries [23, 24].

Redox-flow BES also offer potential candidates for stationary BES. Their main benefits over lithium-ion BES are the longer lifetime (typically >15years) and the lower fire risks [19, 25]. Redox-flow batteries benefits from the possibility to be charged rapidly through their mechanical charging. One of the main drawbacks of redox-flow batteries is their low energy density, which restricts their suitability for mobile applications, but still making them appealing for stationary storage applications at sites where space availability is not an issue [25].

2.2.2 Mechanical Energy Storage

Another form is mechanical energy storage which could take place in different forms, but for this study only CAES and PSH will be discussed. As the name implies, CAES utilises compressed air to store energy produced either from renewable resources or fossil fuel to be extracted later on as electrical energy [26]. The air could be stored in either natural underground salt domes or pressure vessels. The pressure vessels could be placed at atmospheric conditions or offshore and under water. Ongoing research efforts are aimed at developing subsea pressure vessels specifically for CAES applications [14]. A major benefit of CAES systems is their scalability, with the technology offering versatility to be applied for small or large-scale projects. The main drawback with current technology is that CAES requires very large volume storage sites due to their low energy density. In some cases, existing caverns have been used, yet these are geographically restricted. Continuous research is being carried out to overcome this issue through the development of more advanced pressure containment systems, as will later be elaborated [19].

Pumped storage hydropower is one of the most popular technologies, as it encompasses the majority of current installed storage capacity. Pumped storage hydropower works by storing excess energy in the form of potential energy of water by making use of the excess energy to pump water from a lower reservoir to a higher reservoir. The water from the higher reservoir is then extracted through turbines to generate electricity [27]. This technology benefits from their very low-cost storage once they are set-up as they are cheap to run compared to other technologies and could hold large amounts of water. On the negative side they are becoming extremely difficult to build due to the high environmental impact to the natural environment and the lack of appropriate areas having a large supply of water and suitable geographical characteristics [19, 27].

2.2.3 Thermal Energy Storage

One of the simplest forms of thermal energy storage (TES) technologies are those using molten salt, which are integrated with concentrated solar thermal power plants, as presented in Figure 2.2. Molten salt at a temperature of around 290°C is pumped to the top of the tower, where the solar energy receptor is located. Then the hot salt at a temperature of 565°C flows downward in the tower into a storage tank, capable of withstanding the hot and molten fluid. When energy is required, a heat exchanger is utilised to extract the heat from the higher temperature salt, producing a superheated steam. The superheated steam energy is further extracted through a turbine to produce electricity [28].

Another form of TES is liquid air storage. Liquid air storage operates by first liquifying air which is then stored in a well-insulated tank at low pressure. The energy stored can be extracted as the liquid is drawn from the tank, then compressed and heated using the thermal energy from the surrounding environment, following which it is eventually expanded through a turbine to generate electricity. Such a system could increase its efficiency by capturing heat from the compression and cold from the expansion. The low-pressure fluid could be easily stored for months, making such a technology favourable when it has to be used in case of an emergency. A drawback of this technology is the high cost [19, 29].

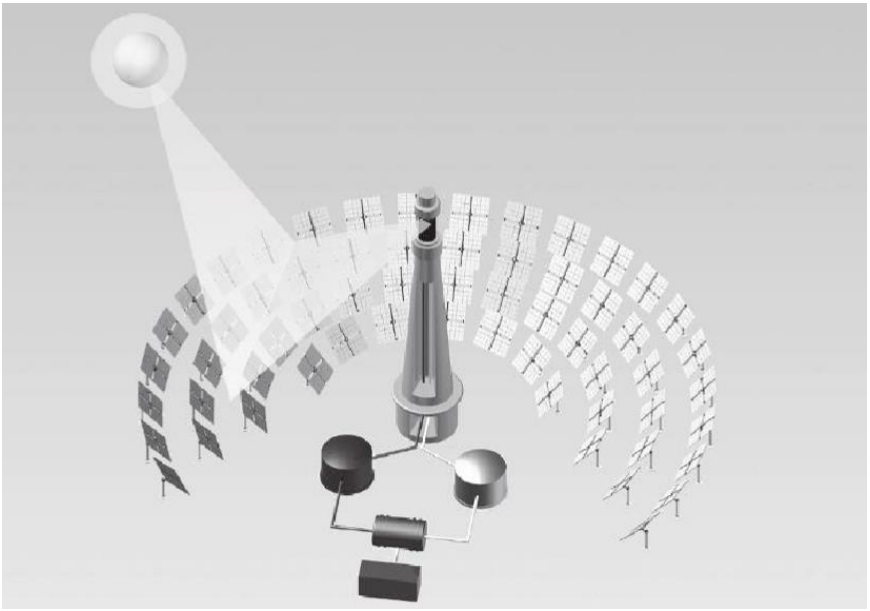

Figure 2.2- Molten salt thermal energy storage [28]

2.2.4 Chemical Energy Storage

Chemical energy storage involves the use of hydrogen, ammonia or several other chemicals. In the scenario of hydrogen, excess energy from renewable sources is used

for electrolyses to produce hydrogen from water. Hydrogen can be stored in either gaseous form or in a liquid form, but in both cases, the infrastructure has to withstand high pressures due to the low mass density of hydrogen. Hydrogen is then converted back to electricity using fuel cells or simply combustion [19, 30]. Chemical energy storage could also take place through ammonia, which could also be produced using the energy from renewables. A benefit of ammonia is that it could be easily stored in storage vessels. The chemical energy stored in ammonia could be converted back into electricity through proton exchange membrane systems [19].

2.2.5 Electrical Energy Storage

Electrical energy storage could take place in capacitors and supercapacitors which unlike BES, they store energy through static charge and no electrochemical conversion process is involved. Capacitors are typically used in the application of high currents but for a short duration due to their low capacitance. To counter act this issue supercapacitors are used, offering high capacitance in small packages. Supercapacitors are composed of; a molecule-thin layer of electrolyte, a relatively large surface area body and an activated carbon agent to act as a means of energy storage [31]. Their efficiency is relatively high as it never falls below 90% while still retaining an indefinite life expectancy. Supercapacitors have a much higher power density as compared to that of BES, however, the energy density is lower [32].

2.2.6 Remarks

After evaluating some of the available ESS technologies, it could be agreed that all of these technologies have their own draw backs, either due to their size, cost or environmental impact. From these technologies, the most developed technologies are BES and mechanical energy storage. In section 2.2.2, it has been discussed that PSH is one of the most advanced ESS while lithium-ion BES are continuously under development. Large industry players are investing hundredths of hours towards BES technology, a main drawback arises at the end of life of the batteries due to the lack of recycling technologies. On the other hand, PSH is less hazardous to the environment, although the initial cost could be greater than that of BES while leading to geographical issues. Hence, the most alternative method for energy storage is CAES. It requires a smaller foot print as already existing salt caverns or pressure vessels, both on land or subsea, could be utilised to store the compressed gas.

2.3 Compressed Air Energy Storage

The idea of storing energy in the form compressed air is not new. In fact, CAES dates back to the 1940s but it was only in the 1960s and 1970s when this technology was significantly studied [26]. Figure 2.3 presents a diagram of a simplified CAES system, where energy from renewable energy sources is utilized to compress ambient air into the natural caverns or salt domes, utilising a compressor. The compressed air is then extracted through a turbine coupled to an electrical generator connected to the electrical grid. Therefore, this process could be simply divided into two, compression and expansion [16]. It is important to mention that the CAES cycle is derived from the Brayton cycle [33].

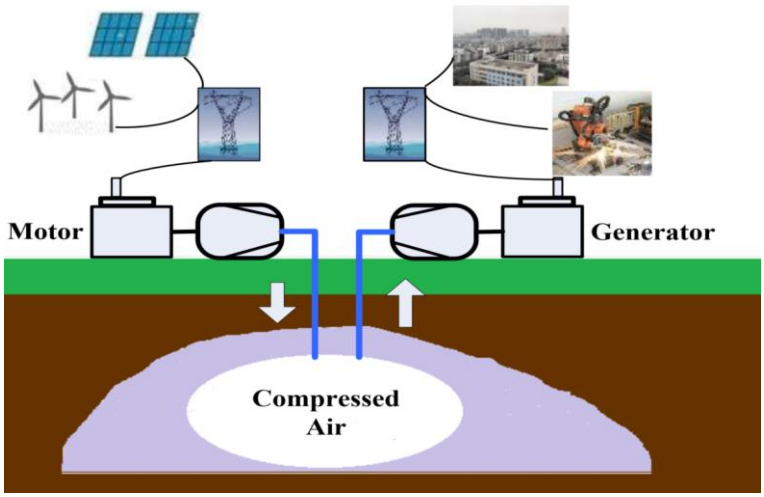

Figure 2.3- Simplified CAES system [16]

The gas compression and expansion cycle involve a considerable amount of heat flow which is strongly correlated to the system's efficiency [14]. Over the last couple of decades, different concepts to increase the energy cycle efficiency were developed. These mainly involve diabatic, adiabatic and isothermal CAES, operating as follows;

- Diabatic CAES (D-CAES): the compressed air within the system is further pressurised by heating it through combusting a fuel and exhausting the air through turbines which consequently generate electricity [14, 26].
- Adiabatic CAES (A-CAES): the heat generated during the compression is stored and utilized to the expansion process to mitigate the need of external heat sources for the discharge phase. This process results in an increase in efficiency when compared to D-CAES [14, 26].
- Isothermal CAES (I-CAES): in contrast to D-CAES and A-CAES, I-CAES tries to mitigate heat generation during the compression phase and temperature drop

during the expansion phase, through the use of a liquid piston, eventually resulting in an isothermal process. The main advantage of this system over the others is that it does not require fossil fuel backup system for the expansion process [14, 26, 34].

The first world utility-scale CAES plant is the Huntorf power plant which was developed in 1978 in Germany. The plant makes use of two salt domes to store the compressed air and it runs on a cycle of 8 hours charging and 2 hours discharging on a daily basis while generating power of 290 MW. This plant was further utilized to black start the electrical grid in the case of an emergency [16, 35, 36]. One of the main draw backs of the Huntorf power plant is its low thermal efficiency (42%) [33]. Another CAES plant was developed in 1991 in McIntosh, Alabama, USA which is the second largest CAES plant producing 110MW of power. This plant has a storage of 2700MWh which is capable of delivering power at its rated condition for up to 26 hours [16, 35, 36]. In both cases salt domes were selected to contain the air under pressure. Both power plants classify as D-CAES [26].

Recent studies are being directed towards testing concrete-lined tunnels and hard rock caverns with water compensation as a substitution for the traditional caverns. In contrast to Figure 2.3, Figure 2.4 provides a well-defined schematic diagram of a typical CAES plant, similar to what is present at the Huntorf and Alabama plants. Figure 2.4 describes a CAES plant and its flow, highlighting the following components;

- a low pressure (LP) and high pressure (HP) compressors;
- an underground cavern to store the compressed air;
- and a recuperator which reuses the wasted heat from the LP turbine to heat up the flowing air [36].

From the CAES of Figure 2.4 the air passing the recuperator passes through the HP turbine and the remaining energy is extracted by the LP turbine while at both inlets of the turbines the air is heated through an external heat source. Finally, both the compressors and turbine arrays are coupled to each other through a mechanical clutch, it includes a generator/motor set-up to either generate electricity through the generator or compress the air through the motor [36].

As one would expect, caverns and salt domes are not always available due to geographical constraints, therefore other methods to replace them had to be sought

after. Caverns and salt domes are replaced by artificial pressure vessels, although they are not suitable for large scale applications [37].

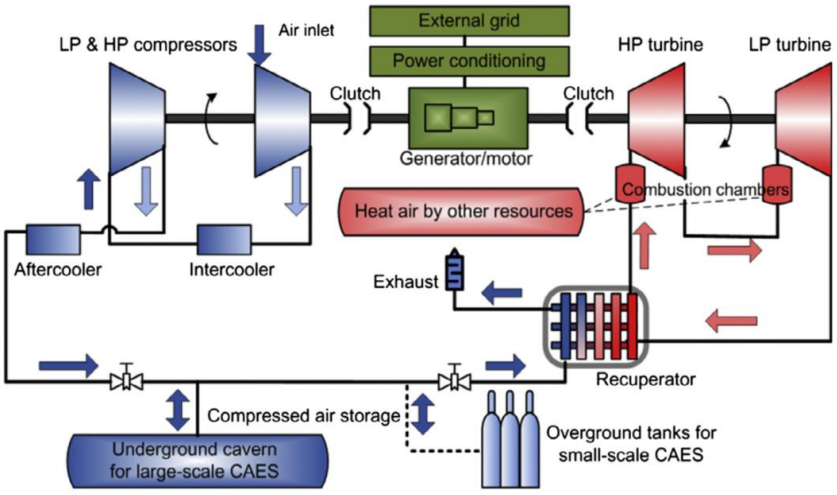

Figure 2.4- Schematic diagram of a CAES plant [36]

Systems operating at constant volume while the pressure is changing, are called isochoric CAES. Due to disadvantages associated with isochoric CAES, researchers studied other methods such as isobaric CAES where the system operates at constant pressure [37, 38]. An isobaric system is more advantageous over an isochoric system since it is capable of delivering the same power while having a reduction in volume up to 77%. Isobaric systems require a deep cavern or a very high altitude to increase the hydro static head. Therefore, it is suitable to place this technology underwater and it is referred to as underwater CAES (UWCAES) [37].

Different UWCAES technology has been developed differing from one another based on the wall of the vessels, either flexible or rigid. Flexible walled vessels, also known as energy bags, are made from coated fabric which could be shaped in different forms [39]. Their shape tends to vary according to the amount of pressure within the vessel, allowing for the system to store energy in an isobaric manner [38]. The main stresses acting on the material of the energy bag are independent of the depth at which the bag is stored but these are a result of net buoyancy and differential pressure [40]. Figure 2.5a illustrates an energy bag prototype having a single point of anchorage.

Rigid vessels, presented in Figure 2.5b, can be constructed with ballasts to avoid floating of the vessel. In contrast to flexible vessels, rigid vessels cannot change shape and resist bending while underload. The increase in structural integrity reflects in their higher cost. Moreover, flexible vessels are more susceptible to damage than rigid vessels and ballast must be added separately for flexible vessels.

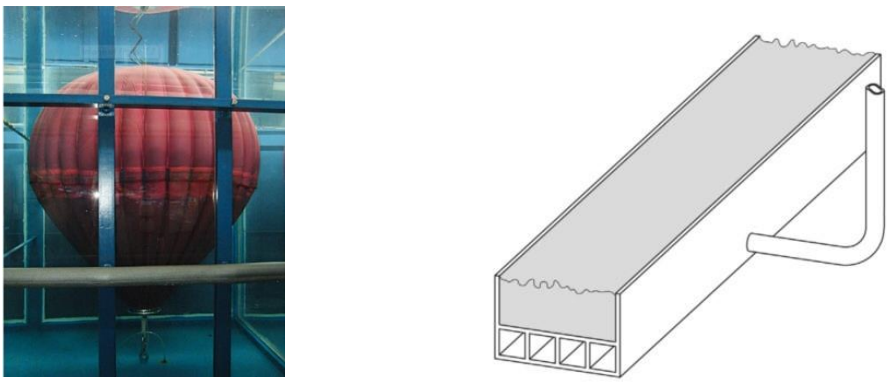

a) b)

Figure 2.5- a) Inflated energy bag prototype with single point anchorage and b) rigid storage vessel with ballast of UWCAES [39]

2.4 Hydro Pneumatic Energy Storage

Compressed air energy storage utilises an array of LP and HP compressors and turbines set-up, which are expensive, especially when the system has to be based off-shore. Due to the physical constraints imposed by CAES systems, development of alternative solutions to overcome these challenges are currently under development. One proposed solution is HPES, which in reality combines PSH and CAES: pre-charged entrapped air within a vessel is pressurised using a hydraulic drive and a liquid, as visually presented through Figure 2.6a. The hydraulic drive allows for high efficiencies due to minimal mechanical losses, while increasing the power density. The entrapped pressurised air expands and uses the potential energy to drive a turbine, typically a Pelton turbine coupled to an electrical generator. The later mentioned process is presented in Figure 2.6b [41, 42, 43].

The mentioned technology tends to exhibit isothermal properties at low pressure ratio during its stages, therefore referred to as an I-CAES system [42]. Coupling HPES systems with pressure vessels expands their applications over CAES systems due to mitigating the need of gas turbines. These advancements of HPES over CAES are more beneficial for offshore applications, where the higher power density would lead to savings in the size of machinery required [44].

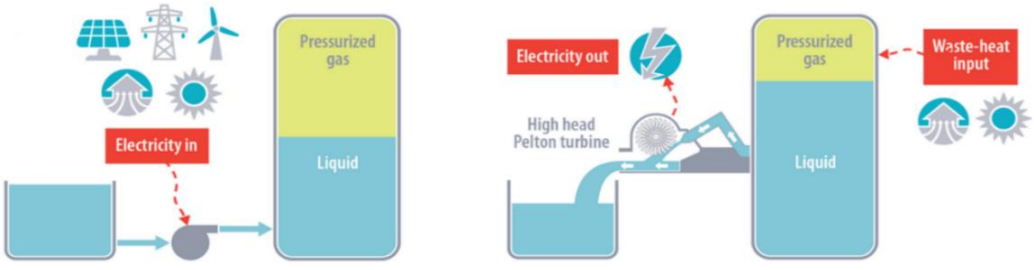

a) b)

Figure 2.6- a) Simplified charging cycle of an HPES system and b) simplified discharging cycle of an HPES system [42]

Due to the systems being closed, with no access to the atmospheric air required to operate, it is possible to deploy HPES systems subsea. Although HPES systems are still in their research and development (R&D) stage, some researchers carried out lab-scale proof-of-concept for both onshore and offshore, as discussed in sections 2.4.1 and 2.4.2.

2.4.1 Onshore HPES

Odukomaiya et al. [17] carried out the first lab-scale proof-of-concept at Oak Ridge National Laboratory (ORNL) for Ground Level Diverse Energy Storage (GLIDES), which is based on the concept of onshore HPES. The system was composed of an 1893 litre water storage tank, four 500 litre pressure vessels with an allowable maximum working pressure of 160 bar and an 11 kW and a 42 litre/min positive displacement pump. The system integrated a Pelton turbine specifically designed for this application, while having 2 jets towards the turbine coupled with a 5kW single phase 120 V alternating current (AC) 60 Hz electrical generator [42]. A schematic representation of the system is presented in Figure 2.7. Figure 2.7a represents the flow process during the charging stage whilst Figure 2.7b represents the discharging stage, the flow of both stages is indicated by the red lines and arrows [17, 42].

The system was designed to deliver a nominal capacity of 3 kWh during the discharging stage as each jet is capable to produce 5.5kW of hydraulic power at peak. The prototype was set to operate between a minimum pressure of 70 bar and a maximum pressure of 130 bar. Figure 2.8a illustrates the overall system including the pressure vessels and Figure 2.8b is the Pelton turbine with the two jets. During the charging stage, air is expected to heat up due to the compression as mentioned in section 2.3. Such behaviour was observed through the infra-red imaging of the pressure vessels, as presented in Figure 2.8c.

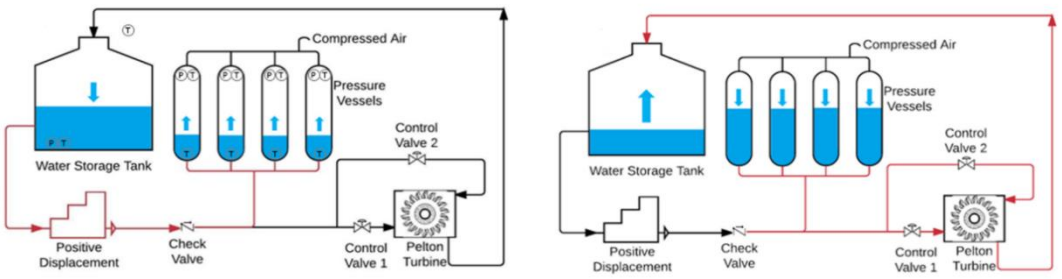

Figure 2.7- Ground-Level Integrated Diverse Energy Storage (GLIDES) a) charging stage and b) discharging stage, the flow of both stages is indicated by the red lines and arrows [17, 42]

Figure 2.8c clearly distinguishes the cool air areas which are in contact with the water while warmer areas are located further away from the water [42]. This also indicates

that the liquid piston enhances the heat exchange [45]. Moreover, Figure 2.8d and e are the charging pump and the electrical generator, respectively.

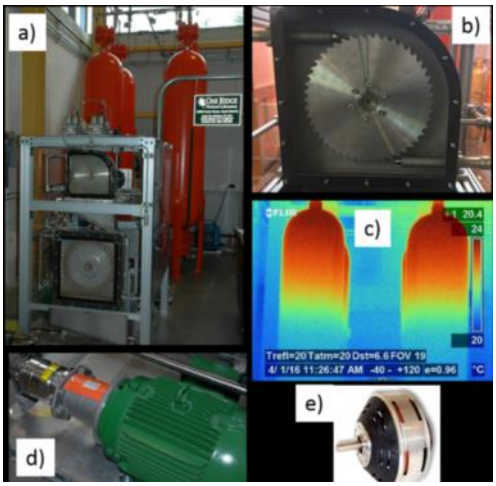

Figure 2.8- a) Overall system including the pressure vessels, b) Pelton turbine with the two jets, c) infra-red imaging of the pressure vessels during the charging cycle, d) charging pump, e) electrical generator [42]

During the experimentation the system went through four different stages, 1) charging stage, 2) hold stage, 3) expansion stage and 4) another hold stage to reach the initial conditions. Each hold stage duration was of 5 hours to observe the temperature and pressure change at a constant volume. Figure 2.9a represents the temperature of the air and water within the vessels against time during all the four stages whilst also showing the change in pressure with time. Figure 2.9b represents the change in pressure of the air within the vessel with respect to the specific volume, 1 to 2 charging stage, 2 to 3 first hold stage, 3 to 4 discharging stage and 4-1 is second hold stage [42].

Figure 2.9a and b indicate that as a result of the compression causes the temperature and pressure of air within the vessel to increase. The latter figure also indicates that during discharging the temperature experiences a drop, causing the final temperature at the end of the discharging stage to be less than that of the surrounding.

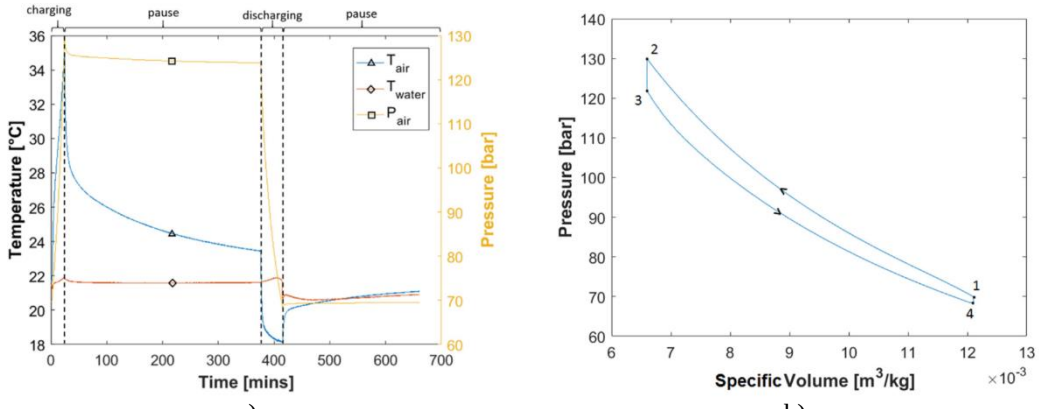

a) b)

Figure 2.9- a) Temperature (°C)/Pressure (bar) against Time (mins) and b) Pressure (bar) against Specific Volume (m^3/kg) for the whole cycle (1-2 charging stage, 2-3 first hold stage, 3-4 discharging stage and 4-1 second hold stage) [42]

During the first hold stage air dissipates heat to its surroundings. In the second hold stage, energy is gained from the surrounding, returning to the initial conditions. The area under the graph of Figure 2.9b for line 1 to 2 indicate the energy stored during charging, while the area under line 3 to 4 indicates the energy recovered during discharging. Therefore, the change in area under lines 1 to 2 and 3 to 4 is the energy lost due to dissipation of heat during first hold stage as the system is not perfectly isothermal during charging [42].

2.4.2 Offshore Energy Storage Systems

Offshore wind turbine technology, both fixed and floating, is advancing steadily making it one of the most mature technologies able to replace conventional energy systems. It is expected that the integration of large offshore wind farms to the electrical grid lead to intermittent power. As discussed, the issue of intermittent power from RES could be mitigated through ESS [46]. Hydro pneumatic energy storage systems would offer a more suitable alternative offshore, given the simple technology involved, high safety and low environment risks [47]. Throughout this section two alternative offshore ESSs are discussed.

2.4.2.1 Storing Energy at Sea (StEnSea)

Puchta et al. [48] proposes a novel system to store electrical energy from RES in subsea concrete hollow spheres, presented in Figure 2.10. The system is charged by pumping water through a pump into the sphere causing the air within to be compressed. The stored energy is then extracted by allowing the air to expand causing the water within the sphere to flow out of the system and generating electricity through the integrated turbine. The StEnSea full-scale sphere unit is approximately 29 m in diameter and 2.72 m wall thickness, resulting in 12,000 m^3 of internal volume installed at sea depth of 750 m while having storage capacity of 18.3 MWh. It is set to operate at a charging and discharging duration of 4 hours each with a round-trip efficiency of 73 % [48, 49, 38].

2.4.2.2 Floating Liquid-piston Accumulator using Seawater under Compression (FLASC)

D. Buhagiar et al. [50] presented the Floating Liquid-piston Accumulator using Seawater under Compression (FLASC), allowing for energy storage as compressed gas on site of an offshore floating wind turbine structure or any other form of floating RES [50].

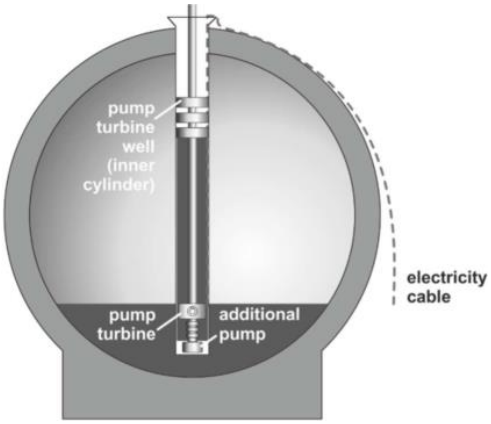

Figure 2.10-StEnSea subsea HPES system [48]

Similar to Odukomaiya et al. [17], D. Buhagiar et al. [50] carried out scaled down experiments for the FLASC system. For experimentation, the selected source of renewable energy was a set of floating solar panels to which a pressure vessel was integrated to, as presented in Figure 2.11a and b. Moreover, the system was also composed of an accumulator at the sea bed pneumatically connected to the pressure vessel of the RES (refer to Figure 2.11a). Splitting of the pressure chambers results in more manageable designs to integrate within existing infrastructure [47, 50, 51, 52].

The accumulator was charged from the hydraulic machine by pumping water into it, while utilising power from the RES. The pumped water into the accumulator compresses the entrapped air into a smaller volume within both chambers, increasing the overall pressure. The prototype was deployed in the Mediterranean island of Malta within its grand harbour, providing a shelter to the system from harsh weather [50].

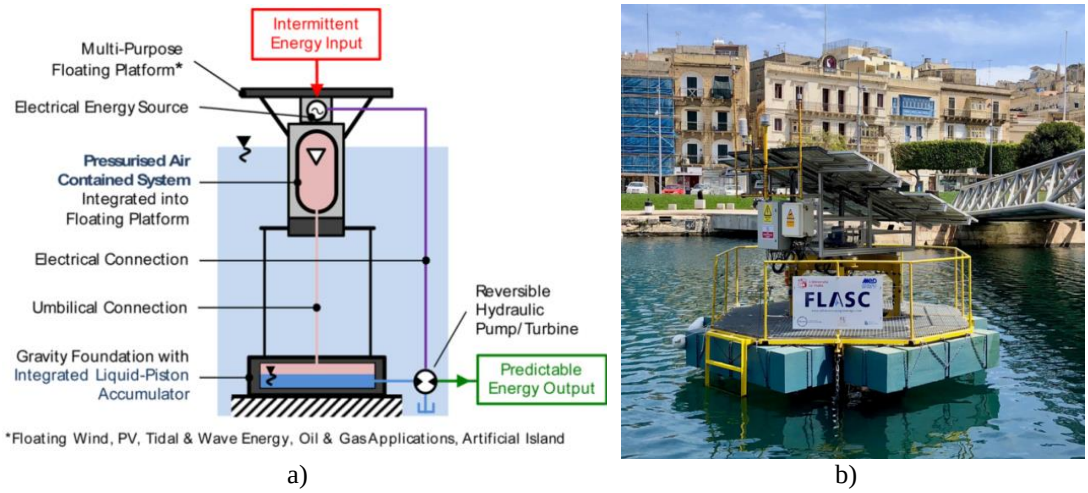

a) b)

Figure 2.11- a) Schematic of the FLASC energy storage device b) installed prototype [50]

During the study, it was observed that the internal air temperature of both vessels was correlated to the surrounding sea water temperature, whilst the air temperature was slightly greater than that of the sea. Since the prototype was sheltered, it was subjected

to relatively low wind speeds, creating a conservative scenario for heat transfer. The study indicated that the system responded quickly to changes in the surrounding sea water temperatures [50].

In their work D. Buhagiar et al. [50] introduces the cycle energy factor (CEF) to quantify the system performance with respect to the energy stored and that recovered, further discussion in section 3.3. Over 400 full charging-discharging cycles were tested, with one cycle spanning across 24 hours, resulted in CEF values exceeded 0.95 for most of the time [50, 52].

D. Buhagiar et al. [50] utilised a photovoltaic system as the RES, which consequently yielded lower CEF values during summer than in winter because during the summer more solar energy is present therefore the hydraulic pump is driven faster. This eventually charges the system at a faster rate which consequently does not allow for the generated heat to be dissipated to its surrounding. Hence, faster charging rates will shift the system away from isothermal conditions [50, 52].

2.5 Carbon Dioxide

Compressed air energy storage systems require a considerable volume to store air due to the low energy density [33]. Researchers have been aware of CAES restriction since the early stages, fuelling interest in liquid air energy storage (LAES) [52]. In recent studies it has been found that LAES systems have a round-trip efficiency of around 70%, which is much greater than the Huntrof plant, mentioned in section 2.3 [53]. As noted earlier, CAES is based on the Brayton cycle and it is well-known that gases like CO_2, that are non-ideal, tend to yield higher efficiencies in a Brayton cycle [33]. If CO_2 had to replace air in a CAES system, the storage density would increase due to the greater mass density [54].

2.5.1 Domestic Applications

Carbon dioxide, also referred to as R744, has been used as a refrigerant for a considerable amount of time due to being a natural refrigerant. It is non-toxic, non-flammable, non-combustible and has no effect on the ozone layer, while it is abundantly and cheaply available since it is a product of burning fuel. One might recall that CO_2 is one of the main contributors to the greenhouse effect, although entrapping the abundant gas on a large scale would reduce this global problem [54, 55, 56, 57]. It possesses a low critical temperature at 31.1°C and a pressure of 73.8 bar, as could be observed through the Mollier chart of CO_2 presented in Figure 2.12 [54, 58, 59].

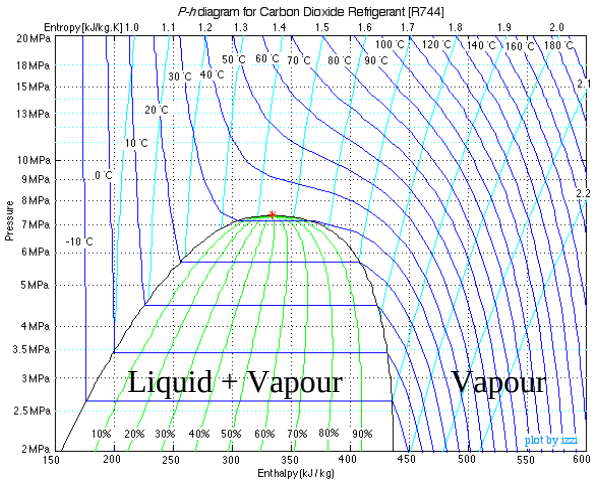

Figure 2.12- Mollier chart of carbon dioxide (CO_2) or R744, Pressure (MPa) against Enthalpy (kJ/kgK) [60]

At room temperature of 25°C, CO_2 operates at a saturation pressure of 64.2 bar which is much greater than other gases that usually operate at 25 bar. Due to the high saturation pressure, being 6 to 7 times greater than that of other refrigerants, CO_2 was set aside back in the 1940's [55]. However, an advantage of the high working pressure is that it results in high vapour density [58]. Further advantages of CO_2 include; 1) it greatly reduces the compression ratio over other gases and 2) it allows for simple operation and service as it requires no recycling, resulting in lower costs [55]. The reduction in the compression ratio allows for higher hydraulic efficiency for the hydraulic pump and recovery turbine.

Due to the low critical temperature of CO_2, it cannot be used in a conventional subcritical refrigeration cycle in an effective manner but it has to be used in a trans-critical cycle. In the trans-critical state, the refrigerant has to operate in the high-pressure gaseous state, requiring components which could withstand these pressures, but due to current technological advancements this is not an issue [54, 58]. Further benefits of CO_2 over other gases were highlighted back in 1997 when a set of studies were carried out by replacing the refrigerant R134a, which is the conventional gas in automotive, and replaced by CO_2. The initial results were favourable towards CO_2 which led to future work and demonstrated its potential. Carbon dioxide is not only applied in refrigerators or air-conditioning systems only but also in heat pumps to heat up water while also in ESS [58].

2.5.2 Energy Storage Systems Using Carbon Dioxide

Researchers are continuously working to replace air with CO_2 in CAES systems, given the underlying benefits. The application of CO_2 in compressed CO_2 energy storage (CCES) systems is discussed in the section 2.6.

2.6 Carbon Dioxide Energy Storage

Similar to air ESS, compression of CO_2 could be imposed through either a mechanical compressor or hydro pneumatically using a hydraulic pump. Section 2.6.1 briefly discusses a selective number of proposed CCES systems while section 2.6.2 discusses HPES systems utilising CO_2 as the compressible gas which are at R&D stage.

2.6.1 Compressed Carbon Dioxide Energy Storage

Hui Liu et al. [33] proposed a CO_2 energy storage system utilizing two saline aquifers to store the CO_2 at different pressures. The first reservoir is for LP CO_2 storage which is exhausted from the turbine and the second reservoir is for HP CO_2 storage which is compressed through the compressor, as presented in Figure 2.13. The ESS could be operated in two different ways; 1) the CO_2 transitions from the supercritical state to the gaseous state within the turbine and 2) the CO_2 gas is operated above the critical pressure. The system operates under the same principle adopted for conventional CAES systems. Unlike the Huntorf plant, the CCES system compresses the CO_2 from the LP reservoir through the compressor and then the compressed gas is stored in the HP reservoir. Moreover, as the HP CO_2 is expanded through the turbine the LP CO_2 is stored again in the LP reservoir. Hence, the CO_2 is enclosed within the system and is always retained [33, 61].

A.H. Alami et al. [62] proposed a LP compressed gas ESS utilising CO_2 as the compressible gas. The system stores CO_2 in caverns at LP while compressing the gas through a low power compressor. The HP CO_2 is stored in cylinders at a maximum pressure of 3 bar, due to the experimental system is composed of 3 cylinders, it stores CO_2 at 2, 2.5 and 3 bar. Then CO_2 is extracted through a gas turbine upon demand and reserved back in the LP cavern.

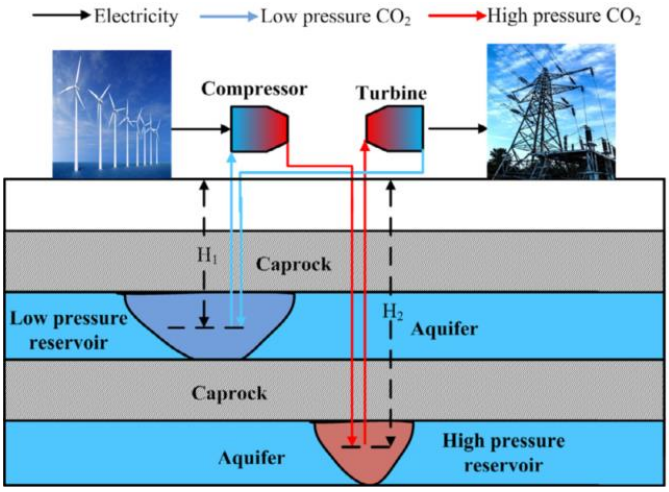

Figure 2.13- Hui Liu et al. [33] schematic illustration of compressed CO_2 energy storage system [33]

Figure 2.14 presents the schematic diagram of the proposed system utilised for experimentations. Through their work it was concluded that due to CO_2 having a higher density than air it resulted in greater energy output at lower pressures [62].

Another system utilising CO_2 for energy storage is Energy Dome which is currently under development. During the charging operation, CO_2 is drawn from an atmospheric gas holder, known as the Dome, which is then compressed by a compressor. The heat generated from the compression cycle is stored through a TES system. As the HP gas is stored in the vessels it reaches room temperature causing the gas to liquify. For the discharging, the liquified CO_2 is set to evaporate and heat is recovered from the TES while generating electricity through the turbines. The stream of CO_2 gas is returned back to the Dome at ambient temperature such that it can be reused to repeat the cycle [63].

2.6.2 Carbon Dioxide in Hydro-Pneumatic Energy Storage

Researchers are also trying to replace air in HPES system by CO_2 to achieve a greater energy storage density, which would lead to a smaller volume per unit of storage capacity. A. Abuheiba et al. [17] presented a numerical model study about improving the energy density of the GLIDES system, described earlier in section 2.4.1. Through the study, air was replaced by a mixture of CO_2 and Nitrogen (N_2), where N_2 was used as a substitute of air since it is easier and less complicated to model. At higher pressures, the CO_2 portion liquifies, occupying a smaller volume than that of N_2 resulting in a higher energy density. Within this study, water was replaced by a mineral oil since both gases are immiscible to it [17, 43].

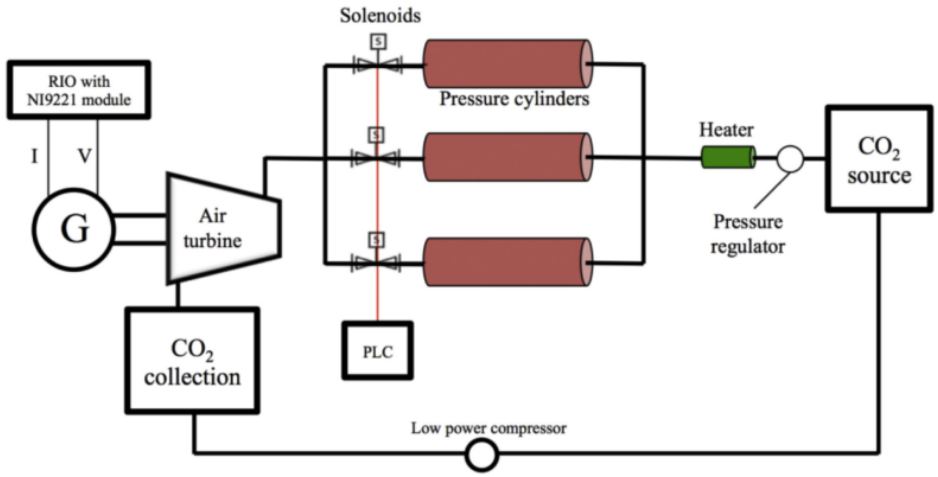

Figure 2.14- A.H. Alami et al. [62] schematic diagram of proposed system [62]

Although CO_2 considerably increases the energy density, the pressure is limited to around 60 bars, depending on the ambient temperature and the rate of heat transfer from the gas to the surrounding. Since the maximum allowable pressure of pressure vessels is around 140 bars, the working pressure of CO_2 is much lower. This indicates that CO_2 is less strenuous on the pressure vessel structure due its lower operating pressure, extending their lifetime [17].

From the study presented by A. Abuheiba et al. [17] the phenomenon of increasing the energy density by making use of gas-liquid phase change concluded interesting results through computational modelling. It was concluded that while making use of 88% CO_2 and 12% N_2 by volume at an initial pressure of 73 bar led to increasing the energy density by 56.8% higher than in the situation of pure N_2. Moreover, in their studies it was noted that compressing the mixture from 30 bar to 128 bar led to 5.26 MJ/m^3 to be stored while the maximum energy stored of N_2 was only of 5.09 MJ/m^3 [17].

Combining the HPES system presented by D. Buhagiar et al. [50] for offshore applications with CO_2 will increase its energy storage density and its efficiency, broadening the system possibility of ESS in the offshore renewable energy industry.

2.7 Carbon Dioxide in Subsea Hydro Pneumatic Energy Storage Applications

Although CO_2 is beneficial to increase the energy density for ESS, it poses some limitations and difficulties if it had to be introduced to subsea HPES systems. So far, no researcher took the initiative to integrate CO_2 within a subsea HPES system. One of the main difficulties that CO_2 poses is its corrosivity to steels but especially to carbon steel, as has been observed in the oil and gas industry [64]. Another difficulty that arises with CO_2 is that under pressure it dissolves in water and creates carbonated water, making it difficult for an HPES system to make use of water and CO_2 [65].

2.7.1 Corrosivity Protection

Corrosivity due to CO_2 is a result of complex mechanisms which are influenced by number of factors such as the physical, metallurgical and environmental parameters. Subjecting iron to CO_2 form iron carbonate film ($FeCO_3$) as a result of chemical and electrochemical processes. The formation of $FeCO_3$ is ideal at higher temperatures and high pH levels, among other factors. Dry CO_2 in itself is non-corrosive to mild steel pipeline but in the presence of water it tends to dissolve into it, forming carbonic acid (H_2CO_3) [66, 67]. Even if the CO_2 had to be separated from the compressing sea water

of the subsea HPES system, it is not guaranteed that no water will make its way towards the CO_2 portion, causing for the formation of H_2CO_3.

Making use of accumulators including high chromium levels such as 13 % to weight would mitigate the corrosivity but this results in an increase to the cost of the system [68]. Hence, corrosion mitigation for this application could take place through several mechanisms such as paint, chromium cladding and high-density polyethylene (HDPE) liner, along with other.

Paint is cheap to buy and apply but one of its draw backs is its serviceability, requiring to be reapplied causing down time of the HPES system. Chromium cladded accumulator include an inner chromium layer metallurgically bonded to the outer steel shell while offering a remarkable corrosive resistance. Fabrication of chromium cladded accumulator would be considerably expensive due to special skill required [69, 70]. High-density polyethylene liner offers necessary corrosion resistivity as chromium cladding at a lower cost, provided that the geometry of the accumulator resembles that of an oil and gas industry pipelines. Figure 2.15a and b present a steel pipeline with chromium cladding and HDPE lining, respectively [70].

2.7.2 Carbon Dioxide and Sea Water Separation Mechanisms

The CO_2 can be separated from the sea water while utilising different mechanisms. It could be assumed that the HPES accumulator geometry is similar to that of pipelines, generally used for gas and oil transportation [71, 72]. The transportation of fuel causes debris to build up within the pipeline causing clogging. Pipeline inspection gauges (PIGs) fit within the pipeline at an interference fit offering cleaning as they get pushed or pulled through.

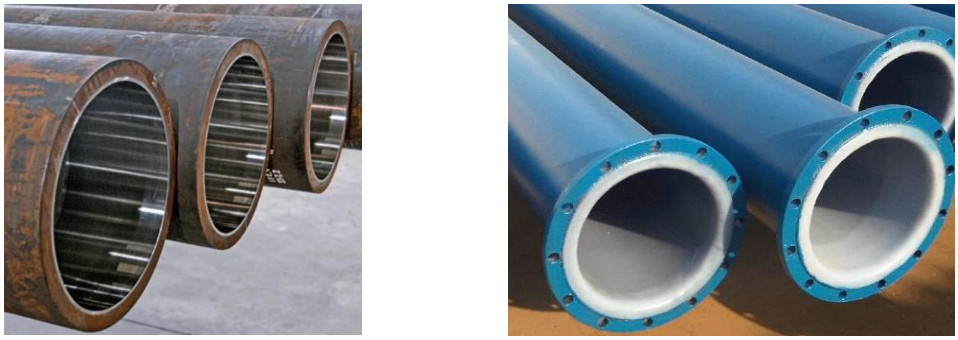

a) b)

Figure 2.15- a) Chromium cladding and b) HDPE lined pipelines [70]

Pipeline inspection gauges (PIGs) could be divided into four categories; 1) foam, 2) cup, 3) bi-directional and 4) intelligent PIGs, as could be observed through Figure 2.16. The foam PIGs are composed from flexible foam, typically one side of the pig is

sealed such that it can be propelled by the fluid flow. They can undergo under large deformations, such as irregularities in the pipeline and bends, reducing the risk of the PIG in getting stuck.

Cup PIGs are composed from a steel tube in the centre and two cups or more made from polyurethane (PU) are attached to it. The cups have a conical shape which should face the direction of motion. The driving force from the fluid flow acts on the cups which consequently leads for them to press onto the pipe wall, causing a tight seal. The tight seal reduces the possibility of any leaking fluids, making cup PIGs ideal for batching purposes. Bi-directional PIGs are also composed from a steel tube to which polyurethane discs are connected to. The discs are straight; therefore, the PIG has no preferred direction of motion, making it feasible to move in either direction and less difficult to get stuck while offering similar benefits to those of cup PIGs. Intelligent PIGs are composed from a series of cups and discs making versatile for different applications, while further containing wheels, scrapers and sensors in between to gather information about the pipeline [73, 74].

Apart from cleaning, cup and bi-directional PIGs are both used to separate liquid from a medium within the pipeline while the liquid is transported through it. This process is known as batching [75]. Such PIG characteristic could be utilised to separate the two fluids, the sea water from the CO_2.

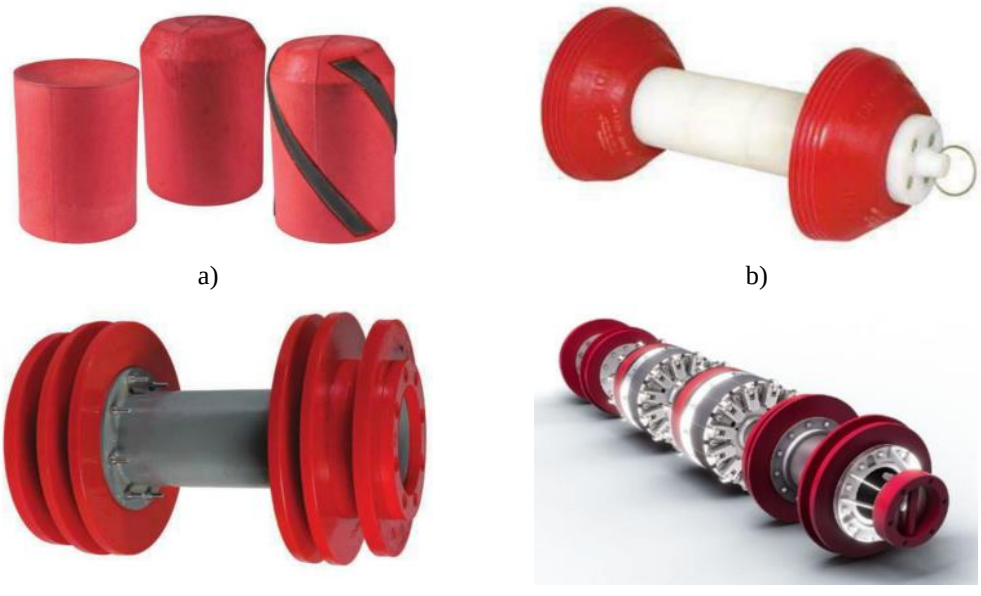

Figure 2.16- Different types of pigs: a) foam, b) cup, c) bi-directional and d) intelligent PIGs [73]

2.7.2.1 Bi-Directional Pipeline Inspection Gauge Frictional Force

Knowledge about frictional force of PIGs within pipelines play an important role. Although the frictional force on the pipeline is yet not clearly understood, the most available knowledge is based on the field experience. Due to not fully understanding the friction, estimating it often involves guess work which consequently leads to a high degree of uncertainty [72].

O'Donoghue [76] back in 1996 developed a simplified wall force model to predict the friction force of the PIG disc. This model considers the moments acting on point A of Figure 2.17, while the moments considered are the result of; 1) the differential pressure acting on the disc, 2) the friction force and the wall force, 3) the induced forces (compressive and tensile) since the disc is bent and 4) the hoop stresses [76].

Similarly, den Heijer [73] recreated the same model during his master thesis at Delft University of Technology. During the study a disparity of 45% was found between the analytical model and the finite element analysis (FEA). Moreover, within the same study a set of experiments were carried out and compared the obtained results to those from the analytical model. It was noted that the previously obtained error between analytical and FEA was also obtained between the analytical model and experiments [73]. The previously mentioned error is because the analytical model assumed that the polyurethane disc obeys Hooke's law, which is not the case. [73, 76] Therefore, using this model as an assumption of the friction model leads to a meaningless prediction [72].

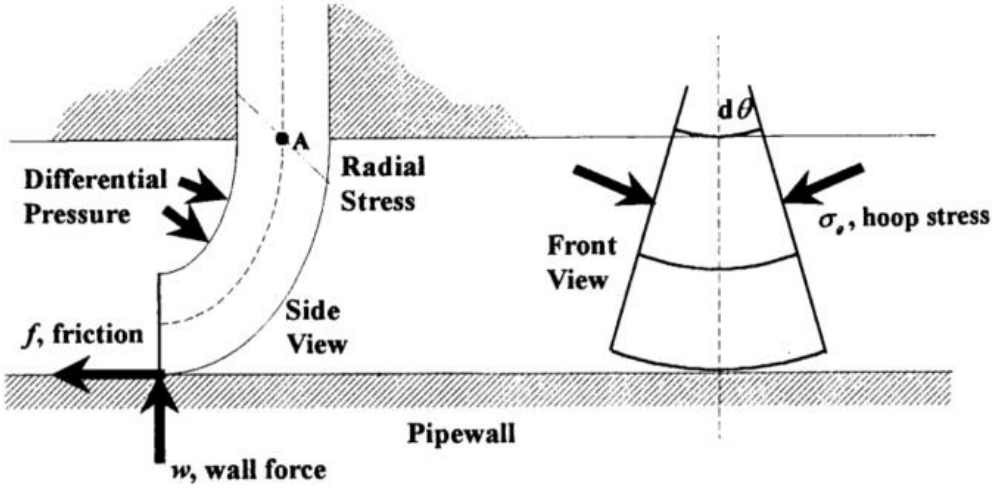

Figure 2.17- Moments acting on the system [76]

Certain analytical models treat the PIG disc as a system of springs and dampers, which is referred to as the four-element model, see Figure 2.18. In the later mentioned figure, A and C are the two linear springs while B and D are the dampers. Chang Liu et al.

[71] created an analytical model based on the four-element model to model a disc PIG while entering into the pipeline. The analytical model presented in their work proved to be reliable for predicting the driving force of the bi-directional PIG as it was compared to experimental data gathered through their work [71].

Since the frictional force is directly correlated to the driving force, such a model could be applied to estimate the friction force. In their work a great emphasis was given towards the importance that each sealing disk from the different manufactures have different spring and dampers parameters which should be determined for each disc through either experimentation, FEA or a combination of both [71].

Several researchers developed a finite element (FE) model to analyse the friction force of the PIG, such work was carried out for cup, foam and even bi-directional PIGS. Jiang et al. [77] modelled the friction for cup PIGs while obtaining results having a relative error of 10.76% [77]. Zhu et al. [72] carried out an FE model analyses to understand the relation of different variables that could affect the friction force for a bi-directional PIG. Moreover, to obtain a better understanding Zhu et al. carried out experimental test for further understanding while varying parameters. Although both experimental and FE models were carried out, it was nowhere mentioned within the study the relation between the results of the two sources [72].

One could simply agree that experimental results give the greatest observations of real-life scenarios, followed by FE modelling and finally analytical models. Although the most accurate method to determine the frictional force is through an experimental procedure, it is not always feasible. A conservative substitution to experimentation is FE models which are the most feasible and provide results within an acceptable margin of accuracy. A drawback of FE models is that they are time consuming, hence when time is an issue one might revert to analytical models while keeping in mind their limitations.

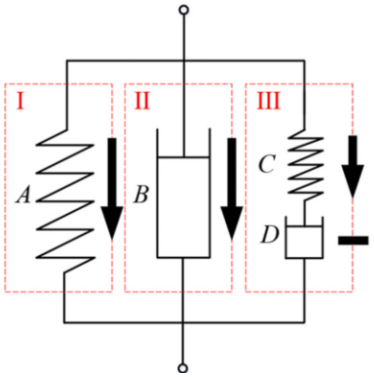

Figure 2.18- Disc modelled as a set of springs (A and C) and dampers (B and D) [71]

For this study, published FEA data are digitised through a curve fitting approach to determine the friction force. Determination of the frictional force through the results of the curve fitting approach provides results in a more computationally efficient manner over other methods.

X. Zhu et. al. [72] carried out FEA analysis on a single polyurethane rubber disc while sliding within a structural steel pipe under four different parameters being; percentage interference (δ), thickness to diameter ratio (ξ), chamfer dimension (k) and clamping rate (ζ), as represented by equations 2.1 to 2.4. In equations 2.1 to 2.4, d_s and d_p relate to the disc outer most diameter and clamping disc diameter. The contact force results presented by X. Zhu et. al. [72] based on the interference and thickness parameters (Figure 2.19a and b) along with the coefficient of friction will aid in determining the friction force of the PIG for a single polyurethane disc as discussed in section 3.2.1.1.1.

$$\delta = (d_{\mathrm{S}} - d_{\mathrm{i}}) \times \frac{100}{d_{\mathrm{i}}} \tag{2.1}$$

$$\xi = \frac{th}{d_{\mathrm{i}}} \tag{2.2}$$

$$k = \frac{r_{\mathrm{c}}}{d_{\mathrm{i}}} \tag{2.3}$$

$$\zeta = \frac{d_{\mathrm{p}}}{d_{\mathrm{i}}} \tag{2.4}$$

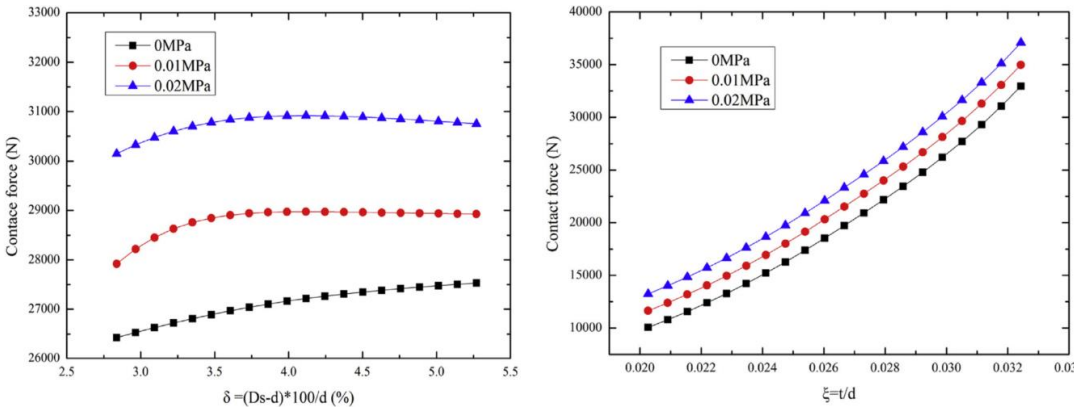

a) b)

Figure 2.19- a) Contact force (N) against percentage interference ratio (δ) and b) Contact force (N) against thickness to diameter ratio (ξ) [72]

2.8 Final Remarks

The literature review has provided an in depth understanding of the importance of ESS in the presence of RES due to their power intermittency. The five main ESS categories were discussed in an in-depth review and it has been highlighted that mechanical energy storage is superior over other ESSs. The following are the important points derived from Chapter 2;

1. The Hantrof and McIntosh plants are the oldest two full scale operational CAES plants to date;
2. CAES plants utilise salt domes and caverns for air storage but these could be replaced by pressure vessels;
3. HPES technology is a result of combining PSH with CAES while requiring smaller geographical footprint. Different HPES technologies were discussed through ongoing prototypes such as GLIDES and FLASC;
4. Carbon dioxide advantages over other gases in ESSs are discussed while highlighting the fact that researchers are continuously researching regarding this issue;
5. A modified GLIDES HPES system incorporating CO_2 as the compressible fluid is discussed while utilising mineral oil as the hydraulic fluid;
6. The main issues of utilising sea water as the compressing fluid for an HPES system while CO_2 is the compressible fluid are discussed along with ways to mitigate the associated challenges.

Through the research of this literature review, the lack of available studies investigating the thermal behaviour of subsea CO_2-based HPES systems in open literature was noted. This literature review also shed light on the limited literature highlighting the concerning issues that would arise when utilising CO_2 in practical applications of HPES systems.

The main aim of this dissertation is to investigate a novel subsea HPES system while utilising a gas experiencing a gas-liquid-gas phase change, which in this study the phase change gas is CO_2. The following chapter proposes a HPES accumulator utilising CO_2 as the compressible gas while applying the necessary measures to mitigate corrosion and dissolvability, per mentioned in Chapter 2. Moreover, this dissertation investigates the transient behaviour of the proposed subsea HPES system utilising both air and CO_2 as the compressible fluid.

3 Theoretical Background

This chapter describes a proposed subsea HPES accumulator utilising CO_2 as the compressible gas from the knowledge gained in Chapter 2. It also delves into the theory behind the mathematical modelling of the proposed accumulator utilising both air and CO_2.

3.1 Proposed Accumulator

The proposed subsea HPES accumulator, presented in Figure 3.1, is constructed from a long commercial steel pipeline laid on the seabed. Inside the steel pipeline, the HDPE inner liner is installed to mitigate the corrosive effect of liquid CO_2 at high pressures, as discussed in Chapter 2. A piston, which is also referred to as the PIG, is utilised to separate the sea water from the CO_2 to avoid any of the high-pressure gas from dissolving into the sea water. The PIG also aids to avoid water being entrapped in the pipeline due to uneven seabed. The gas is housed within the pressure chamber and is not allowed to leave the system, thus being a non-flow system. Moreover, the accumulator is enclosed from both ends with an outer plate while the chamber which does not house the gas allows water to flow in and out. The water is assumed to flow horizontally as shown in Figure 3.1.

As mentioned in section 2.4, the HPES system operates with four different stages: charging stage, first hold stage, discharging stage and second hold stage. During the first stage, a hydraulic pump is used to pump the surrounding sea water into the system, compressing the gas within the pressure chamber as a result of the change in volume caused by the pressurised sea water injected by the pump into the enclosed accumulator.

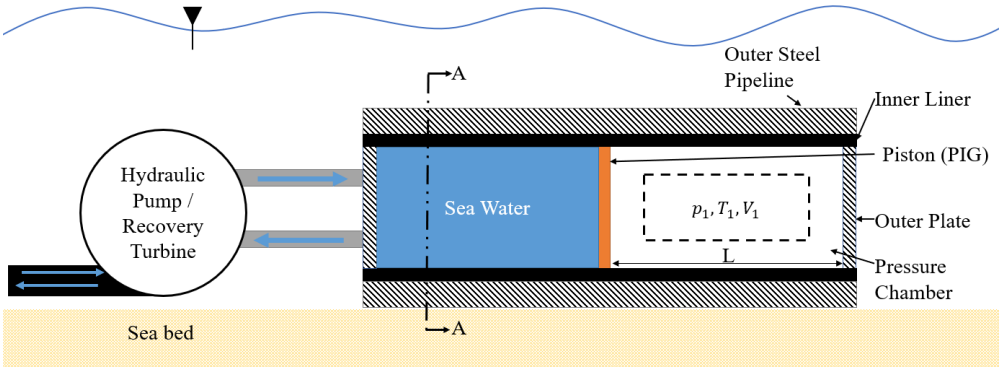

Figure 3.1- Subsea accumulator cross-section including the hydraulic pump and the recovery turbine

During the hold stages, both first and second, no work is done on or by the system as heat is lost or gained from the surrounding walls of the system and the sea water. As

the system discharges, the gas within the pressure chamber is allowed to expand to the initial pressure, causing the sea water to flow out of the system to a Pelton wheel turbine (recovery turbine) coupled with a generator. The outer steel pipeline has an outer diameter d_o and an inner diameter d_m, the outer diameter of the inner liner is equal to the inner diameter of the outer pipeline causing a transition fit, while the inner liner has inner diameter d_i, as presented in Figure 3.2.

The thermal performance characteristics of the proposed system being investigated could be evaluated in two different methods (or both): a) scaled down experimental set-up or b) numerical modelling techniques. Scaled down experimental set-ups require greater budgets than those required for numerical modelling techniques where computations could be carried out on a simple personal computer (PC). Hence, numerical modelling techniques are ideal in this case to provide preliminary understanding of the system characteristics.

Prior to carrying out numerical modelling, the following assumptions were considered; 1) the pipeline length-to-diameter ratio is relatively large such that the heat transfer between the gas to the outer plate (Figure 3.1) and the gas to the PIG are negligible, 2) the contact point of the pipeline with the seabed is negligibly small such that the outer wall of the steel pipeline is completely in contact with the surrounding sea water, 3) the inner diameter of the outer pipeline and the outer diameter of the inner liner are in direct contact to one another thus no contact resistance, 4) frictional losses are not present as the sea water is pumped into the accumulator, 5) the PIG perfectly seals the compressible gas from the compressing sea water (no dissolution of CO_2 and air into sea water) and 6) the mass of the PIG is ignored. The stated assumptions are implemented in the mathematical model of section 3.2.

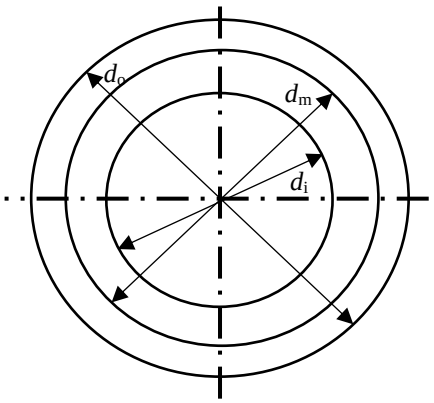

Figure 3.2- Section A-A outer steel pipeline and HDPE inner liner diameters

3.2 Mathematical Modelling

The thermal behaviour of the proposed HPES accumulator was observed with respect to time, while modelling the system using a discrete time marching approach. The change in internal energy between each time step of the system could be expressed in terms of the work done by/on the compressed fluid and the heat emitted/absorbed by the compressed fluid. The latter relation is expressed by equation 3.1, also referred to as the first law of thermodynamics. Equation 3.1 is divided into three major parts; part 1 is the work done (W) by/on the gas, part 2 is the heat transfer from/to the surrounding wall (Q) and part 3 is the internal energy of the system (ΔU).

$$\overset{prt\,3}{\widetilde{\Delta U}} = - \overset{prt\,1}{\widetilde{W}} + \overset{prt\,2}{\widetilde{Q}} \tag{3.1}$$

Positive work done indicates that work was done by the compressed gas while negative work done indicates work was done on the gas. Positive heat transfer indicates heat being absorbed from the surroundings, while negative indicates heat being emitted to the surroundings. Prior to modelling the CO_2 system, an air-based system was modelled. The theory behind the mathematical models for air and CO_2 are described in great depth in section 3.2.1and section 3.2.2.

3.2.1 Air System

The theory behind the model of the air system is divided into three main parts, similar to the first law of thermodynamics described in equation 3.1. In this case the compressible fluid remains in the gas state throughout the entire storage cycle.

3.2.1.1 Work Done (part 1)

Work done on the gas is a result of the change in volume induced by the hydraulic pump as sea water is injected into the pipeline. On the other hand, work done by the gas occurs as the pressurised seawater is allowed to flow through the turbine. The rate at which the water flows into or out of the system ($\dot{V}$) is defined by the system charging/discharging energy (E_{c-d}), the system charging/discharging duration ($t_{\mathrm{c-d}}$) and the pressure on/by the injected sea water ($p_{\mathrm{sw\,(c-d)}}$), as defined in equation 3.2. A positive flow rate indicates that the gas is being pressurised while a negative flow rate indicates that the gas is expanding. The pump pressure is a sum of the pressure within the chamber ($p_{\mathrm{ch(i-1)}}$) and the friction force (F_{f}) resulting from the PIG separating the hydraulic fluid (sea water) and the gas, as defined in equation 3.3.

$$\dot{V} = \frac{E_{\mathrm{c-d}}}{t_{\mathrm{c-d}} \times p_{\mathrm{sw\,(c-d)}}} \tag{3.2}$$

$$p_{\mathrm{sw\,(c-d)}} = \frac{\left(p_{\mathrm{ch\,(i-1)}} \times A_{\mathrm{PIG}}\right) \pm F_{\mathrm{f}}}{A_{\mathrm{PIG}}} \tag{3.3}$$

Equation 3.4 calculates the change in volume (ΔV_{i}) for the current time step, caused by the volume flow rate of the pump, while its result is used to calculate the new volume (V_{i}) within the pressure chamber through equation 3.5. The change in volume could be positive or negative depending on the stage, either charging or discharging. Furthermore, the result of equation 3.4 is used to calculate the work done (W) on/by the gas using equation 3.6. The change in volume causes the density of air within the chamber ($\rho_{\mathrm{ch\,(i)}}$) to change where the new density is calculated using equation 3.7.

$$\pm \Delta V_{\mathrm{i}} = \dot{V} \times \Delta t \tag{3.4}$$

$$V_{\mathrm{i}} = V_{\mathrm{(i-1)}} \pm \Delta V_{\mathrm{i}} \tag{3.5}$$

$$W = p_{\mathrm{ch\,(i-1)}} \times \Delta V_{\mathrm{i}} \tag{3.6}$$

$$\rho_{\mathrm{ch\,(i)}} = \frac{m}{V_{\mathrm{i}}} \tag{3.7}$$

3.2.1.1.1 Pipeline Inspection Gauge Frictional Force

The results of the contact force due percentage interference (δ) presented in Figure 2.19a were digitised through a forth order polynomial to obtain an equation in the form of $y = ax^4 + bx^3 + cx^2 + dx + e$, where the constants depend on the change in pressure (Δp) between the two surfaces of the PIG disc. Moreover, the constants a, b, c, d and e of the 3 curves at 0 Mpa, 0.01 Mpa and 0.02 Mpa were plotted to obtain an equation to determine the constant based on the Δp. The difference in pressure between the two surfaces of the disc is calculated using equation 3.8. The equations to determine the constants a, b, c, d and e at the current time step (t) are presented by equations 3.9 to 3.13, respectively. The constants obtained from equations 3.9 to 3.13 are then substituted into equation 3.14 to obtain the contact force of the disc on the wall of the pipeline based on the experimental results of X. Zhu et. Al. [72].

$$\Delta p_{\mathrm{i}} = p_{\mathrm{sw\,(i-1)}} - p_{\mathrm{ch\,(i-1)}} \tag{3.8}$$

$$a = 1017619\Delta p^2 - 15535\Delta p - 44.89 \tag{3.9}$$

$$b = -18260100.5\Delta p^2 + 290361.15\Delta p + 752.26 \tag{3.10}$$

$$c = 121522535\Delta p^2 - 2006199.5\Delta p - 4796.12 \tag{3.11}$$

$$d = -354132150.50\Delta p^2 + 6033901.05\Delta p + 14128.69 \quad (3.12)$$

$$e = 381412692\Delta p^2 - 6481194.55\Delta p + 10747.46 \quad (3.13)$$

$$C_{\mathrm{f}} = a\delta^4 + b\delta^3 + c\delta^2 + d\delta + e \quad (3.14)$$

In their work, X. Zhu et. Al. [72] utilised a pipe having an internal diameter (d_{i}) of 986.8 mm and a PIG disc having a thickness (th) of 30 mm, leading to a thickness to diameter ratio of 0.03. Hence, the resulting contact force for the different values of the thickness to diameter ratios (ξ), from Figure 2.19b, were set as a ratio of the contact force when the disc thickness to diameter ratios was equal to 0.03 and a difference in pressure of 0.1 Mpa, as presented in Figure 3.3.

Applying the curve fitting approach to the curve in Figure 3.3, equation 3.15 is obtained to determine the contact force ratio (C_{fr}) while indicating a good agreement with that of X. Zhu et. Al. [72] due to an R^2 of 0.999 relatively close to 1. The result of equation 3.15 and equation 3.14 are then applied to equation 3.16, obtaining the friction force as a result of the δ and ξ. In equation 3.16 the subscripts s and k for the coefficient of friction (μ) indicate static or kinetic friction. Static friction is considered at the initial time step when the disc starts moving, while kinetic friction is considered for the remaining time steps. Since the digitized relations from X. Zhu et. Al. [72] work only yields friction values related to the diameter of the pipeline utilized for their experimentation, an additional correction was introduced in equation 3.16 to convert the friction results from their diameter to the diameters considered in this study.

$$C_{\mathrm{fr}} = 0.0676e^{89.7719\,\xi} \quad (3.15)$$

$$F_{\mathrm{f}} = (C_{\mathrm{f}} \times C_{\mathrm{fr}}) \times \mu_{\mathrm{s/k}} \times \left(\frac{d_{\mathrm{i}}}{0.9868}\right) \quad (3.16)$$

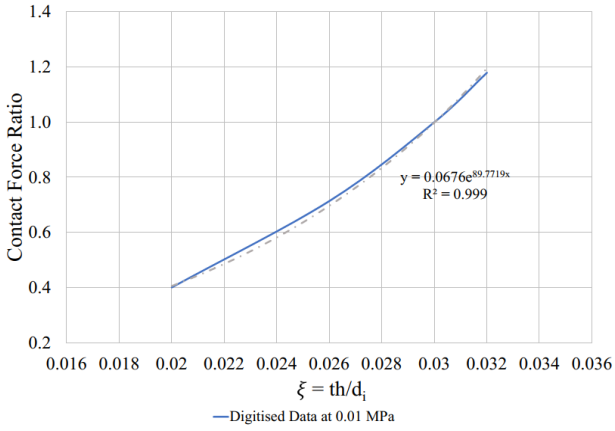

Figure 3.3- Contact force ratio against thickness to diameter (ξ) ratio

3.2.1.2 Heat Transfer (part 2)

The second part of equation 3.1 takes into account the heat transfer from the gas to the surrounding wall. The heat generated from the gas during compression is initially lost to the inner liner, then to the pipeline and finally from the steel pipeline to the surrounding sea water. On the other hand, as the gas expands, the temperature loss of the gas is gained from the inner liner, the inner linear gains heat from the outer pipeline, whilst the pipeline gains energy from the surrounding sea water. For the energy to be transferred to or from the gas, it has to pass through a series of resistances as presented in Figure 3.4. The resistances under study only consider convection and conduction. The nodes of the inner liner and outer steel pipeline were placed in the middle of both parts, as an indication of the material temperature.

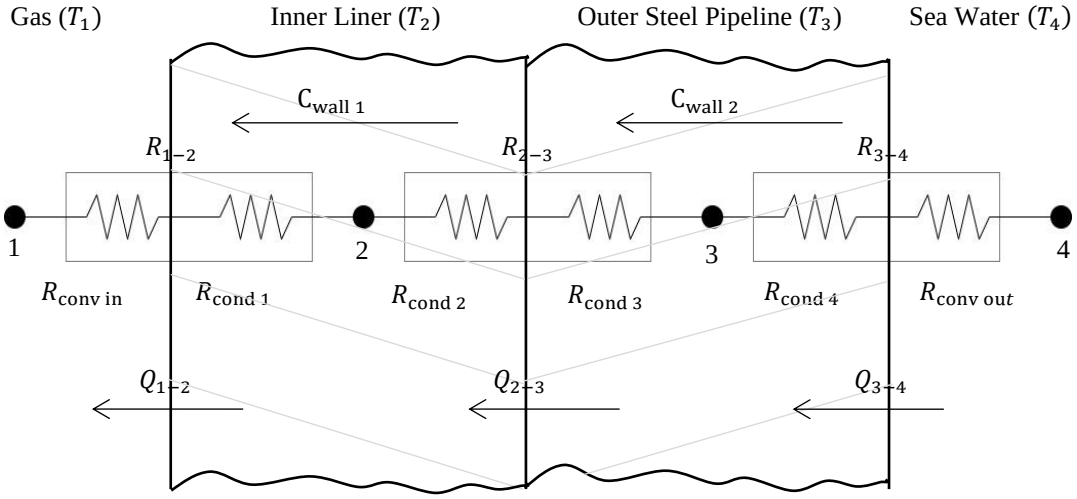

Figure 3.4- Resistances and capacitance model of the accumulator wall

The first resistance is the convective resistance of the compressible gas, presented by equation 3.17. The radius of the node for the HDPE inner liner and the outer steel pipeline are presented by equations 3.18 and 3.19, respectively. Conductive resistance of the first and second halves for the liner are presented by equations 3.20 and 3.21, where k_{inl} is the thermal conductivity of the inner liner and L_{ch} is the length of the liner in contact with the gas.

The conductive resistances of the two halves of the steel pipeline are presented by equation 3.22 and 3.23, where k_{osp} is the thermal conductivity of the outer steel pipeline while L_{ch} is the same as that of equations 3.20 and 3.21. The final resistance present within the system is that due to the thermal boundary layer of the sea water on the outer surface of the pipeline. This is presented by equation 3.24. The convective heat transfer coefficients for the inside gas and outside sea water, h_{in} and h_{out} are calculated through established equations depending on the fluid's properties.

$$R_{\text{conv in}} = \frac{1}{h_{\text{in}} A_{\text{i}}} \tag{3.17}$$

$$r_{\text{x}} = \frac{d_{\text{i}} + d_{\text{m}}}{4} \tag{3.18}$$

$$r_{\text{y}} = \frac{d_{\text{o}} + d_{\text{m}}}{4} \tag{3.19}$$

$$R_{\text{cond 1}} = \frac{\ln\left(\frac{r_{\text{x}}}{r_{\text{i}}}\right)}{2\pi k_{\text{inl}} L_{\text{ch}}} \;\&\; R_{\text{cond 2}} = \frac{\ln\left(\frac{r_{\text{m}}}{r_{\text{x}}}\right)}{2\pi k_{\text{inl}} L_{\text{ch}}} \tag{3.20 \& 3.21}$$

$$R_{\text{cond 3}} = \frac{\ln\left(\frac{r_{\text{y}}}{r_{\text{m}}}\right)}{2\pi k_{\text{osp}} L_{\text{ch}}} \;\&\; R_{\text{cond 4}} = \frac{\ln\left(\frac{r_{\text{o}}}{r_{\text{y}}}\right)}{2\pi k_{\text{osp}} \text{L}_{\text{ch}}} \tag{3.22 \& 3.23}$$

$$R_{\text{conv out}} = \frac{1}{h_{\text{out}} A_{o}} \tag{3.24}$$

Two different convective heat transfer coefficient correlations have to be considered for the gas and the surrounding sea water. For the outside convective heat transfer coefficient (h_{out}), it is assumed that the outside wall of the outer pipeline is subjected to free convective heat transfer rather than forced convection. Several correlations were developed for free convection over a horizontal pipe such as the Churchill and Chu correlation. The Churchill and Chu correlation calculates the average Nusselt number through equation 3.25 while assuming uniform heating throughout the cylindrical wall and uniform wall temperature [78]. The Rayleigh number used in the correlation is calculated through equation 3.26. The Grashof number and Prandtl number for sea water are calculated using equations 3.27 and 3.28, respectively. The constants for equation 3.26 and 3.27 are to be obtained from available literature for sea water at a temperature of 283K and salinity of approximately of 35 g/kg, as discussed in chapter 5 [79, 80]. After calculating the Nusselt number, the h_{out} is calculated through equation 3.29 which is then implemented into equation 3.24.

$$Nu_{\text{out}} = \left(0.6 + \frac{0.387 \times Ra_{\text{sw}}^{\frac{1}{6}}}{\left[1 + \left(\frac{0.559}{Pr_{\text{sw}}}\right)^{\frac{9}{16}}\right]^{\frac{8}{27}}} \right)^2 \qquad 10^{-7} < Ra < 10^{13} \tag{3.25}$$

$$Ra_{\mathrm{sw}} = Gr_{\mathrm{sw}} \times Pr_{\mathrm{sw}} \tag{3.26}$$

$$Gr_{\mathrm{sw}} = \frac{g\beta\left(T_{3\,(\mathrm{i}-1)} - T_{4\,(\mathrm{i}-1)}\right)d_{\mathrm{o}}^{3}}{v^{2}} \tag{3.27}$$

$$Pr_{\mathrm{sw}} = \frac{\nu}{D} = c_{\mathrm{p\,(sw)}}.\frac{\eta_{\mathrm{sw}}}{k_{\mathrm{sw}}} \tag{3.28}$$

$$h_{\mathrm{out}} = Nu_{\mathrm{out}} \times \frac{k_{\mathrm{sw}}}{d_{\mathrm{o}}} \tag{3.29}$$

Within the chamber, the system is considered as a non-flow system during charging and discharging stages, as already established. Few researchers carried out experimentation to determine the heat transfer correlations for non-flow systems but the available literature only considers vertical pipes with liquid pistons, as presented by Neu et al. [81, 82] The correlation derived from their experimentations considered a relatively small system compared to the one under study while the piston speeds were much greater than those expected, hence making them inapplicable for this work. The correlations for the Nusselt number from Neu et al. [81, 82] works are presented by equations 3.30 and 3.31. Selection between equation 3.30 and 3.31 depends on the length of the compression chamber whilst compared to the transitional length which is defined by equation 3.32, dependent on the piston velocity defined by equation 3.33.

$$Nu_{\mathrm{in}} = 6.67\left(Re_{\mathrm{in}} \times Pr_{\mathrm{in}}\left(\frac{d_{\mathrm{i}}}{L_{\mathrm{ch}}}\right)\right)^{0.36} \tag{3.30}$$

$$Nu_{\mathrm{in}} = 6.17\left(Re_{\mathrm{in}} \times Pr_{\mathrm{in}}\left(\frac{d_{\mathrm{i}}}{L_{\mathrm{ch}}}\right)\right)^{0.48} \tag{3.31}$$

$$L_{\mathrm{tr}} = \left(-0.0344L_{\mathrm{ch}} + 109U_{\mathrm{PIG}}d_{\mathrm{i}}^{2} + \frac{0.0227}{d_{\mathrm{i}}}\right)\left(\frac{p_{\mathrm{ch\,(i=0)}}}{p_{\mathrm{ref}}}\right)^{-0.645\sqrt{U_{\mathrm{PIG}}}} \tag{3.32}$$

$$U_{\mathrm{PIG}} = \frac{\dot{V}}{A_{\mathrm{PIG}}} \tag{3.33}$$

Since the available Nusselt correlations to cater for large non-flow systems are not yet available in open literature, it is assumed that the gas moves within the system at the same rate as the sea water is pumped into or out of the accumulator during the charging and discharging stages. For this study the flow within the pipeline is divided into two flows, laminar and turbulent flow. Laminar flow is assumed to be present at a Reynolds

number less than 3000, while at a greater value turbulent flow occurs. For laminar flow the Nusselt number is constant as presented by equation 3.34. On the other hand, several turbulent flow models exist, such as those developed by Dittus & Boelter, Sieder & Tate and Gnielinski, presented from equations 3.35 to 3.37, respectively. The correlation presented by Dittus & Boelter and Sieder & Tate are more convenient to use due to their simplicity but a drawback of these two correlations is that they could lead to errors of up to 25% while the Gnielinski correlation only leads to 10% error. Hence, for this study the Gnielinski correlation is to be used when calculating the Nusselt number within the pipeline. Applying the Gnielinski, assumes that the surface heat flux is uniform and also the temperature [50, 83, 84].

$$Nu_{\text{in}} = 4.36, \qquad Re \leq 3{,}000 \tag{3.34}$$

$$Nu_{\text{in}} = 0.023 Re_{d_{\text{i}}}^{\frac{4}{5}} Pr^{n}{}_{\text{in}} \text{ where } \begin{matrix} n = 0.4 \text{ for heating} \\ n = 0.3 \text{ for cooling} \end{matrix} \tag{3.35}$$

$$Nu_{\text{in}} = 0.027 Re_{d_{\text{i}}}^{\frac{4}{5}} Pr^{\frac{1}{3}}{}_{in} \left(\frac{\eta}{\eta_{\text{s}}}\right)^{0.14} \begin{cases} 0.6 \leq Pr_{\text{in}} \leq 160 \\ Re_{\text{in}} \geq 10{,}000 \\ \dfrac{L_{\text{ch}}}{d_{\text{i}}} \geq 10 \end{cases} \tag{3.36}$$

$$Nu_{\text{in}} = \frac{\frac{f_{\text{fr}}}{8}(Re - 1000) Pr_{\text{in}}}{1 + 12.7\left(\frac{f_{\text{fr}}}{8}\right)^{\frac{1}{2}}\left(Pr^{\frac{2}{3}}{}_{\text{in}} - 1\right)} \tag{3.37}$$

In equation 3.37, the friction factor (f_{fr}) of the pipe, defined by equation 3.38, is dependent on the material of the pipeline and its roughness value (ϵ). Moreover, the Reynolds and Prandtl equations for the inside of the pipe are obtained from equations 3.39 and 3.40, respectively, depending on the temperature of the gas. Using the result of the Nusselt number of equation 3.37, the internal convective heat transfer coefficient (h_{in}) could be estimated through equation 3.41 to be substituted into equation 3.17.

$$f_{\text{fr}} = \left(-1.8\, log\left[\left(\frac{6.9}{Re}\right) + \left(\frac{\epsilon}{3.7 d_{\text{i}}}\right)^{1.11}\right]\right)^{-2} \tag{3.38}$$

$$Re_{\text{in}} = \frac{\rho_{\text{g}} U_{\text{PIG}} d_{\text{i}}}{\eta_{\text{g}}} \tag{3.39}$$

$$Pr_{\text{in}} = \frac{c_{\text{p(g)}} \eta_{\text{g}}}{k_{\text{g}}} \tag{3.40}$$

$$h_{\text{in}} = Nu_{\text{in}} \times \frac{k_{\text{in}}}{d_{\text{i}}} \tag{3.41}$$

In literature, the h_{in} is stated to range from 2 to 25 W.m^{-2}K^{-1} for free convection, as the accumulator experience during the first and second hold stages. Therefore, to be conservative the h_{in} would be ideally set to 10 W.m^{-2}K^{-1} for both hold stages [85, 83].

3.2.1.3 Change in Internal Energy (part 3)

The resistances between each node act in series to one another, therefore the summation of resistances between node 1-2, 2-3 and 3-4 of Figure 3.4 are presented by equations 3.42 to 3.44, respectively. Moreover, the heat transfer between each node is presented by equation 3.45 to 3.47, where the temperature of each node is that of the previous time step.

$$R_{2-1} = R_{\text{conv in}} + R_{\text{cond 1}} \tag{3.42}$$

$$R_{3-2} = R_{\text{cond 2}} + R_{\text{cond 3}} \tag{3.43}$$

$$R_{4-3} = R_{\text{cond 4}} + R_{\text{conv out}} \tag{3.44}$$

$$Q_{2-1} = \frac{(T_2 - T_1)_{\text{i}-1}}{R_{2-1}} \times \Delta t \tag{3.45}$$

$$Q_{3-2} = \frac{(T_3 - T_2)_{\text{i}-1}}{R_{3-2}} \times \Delta t \tag{3.46}$$

$$Q_{4-3} = \frac{(T_4 - T_3)_{\text{i}-1}}{R_{4-3}} \times \Delta t \tag{3.47}$$

To determine the temperature of the gas, the result of equation 3.6 and the result of equation 3.45 are both substituted into equation 3.1. Equation 3.1 is then transformed into equation 3.48 to obtain the new temperature of the gas within the chamber at the current time step.

$$mc_v(T_{\text{i}} - T_{\text{i}-1}) = -W + Q_{2-1}$$

$$T_{1\,(\text{i})} = \frac{(-W + Q_{1-2})}{mc_{\text{v}}} + T_{1\,(\text{i}-1)} \tag{3.48}$$

The energy equation, presented by equation 3.49, is transformed to equation 3.50 to determine the temperature of the HDPE inner liner, while its volume is calculated through equation 3.51. Equation 3.52 is used to determine the temperature of the outer steel pipeline, while its volume is equated through equation 3.53.

$$\dot{E}_{\text{in}} - \dot{E}_{\text{out}} + \dot{E}_{\text{gen}} = \rho c V \left(\frac{dT}{dt}\right) \tag{3.49}$$

$$T_{2\,(\text{i})} = \left(\frac{Q_{2-1} - Q_{3-2}}{\rho_{\text{inl}} \times V_{\text{inl}} \times c_{\text{inl}}}\right) + T_{2\,(\text{i}-1)} \tag{3.50}$$

$$V_{\text{inl}} = \left(\frac{\pi(d_{\text{m}}^2 - d_{\text{i}}^2)}{4}\right) \times L_{\text{ch}} \tag{3.51}$$

$$T_{3\,(\text{i})} = \left(\frac{Q_{3-2} - Q_{4-3}}{\rho_{\text{osp}} \times V_{\text{osp}} \times c_{\text{osp}}}\right) + T_{3\,(\text{i}-1)} \tag{3.52}$$

$$V_{\text{osp}} = \left(\frac{\pi(d_{\text{o}}^2 - d_{\text{m}}^2)}{4}\right) \times L_{\text{ch}} \tag{3.53}$$

Equation 3.50 and 3.52 are obtained from equation 3.49 since in both cases no internal energy ($\dot{E}_{\text{gen}}$) is being generated, thus reaching zero while the energy input into the nodes ($\dot{E}_{\text{in}}$) and the energy output from the nodes ($\dot{E}_{\text{out}}$) remain for both cases. For instance, as heat dissipated from the gas, energy transfer between nodes 1 and 2 act as an input ($\dot{E}_{\text{in}}$) into node 2 while energy transfer between 2 and 3 acts as an output ($\dot{E}_{\text{out}}$), depicted by Figure 3.4. Similarly, the energy between nodes 2 and 3 acts as an input ($\dot{E}_{\text{in}}$) into node 3 while energy transfer between 3 and 4 acts as an output ($\dot{E}_{\text{out}}$).

3.2.1.4 Chamber Pressure

The air within the system is considered to be a real gas since during operation it is assumed to operate near isothermal conditions at high pressure and low temperatures. Through research it was noted that air is assumed to be an ideal gas at high pressures and high temperatures or low pressures and low temperatures [86]. Therefore, since within this study it was expected for the gas to operate at high pressures and low temperatures, the gas was assumed to be real. Consequently, equation 3.54 was not considered to be applicable for such scenario.

$$p_{\text{ch (i)}} = \frac{mRT_{1\,(\text{i})}}{V_{(\text{i})}} \tag{3.54}$$

Introducing the compressibility factor (Z) to equation 3.54 modify the results towards real scenarios through a constant, as presented by equation 3.55. The compressibility factor is dependent on two constants; the reduced pressure and reduced temperature, defined by equation 3.56 and 3.57. In equation 3.56, p_{cr} is the critical pressure and in equation 3.57 T_{cr} is the critical temperature. For air the critical pressure is of 37.86 bar and the critical temperature is of 132.48 K [87]. Depending on the gas, the Z-value could be obtained from Figure 3.5, depending on the values of P_{R} and T_{R}.

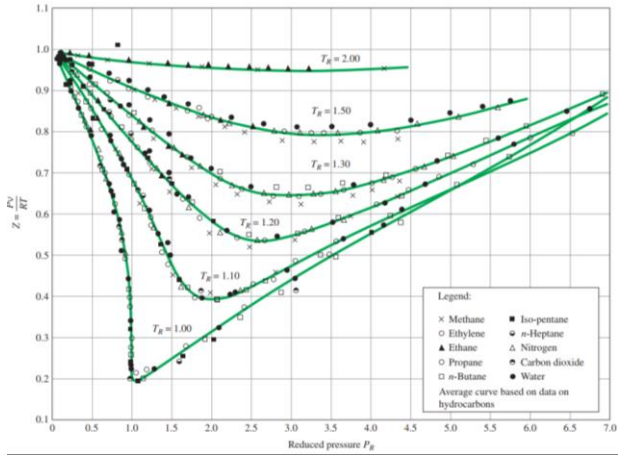

Figure 3.5- Compressibility factor as a result of the reduced pressure and temperature [86]

The present HPES is assumed to operate at a maximum allowable pressure of 60 bar and a temperature of approximately 283K, assuming that the system operates close to isothermal. Utilising equation 3.56 and 3.57, P_{R} results to be equal to 1.585 and T_{R} equal to 2.136. The value of T_R is outside the range of the values presented in Figure 3.5, therefore other analytical equations are considered for the air pressure [86].

$$p_{\mathrm{ch\ (i)}} V_{\mathrm{(i)}} = Z_{\mathrm{(i)}} R T_{1\ \mathrm{(i)}} \tag{3.55}$$

$$P_R = \frac{p_{\mathrm{ch\ (i)}}}{p_{\mathrm{cr}}} \tag{3.56}$$

$$T_R = \frac{T_{1\ \mathrm{(i)}}}{T_{\mathrm{cr}}} \tag{3.57}$$

Several equations through experimentations have been developed to model the pressure of a real gas as a result of the temperature and volume of the chamber, such as: 1) the van der Waals Equation of State, equation 3.58, 2) the Beattie-Bridgeman Equation of State, equation 3.59 and 3) the Benedict-Webb-Rubin Equation of State, equation 3.60. Van der Waals equation of state constants are determined through the p_{cr} and T_{cr}, previously mentioned for the compressibility factor, while also applying the universal gas constant, R, of 8.3145 J.mol^{-1}.K^{-1}. The constants of air for the Beattie-Bridgeman equation of state are illustrated in Table 3.1 along with those for the Benedict-Webb-Rubin equation of state but for Nitrogen. For the Benedict-Webb-Rubin, constants of air are not yet defined but since air is almost 78% Nitrogen, N_2, its constants could be considered [86, 88].

$$\left(p_{\text{ch (i)}} + \frac{a}{\bar{v}^2}\right)(\bar{v} - b\,) = RT_{1\text{ (i)}}$$

$$a = \frac{27R^2T_{\text{cr}}^2}{64p_{\text{cr}}} \quad \text{and} \quad b = \frac{RT_{\text{cr}}}{8\,p_{\text{cr}}} \tag{3.58}$$

$$p_{\text{ch (i)}} = \frac{RT_{1\text{ (i)}}}{\bar{v}^2}\left(1 - \frac{c}{\bar{v}T_{1\text{ (i)}}^3}\right)(\bar{v} + B) - \frac{A}{\bar{v}^2}$$

$$A = A_0\left(1 - \frac{a}{\bar{v}}\right) \text{ and } B = B_0\left(1 - \frac{b}{\bar{v}}\right) \tag{3.59}$$

$$p_{\text{ch (i)}} = \frac{RT}{\bar{v}} + \left(B_0RT_{1\text{ (i)}} - A_0 - \frac{C_0}{T_{1(\text{i})}^2}\right)\left(\frac{1}{\bar{v}^2}\right) + \frac{bRT_{1\text{ (i)}} - a}{\bar{v}^3} + \frac{a\alpha}{\bar{v}^6} + \frac{c}{\bar{v}^3T_{1(\text{i})}^2}\left(1 + \frac{\gamma}{\bar{v}^2}\right)e^{-\frac{\gamma}{\bar{v}^2}} \tag{3.60}$$

Table 3.1-Beattie-Bridgeman and Benedict-Webb-Rubin equations of state constants **[86]**

Beattie-Bridgeman Equation of State Constants								
Air	A_0	a	B_0	b	c			
	131.8441	0.01931	0.04611	-0.001101	4.34×10^4			
Benedict-Webb-Rubin Equation of State Constants								
Nitrogen, N_2	a	A_0	b	B_0	c	C_0	α	γ
	2.54	106.73	0.00233	0.04074	7.379×10^4	8.164×10^5	1.272×10^{-4}	0.0053

The equation presented by van der Waals has its accuracy range limited, while the Beattie-Bridgeman equation applies up to a chamber density of 0.8 times that of the critical density (ρ_{cr}) of air ($\rho_{\text{ch}} \leq 0.8\rho_{\text{cr}}$). The critical air density is of 231 kg.m^{-3}. [88] Moreover, the Benedict-Webb-Rubin applies up to a chamber density of 2.5 times that of the critical density of air ($\rho_{\text{ch}} \leq 2.5\rho_{\text{cr}}$). Since the Benedict-Webb-Rubin equation of state considers 8 constants, this would be computationally expensive as compared to the Beattie-Bridgeman equation which considers only 5 constants (Table 3.1). Hence, the Beattie-Bridgeman equation of state is implemented given the advantages of this real gas model over the other models, while also ensuring that the condition of the critical density is satisfied.

3.2.2 Carbon Dioxide System

Carbon dioxide is one of the main gases causing the greenhouse effect, hence capturing CO_2 reduces the greenhouse effect and potentially be used for refrigeration or energy storage. [89] Compressing CO_2 in a gaseous state to a temperature and pressure below its critical point leads to partial condensation as the liquid-vapour state is reached, with the CO_2 existing a two-phase fluid, in vapour and liquid form (refer to Figure 2.12).

Carbon dioxide in its liquid form allows for greater energy storage densities since the fluid is in its saturated liquid form occupying less volume than in its saturated vapour form or superheated form.

To establish whether the gas is initially liquefied or not, the dryness fraction is calculated through equation 3.61. A dryness fraction less than 1 indicates that the CO_2 is partially liquified. In equation 3.61 v_{spec} is the specific volume which is calculated through equation 3.62. Similarly, to the air-based HPES system, the CO_2 HPES 4 stages could be described by the first law of thermodynamics, equation 3.1.

$$x = \frac{v_{\text{spec}} - v_{\text{L}}}{v_{\text{V}} - v_{\text{L}}} \tag{3.61}$$

$$v_{\text{spec}} = \frac{V_{(\text{i})}}{m} \tag{3.62}$$

3.2.2.1 Work Done (part 1)

The work done on the carbon dioxide is also done hydraulically via a hydraulic pump which injects sea water into the system causing the volume of the system to change while overcoming the piston friction, similarly to section 3.2.1.1. The pump flow rate is calculated using equation 3.2 while the pump pressure is calculated from equation 3.3. The change in volume within the pressure chamber as a result of the pump flow rate for the current time step is calculated using equation 3.4, while the new volume of the chamber is calculated through equation 3.5.

The work done by the seawater on the gas as a result of the change in volume is calculated through equation 3.6. The new volume causes the density of the system to change since it is a non-flow system while the mass remains constant, hence the new density is calculated by utilizing equation 3.7. The frictional force imposed by the PIG remains dependent on its interference ratio, defined by equation 2.1 and the thickness to diameter ratio defined by equation 2.2. Moreover, the previously determined digitized correlations for friction still apply.

3.2.2.2 Heat Transfer (part 2)

Similarly to section 3.2.1.2, the heat transfer direction of the compressible fluid relies on the stage of the HPES cycle and the respective temperature of the fluid. The thermal resistances presented in Figure 3.4 for air apply for carbon dioxide as well. Heat transfer for CO_2 also depends on the resistances illustrated by equations 3.17 and 3.20 to 3.24. The mixture of liquid and vapour CO_2 introduces new challenges over those of air, such as calculating the internal convective heat transfer coefficient depending

on the dryness fraction (x). On the other hand, the state of the fluid does not impact the conduction of the outer pipeline and the inner liner nor the convective heat transfer on the outer pipeline. Thus, the Churchill and Chu correlation for the Nusselt number on the outer pipeline presented by equation 3.25 also apply for CO_2. [78] Within the pressure chamber (accumulator), the convective heat transfer coefficient requires to be considered at two separate states: 1) the gaseous state only and 2) the liquid-vapour mixture state.

During the gaseous state, similar to that of air, the Nusselt number of carbon dioxide also depends on the flow type, that is whether laminar or turbulent. Similar to air, the flow type depends on the Reynolds number where for a Reynolds number less than 3000 the CO_2 in its gaseous state is considered to be laminar, while greater than 3000 it is considered as turbulent. For laminar flow the Nusselt number is presented by equation 3.34, while for turbulent flow the Nusselt number is calculated through the Gnielinski correlation presented by equation 3.37. The Gnielinski constants of the gas are calculated using equations 3.38 to 3.40 while substituting the necessary constants of CO_2 depending on the temperature and pressure within the pressure chamber.

When a fluid changes its phase from liquid to vapour, it is referred to as evaporating while when the vapour is transforming to liquid it is said to be condensing. The CO_2 is expected to experience condensation during the charging and evaporation during the discharging. Condensation of the CO_2 gas occurs when the temperature of the gas is greater than that of the surrounding wall, causing it to condensate. On the other hand, when the temperature of the CO_2 is less than that of the surrounding wall, the gas evaporates. These two different scenarios greatly influence the internal convective heat transfer coefficient (h_{in}). Several correlations were developed through time for both condensation and evaporation, but due to some limitations within certain correlations, only one correlation had to be selected for evaporation and condensation [90].

After reviewing a number of correlations for condensation, the Thome et al. [90] model was selected due to being most appropriate model to use due to its simplicity, ease of use and accuracy across a wide range of refrigerants. The local condensing heat transfer coefficient is presented by equation 3.63 which was derived by Thome et al. [90] during their work.

$$h_{\mathrm{in}} = \frac{h_{\mathrm{f}} r_{\mathrm{i}} \theta + (2\pi - \theta) r_{\mathrm{i}} h_{\mathrm{c}}}{2\pi r_{\mathrm{i}}} \tag{3.63}$$

The falling film angle (θ) presented in Figure 3.6, is equal to the stratified angle ($\theta_{\text{strat}} = \theta$) for a stratified flow. The stratified angle is obtained by solving equation 3.64 and the cross-sectional area occupied by the liquid (A_{L}) is calculated from equation 3.65. Moreover, the area occupied by the vapour is determined through equation 3.66 [90].

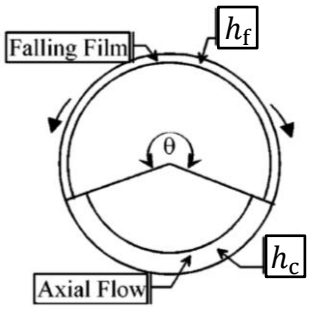

Figure 3.6- Representation of the angle and the falling film for liquefied carbon dioxide [90]

$$A_{\text{L}} = \frac{d_{\text{i}}^2}{8}[(2\pi - \theta_{\text{strat}}) - \sin(2\pi - \theta_{\text{strat}})] \tag{3.64}$$

$$A_{\text{L}} = (1 - \alpha)A \tag{3.65}$$

$$A_{\text{V}} = \text{A} - A_{\text{L}} \tag{3.66}$$

The local vapour void fraction (α) is calculated through equation 3.67 while its parameters are calculated from equation 3.68 and 3.69. Equation 3.68 is based; 1) on the total mass velocity/flux of liquid and vapour (G) which defines the flow of the fluid, 2) the surface tension (σ), 3) dryness fraction (x) and 4) the liquid and vapour densities(ρ_{L} and ρ_{V}) [91].

Equation 3.70 calculates the convective heat transfer coefficient for condensation (h_{c}), where the Reynolds number, Prandtl number and interfacial roughness correction factor are calculated through equation 3.71, 3.72 and 3.73, respectively. The liquid film thickness (δ) is calculated by solving equation 3.74 while making use of the result of equation 3.65. To determine the interfacial roughness correction factor, the G of stratified flow is required which is calculated from equation 3.75. Equation 3.63, requires the film condensation heat transfer coefficient at the top perimeter (α_{f}) which is calculated through equation 3.76 [90]. Moreover, the necessary results obtained from equations 3.64 to 3.76 are substituted into equation 3.64 to obtain the h_{in}.

$$\alpha = \frac{(\alpha_{\mathrm{h}} - \alpha_{\mathrm{ra}})}{\ln\left(\frac{\alpha_{\mathrm{h}}}{\alpha_{\mathrm{ra}}}\right)} \tag{3.67}$$

$$\alpha_{\mathrm{ra}} = \frac{x}{\rho_{\mathrm{V}}}\left([1 + 0.12(1-x)]\left[\frac{x}{\rho_{\mathrm{V}}} + \frac{1-x}{\rho_{\mathrm{L}}}\right] + \frac{(1.18(1-x)[g\sigma(\rho_{\mathrm{L}} - \rho_{\mathrm{V}})]^{0.25})}{G\rho_{\mathrm{L}}^{0.5}}\right)^{-1} \tag{3.68}$$

$$\alpha_h = \left[1 + \frac{1-x}{x}\left(\frac{\rho_{\mathrm{V}}}{\rho_{\mathrm{L}}}\right)\right]^{-1} \tag{3.69}$$

$$h_{\mathrm{c}} = \frac{\mathrm{cRe}_{\mathrm{L}}^{\mathrm{n}}\mathrm{Pr}_{\mathrm{L}}^{\mathrm{m}}k_{\mathrm{L}}\mathrm{f_i}}{\delta} = \frac{0.003\mathrm{Re}_{\mathrm{L}}^{0.74}\mathrm{Pr}_{\mathrm{L}}^{0.5}k_{\mathrm{L}}\mathrm{f_i}}{\delta} \tag{3.70}$$

$$Re_{\mathrm{L}} = \frac{4\mathrm{G}(1-\mathrm{x})\delta}{(1-\varepsilon)\eta_{\mathrm{L}}} \tag{3.71}$$

$$Pr_{\mathrm{L}} = \frac{c_{\mathrm{p(L)}}\eta_{\mathrm{L}}}{\lambda_{\mathrm{L}}} \tag{3.72}$$

$$f_{\mathrm{i}} = 1 + \left(\frac{u_{\mathrm{V}}}{u_{\mathrm{L}}}\right)^{\frac{1}{2}}\left(\frac{(\rho_{\mathrm{L}} - \rho_{\mathrm{V}})g\delta^2}{\sigma}\right)^{\frac{1}{4}}\left(\frac{G}{G_{\mathrm{strat}}}\right) \tag{3.73}$$

$$A_{\mathrm{L}} = \frac{2\pi - \theta}{8}[d_{\mathrm{i}}^2 - (d_{\mathrm{i}} - 2\delta)^2] \tag{3.74}$$

$$G_{\mathrm{strat}} = \left\{\frac{(226.3)^2 A_{\mathrm{Ld}}A_{\mathrm{Vd}}\rho_{\mathrm{V}}(\rho_{\mathrm{L}} - \rho_{\mathrm{V}})\eta_{\mathrm{L}}g}{x^2(1-x)\pi^3}\right\}^{1/3} + 20x \tag{3.75}$$

$$h_{\mathrm{f}} = 0.655\left[\frac{\rho_{\mathrm{L}}(\rho_{\mathrm{L}} - \rho_{\mathrm{V}})gh_{\mathrm{LV}}\lambda_{\mathrm{L}}^3}{\eta_{\mathrm{L}}d_{\mathrm{i}}q}\right]^{\frac{1}{3}} \tag{3.76}$$

There are specific correlations developed for CO_2 only to model the convective heat transfer coefficient correlations during evaporation. The selected correlations to calculate the Nusselt number for evaporation, the Fang model, is presented by equation 3.77 [89].

$$Nu_{\mathrm{in}} = \frac{0.00061(S+F)Re_{\mathrm{L}}Fa^{0.11}Pr_{\mathrm{L}}^{0.4}}{\left[\ln\left(\frac{1.024\eta_{\mathrm{L.f}}}{\eta_{\mathrm{L,w}}}\right)\right]} \tag{3.77}$$

The constants for the Fang Nusselt number are presented by equations 3.78 to 3.80. The Reynolds number, the boiling number and the new dimensionless number are equated through equation 3.81 to 3.83. A drawback of the Fang correlation is that it is not capable to predict the Nusselt number towards the saturated gas line, when the

dryness fraction is between 0.998 and 1 [89]. Finally, the $h_{\text{in}}$for the two-phase condensing fluid is calculated from equation 3.84.

$$S = 41000Bo^{1.13} - 0.275 \tag{3.78}$$

$$F = \left(\frac{x}{1-x}\right)^{a}\left(\frac{\rho_L}{\rho_V}\right)^{0.4} \tag{3.79}$$

$$a = \begin{cases} 0.48 + 0.00524(Re_{\text{L}}Fa^{0.11})^{0.85} - 5.9\times10^{-6}(Re_{\text{l}}Fa^{0.11})^{1.85} \\ Re_{\text{L}}Fa^{0.11} < 600 \\ \\ 0.87 \\ 600 \le Re_{\text{L}}Fa^{0.11} \le 6000 \\ \\ 160/(Re_{\text{L}}Fa^{0.11})^{0.6} \\ Re_{\text{L}}Fa^{0.11} > 6000 \end{cases} \tag{3.80}$$

$$Re_{\text{L}} = \frac{(1-x)GD_h}{\eta_{\text{L}}} \tag{3.81}$$

$$Bo = \frac{q}{Gh_{\text{LV}}} \tag{3.82}$$

$$Fa = \frac{(\rho_{\text{L}} - \rho_{\text{V}})\sigma}{G^2 D_{\text{h}}} \tag{3.83}$$

$$h_{\text{in}} = Nu_{\text{in}} \times \left(\frac{k_L}{d_{\text{i}}}\right) \tag{3.84}$$

In both correlations, condensation and evaporation, one of the most important factors is the system total mass flux, being the mass leaving the system per second. Since the HPES system under study involves a non-flow process and the mass of the CO_2 remains constant, therefore the mass flux had to be pre-determined. To be conservative a mass flux of 30 kg/m^{2}s was selected for both correlations, resulting in a stratified flow. Greater mass flux values result in different flow which yield greater convective heat transfer coefficients.

From literature, the internal convective heat transfer coefficient during the first and second hold stages is ideally set to 10 W.m^{-2}K^{-1} for CO_2 in its gaseous state and 1000 W.m^{-2}K^{-1} in the two-phase region [85, 83, 92].

3.2.2.3 Change in Internal Energy (part 3)

The third part of equation 3.1, deals with the change in internal energy of the system. For the gaseous state, the change in internal energy is expressed by equation 3.85, as

previously described in section 3.2.1.3 for air. Furthermore, the temperature of CO_2 in the gaseous state at the current time step is calculated from equation 3.48.

$$\Delta U = mc_{\mathrm{V}}\left(T_{1\,(\mathrm{i})} - T_{1\,(\mathrm{i}-1)}\right) \tag{3.85}$$

Since the specific heat at constant volume, c_{V}, of CO_2 for the two-phase region is not yet well-defined, other methods had to be implemented. The specific internal energy of the two-phase region could be described by equation 3.86. Equation 3.87 provides a modified version of the first law of thermodynamics, where the specific internal energy of the current time step is in terms of the specific work done, heat transfer and internal energy of the previous time step. The specific enthalpy of the current time step for equation 3.86 is calculated through equation 3.88 where the specific enthalpy of the liquid and vapour state depend on the temperature of the current time step.

$$u_{(\mathrm{i})} = h_{(\mathrm{i})} - p_{\mathrm{ch\,(i)}} v_{\mathrm{spec\,(i)}} \tag{3.86}$$

$$u_{\,\mathrm{eqn\,(i)}} = u_{(\mathrm{i}-1)} + \frac{W_{(\mathrm{i})}}{m} - \frac{Q_{(\mathrm{i})}}{m} \tag{3.87}$$

$$h_{(\mathrm{i})} = h_{\mathrm{L\,(i)}} + x(h_{\mathrm{V\,(i)}} - h_{\mathrm{L\,(i)}}) \tag{3.88}$$

In theory, if the temperature used to find the specific enthalpies at the liquid and vapour state corresponds to the actual temperature of the current time step, there should be no difference between the specific internal energy (u) calculated from equation 3.86 to that of equation 3.87. If the u from equation 3.86 is different than that of equation 3.87, then the temperature is increased or decreased at a specified increment, T_{inc}, accordingly where T_{inc} is defined in section 7.1. The specific enthalpy is then recalculated for the new temperature properties while recalculating the dryness fraction for the new temperature, as well. This process is repeated until the difference between the results of equation 3.86 to equation 3.87, calculated by equation 3.89, reach the acceptable minimal value. The temperature satisfying the condition is set as the current time step temperature.

$$u_{\mathrm{dif\,(i)}} = \left|\frac{u_{\,\mathrm{eqn\,(i)}} - u_{(\mathrm{i})}}{u_{\mathrm{eqn\,(i)}}}\right| \times 100 \tag{3.89}$$

As already established, the state of the CO_2 does not influence the heat transfer towards nodes 2 and 3 of Figure 3.4. Therefore, the temperature of nodes 2 and 3 is calculated

through equations 3.50 and 3.52, while the heat transfer of node 1 to 2, 2 to 3 and 3 to 4 are calculated through equations 3.45 to 3.47.

3.2.2.4 Chamber Pressure

For the gaseous state different methods could be implemented to determine the new pressure at the current time step. The Beattie-Bridgeman equation of state could be implemented for CO_2 with the necessary constants of Table 3.2 into equation 3.59. Another equation of state is that defined by Redlich-Kwong, presented by equation 3.90, where its constant a and b require the critical pressure (p_{cr}) and temperature (T_{cr}) of CO_2. Moreover, the pressure at the current time step could also be obtained through the *CoolProp* (*CP*) library presented by the *Python*® while utilising the *PropSI* function as presented in equation 3.91. [93]

Table 3.2-Beattie-Bridgeman Equation of State Constants [86]

	A_0	a	B_0	b	c
Carbon Dioxide, CO_2	507.2836	0.07132	0.10476	0.07325	6.60×10^5

$$p_{\text{ch (i)}} = \frac{RT_{1\text{ (i)}}}{\bar{v} - b} - \frac{a}{\sqrt{T_{1\text{ (i)}}}\bar{v}(\bar{v} + b)}$$
$$a = 0.42748\left(\frac{R^2 T_{cr}^{2.5}}{p_{cr}}\right) \text{ and } b = 0.08664\left(\frac{RT_{cr}}{p_{cr}}\right) \quad (3.90)$$

$$p_{\text{ch (i)}} = CP.PropsSI('P',\ 'T', T_{1\text{ (I)}},\ 'D', \rho_{\text{ch (i)}}, R744) \quad (3.91)$$

The three different methods were compared to each other during the charging and discharging stages, as presented in Figure 3.7. It could be observed that the Redlich-Kwong equation of state gave higher pressures than the other two methods. The library method and Beattie-Bridgeman equation of state gave results close to one another.

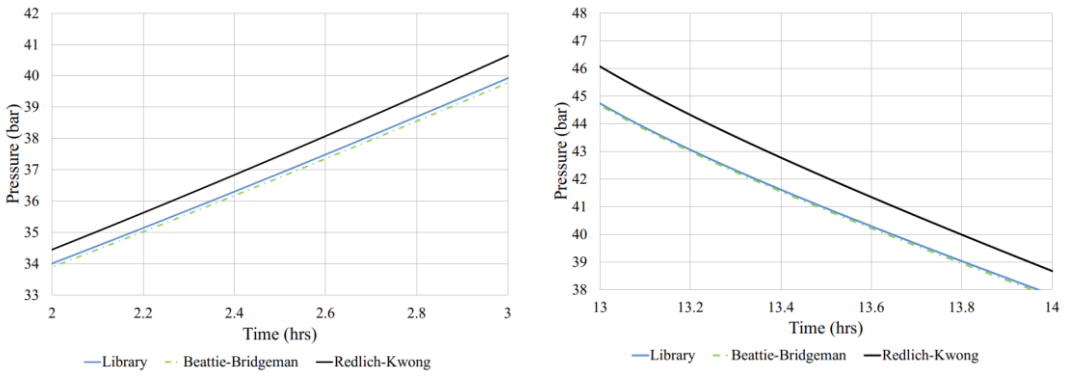

Figure 3.7- Library, Beattie-Bridgeman equation of state and Redlich-Kwong equation of state pressure finding methods, a) charging and b) discharging stages (Pressure (bar) against Cycle Time (hrs))

During the liquid-vapour state of CO_2, the pressure is to be obtained from the *CoolProp* library using equation 3.92 according to the final temperature which satisfies the acceptable minimal value of the specific internal energy (u_{dif}), equation 3.89. Since for the liquid-vapour state the library is used, it is ideal to make use of the library for the gaseous state, therefore using equation 3.91 [93].

$$p_{\mathrm{ch\,(i)}} = CP.PropsSI('P',\ 'T', T_{1\,(\mathrm{i})}, 'Q', 1, R744) \tag{3.92}$$

3.3 The Cycle Energy Factor

To quantify the efficiency of the HPES accumulator across the entire storage cycle, the term cycle energy factor (CEF) is used. The CEF is defined as the ratio between the hydraulic energy extracted to that injected into the accumulator. The CEF is used since, under real operating conditions, the sea water temperature may change during the entire cycle due to sea water temperature increase as a result of the solar radiation. Such behaviour was experienced by D. Buhagiar et al. [47] during their prototype testing. Therefore, the term efficiency would become inappropriate since other external sources are acting on the system apart from those of the pump.

Throughout this thesis CEF is used to avoid any ambiguity as already done in other publications, such as those presented in D. Buhagiar et al. [47]. Yet, it is important to note that when the sea water temperature remains unchanged during the entire storage cycle, as should be the case in this study, the CEF is equal to the system efficiency. The energy stored during the charging stage is calculated by equation 3.93 while the energy recovered during the discharging stage is presented by equation 3.94, where p_{h} is the pressure of the seawater column acting on the accumulator, calculated by equation 3.95. The CEF of the system is finally equated through equation 3.96.

$$E_{\mathrm{ch}} = \int_{V_1}^{V_2} p dV = \sum_{i=1}^{N_{\mathrm{st}}} \left[(p_{\mathrm{ch}} - p_{\mathrm{h}}) \times \left(\dot{V}_{\mathrm{in\,(t)}} \times \Delta t \right) \right]_{\mathrm{i}} \tag{3.93}$$

$$E_{\mathrm{dis}} = \sum_{i=1}^{N_{\mathrm{dis}}} \left[(p_{\mathrm{sw}} - p_{\mathrm{h}}) \times \left(\dot{V}_{\mathrm{out\,(i)}} \times \Delta t \right) \right]_{\mathrm{i}} \tag{3.94}$$

$$p_{\mathrm{h}} = \rho_{\mathrm{sw}} g h_{\mathrm{depth}} \tag{3.95}$$

$$CEF = E_{\mathrm{dis}} / E_{\mathrm{ch}} \tag{3.96}$$

4 Modelling in Python

This chapter delves into the developed scripts for the air and CO_2 based HPES accumulators. It explains how the theory presented in Chapter 3 is coded and utilised to numerically simulate and estimate the HPES accumulator behaviour under different parameters.

4.1 Air-Based HPES Code

The mathematical equations derived and described in Chapter 3 were coded in *Python*® V3.8 language using *Spyder* Integrated Development Environment (*IDE*). *Python*® was preferred over other programming languages due to its user-friendly data structures, the extensive support libraries and its high computational efficiency. [94] The numerical model of the proposed accumulator using air is composed of multiple scripts as presented by the flow chart in Figure 4.1. The code is divided into three separate parts; 1) inputting of data from the *Input* script, 2) main flow of program through the *Main_script* and 3) sub scripts including multiple functions.

The code is initiated from the *Main_script* which is mainly divided into the four main stages of an HPES system and follows the flowchart presented in Figure 4.2. Initiating the code imports data from the *Input* script, which in turn imports data from the *Inputs.csv* file, as illustrated in Figure 4.3.

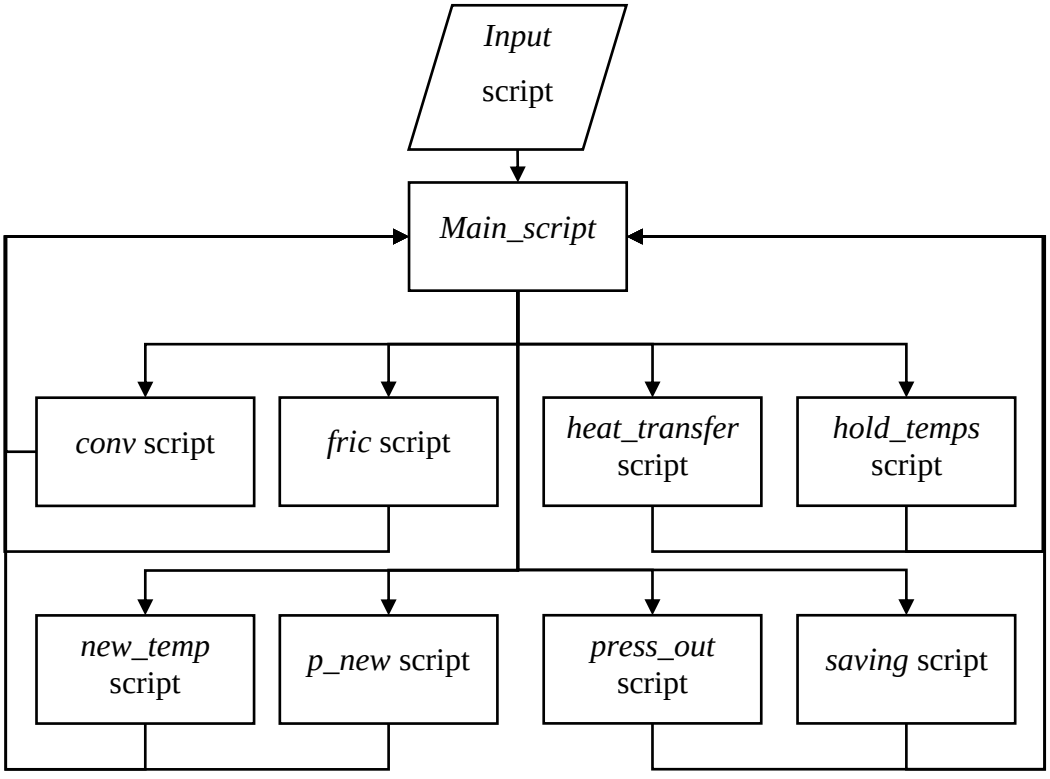

Figure 4.1- Flow of scripts for the air-based accumulator code

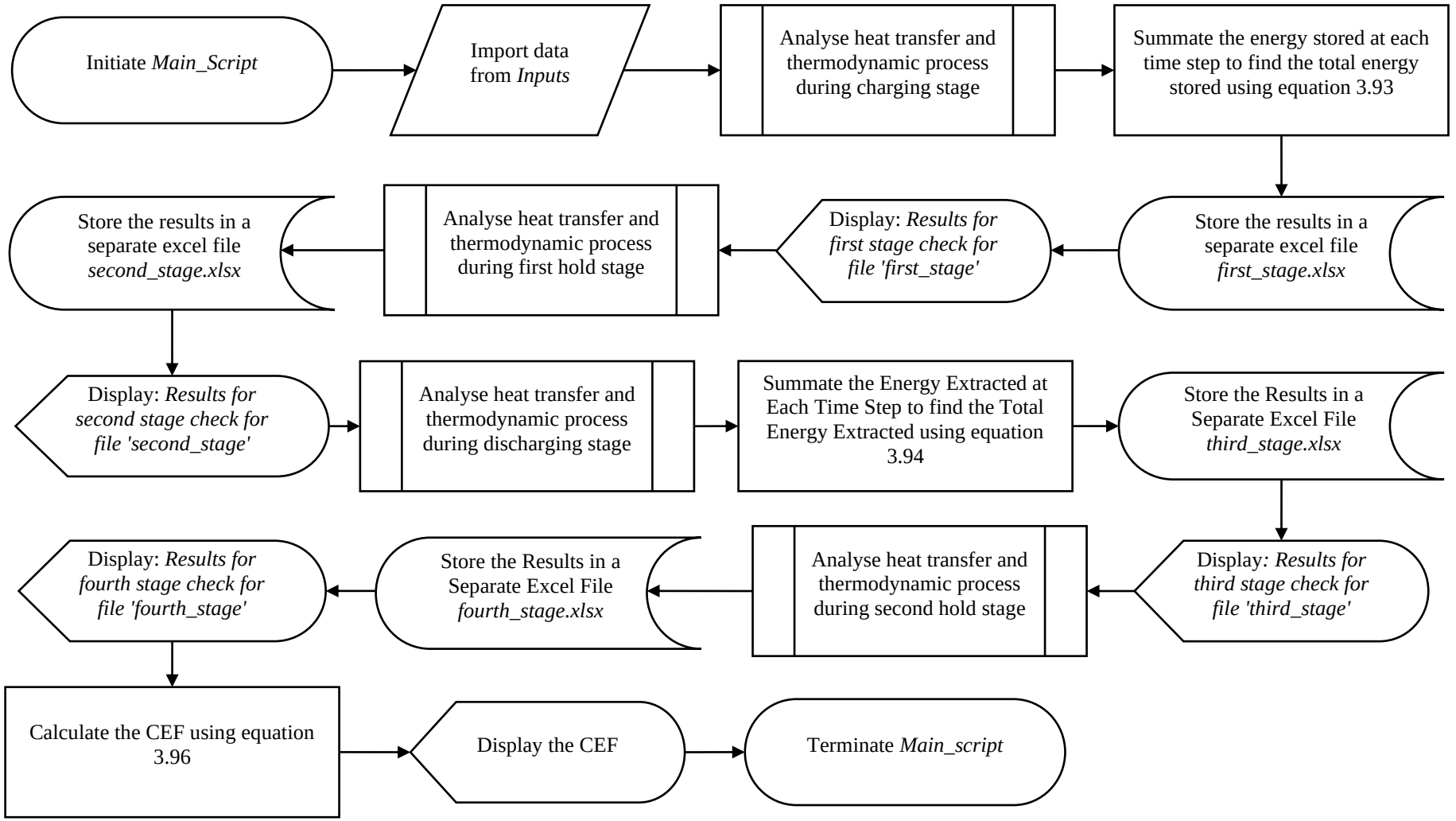

Figure 4.2- Flow Chart for *Main_Script*

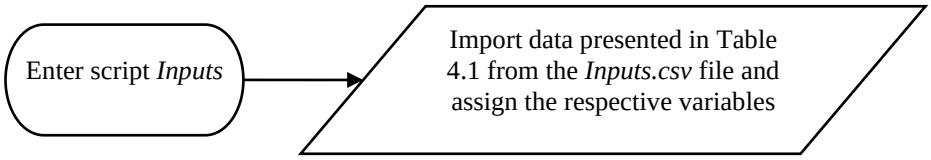

Figure 4.3- Inputs script flow chart

The flowchart followed by the charging stage to calculate the thermodynamic behaviour in the *Main_script* is presented in Figure 4.4 and Figure 4.5. The sequence of steps shown in the mentioned figures is repeated until the chamber pressure (p_{ch}) reaches the final chamber pressure (p_{f}) as prescribed by the user. Since the system is time dependent, the time for each iteration is calculated using equation 4.1. After the charging stage is finalised, the results are stored in an excel file as outputs.

$$t_{\mathrm{i}} = t_{\mathrm{i}-1} + \frac{\Delta t}{3600} \tag{4.1}$$

After the charging stage, the HPES gas is allowed to set for a period of time, referred to as the first hold stage, where the heat gained from compression is lost to the surrounding sea water. The first hold stage calculations follow the flowchart presented in Figure 4.6. As presented in Figure 4.6, the code follows a while loop until the predefined duration expires. The predefined duration for the hold stages in hours (hld_{t}) is calculated as a number of iterations, a, through equation 4.2 which is then used for the while loop statement. In Figure 4.6, k is the number of the current increment of the current loop, which at the final stage reaches the value of $a + 1$. The pressure and temperature of the discharging stage as the gas expands, the code follows the flowchart presented in Figure 4.7, Figure 4.8 and Figure 4.9. During the second hold stage the code follows the flowchart presented in Figure 4.10, similar to that of the first hold stage.

$$a = \frac{hld_t * 3600}{\Delta t} - 1 \tag{4.2}$$

The friction imposed by the PIG is calculated through the *fric* script while utilising the *fric_extra* function which is defined by the flowchart presented in Figure 4.11. The internal and external convective heat transfer coefficients are calculated by utilising the *conv* script from which the functions *conv_coef_in* and *conv_coef_out* are utilised, respectively. Internal and external convective heat transfer coefficients functions follow the flowchart presented in Figure 4.12 and Figure 4.13.

Heat transfer between the first and second node of Figure 3.4 is calculated through the function *transfer* which is defined in the *heat_transfer* script, following the flowchart presented in Figure 4.14. The new temperatures of the second and third nodes are obtained from the script *new*_temp and the functions *new_temp_comp* for compression or *new_temp_exp* for expansion, while both functions follow the flowchart presented in Figure 4.15.

During the hold stages, the temperature of each node is calculated simultaneously in the function *hold* defined in the script *hold_temps*, following the flowchart presented in Figure 4.16. The pressure of the chamber at the current increment is calculated from the function *press* situated in the script *p_new*, having the structure presented in Figure 4.17. Prior to initiation of the scripts and the required functions, data is retrieved for each function from the *Main_script* and the results are transferred back. The code for air will be referred to as *C-Air* in future chapters.

4.2 Code Modification for CO2-based Accumulators

The code developed for air required some minor modifications to cater for carbon dioxide due to two phase flow. Mainly the developed code follows the same structure as that presented by Figure 4.1. Along with the scripts of the latter mentioned figure, a new script, named *press_temp_ent*, was developed to calculate the pressure, temperature, enthalpy and dryness fraction of the current time step. The *Main_script* and *Inputs* scripts utilised for air were utilised for CO_2 with minor adjustments in the four main stages. The new flowchart for the charging stage, hold stages and discharging stage are presented from Figure 4.18 to Figure 4.26.

Determination of the internal convective heat transfer coefficients utilises a combination of while loops depending on the dryness fraction, x. Through the code development it was noted that for a value of x relatively close to 1 the Thome model fails, yielding no results. Thus h_{in} at x relatively close to 1 was set to a constant, as exhibited in Figure 4.19. The *lim* function mentioned in the charging stage flow charts is presented in Figure 4.27, which ensures to stop the code at a dryness fraction of 0.2 or a pressure of 60 bar. The function to calculate the dryness fraction at each time step is presented in Figure 4.28. The flowchart for the new temperature, pressure and specific enthalpy during the gaseous state is presented in Figure 4.29. Moreover, the flowchart of the function for the temperature, pressure, specific enthalpy and new dryness fraction during the liquid-vapour phase is presented in Figure 4.30 and Figure 4.31. In future sections, the code developed for CO_2 will be referred to as C^2O_2.

Table 4.1-Generic input data in the developed code

	Description	**Code Symbol**	**Units**
	Diameters		
1.	Inner Diameter	d_i	m
2.	Middle Diameter	d_m	m
3.	Outer Diameter	d_o	m
	Material Properties		
4.	Inner liner conductivity	k_in	$W.m^{-1}K^{-1}$
5.	Outer pipeline conductivity	k_out	$W.m^{-1}K^{-1}$
6.	Inner liner density	rho_2	$kg.m^{-3}$
7.	Outer steel pipeline density	rho_3	$kg.m^{-3}$
8.	Inner liner heat capacity	c_2	$J.kg^{-1}K^{-1}$
9.	Outer steel pipeline heat capacity	c_3	$J.kg^{-1}K^{-1}$
	Sea Water Properties		
10.	Coefficient of thermal expansion	bta_ht	K^{-1}
11.	Kinematic viscosity	v_ht	$m^2.s^{-1}$
12.	Dynamic viscosity	mu_ht	Pa.s
13.	Specific heat capacity	Cp_ht_ext	$J.kg^{-1}K^{-1}$
14.	Thermal conductivity	k_ht_ext	$W.m^{-1}K^{-1}$
15.	Density	rho	$kg.m^{-3}$
	Pump properties		
16.	Pump static head	H_p_s	m
	Pressure Chamber		
17.	Initial volume	Vol	m^3
18.	Initial pressure	p_i	Pa
19.	Final pressure	p_f	Pa
20.	Pipe roughness	e_p	m
	Hold Stage		
21.	First hold stage	hld_t_1	hours
22.	Second hold stage	hld_t_2	hours
	PIG properties		
23.	Number of discs	n	/
24.	Disc thickness	th	m
25.	Static friction	mu_s	/
26.	Kinetic friction	mu_k	/
27.	Disc radius	rs	m
	Simulation properties		
28.	Charging/discharging time	t_c_d	hours
29.	Acceleration due to gravity	g	$m.s^{-2}$
30.	Incremental time step size	inc	sec
31.	Initial temp	T_i	K

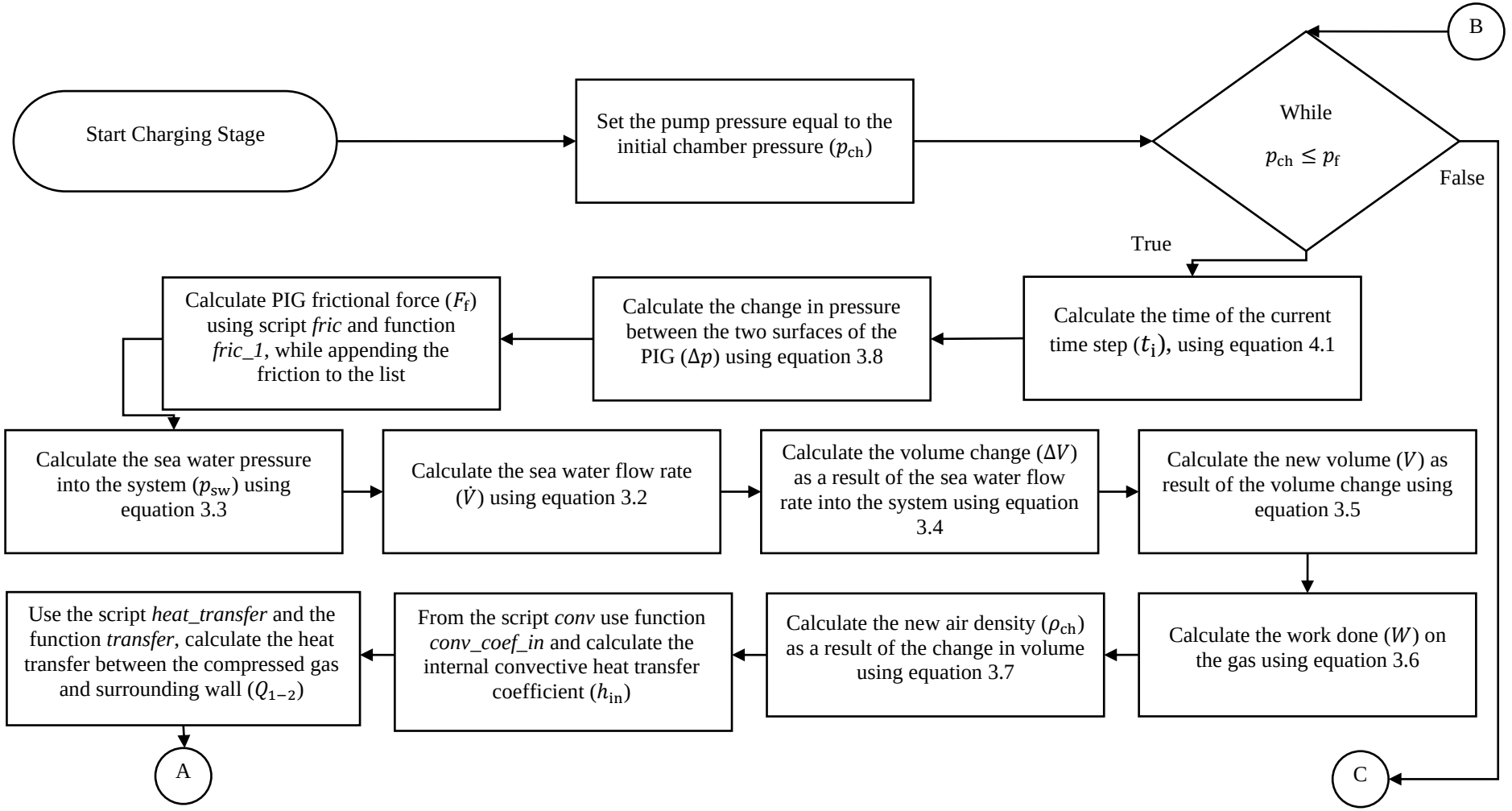

Figure 4.4- Flow chart for the charging stage of air (part 1)

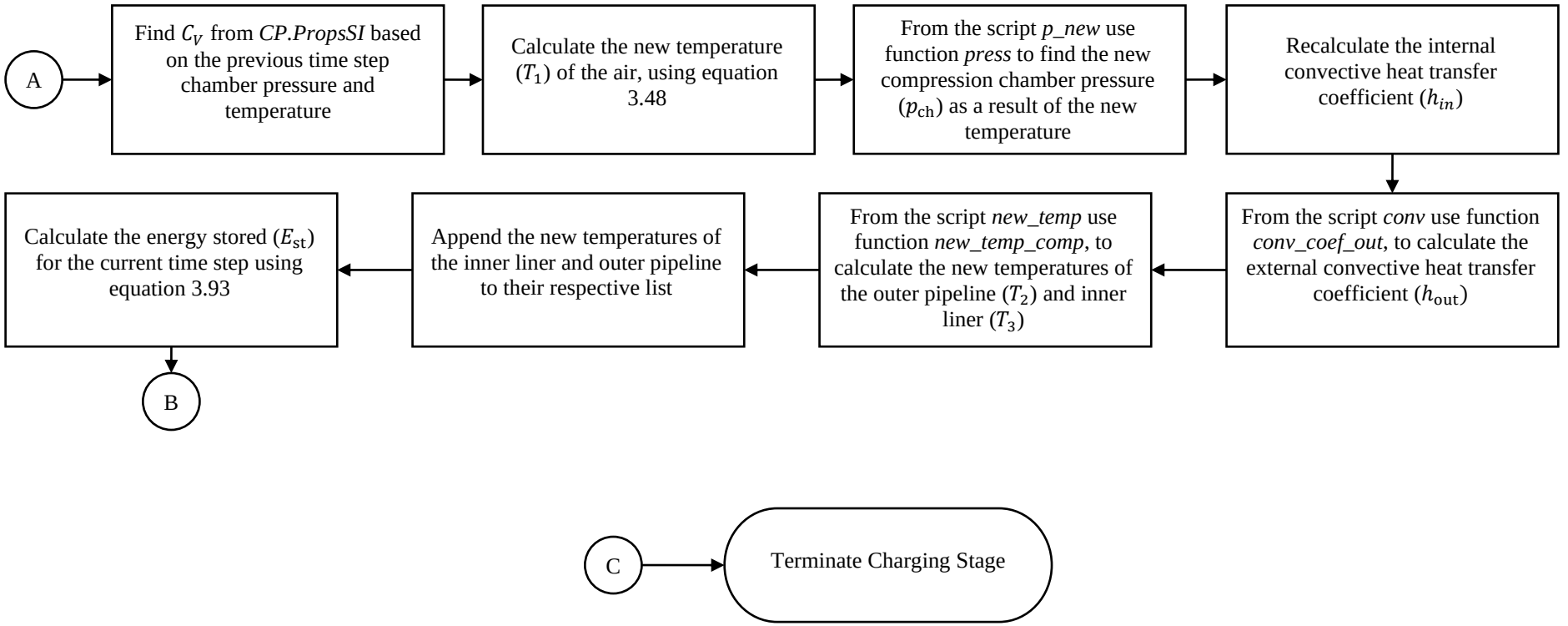

Figure 4.5- Flow chart of the charging stage for air (part 2)

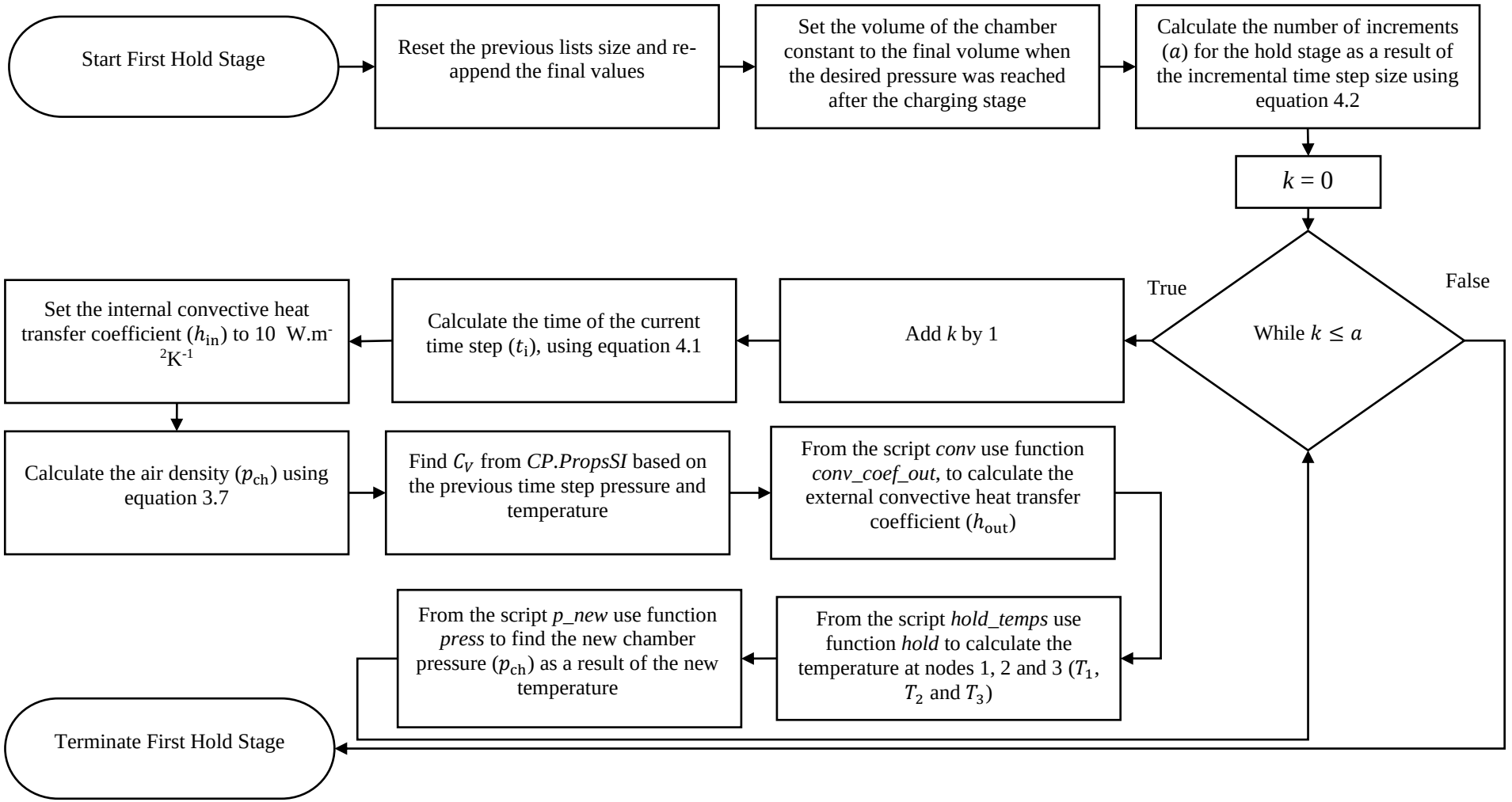

Figure 4.6-Flow chart of air first hold stage

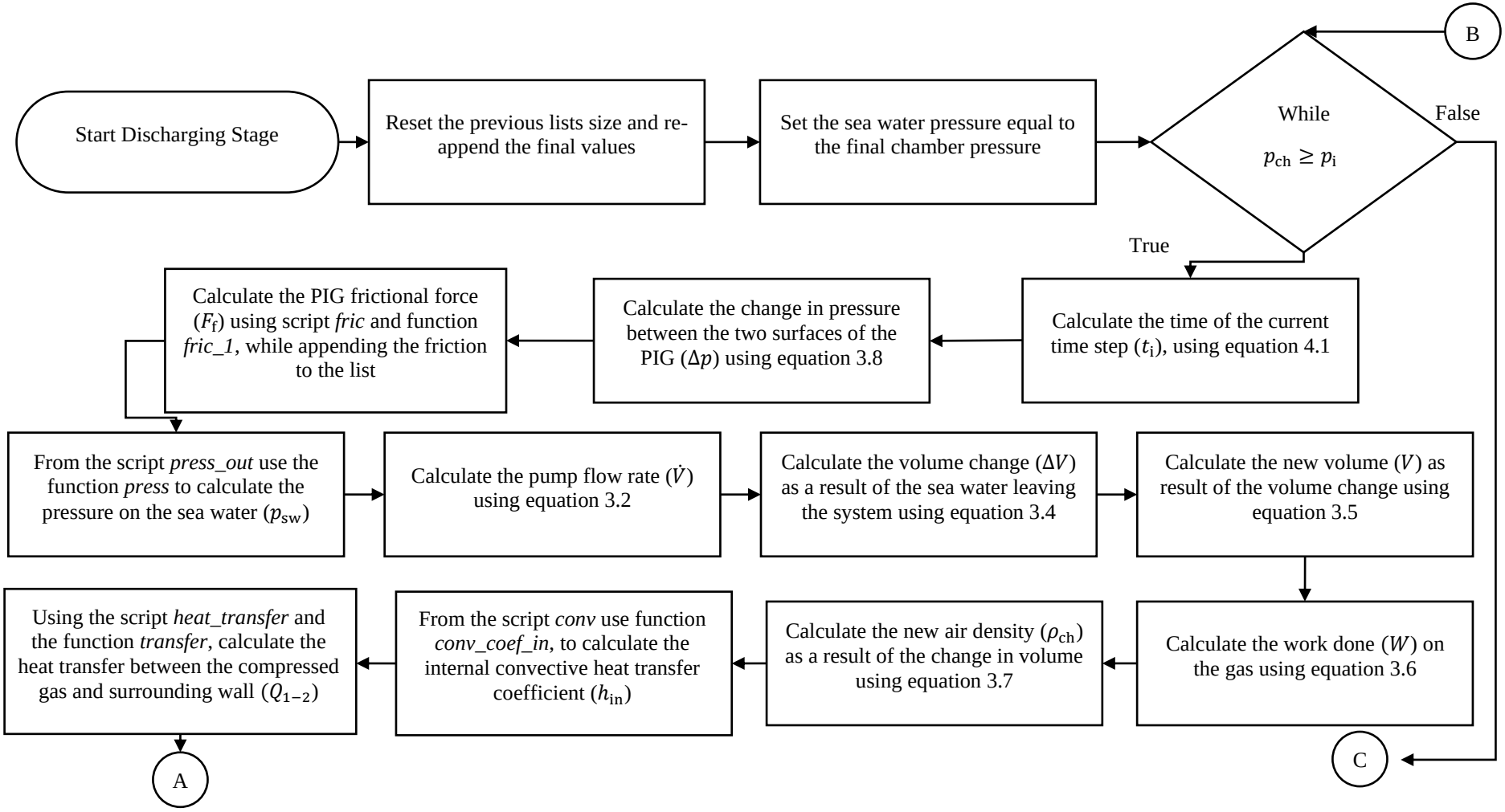

Figure 4.7- Flow chart of the discharging stage of air (part 1)

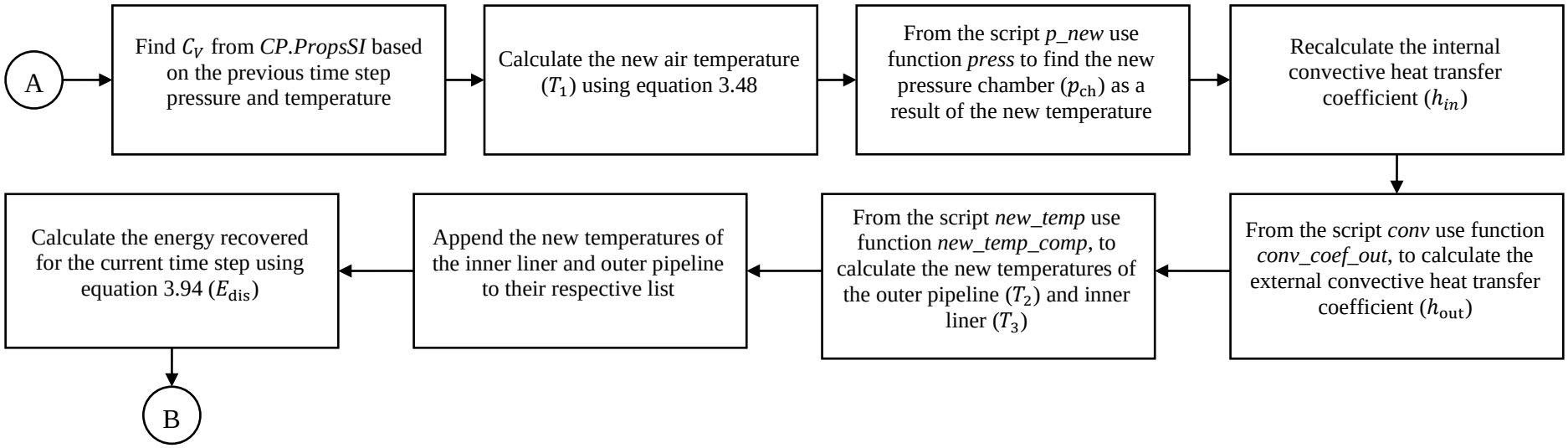

Figure 4.8- Flow chart of the discharging stage of air (part 2)

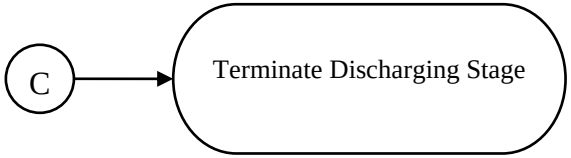

Figure 4.9- Flow chart of the discharging stage of air (part 3)

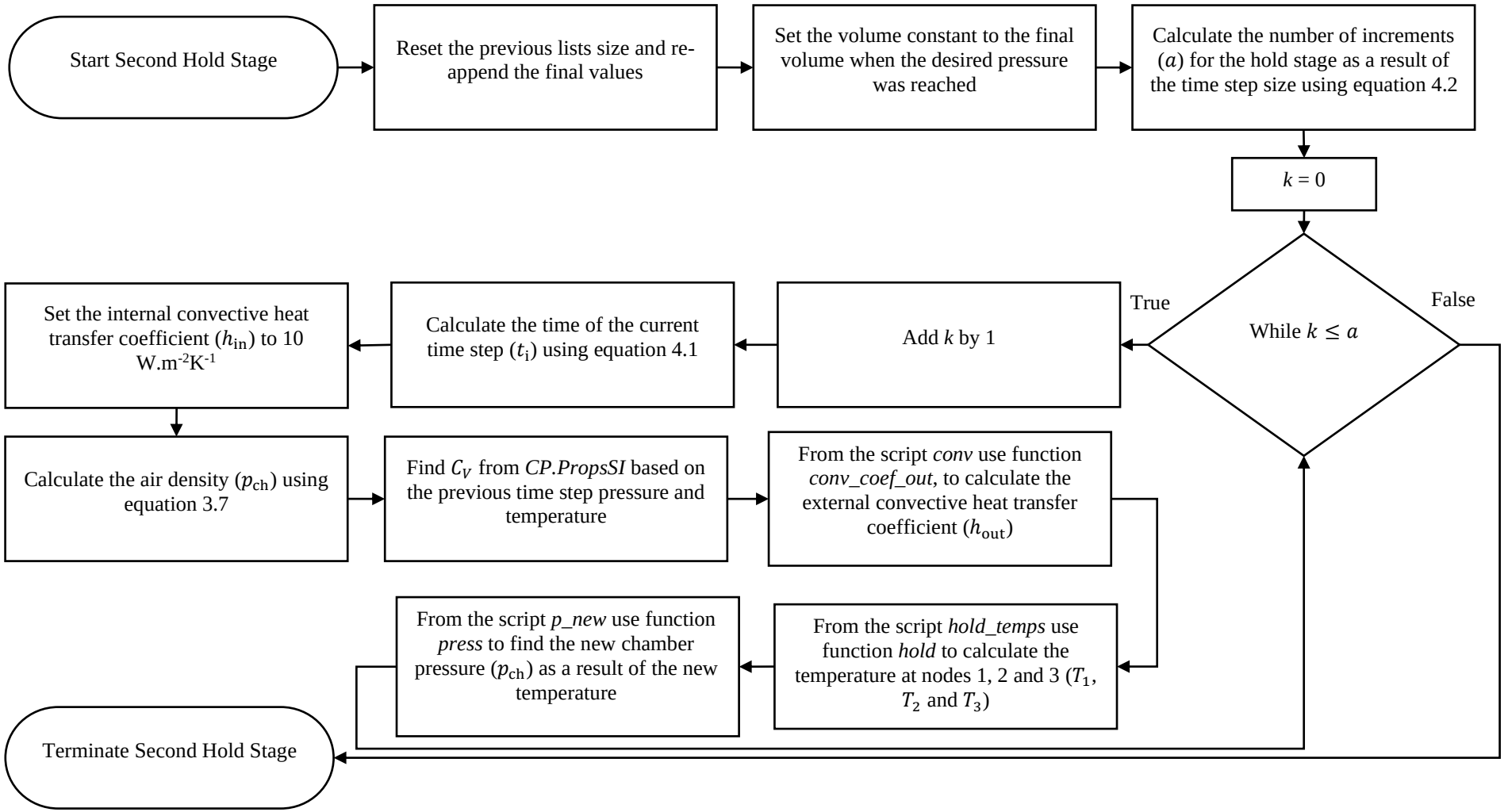

Figure 4.10- Flow chart of the second hold stage for air

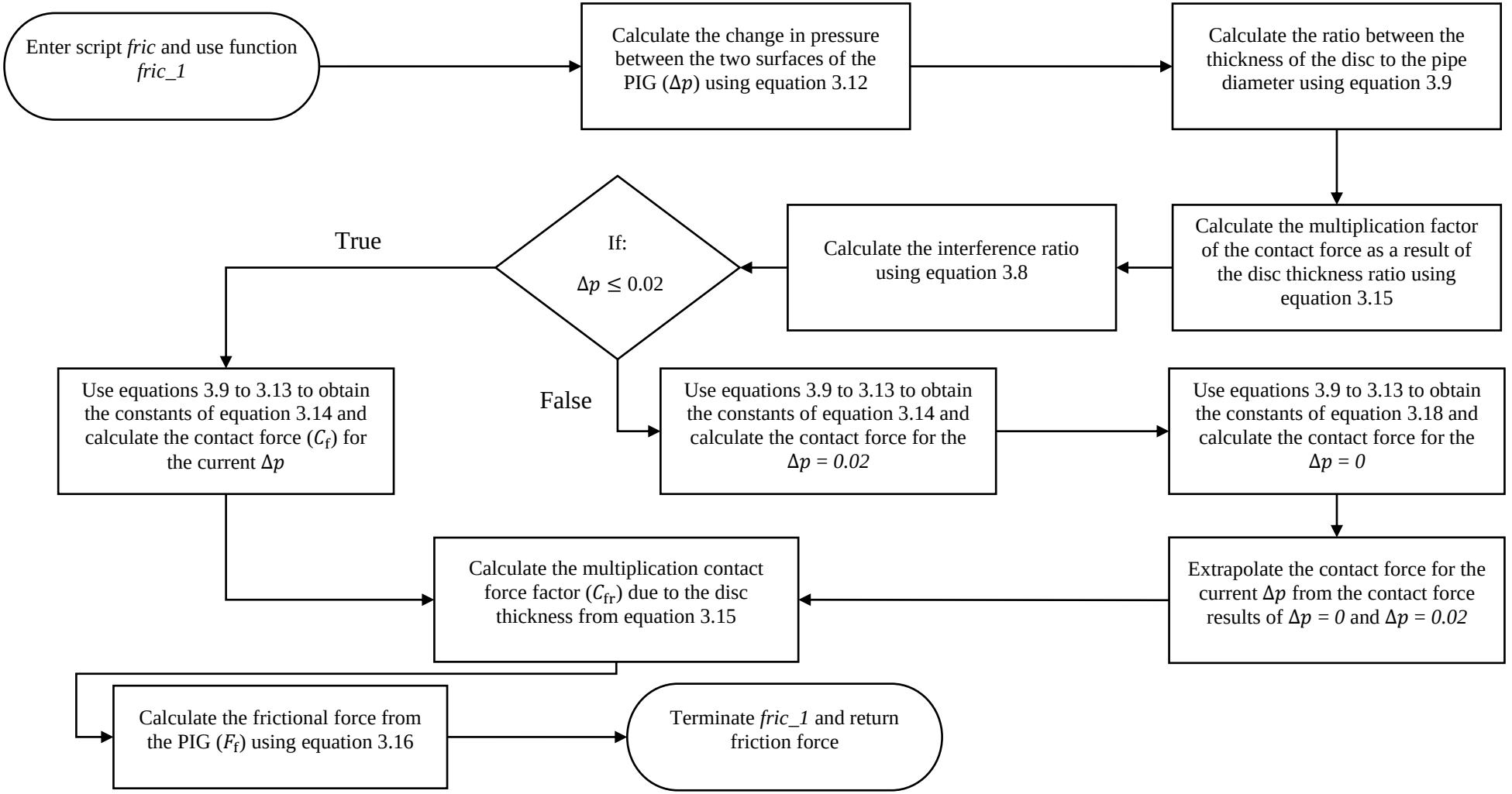

Figure 4.11- Function *fric_1* to calculate the pipeline inspection gauge friction

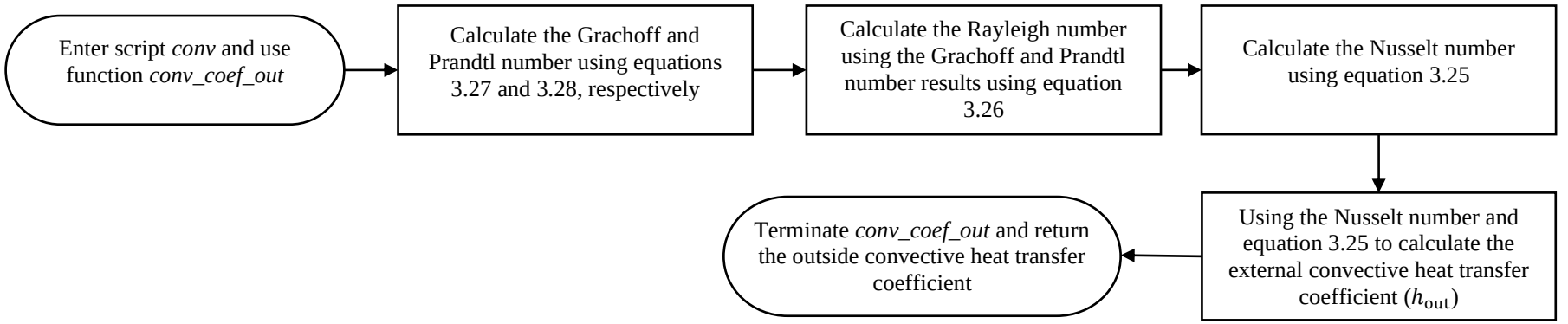

Figure 4.12- Function *conv_coef_out* flow chart to determine the external convective heat transfer coefficient

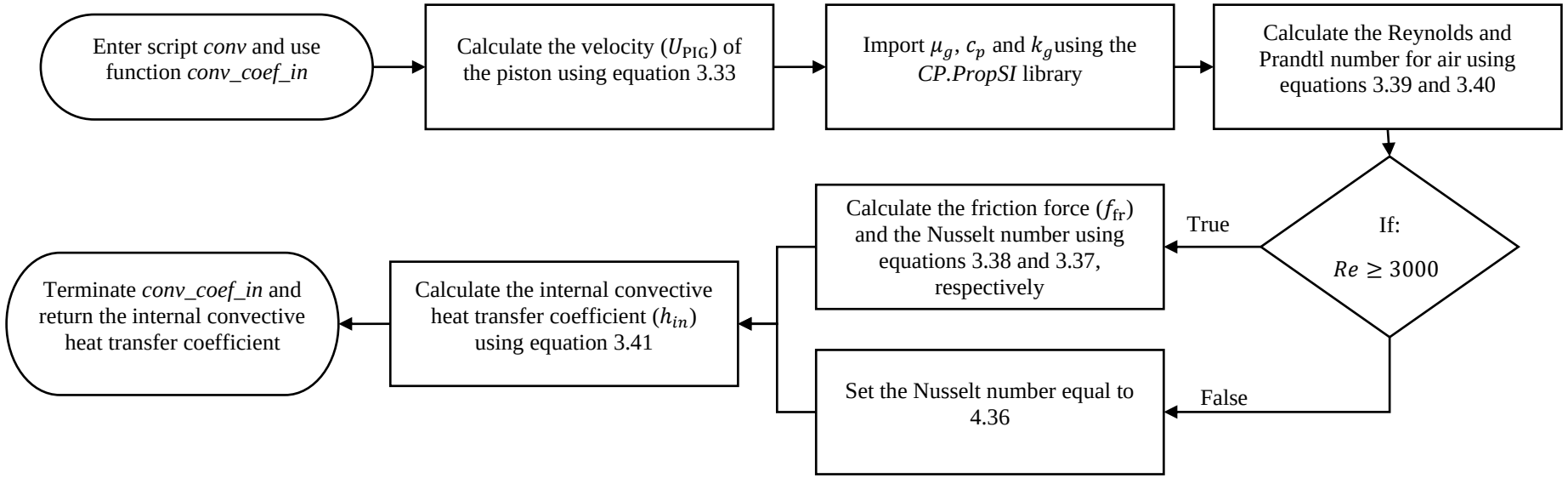

Figure 4.13- Function *conv_coef_in* flow chart to determine the internal convective heat transfer coefficient for air and carbon dioxide in its gaseous state

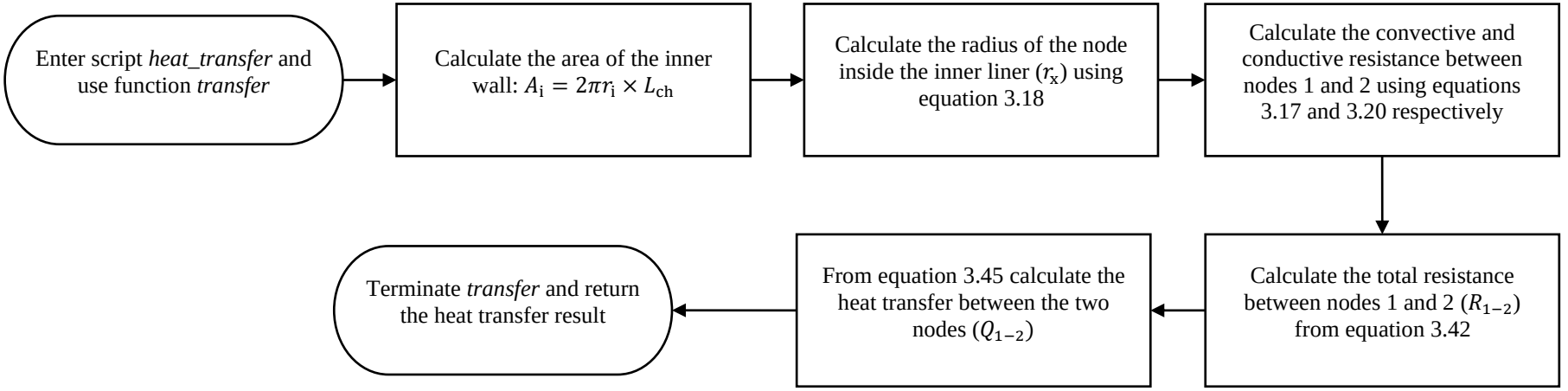

Figure 4.14- Function *transfer* flow chart to calculate the heat transfer between node 1 and 2 due to temperature difference

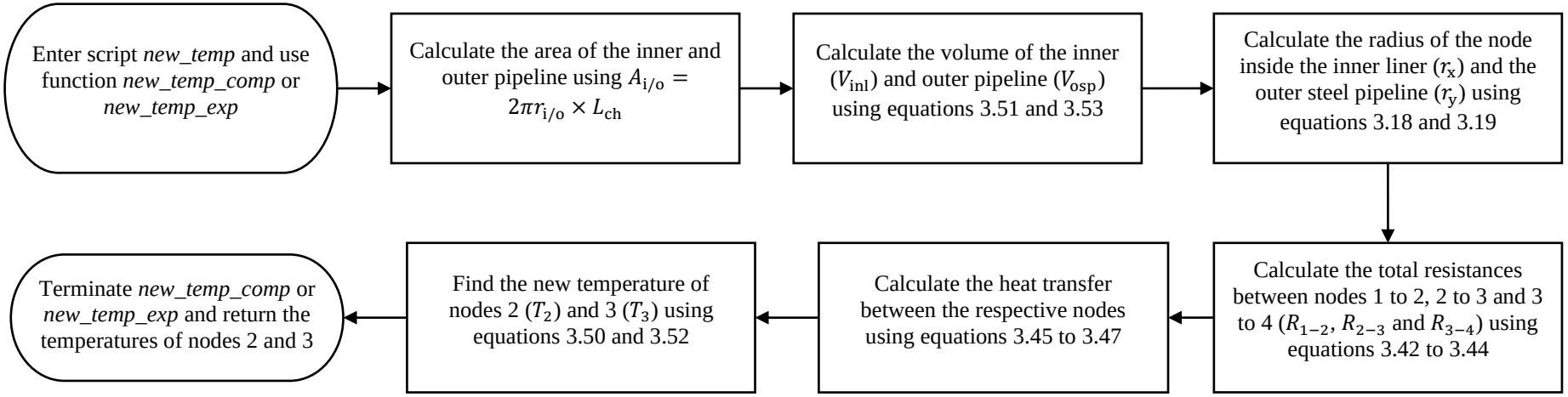

Figure 4.15-Functions for *new_temp_comp* and *new_temp_exp* flow chart to determine the temperature of the inner liner and outer steel pipeline during charging and discharging

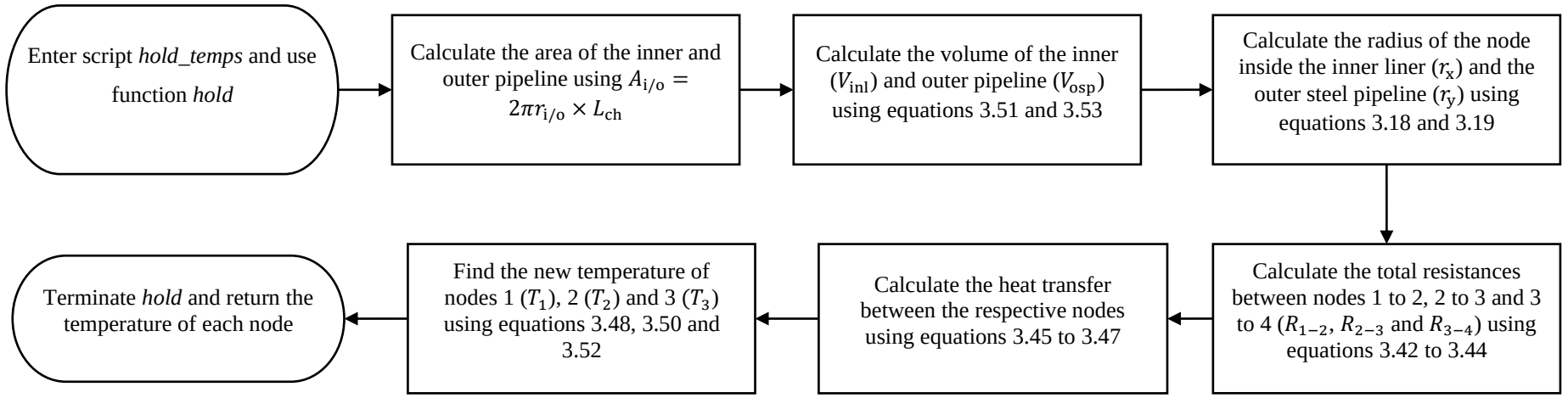

Figure 4.16- Function *hold* flow chart to calculate the temperature of the air, inner liner and outer steel pipeline during the hold stages

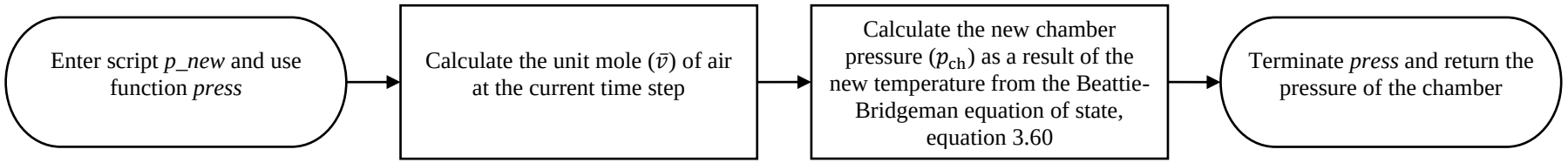

Figure 4.17- Function *p_new* flow chart to calculate the new compression chamber pressure of air

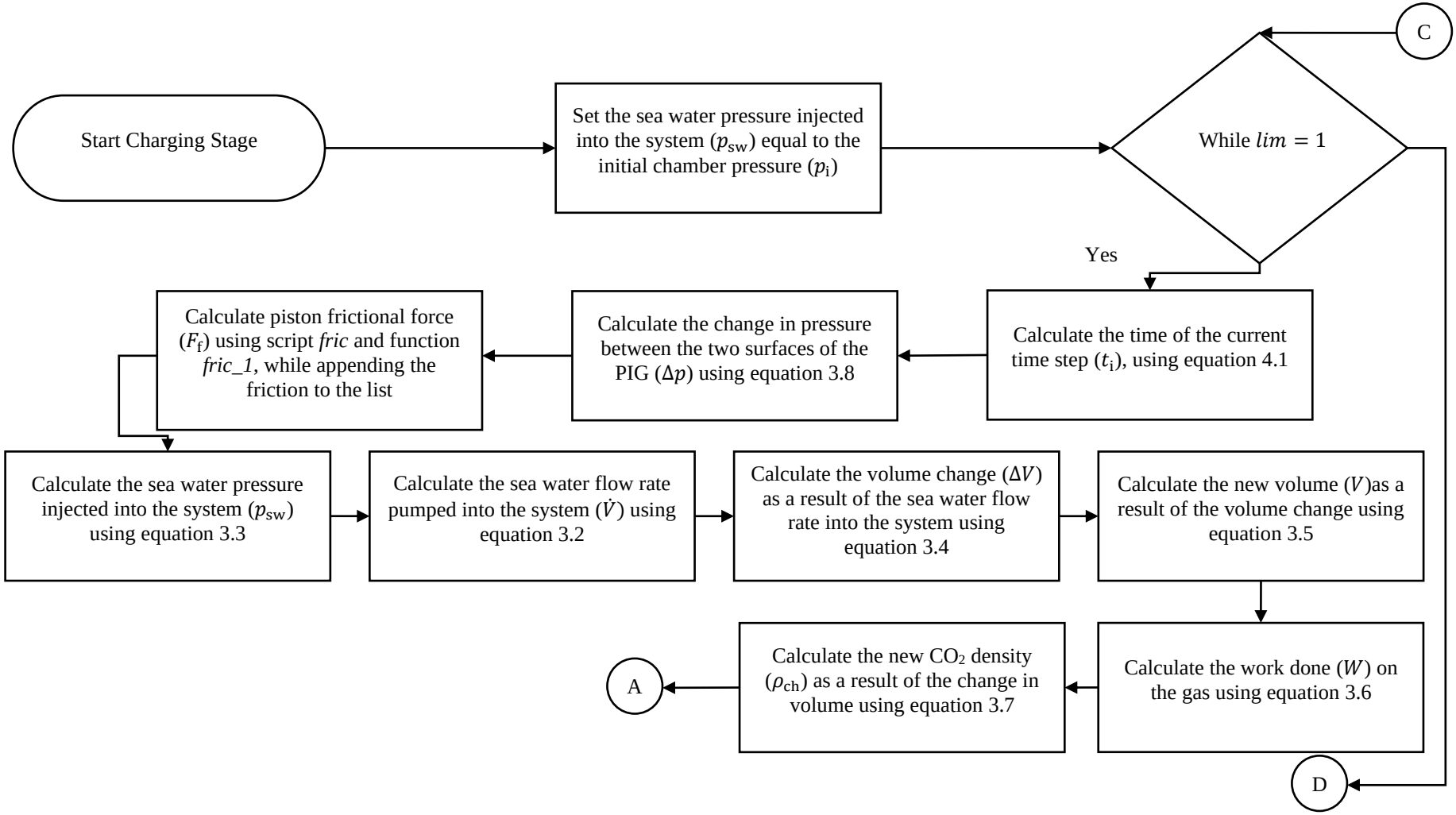

Figure 4.18- Charging stage for carbon dioxide (part 1)

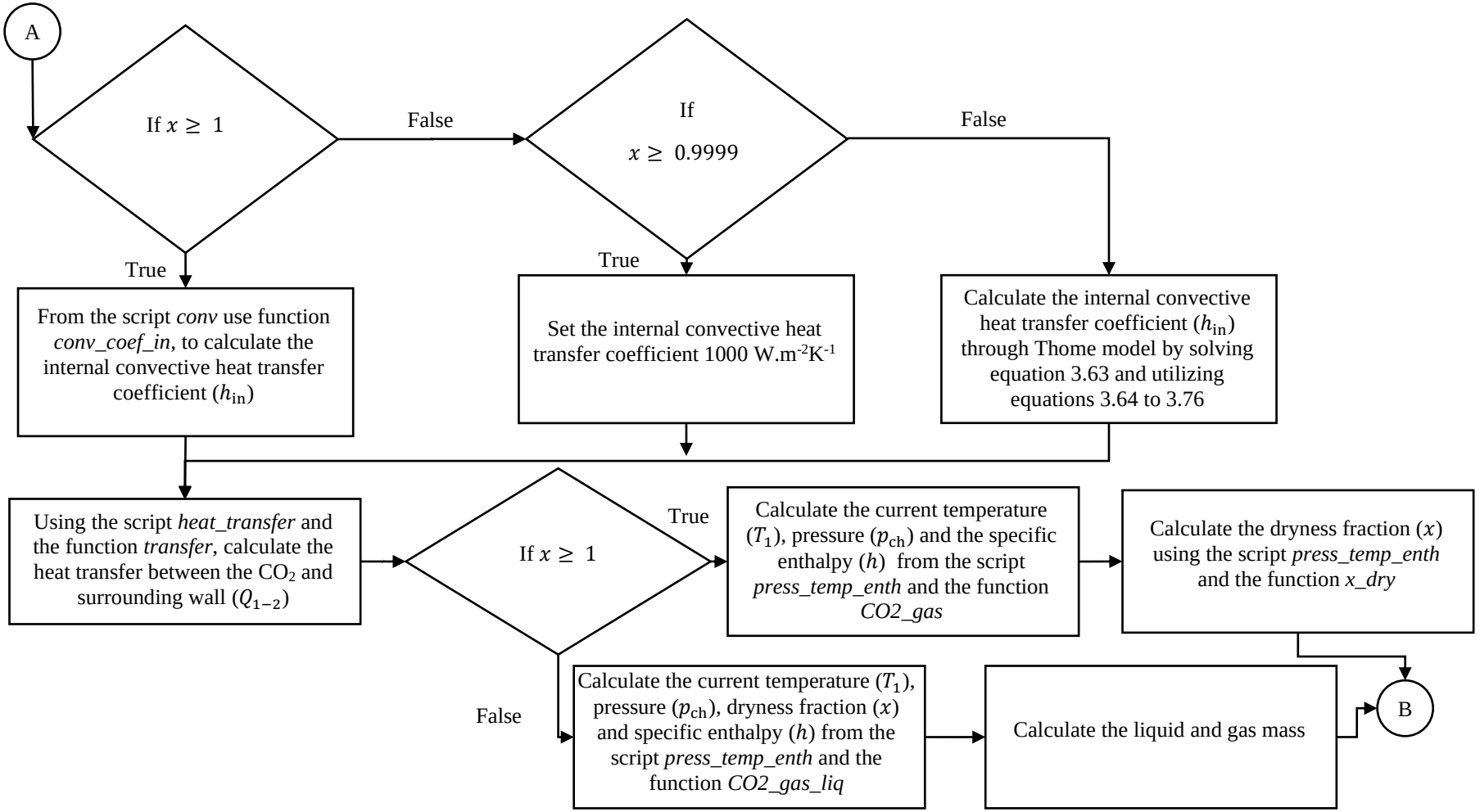

Figure 4.19- Charging stage for carbon dioxide (part 2)

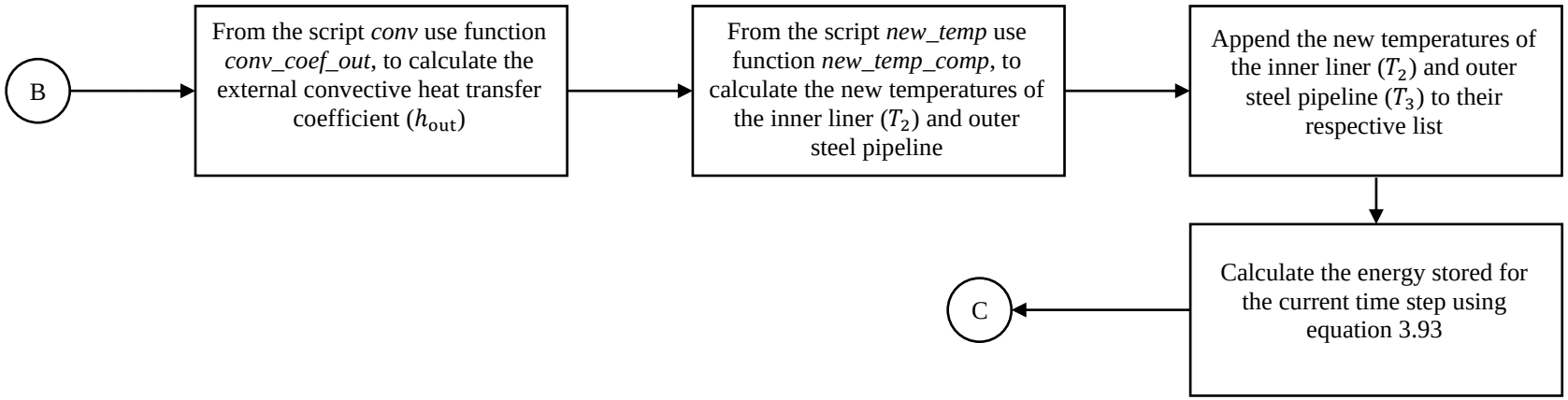

Figure 4.20- Charging stage for carbon dioxide (part 3)

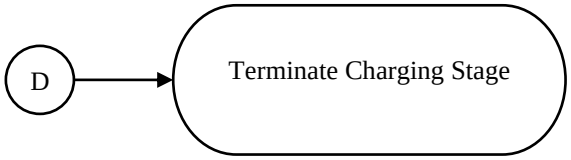

Figure 4.21- Charging stage for carbon dioxide (part 4)

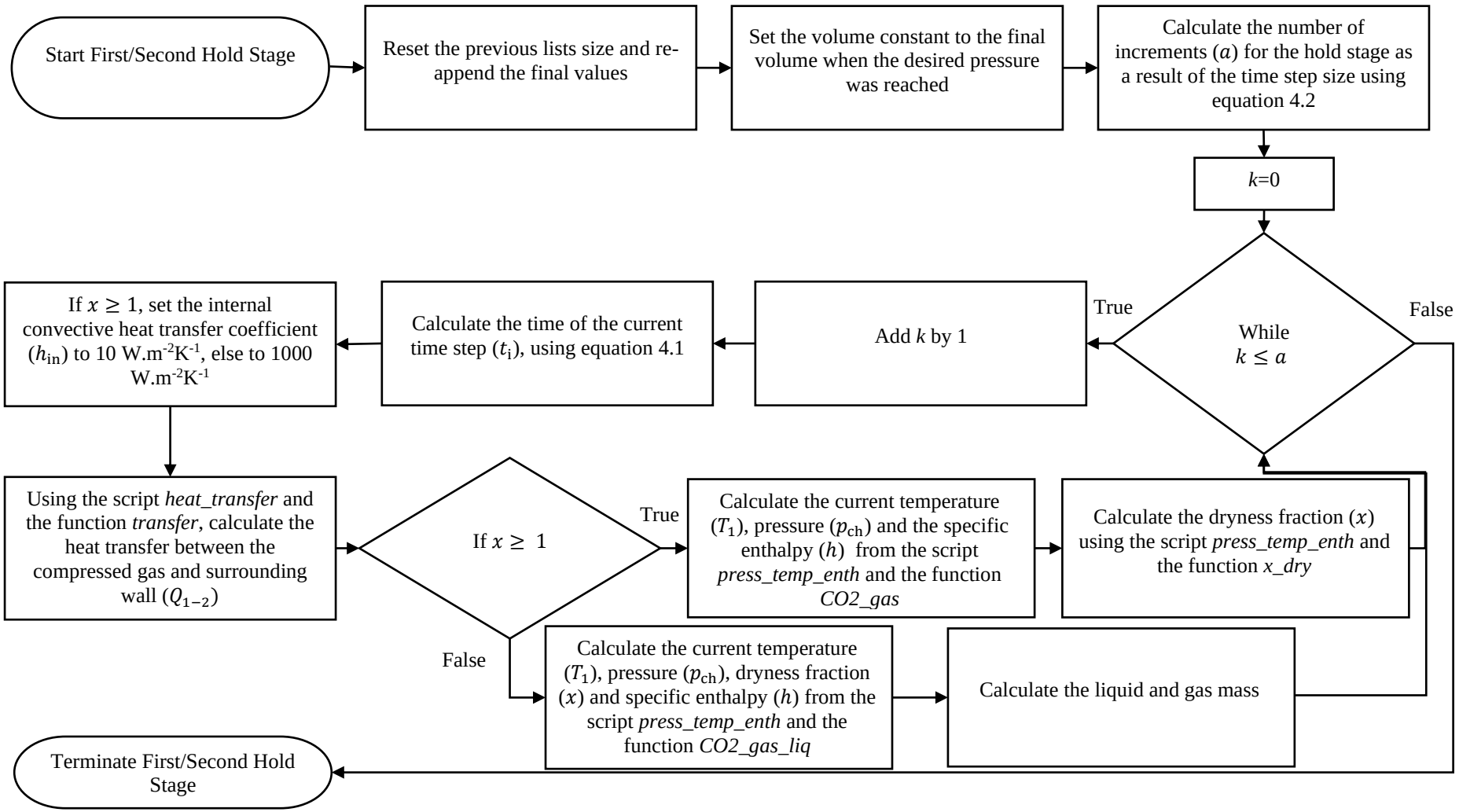

Figure 4.22- First and second hold stages for carbon dioxide

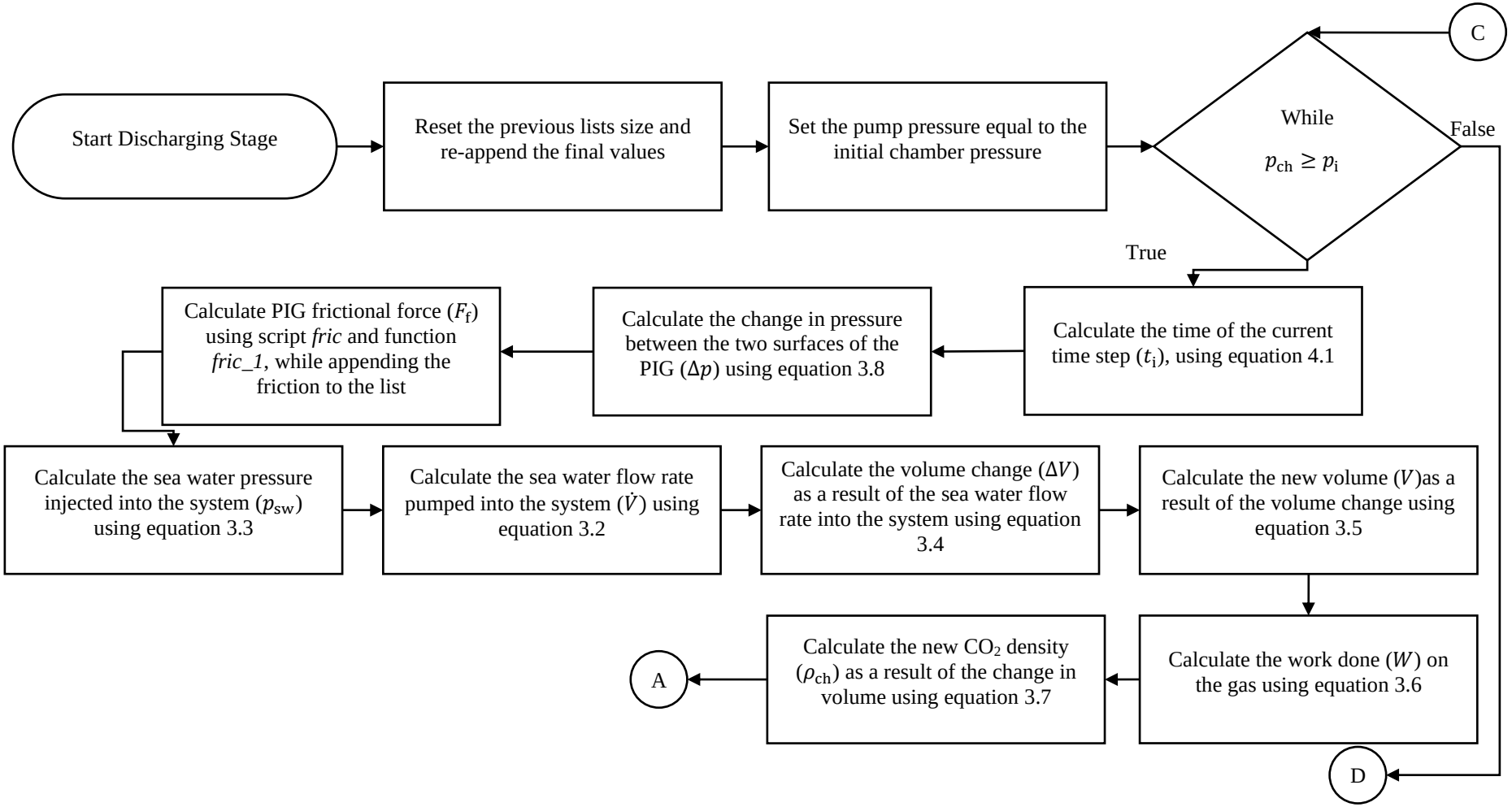

Figure 4.23- Discharging stage for carbon dioxide (part 1)

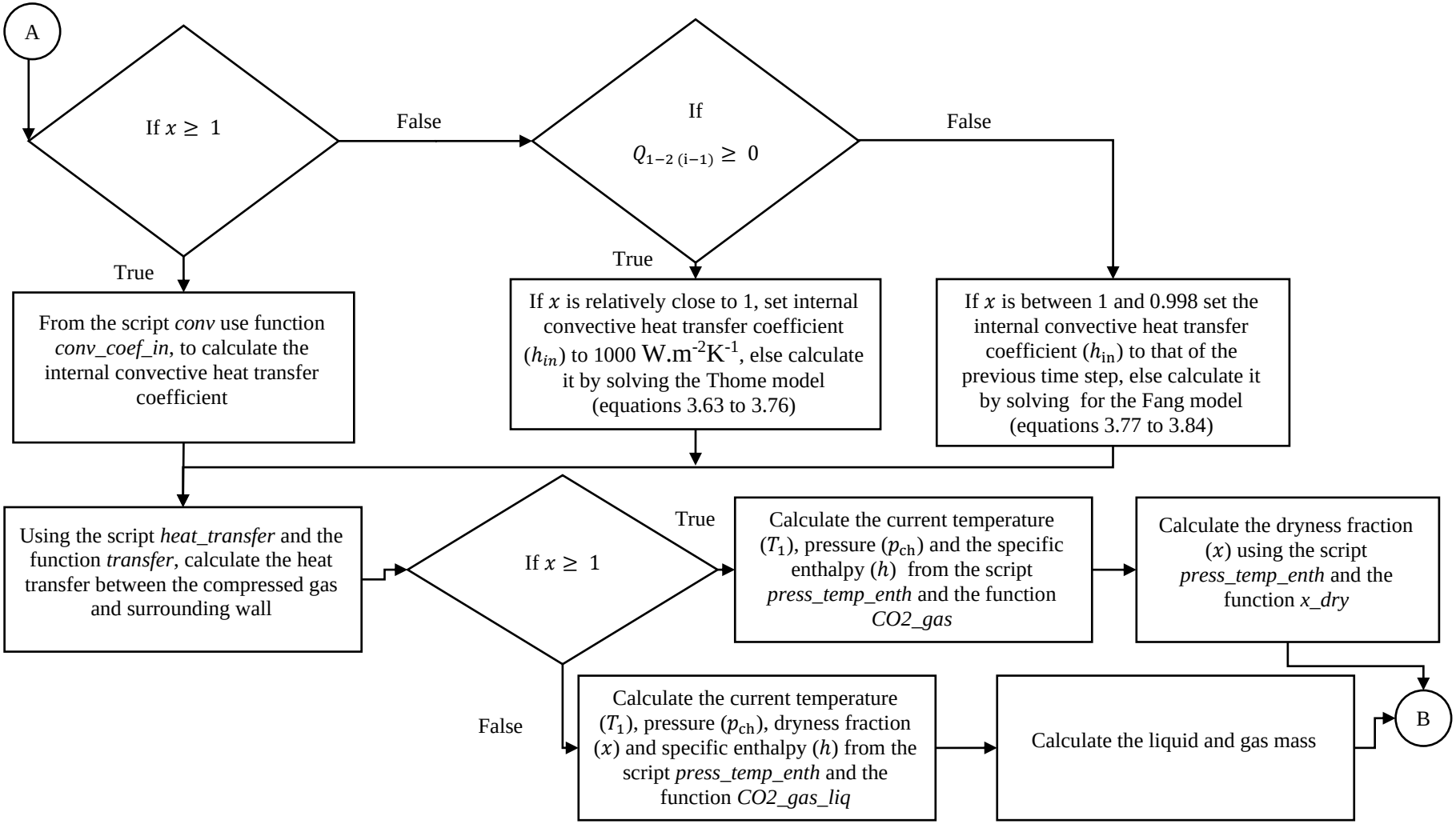

Figure 4.24- Discharging stage for carbon dioxide (part 2)

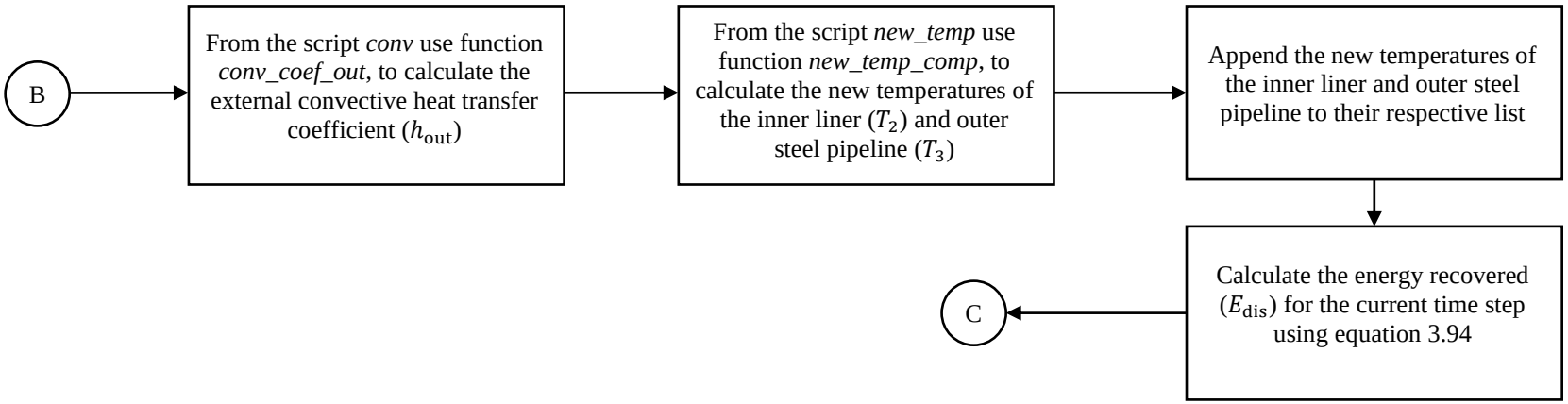

Figure 4.25- Discharging stage for carbon dioxide part 3

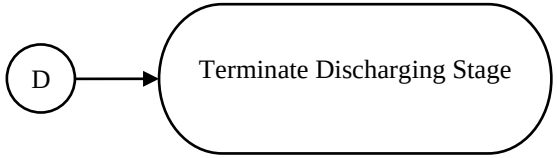

Figure 4.26- Discharging stage for carbon dioxide (part 4)

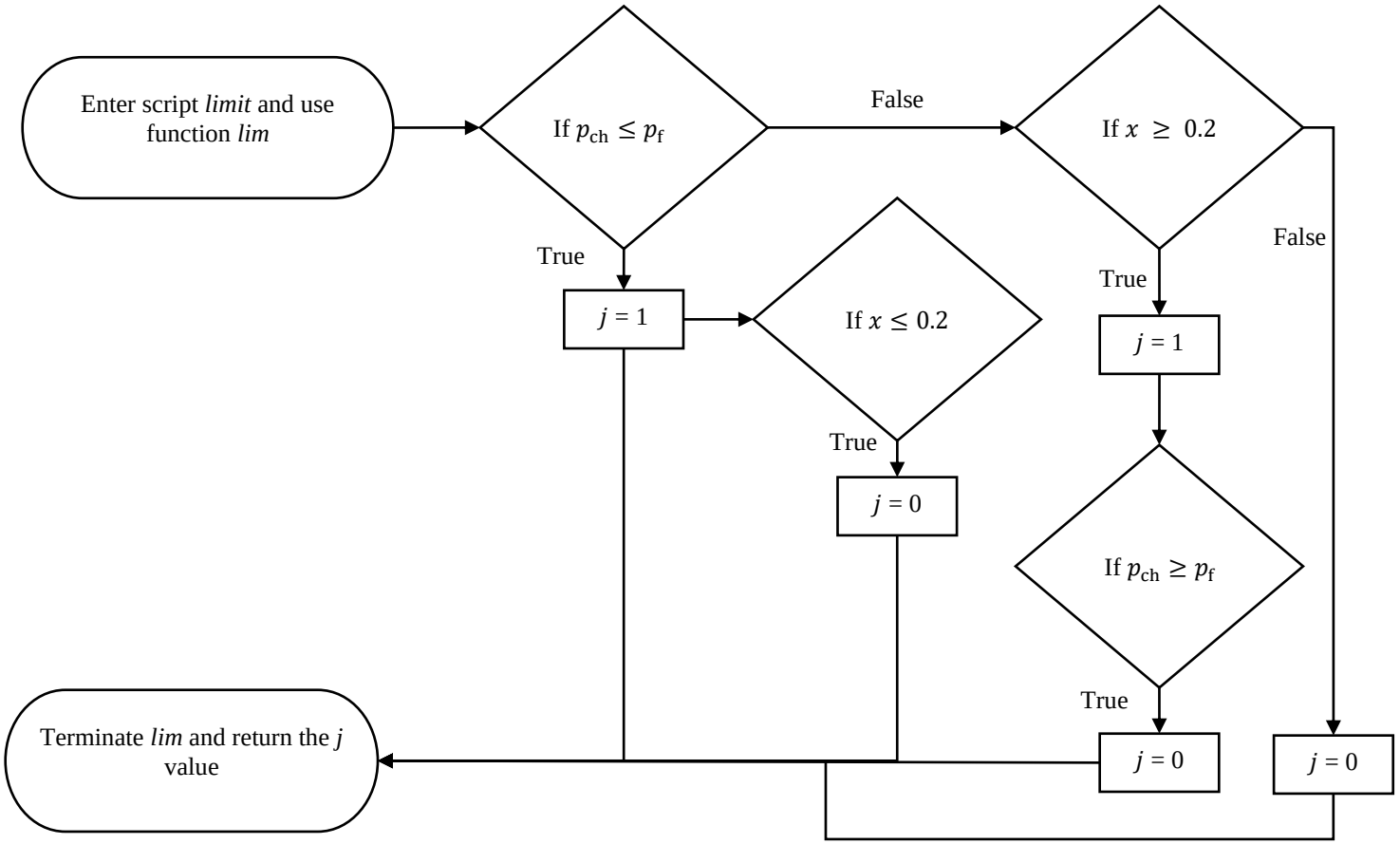

Figure 4.27- Function *lim* flow chart where ***j*** is a temporary variable

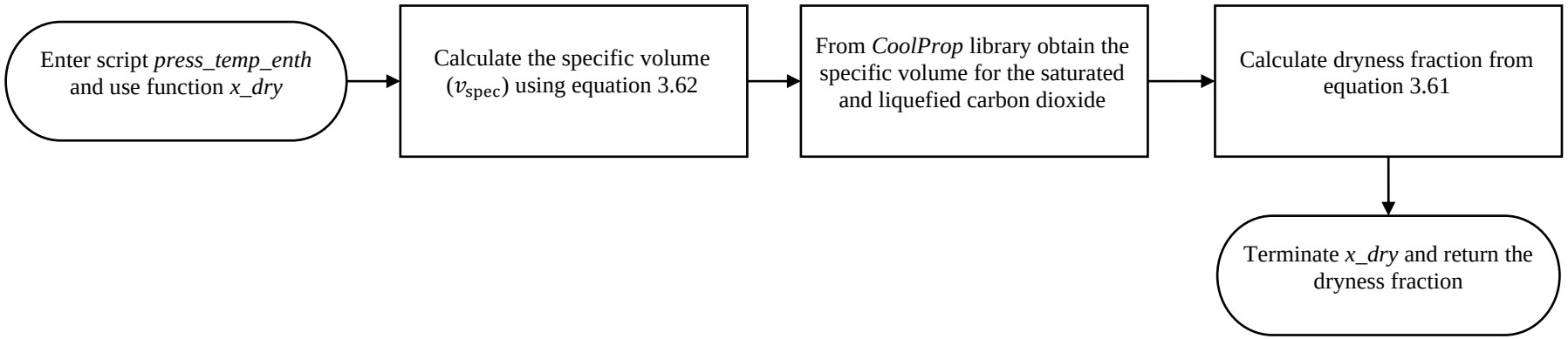

Figure 4.28- Function *dry* flow chart

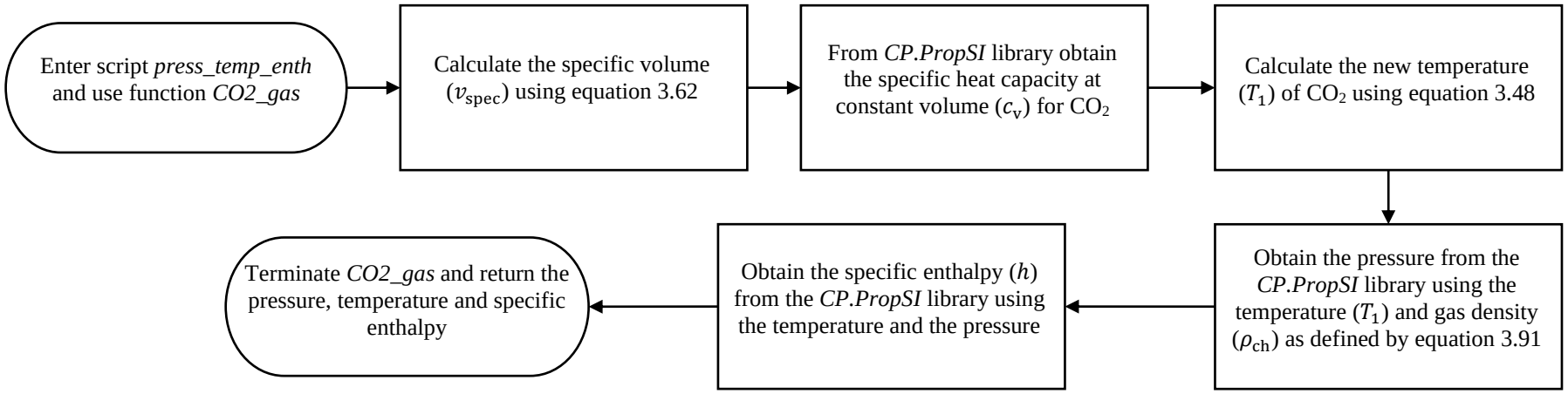

Figure 4.29- Function *CO2_gas* flow chart

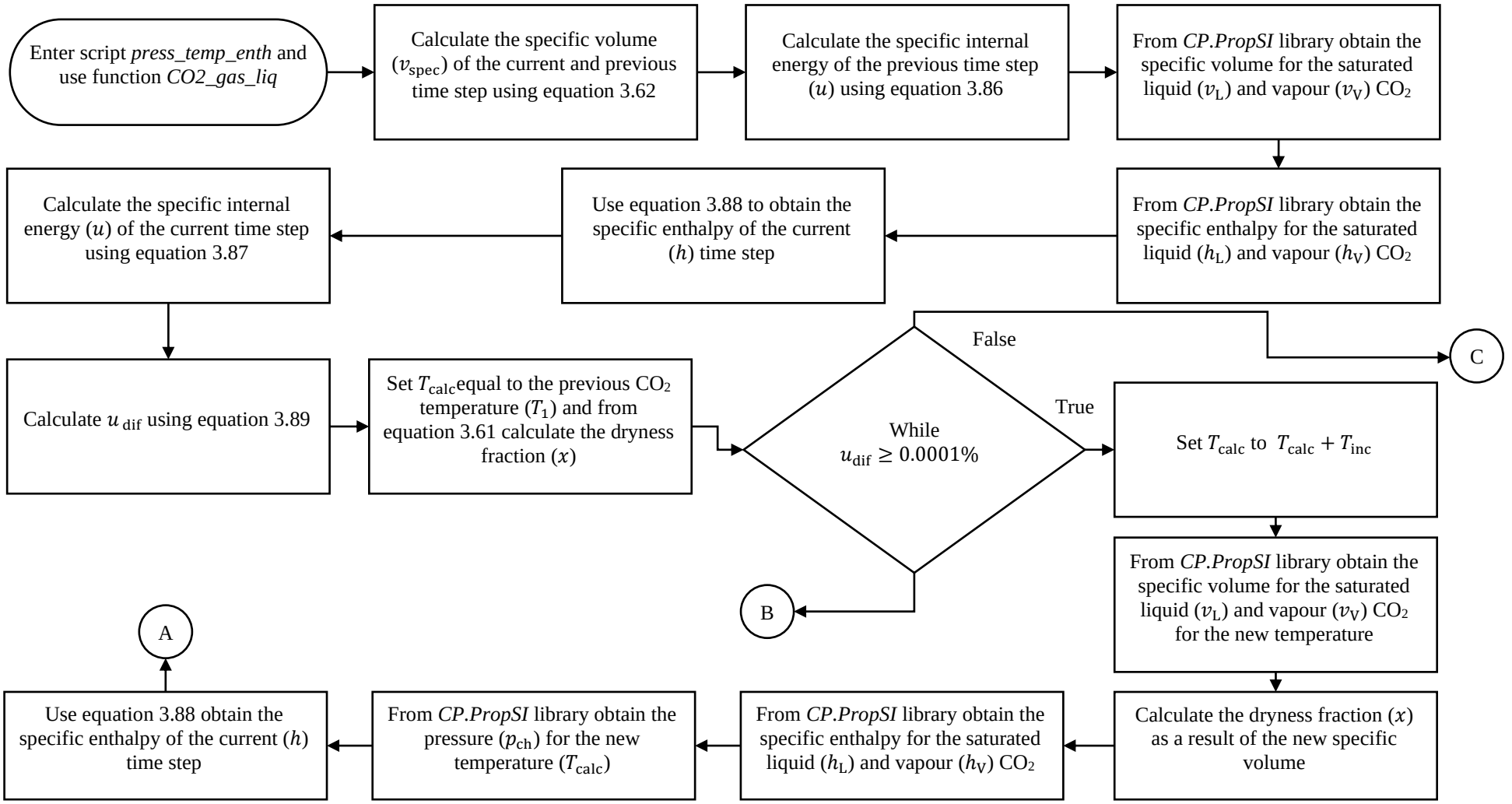

Figure 4.30- Function *CO2_gas_liq* flow chart (part 1)

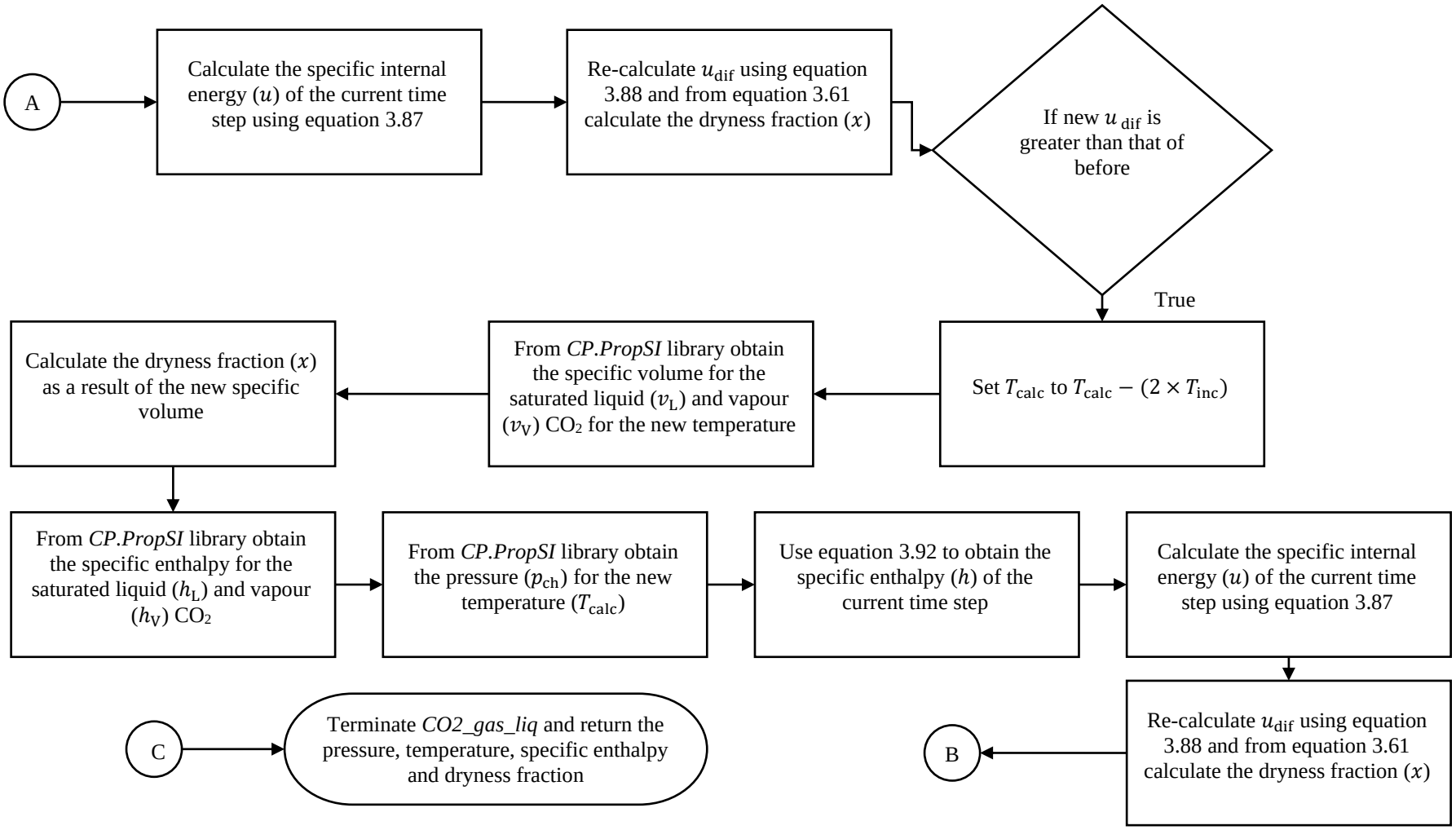

Figure 4.31 -Function *CO2_gas_liq* flow chart (part 2)

5 Numerical Simulations

The code described in Chapter 4 was used to run a number of simulations to understand the behaviour of the HPES accumulator described in Chapter 3. The different numerical simulations, were carried out by varying parameters of the baseline system. The baseline system parameters and the different simulations along with the developed code will be discussed throughout the following sections.

5.1 Default Numerical Simulation Parameters

The accumulator consists of a 36-inch steel pipeline grade X70 having an external diameter of 0.914 m, an internal diameter of 0.884 m and an internal volume of 1782.72 m^3. [95] These dimensions were determined through the in-house code *Smart PVB* developed by Cutajar et al. [96], based on Von Mises theory and SM EN 13445-3:2014 [96]. The accumulator was designed for a pump power of 250 kW, with an initial pre-charge pressure of 24 bar and a peak working pressure of 60 bar for air as the compressible gas. The simulations for the CO_2-based accumulator were limited to a peak working pressure of 60 bar and a dryness fraction (x) of 0.2. This means that the charging stage for CO_2 was terminated when the pressure reached 60 bar or the dryness fraction reached 0.2, whichever value was reached first. The thermal resistance model presented in Figure 3.4 (section 3.2.1.2) considers four nodes, thus when the inner liner is not present, the thickness of the outer pipeline is split into two to mimic the two bodies. Moreover, Table 5.1 presents the thermal properties, density and roughness of the outer steel pipeline.

Table 5.1- Outer steel pipeline dimensions along with its properties [96, 97, 98]

Description	Values	Units
Inner Diameter (d_i)	0.884	m
Middle Diameter (d_m)	0.899	m
Outer Diameter (d_o)	0.914	m
Thermal Conductivity (k_{osp})	45	$W.m^{-1}K^{-1}$
Density (ρ_{osp})	7850	$kg.m^{-3}$
Specific Heat Capacity (c_{osp})	475	$J.kg^{-1}K^{-1}$
Wall Roughness (ϵ)	4.5×10^{-5}	m

Clear guidelines for determining the optimal wall thickness of HDPE liner could not be easily found in open literature. Jim Schmitz [99] states that for CO_2 transportation the ratio of the outer diameter to the wall thickness should be of 41. The stated ratio is driven by the extrusion process through the pipeline. The HDPE inner liner outer

diameter is equivalent to the inner diameter of the outer pipeline. Hence, the outer and inner diameter of the inner liner were set to 0.884 m and 0.841 m, respectively (Table 5.2). Table 5.2 also specifies the thermal properties, density and wall roughness.

Table 5.2- High Density Polyethylene protective inner liner dimensions and parameters [98, 100, 101, 102, 103, 104]

Description	Values	Units
Inner Diameter (d_{i})	0.841	m
Outer Diameter (d_{m})	0.884	m
Thermal Conductivity (k_{inl})	0.4	$W.m^{-1}K^{-1}$
Density (ρ_{inl})	950	$kg.m^{-3}$
Specific Heat Capacity (c_{inl})	950	$J.kg^{-1}K^{-1}$
Wall Roughness (ϵ)	1.5×10^{-6}	m

The default power values of the hydraulic pump and energy recovery turbine were both set to 250 kW. The duration of both hold stages (post charging and post discharging) was also set to 4 hours. The system was set to operate at a sea depth of 30 m while having the surrounding sea water temperature at 283 K [96]. The properties of the sea water are specified at 283 K and a salinity of 35 g/kg, presented in Table 5.3.

The resistive force imposed by the PIG disc depends on its dimensions, while also dependent on the interfering surface. Equation 2.1 was re-arranged to obtain the disc diameter (d_{s}) for the system with and without the inner liner while maintaining a percentage interference ratio (δ) of 4.5, as presented in Table 5.4. Similarly, the disc thickness (th) was derived by modifying equation 2.2 and maintaining a constant thickness ratio (ξ) of 0.022. The disc thickness with/without inner liner are presented in Table 5.4.

Table 5.3- Sea water properties at 283 K and salinity of 35 g/kg [79, 80, 105]

Description	Values	Units
Coefficient of Thermal Expansion (β)	0.000175	K^{-1}
Kinematic Viscosity (μ_{sw})	1.36×10^{-6}	$m^2.s^{-1}$
Dynamic Viscosity (v)	0.001397	Pa.s
Specific Heat Capacity ($c_{\mathrm{p\ (sw)}}$)	3994.9	$J.kg^{-1}K^{-1}$
Thermal Conductivity (k_{sw})	0.57	$W.m^{-1}K^{-1}$
Density (ρ_{sw})	1027	$kg.m^{-3}$

X. Zhu et al. [72] conducted experiments and established that the coefficient of friction (μ) between the steel pipeline and PU PIG disc is of 0.6 for static conditions and 0.5 for kinetic. Ideally the value of μ for PU PIG discs against HDPE inner liner is established through experimentation. Due to lack of time other methods had to be

considered. For a preliminary understanding of this, the μ between polypropylene and the HDPE liner was considered from Cho et al. [106] work. Cho et al. [106] in their work studies the static and kinetic friction PP, PET and HDPE. Hence, for future studies including the PIG and HDPE liner, a coefficient of friction of 0.2 during static conditions and 0.12 during kinetic conditions were considered.

Table 5.4- Pipeline inspection gauge disc diameter, thickness, kinetic and static friction for the accumulators with and without the inner liner [72, 106]

Description	**Values**	**Units**
Without Inner Liner		
Diameter (D_s)	0.924	m
Thickness (th)	0.0195	m
Static Friction (μ_s)	0.60	/
Kinetic Friction (μ_k	0.50	/
With Inner Liner		
Diameter (D_s)	0.879	m
Thickness (th)	0.0185	m
Static Friction (μ_s)	0.20	/
Kinetic Friction (μ_k)	0.12	/

An initial observation is that for the same accumulator volume, the system stores a greater mass of carbon dioxide than of air, 95390 kg and 53190 kg, respectively. For the initial pressure of 24 bar and temperature of 283 K, the density of carbon dioxide is almost twice of air at 53.51 kg/m^3 and 29.84 kg/m^3, respectively. Different families of trees exist, making it difficult to determine the amount of CO_2 absorbed per year for a single tree. However, through research it has been concluded that, on average, a typical average sized tree absorbs 21 kg per year of CO_2. Therefore, the accumulator stores the same amount of CO_2 absorbed by 4543 trees in one year [107, 108].

5.2 Computers Specifications

The simulations were carried out on a total of five different desktop computers to obtain results within a reasonable time frame. The utilised computers along with their specifications are specified in Table 5.5, from which it can be observed that all the computers have similar specifications to one another.

5.3 Simulations

As established in Chapters 3 and 4 it is mentioned that two separate codes were developed for the two different gases. Due to the codes being different they required separate verification processes as will be discussed in section 6.1 for air and section 7.1 for CO_2. A number of numerical simulations were carried out to understand the

system behaviour for the air-based and carbon dioxide-based HPES as presented in Figure 5.1 and Figure 5.2.

One of the studies on both the air-based and CO_2-based HPES systems was to investigate the influence of the length-to-diameter ratio on thermal performance. Along with the 36-inch diameter pipeline, a 48, 60 and 84-inch diameter pipelines were selected (Table 5.6), whose dimensions were determined from *Smart PVB* [95]. Another study for the CO_2-based HPES system requires to understand the influence of the surrounding sea water temperature. Along with the default temperature of the sea water of 283 K, it was varied to 273 K, 278 K, 288 K and 293 K which the respective sea water properties are presented in Table 5.7.

5.4 *CoolProp* Verification and Python Code Initial Observations

Chapters 3 and 4 highlights that the developed code for CO_2 utilises the *CoolProp* library to obtain properties of the gas depending on the pressure and temperature. Bell et al. [109], validated the library using independent libraries such as *REFPROP 9.1*. The specific enthalpies at x equal 1 and 0 between 273 K to 293 K at increments of 1 K from the *CoolProp* library were compared to that obtained from the Ohio University pressure-enthalpy chart, Figure 2.12. In this comparison a percentage difference of less than 1% was obtained in both cases, showing great agreement between the two. Similar agreement was observed for the pressure and the temperature. The data from the library was compared to that of Ohio chart in the superheated vapour region from 20 bar to 70 bar at a maximum temperature 323 K. It was noted that for the selected points a percentage difference of less than 1 % was obtained in all cases. These results confirm the very good agreement between the chart and those from the library[60, 93].

Table 5.5- Computers utilised for the numerical simulations and the respective specification

Computer Number	OS	CPU Type	Clock Speed (GHZ)	RAM (GB)	HDD Type
1.	Microsoft Windows 10 Home	AMD Ryzen 7 5800H	3.20	16	SSD
2.	Microsoft Windows 10 Pro	Intel Core i7-7800X	3.50	48	SSD
3.	Microsoft Windows 10 Pro	Intel Core i7-7800X	3.50	32	SSD
4.	Microsoft Windows 10 Pro	Intel Core i7-7800X	3.50	32	SSD
5.	Microsoft Windows 10 Pro	Intel Core i7-7800X	3.50	48	SSD

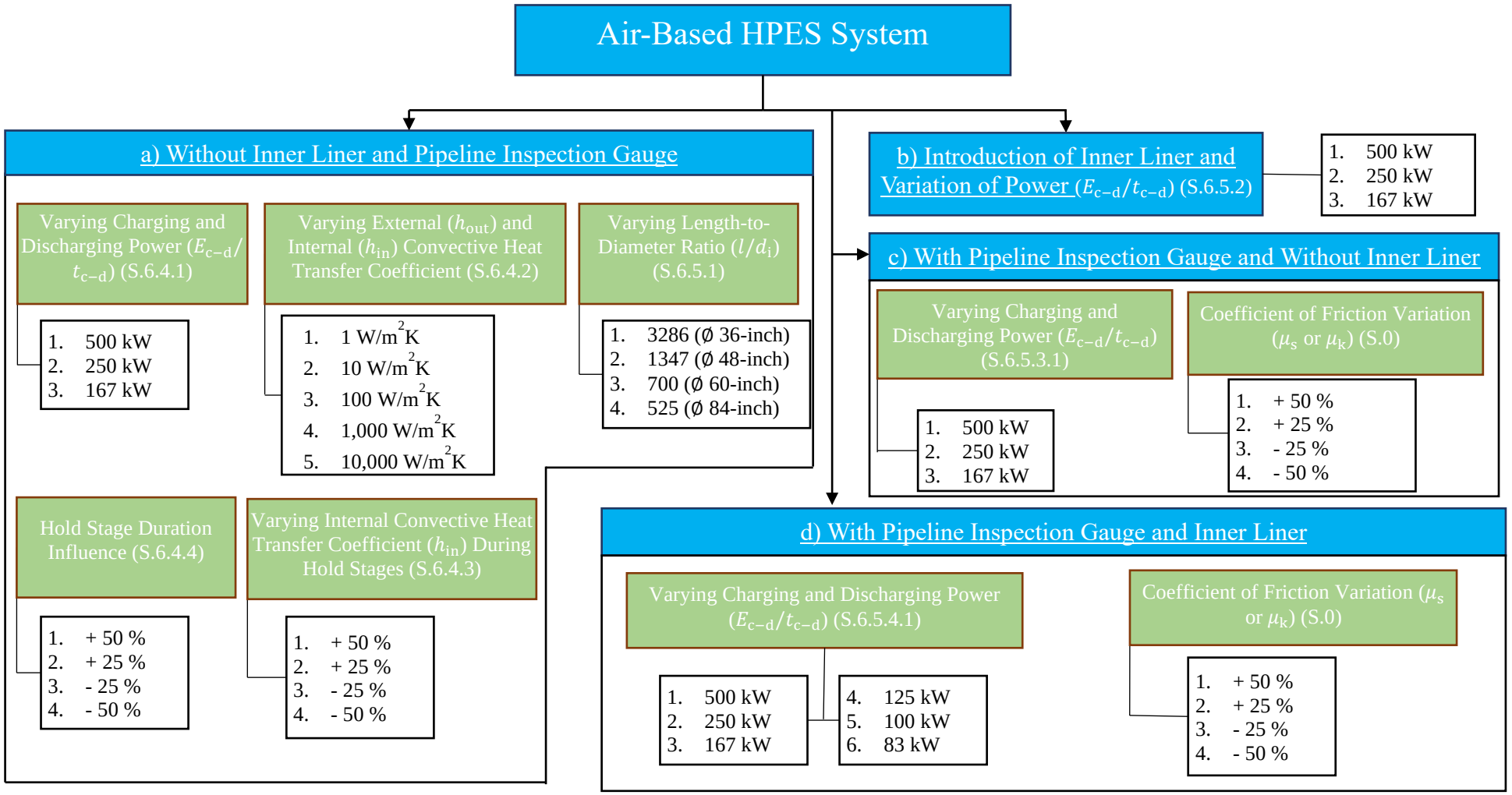

Figure 5.1- Air-Based HPES system simulations, excluding verification and validation simulations

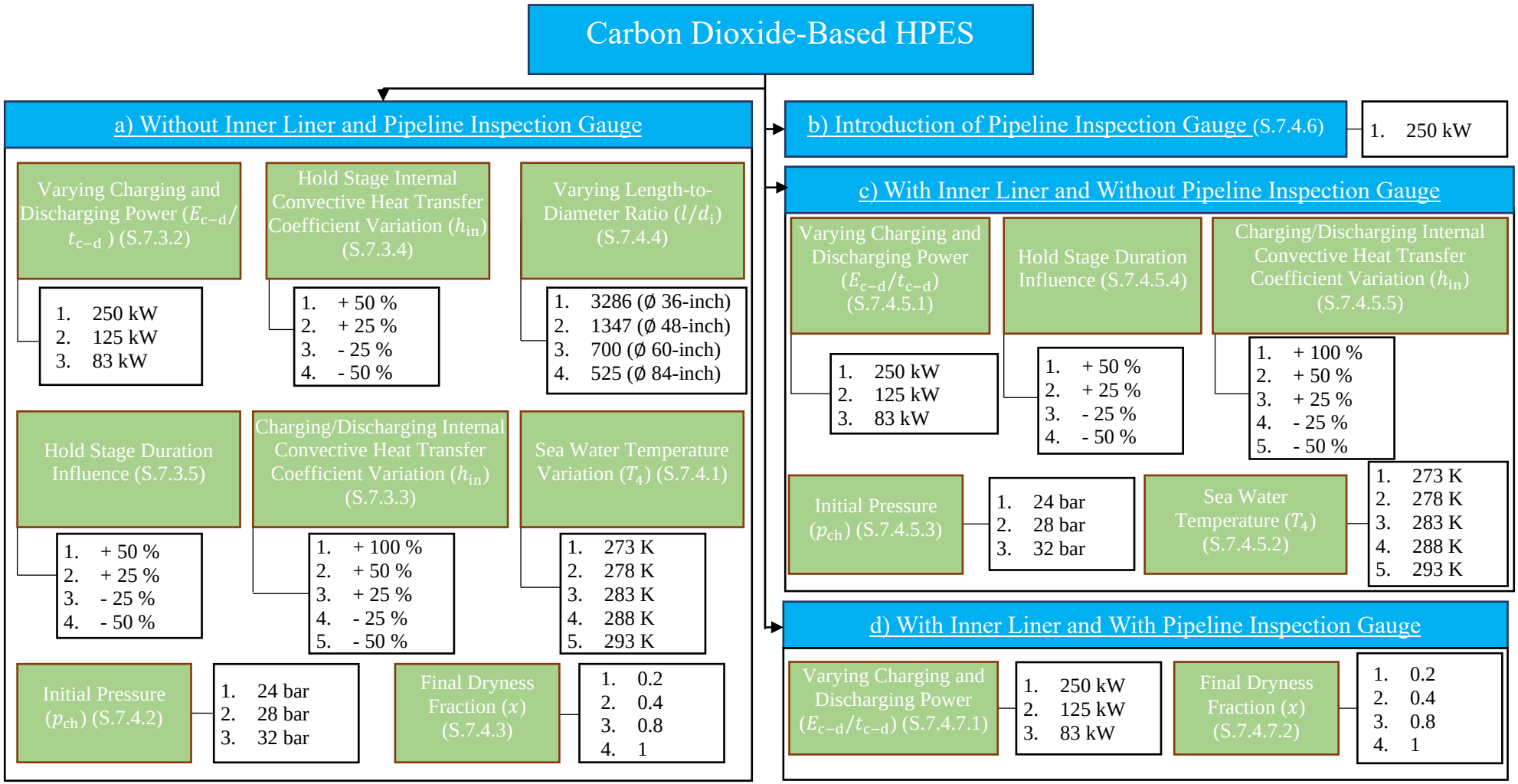

Figure 5.2- Carbon Dioxide-Based HPES system simulations, excluding verification simulations

Table 5.6- Pipeline diameter and the respective dimensions determined from *SmartPVB* [96] based on Von Mises theroy SM EN 13445-3:2014

Pipeline Diameter (inch)	Outer Diameter (m)	Inner Diameter (m)
48	1.22	1.19
60	1.52	1.48
84	2.13	2.08

Table 5.7- Sea water properties for the different temperatures [79, 80, 105]

Properties	Sea Water Temperature (K)			
	273	**278**	**288**	**293**
Coefficient of Thermal Expansion (K^{-1})	0.00005	0.00011	0.00021	0.00025
Kinematic Viscosity (x10-6) ($m^2.s^{-1}$)	1.85	1.61	1.21	1.05
Dynamic Viscosity (Pa.s)	0.001906	0.001652	0.001237	0.001077
Specific Heat Capacity ($J.kg^{-1}K^{-1}$)	3990.1	3992.5	3996.9	3998.9
Thermal Conductivity ($W.m^{-1}K^{-1}$)	0.55	0.56	0.58	0.58
Density ($kg.m^{-2}$)	1028	1027.5	1025.95	1024.9

For further clarification, the results for 283 K from the *CoolProp* library were plotted over those of the Ohio chart, presented in Figure 5.3a. Such a result further indicates the very good agreement between the two sources.

The developed code was designed to save the data files in MS Excel format for each stage, as discussed in Chapter 4. After each stage, the code outputs a message for the user to check for the saved file, as presented in Figure 5.3b. This also provides an indication of the progress of the code. Moreover, the code outputs a message of the energy stored and energy recovered along with the system CEF. For a better evaluation of the numerical simulations, it outputs the duration for each simulation as well.

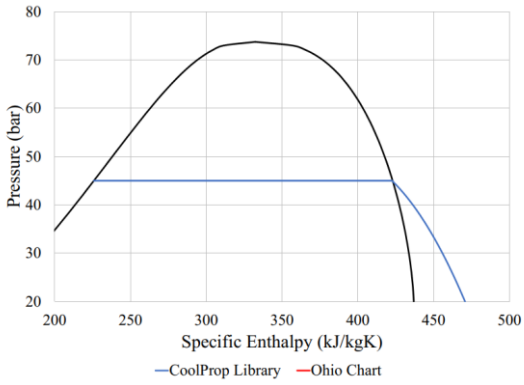

a)

```
Results for first stage check for file 'first_stage'

Results for second stage check for file 'second_stage'

Results for third stage check for file 'third_stage'

Results for fourth stage check for file 'fourth_stage'

-------------------------------------------------------

Energy Stored  = 0.9957 MWhr

Energy Recovered = 0.9466 MWhr

-------------------------------------------------------

CEF = 95.0670 %

-------------------------------------------------------

time_elapsed = 45.16 seconds
```

b)

Figure 5.3- a) Pressure (bar) against Specific Enthalpy (J/kgK) for a temperature of 283 K and b) *Spyder IDE* console output for the baseline air-based HPES accumulator without the inner liner and PIG

6 Air-Based HPES System

Throughout this chapter the air-based HPES code *CAIR* is verified, validated and studied under different conditions. Although in reality the filling of the accumulator would occur vertically when the PIG is not present, in this study it is assumed that irrespective of the PIG being present or not filling of the accumulator would occur horizontally as presented in Figure 6.1 for $i-1$ and i. The mentioned assumption aids in the analysis of the different set ups considered.

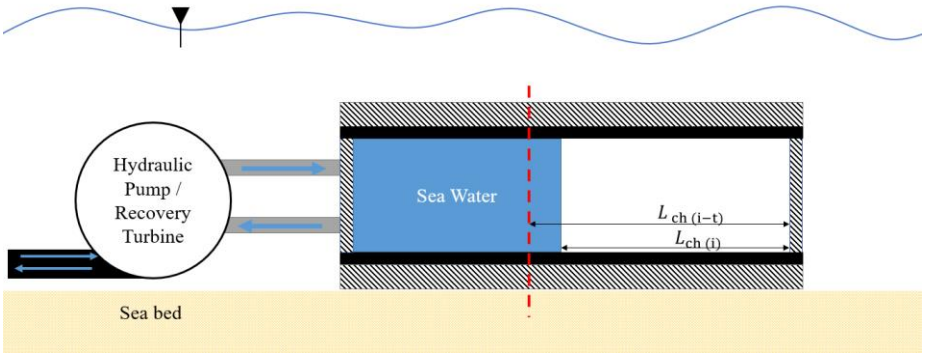

Figure 6.1- Horizontal filling of the proposed system without the pipeline inspection gauge

6.1 Verification for the Air-based HPES Code

Prior to utilising *CAIR* for the hydro pneumatic energy storage (HPES) system, the code was verified. The incremental time step size (Δt) was varied as shown in Table 6.1. Irrespective of the Δt the accumulator operated with 250 kW for the charging and discharging stages while having 4 hours for both hold stages.

Table 6.1- Cycle energy factor and simulation time for the incremental time step sizes

No.	Time step size (s)	Cycle Energy Factor (%)	Simulation time (s)
1	5	-	-
2	3	95.0924	7.50
3	1	95.0724	19.27
4	0.8	95.0722	23.14
5	0.4	95.0670	44.35
6	0.2	95.0657	90.70

For a time step size of 5 seconds, the code did not yield any results and a display error was noted. Initial evaluation of the cycle energy factor (CEF), presented in Table 6.1, indicates that irrespective of the time step size, the CEF remains relatively unchanged, with the difference between the second and sixth CEF only being of -0.028%. Moreover, from Table 6.1, it is evident that results are always obtained in a time frame

of less than 2 minutes. The CEF presented for the baseline system already shows good agreement with that presented by D. Buhagiar et al. [50], as stated in section 2.4.2.2.

The maximum and minimum temperatures of each stage for the different Δt were recorded and it was noted that the temperatures were identical to one another up to 2 decimal places (dp) with minor variation up to 4 dp. To obtain a better understanding of the variation of the compressed air temperature with respect to that of the surrounding sea water, equation 6.1 was used. Equation 6.1 is the root mean square (RMS) of the difference between the temperature of the compressed gas and that of the84ffect84dding sea water. This is used as a measure to assess the degree to which the thermodynamic processes during the different stages of the storage cycle follow isothermal conditions. An RMS value of zero would indicate purely isothermal conditions.

Observing the results presented in Table 6.2 computed using equation 6.1, it could be noted that all the values for each stage at each time step are relatively similar to one another while converging to a single value at finer incremental time step size. Results from Table 6.2 highlight that the Δt has a minimal effect on the RMS values at all four stages of the cycle.

$$\tau_{\text{iso}} = \sqrt{\left(\frac{1}{N}\right)\sum_{i=1}^{N}(T_{1\,(\text{t})_{\text{i}}} - T_4)^2} \tag{6.1}$$

For a time step size of 0.2 seconds, it could be assumed that the data is more refined than that when the time step is of 3 seconds, hence the results of the greater time step sizes could be compared to it for pressure. Analysis of the pressure is carried out through the percentage difference between the pressure at a given time step with respect to that obtained for a time step of 0.2 seconds, see equation 6.2.

Table 6.2- Root mean square values for time step sizes for the four stages of the storage cycle

Time Step Size (s)	Root Mean Square (K)			
	Charging Stage	**First Hold Stage**	**Discharging Stage**	**Second Hold Stage**
3	4.6695	1.4263	4.4924	0.4339
1	4.6659	1.4256	4.4992	0.4336
0.8	4.6647	1.4256	4.4975	0.4336
0.4	4.6630	1.4255	4.5013	0.4335
0.2	4.6620	1.4254	4.5017	0.4335

Observing the maximum, minimum and average percentage difference of the pressure for the charging and discharging stages, presented in Table 6.3, it is evident that for the charging stage the smaller the time step size, the less the percentage difference for all the cases. Similarly, for the discharging stage the percentage difference for the maximum and average values tend to converge towards 0% the closer the time step is to 0.2 seconds increment, but such behaviour is not present for the minimum value.

$$\Delta p_{\mathrm{ch}(\Delta \mathrm{t}-0.2)} = \left(\frac{p_{\mathrm{ch}\ (\Delta \mathrm{t})} - p_{\mathrm{ch}\ (0.2)}}{p_{\mathrm{ch}\ (0.2)}} \times 100 \right)_t \tag{6.2}$$

From the results of this study, it could be concluded that, irrespective the time step size, the results would be obtained with a reasonable accuracy and within a reasonable time frame. Hence, since the time step does not impact the time frame nor the accuracy, as has been verified, a time step of 0.4 seconds is selected for future simulations.

6.2 Quantitative Validation

The code was validated by calculating the polytropic index for two scenarios: 1) no heat transfer across the accumulator boundary (adiabatic) and 2) very high convective heat transfer coefficient (isothermal). For the system to have no heat transfer from the gas to the surrounding wall, the heat transfer model within the code was switched off. For the isothermal case the convective heat transfer coefficient, both for the inside and outside accumulator walls, was set to an extremely high value of 10,000 W/m^{2}K.

Table 6.3- Percentage difference in pressure for a given time step with respect to that at a timestep of 0.2 seconds

Charging Stage			
	Maximum (%)	**Minimum (%)**	**Average (%)**
0.4-0.2	0.0005	0.0000	0.0003
0.8-0.2	0.0016	0.0000	0.0008
1-0.2	0.0021	0.0000	0.0011
3-0.2	0.0074	0.0000	0.0038
Discharging Stage			
	Maximum (%)	**Minimum (%)**	**Average (%)**
0.4-0.2	0.0010	-0.0002	0.0007
0.8-0.2	0.0030	-0.0028	0.0022
1-0.2	0.0040	-0.0018	0.0029
3-0.2	0.0195	-0.0095	0.0157

The CEF estimated by the code for the above two scenarios was found to be close to 100% (refer to Table 6.4). For the system having no heat transfer, it could be observed from Table 6.4 that it stores less energy than for the system having high convective

heat transfer coefficient, while in both cases the desired pressure of 60 bar is attained. The mentioned observation indicates a preliminary advantage of operating the system in an isothermal state rather than adiabatic.

Table 6.4- Cycle energy factor, energy stored and energy recovered for no heat transfer and high convective heat transfer coefficient

	Cycle Energy Factor (%)	Energy Stored (MWhr)	Energy Recovered (MWhr)
No Heat Transfer	100.00	0.8079	0.8080
High Convective Heat Transfer Coefficient	99.98	1.0073	1.0071

Plotting the results of the adiabatic system over a pressure against volume graph, Figure 6.2a, it is evident that both the charging and discharging stages paths overlap one another. This indicates that no heat was lost nor gained during the hold stages. Similarly, could be observed for the pressure against volume for the isothermal system, Figure 6.2b. The pressure of 60 bar was reached at a smaller volume for the isothermal than the adiabatic system, as could be observed from the comparison of Figure 6.2a and b. This behaviour is present since the temperature of the adiabatic increases at a faster rate than that of the isothermal, causing for the pressure to be reached at a greater volume in the pressure chamber.

During the charging stage of the adiabatic system, air within the pressure chamber experiences a temperature rise from an initial temperature of 283 K, up to 364.84 K, due to no heat transfer. On the other hand, the isothermal system retains a temperature relatively similar to that of the initial conditions, equal to 283.03 K.

The polytropic index (n) was calculated for each time step for the charging and discharging stages using equation 6.3, both for the adiabatic and isothermal systems. Moreover, the average of the polytropic index for the whole stage was calculated using equation 6.4 to obtain a better indication of the cycle behaviour.

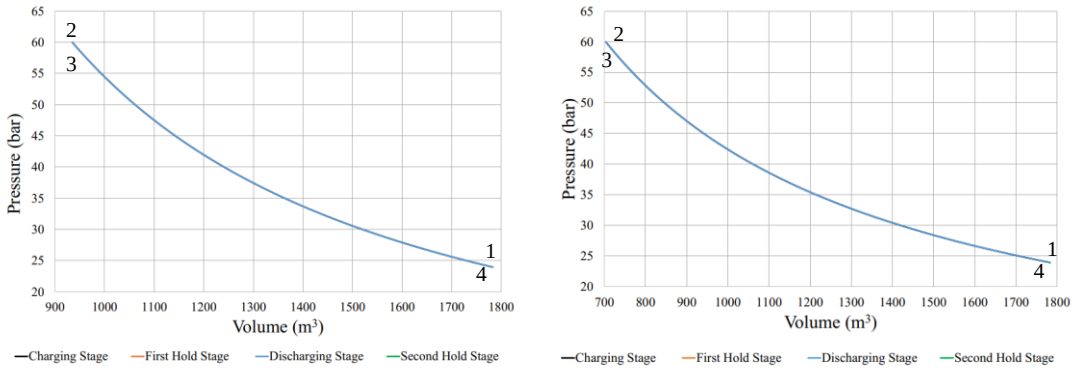

a) b)

Figure 6.2- Pressure (bar) against Volume (m^3) for a) no heat transfer system and b) system with a high convective heat transfer (1-2 charging stage, 2-3 first hold stage, 3-4 discharging stage and 4-1 second hold stage)

$$n_{\mathrm{i}} = \frac{\ln\left(\frac{p_{\mathrm{ch}_{(\mathrm{i}-1)}}}{p_{\mathrm{ch}_{(\mathrm{i})}}}\right)}{\ln\left(\frac{V_{\mathrm{ch}_{(\mathrm{i})}}}{V_{\mathrm{ch}_{(\mathrm{i}-1)}}}\right)} \tag{6.3}$$

$$n_{\mathrm{avg}} = \frac{\sum_{i=1}^{N} n_{\mathrm{i}}}{N} \tag{6.4}$$

For both the charging and discharging stages, the average polytropic index for the adiabatic system was predicted by the code to be equal to 1.42 while the corresponding values for the isothermal system were found to be equal 1. Thermodynamics theory indicates that for a polytropic index close to 1.4, the process is adiabatic, while for a polytropic index 1 the process is isothermal [110]. This confirmed the consistency of the code predictions with fundamental theory.

6.3 Initial System Observation of the Time Response Characteristics for Air

Prior to carrying out further analysis of the *Python*® code some observations were carried for each of the four stages of the energy storage cycle, ensuring that the code is working as intended. The baseline study had a power of 250 kW during the charging and discharging stages and having 4 hours for both hold stages while considering a system without the inner liner and the PIG.

6.3.1 Charging Stage

The temperature of air for the charging stage initially suffers from a rapid increase while then it settles to a gradual increase for the remaining stage as presented in Figure 6.3a. This behaviour is present since at the initial time step the temperature of air is similar to that of the surrounding sea water, causing a lower heat transfer rate. This causes, the gas being compressed to heat up at a faster rate than that at which heat is dissipated to the surrounding sea water. With time the heat transfer rate increases since the temperature of the gas is greater than that of the surrounding.

From the plot of the pressure against volume, Figure 6.3b, one can note the rate at which the pressure is increasing with respect to the reduction in volume during the compression stage. The circumferential area of the cylindrical wall of the compressed air volume decreases as more sea water is injected into the accumulator (see Figure 6.3c). The decrease in wall area leads to a reduction in the heat transfer as could be observed in Figure 6.3c from the negative slope of the curve between the 1st hour till

the end. The first part of Figure 6.3c highly correlates to the first part of Figure 6.3a, indicating that initially the heat transfer is low causing a rapid increase in the temperature of the gas.

Figure 6.3d depicts the flow rate of the system with the change in pressure. This result is expected, given that the pump power for charging remains constant at 250 kW throughout the whole charging stage, therefore the flow rate will decrease as the injected sea water pressure (p_{sw}) increases.

6.3.2 First Hold Stage

During the first hold stage it was ensured that the system volume remains constant at the final volume of the charging stage while no work done was applied (i.e. no sea water injected into the accumulator by the pump). Initially, the temperature of the air is greater than that of the surrounding wall and sea water, while the gas experiences a temperature drop until the temperature of air reaches that of the surrounding sea water. Between the 4th and 5th hour of Figure 6.4a, the gas experiences a greater temperature drop than between the 5th hour till the end of the stage. Such occurrence is present due to the gas temperature initially being greater than that of the surrounding seawater, hence having a greater heat transfer rate.

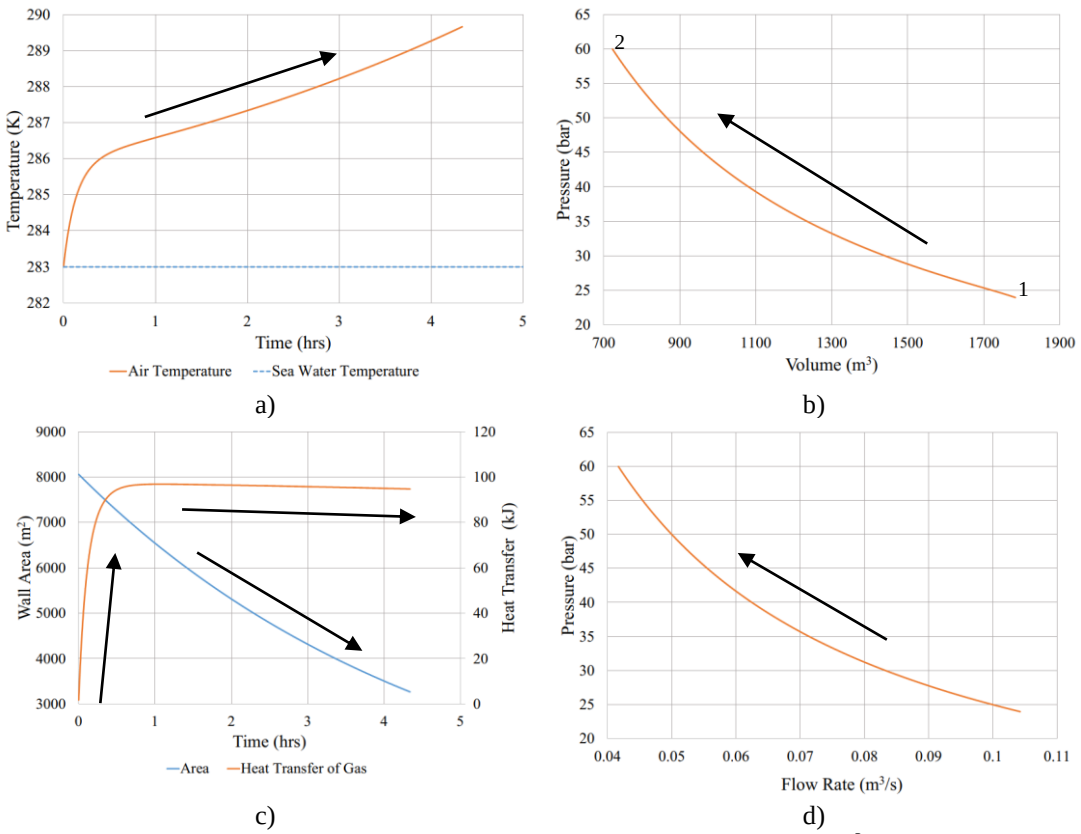

Figure 6.3- a) Temperature (K) against Time (hrs), b) Pressure (bar) against Volume (m^3) (process from 1 to 2) c) Wall Area (m^2) and Heat Transfer (kJ) against Time (hrs) and d) Pressure (bar) against Flow Rate (m^3/s) for the charging stage with arrows indicating the direction

As already established, the temperature of the gas highly impacts the pressure of the gas within the chamber, therefore the profile of pressure presented in Figure 6.4b follows the same trend as that of Figure 6.4a. Moreover, it could be noted that during the first hold stage air experience a pressure drop of only 1.6 bar for a temperature drop of approximately 6 K. The 6 K temperature drop during the first hold stage indicates that during the charging stage air is at a temperature close to that of the surrounding sea water, offering quasi-isothermal conditions.

6.3.3 Discharging Stage

During the discharging stage the air within the pressure chamber expands as the sea water is allowed to flow out from the accumulator and discharge through the energy recovery turbine. This causes the gas to expand and experience a pressure drop. Consequently, the air temperature also decreases as predicted by the code in Figure 6.5a, where the temperature is less than that of the surrounding sea water. Between the 8th and 9th hour of the cycle air suffers a rapid temperature drop due to the limited heat transfer from the surrounding sea water to the air while the volume is increasing. At approximately the 9.5th hour of the cycle the gas reaches a constant heat transfer rate, Figure 6.5b, the temperature of the gas increases as well with the volume. Such occurrence is present since the heat transfer increases and so does the inner cylindrical area. For this study emitted heat energy is considered as positive heat transfer while absorbed is negative. Such convention was considered in the equations of Chapter 3.

The inner cylindrical wall area increases with respect to time as the gas expands (Figure 6.5c), the reverse process of what has been observed for the charging stage. The wall area is relatively small when the gas starts to expands, hindering the heat flow from the surrounding sea water to the stored air. Moreover, Figure 6.5d represents the pressure with respect to the chamber volume as the pressure of air drops.

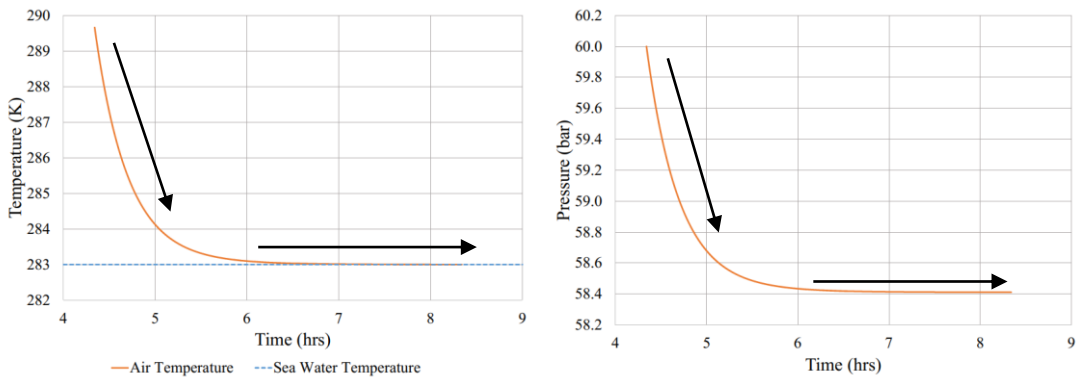

a) b)

Figure 6.4- a) Temperature (K) and b) Pressure (bar) against Whole Cycle Time (hrs) with arrows indicating direction

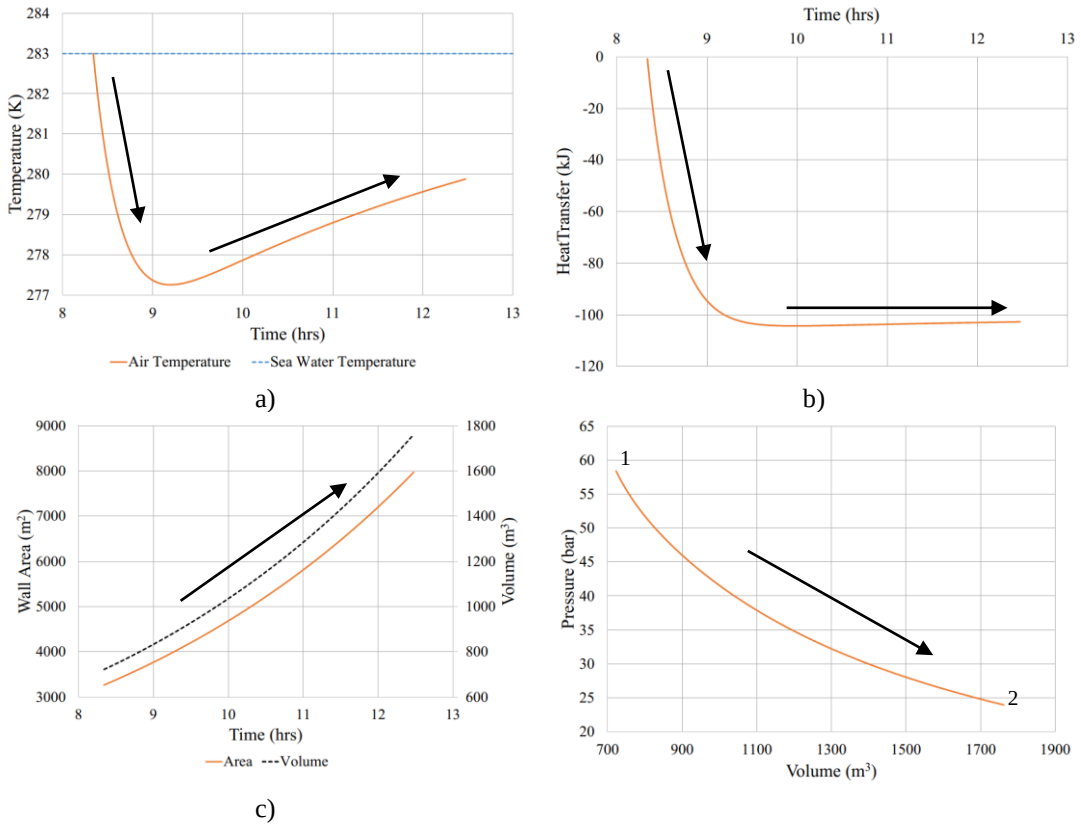

Figure 6.5- a) Temperature (K) against Time (hrs), b) Heat Transfer Rate (kJ) against Time (hrs), c) Wall Area (m^2) and Volume (m^3) against Time (hrs), and d) Pressure (bar) against Volume (m^3) (process from 1 to 2) while including arrows indicating direction

6.3.4 Second Hold Stage

The initial temperature of air during the second hold stage is less than that of the surrounding sea water, therefore energy from the surrounding sea water is absorbed by the air to increase its temperature. Air rapidly gains energy from the surrounding sea water to reach thermal equilibrium to its surroundings, almost in less than an hour as could be observed from Figure 6.6a. For this stage, air gains only 3 K from the surrounding sea water, indicating the difference between the air and the surrounding during discharging is minimal, offering quasi-isothermal conditions. As air temperature reaches that of the surrounding sea water, its pressure also increases to a constant while the volume of the chamber remains unchanged (isochoric), Figure 6.6b.

6.4 Initial Parametric Code Analysis

Initially analysing the code, a series of parametric simulations were considered to analyse the code results under different conditions such as; 1) variation of the charging and discharging power, 2) influence of the convective heat transfer coefficient for the charging and discharging stages, 3) influence of both hold stages internal convective heat transfer coefficient and 4) both hold stages duration.

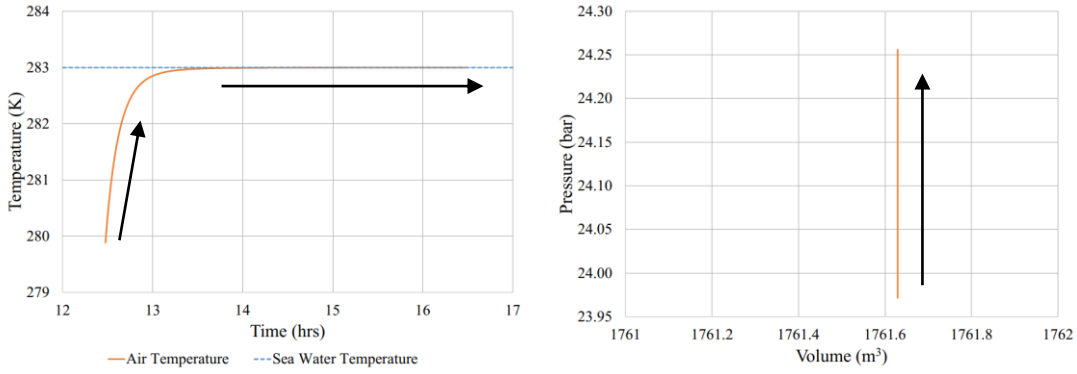

a) b)

Figure 6.6- a) Temperature (K) against Time (hrs) and b) Pressure (bar) against Volume (m^3) with arrows indicating direction

6.4.1 Variation of the Charging and Discharging Power

The charging and discharging stage power was varied to 3 different values equal to 500 kW, 250 kW and 167 kW. Observing the CEF of the different charging/discharging stages power presented in Table 6.5 it could be noted that the lower the power the greater the achievable CEF.

The final temperature of the charging stage resulted to be influenced by the power as presented in Table 6.5, where lower power led to a lower final temperature. Thus, having lower powers allow internally generated heat to be dissipated through the surrounding wall while reaching the final pressure of 60 bar. Lower power also impact the final temperature for the discharging stage, due to the final temperature getting closer to that of the surrounding sea water. Such an instance occurs because lower power allows for more heat to be absorbed from the surrounding.

For each increment, the difference between the temperature of air within the accumulator to that of the surrounding sea water (ε) was calculated using equation 6.5. The results for the temperature difference were grouped in 14 groups from 0 K to 7 K in increments of 0.5 K, as presented in the histogram of Figure 6.7a.

Table 6.5- Cycle energy factor and the final temperature for the charging/ discharging stages for the different power and hydraulic power

Hydraulic Power (kW)	Cycle Energy Factor (%)	Final Temperature (K)	
		Charging	Discharging
500	94.3	290.70	279.32
250	95.1	289.66	279.88
167	95.5	289.12	280.17

The first group in Figure 6.7a holds the frequency of the results of ε less than or equal to 0 K, the second group hold the result for $0\ \text{K} < \varepsilon \leq 0.5\ \text{K}$ and so on. From Figure 6.7a it could be observed that smaller pump and turbine power result in less increments

temperature deviating from that of the surrounding sea water. For a charging power of 500 kW and 250 kW the greatest temperature difference is between 6.5 K $< \varepsilon \leq$ 7 K while for 167 kW is between 6 K $< \varepsilon \leq$ 6.5 K. Moreover, the maximum frequency deviates further away from 0 K as the power of the charging stage increases.

$$\varepsilon = (T_{1\,(i)} - T_4) \tag{6.5}$$

Figure 6.7b shows the corresponding histogram for the discharging process. The temperature of the gas is less than that of the surrounding sea water since during expansion the temperature drops. From Figure 6.7b it is visible that the greater the discharging power the greater the temperature deviations of the gas from the surrounding sea water. Also, it could be observed that the frequency of the difference is well distributed throughout the different groups, that is, for a discharging power of 167 kW, the frequency for the difference of -3 K is approximately close to that of -5 K. Similar behaviour is present for other charging and discharging powers for different frequency groups.

The different power values during both charging and discharging stages also impacts the final volume at which the desired pressure is reached, as presented in Figure 6.8. It could be deduced that for lower powers, the maximum pressure of 60 bar is reached at a smaller volume due to a lower air temperature. Moreover, similar behaviour was observed during the discharging process, where the final pressure of 24 bar was reached at a smaller volume with a set power of 500 kw than that of 167 kW.

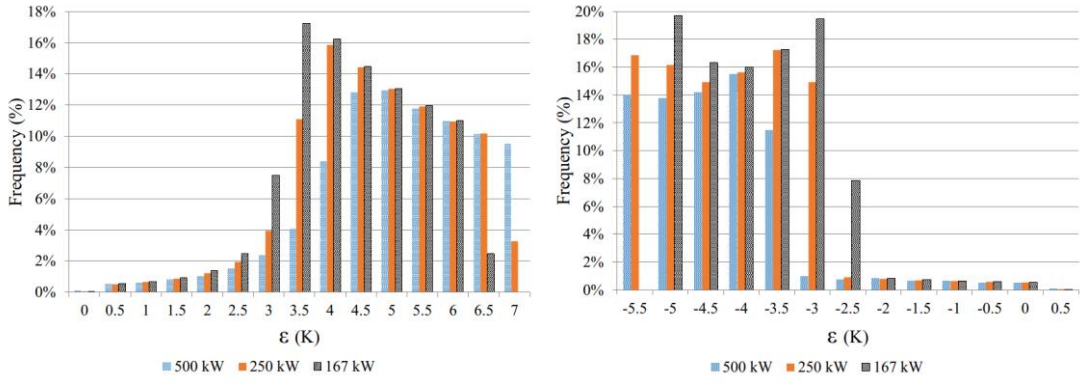

a) b)

Figure 6.7- Frequency (%) against $\boldsymbol{\varepsilon}$ (K) for the a) charging stage and b) discharging stage

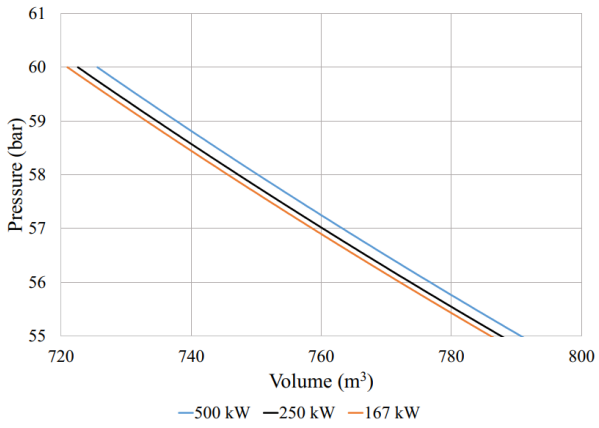

Figure 6.8- Pressure (bar) against Volume (m^3) towards the end of the charging stage at different powers

The observed behaviour of the final temperature and volume is a result of the pump flow rate which is affected from its power. Reverting to equation 3.2 in section 3.2.1.1, varying the charging/discharging power, the flow rate is varied as well. For smaller charging/discharging pump power the pump flow rate is decreased accordingly for the same pressure.

The average polytropic index (n_{avg}) (equation 6.4) was calculated for both the charging and discharging stages while tabulated in Table 6.6. During charging, the code yields an index that approaches unity for lower pump power, given that internally generated heat is allowed to be dissipated through the accumulator wall and maintain quasi-isothermal conditions. On the other hand, during discharging the polytropic index is greater than 1 for 500 kW while for 250 kW and 167 kW n is less than 1. For 500 kW of discharging, the heat transfer between the gas to the surrounding wall is much greater than that for 250 kW and 167 kW due to greater temperature difference.

Hence, for 250 kW and 167 kW the air within the chamber regains more thermal energy from the surrounding than for 500 kW as the gas expands. According to X. Wang et al. [111], the polytropic index is less than 1 during discharging since the heat absorption from the surrounding wall is large enough to raise the air temperature [111]. X. Wang et al. [111] statement validates the results obtained during discharging since at 250 kW and 167 kW the duration is long enough for the air within the chamber to absorb heat from the wall to significantly raise the temperature at a greater rate than at 500 kW.

Table 6.6-Charging and discharging power polytropic index

Charging/Discharging Power (kW)	Charging	Discharging
500	1.021	1.002
250	1.016	0.999
167	1.013	0.998

6.4.2 Influence of the Heat Transfer Coefficient During Charging and Discharging

The internal convective heat transfer coefficient (h) for the charging and discharging stages was varied from 1 to 10,000 W.m^{-2}K^{-1} for the inside and outside accumulator surfaces. Logarithmic scaling for the variation of h was applied. The prediction of h from the Gnielinski correlation for the internal gas and the Churchill and Chu correlation for the external sea water were switched off while the overall h value was set to the stated constants within the *Python*® code. The convective heat transfer coefficients for the internal air and external sea water were not modified for the hold stages. Moreover, for this study the pump and turbine power were set to 250 kW while all the remaining constants were unchanged throughout this study.

For higher h values, the CEF value approaches 100 %, as shown in Figure 6.9. This result is logical since higher h values allow for better heat transfer over a given charging stage. Consequently, the final temperature is closer to that of the surrounding sea water. As a result, the temperature drop experienced by air during the first hold stage would be less. This indicates that a greater fraction of the pump power during the charging stage is converted to increase the gas pressure rather than the temperature for high values of h.

Analysing the polytropic index with the respective different convective heat transfer coefficients, as presented in Table 6.7, it could be noted that small values of h result in higher polytropic index. During the charging stage, the maximum temperature tends to be the greatest the smaller the value of h, as presented in Table 6.7, similarly for the minimum discharging temperature.

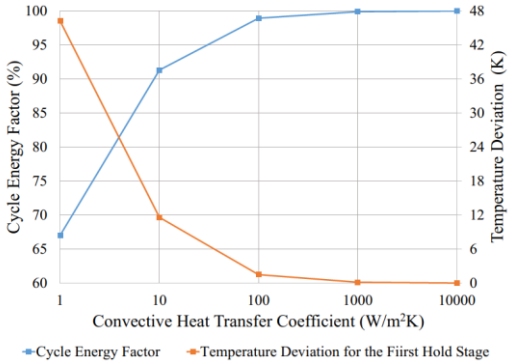

Figure 6.9- Cycle Energy Factor (%) and Temperature Deviation experienced by the gas during the first hold stage (K) against Convective Heat Transfer Coefficient (W/m^{2}K)

The value of the polytropic index is further validated by calculating the RMS, where for a value of h of 1W.m^{-2}K^{-1} has τ_{iso} of 29.53 K while for h of 10,000 W.m^{-2}K^{-1} has

τ_{iso} of 0.03 K, during charging as presented in Table 6.7. Similar results were observed during the discharging stage for τ_{iso}. Hence, the value of h has a significant effect on the heat transfer, effecting the maximum and minimum temperatures during the charging and discharging stages while also impacting the polytropic index.

Table 6.7- Convective heat transfer coefficient with the respective polytropic index and temperatures for the charging and discharging stages while taking into account the root mean square for the charging stage

Convective Heat Transfer Coefficient ($W.m^{-2}K^{-1}$)	Polytropic Index		Temperature (K)		Root Mean Square Charging (K)
	Charging	Discharging	Maximum Charging	Minimum Discharging	
1	1.211	1.209	329.190	249.058	29.53
10	1.039	1.018	294.614	274.600	7.52
100	0.993	0.989	284.516	281.634	1.02
1,000	0.987	0.986	283.178	282.824	0.12
10,000	0.986	0.986	283.041	282.959	0.03

The value of h also impacts the final volume of the charging stage to reach the peak working pressure of the accumulator, as presented in Table 6.8 and Figure 6.10. For low values of h the heat transfer during the charging stage occurs at a slower rate than that of higher value, causing the final pressure to be reached at a greater volume.

For low values of h the desired pressure is reached at a greater rate with respect to volume, as presented in Figure 6.10 and the gradient of the different convective heat transfer coefficients. Moreover, observing the plots of Figure 6.10 it could be understood that the area under the graph is less for smaller values of h, therefore less energy stored. This is also reflected in the results presented in Table 6.8.

This study validates that high values of the convective heat transfer coefficient aid in the heat transfer of the gas and it has a considerable impact on the overall system performance. It has also been validated that the system CEF is highly dependent on the heat transfer of the gas to the surrounding wall.

Table 6.8- Convective heat transfer coefficient with the respective final volume and the energy stored during the charging stage

Convective heat transfer coefficient ($W.m^{-2}K^{-1}$)	Final Volume (m^3)	Energy Stored (MWhr)
1	835.5	0.907
10	736.9	0.984
100	707.5	1.005
1,000	703.6	1.007
10,000	703.2	1.007

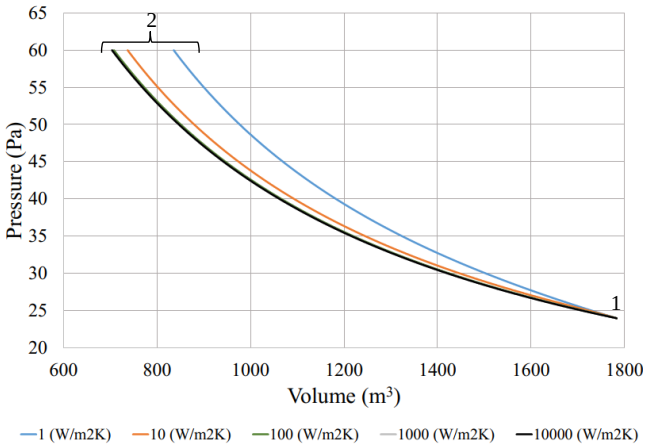

Figure 6.10- Pressure (bar) against Volume (m^3) for the charging stage and the different convective heat transfer coefficients (process from 1 to 2)

6.4.3 Influence of the Internal Convective Heat Transfer Coefficients During the Hold Stages

The internal convective heat transfer coefficient (h_{in}) during the first and second hold stages was initially set to a constant of 10 $W.m^{-2}K^{-1}$, as discussed in section 3.2.1.2. To understand the influence of the h_{in} over the system performance, it was varied to four different constants being $\pm$ 25 % and $\pm$ 50 % of 10 $W.m^{-2}K^{-1}$, resulting in the values presented in Table 6.9. The HPES cycle was set to operate at a pump and recovery turbine power of 250 kW and 4 hours for hold stages.

The different values of h_{in} had minimal to no influence on the CEF. For an h of 5 $W.m^{-2}K^{-1}$ and 7.5 $W.m^{-2}K^{-1}$ a CEF of 95.0671% was obtained while for an h of 10 $W.m^{-2}K^{-1}$, 12.5 $W.m^{-2}K^{-1}$ and 15 $W.m^{-2}K^{-1}$ a CEF of 95.0670% was obtained. The different values of h_{in} highly influence the rate at which thermal energy of the gas is lost or gained from or to the surrounding wall, as could be observed from Figure 6.11 for the first hold stage. From Figure 6.11 it could be noted that the temperature of air returns back to that of the surrounding seawater within the 4-hour duration irrespective of the h_{in} value. Moreover, further analysis of Figure 6.11 indicate that if the first hold stage duration is less than 2 hours, h_{in} would highly impact the final temperature and the CEF of the system since less energy would be dissipated.

Table 6.9- Convective heat transfer coefficients percentage deviation and the respective values

Sensitivity of the Convective Heat Transfer Coefficient (%)	Convective Heat Transfer Coefficient ($W.m^{-2}K^{-1}$)
-50	5
-25	7.5
0	10
+25	12.5
+50	15

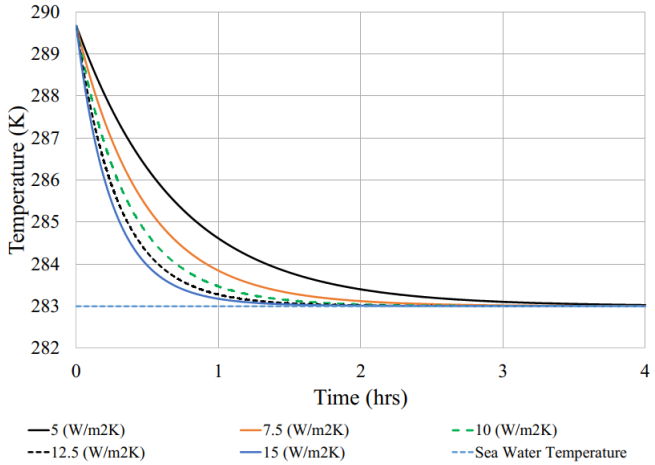

Figure 6.11- Temperature (K) against duration Time (hrs) for the first hold stage

As already mentioned, the h_{in} impacts the final temperature of the hold stage, as could be observed in Table 6.10. The value of the h_{in} impacts the final temperature of the first hold stage more than that of the second. In an ideal scenario, the final temperature of the air eventually returns back to that of the surrounding seawater at 283 K, if enough time is allowed. Therefore, comparing the final temperature of both hold stages to the that of the surrounding sea water, it results in a percentage deviation of less than $\pm$ 0.1 %, as exhibited in Table 6.10.

The mentioned observation highlights that for a 4 hour hold duration, the different values of h_{in} have minimal to no effect over the system performance. The results indicate that h_{in} value highly influence the rate at which thermal energy is gained or lost from or to the surrounding sea water while the final temperature is similar to one another irrespective of the value.

Table 6.10- Convective heat transfer coefficient and the final temperatures for the first and second hold stages along with the percentage gas temperature deviation from the surrounding sea water

Convective heat transfer coefficient ($W.m^{-2}K^{-1}$)	**Final Temperature (K)**		**Percentage Gas Temperature Deviation from the Surrounding Sea Water**	
	First Hold Stage	**Second Hold Stage**	**First Hold Stage**	**Second Hold Stage**
5	283.0301	282.9995	0.0106%	-0.0002%
7.5	283.0052	282.9997	0.0018%	-0.0001%
10	283.0020	282.9997	0.0007%	-0.0001%
12.5	283.0012	282.9997	0.0004%	-0.0001%
15	283.0009	282.9997	0.0003%	-0.0001%

It could be concluded that the h value does not impact the final temperature for 4 hours durations or greater. Further work must be carried out to derive a correlation to determine free internal convection heat transfer coefficient within a horizontal cylindrical tube for an enclosed system.

6.4.4 Influence of the Duration in the Hold Stages

The duration of the hold stages was varied to ± 25 % and ± 50 % of the 4-hour duration, leading to the durations listed in Table 6.11. For this study the charging and the discharging power were retained 250 kW, while for both hold stages the internal convective heat transfer coefficient was set at 10 $W.m^{-2}K^{-1}$. Initially analysing the CEF of the different durations from Table 6.11, it could be noted that for 2 hours the resulting CEF is greater than those of longer durations. Such occurrence exists since a duration of 2 hours does not allow for the heat gained during the charging stage to be completely dissipated to the surrounding, resulting a greater CEF value than for longer durations.

Analysing the air temperature against hold stage duration plots presented in Figure 6.6, during the first and second hold stages, it could be noted that after 2 hours the final temperature of the air is close to that of the surrounding sea water. Moreover, from Figure 6.6 it is evident that after 3 hours the final temperature for both stages is similar to that of the surrounding sea water. This result is also present in the system CEF since after 3 hours the CEF remains relatively constant. Thus, it could be concluded that the influence of the hold stage duration on the CEF and time-varying gas temperature is negligible.

Table 6.11- Hold stage duration percentage sensitivity with the respective hours and the cycle energy factor

Sensitivity of the Hold Stage Duration (%)	Hold Stage Duration (hrs)	Cycle Energy Factor (%)
-50	2	95.0697
-25	3	95.0671
0	4	95.0670
+25	5	95.0670
+50	6	95.0670

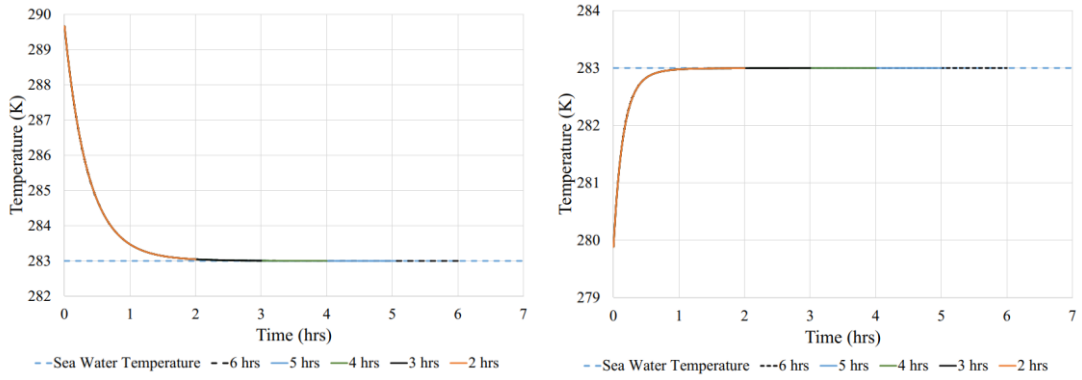

Figure 6.12- Temperature (K) against Time (hrs) for different hold stage durations for a) the first hold stage and b) the second hold stage

6.5 Influence of Mechanical Design of System Performance

Further numerical investigations were conducted to understand the influence of the four following mechanical design parameters in the performance of the air-based HPES systems; 1) diameter of the pipeline, 2) inner liner, 3) pipeline inspection gauge and 4) pipeline inspection gauge with inner liner.

6.5.1 Influence of the Accumulator Pipeline Length-to-Diameter Ratio

The external diameter of the pipeline was varied from 36 to 84 inches (refer to section 5.3) as presented in Table 6.12, while maintaining the original volume fixed at 1782.72 m^3. Varying the pipeline diameter with a fixed volume causes the length of the pipeline and the length-to-diameter ratio to vary as indicated in Table 6.12. Observing the CEF of the four different systems of Table 6.12, it is evident that greater pipeline diameters reduce the CEF. This indicates that the length-to-diameter ratio influences the rate of heat transfer from the gas to the surrounding during charging, as identified by the final temperature of the charging stage, Table 6.12.

Table 6.12-Pipeline diameters, internal diameters with the respective lengths, cycle energy factor and final temperature for the charging stage

Pipeline Diameter (inch)	Internal Diameter (m)	Pipeline Length (m)	Internal Length-to-Diameter Ratio	Cycle Energy Factor (%)	Final Temperature During Charging Stage (K)
36	0.884	2905	3286	95.1	289.19
48	1.19	1603	1347	89.8	296.40
60	1.48	1036	700	82.7	306.21
84	2.08	525	252	68.7	328.19

As established before, the heat transfer rate is correlated to the area of the cylindrical wall in contact with air. Its effect is further highlighted by the following derivation of equation 6.6 to 6.11. Equation 6.6 represents the system internal volume, which remains constant irrespective of the diameter. It is modified to obtain the length in terms of volume and the diameter, resulting in equation 6.7. The internal area of the cylindrical wall, to which the air is in contact to is presented by equation 6.8, substituting for the length in equation 6.8 using the result of equation 6.7, equation 6.9 is obtained. Since the numerator of equation 6.9 remains constant, then it is the constant of proportionality, k, of equation 6.10. Hence, this results in the relation presented by equation 6.11, where the internal area is inversely proportional to the internal diameter. Such relation indicates that increasing the diameter of the pipeline causes the area to reduce while its effect is highlighted by the final temperature of the

charging stage presented in Table 6.12. Moreover, the final temperatures also indicate that the greater the diameter and the length-to-diameter ratio, the less isothermal the system is.

$$V = \frac{\pi d_{\mathrm{i}}^2}{4} \times L \tag{6.6}$$

$$L_{\mathrm{ch}} = \frac{V \times 4}{\pi d_{\mathrm{i}}^2} \tag{6.7}$$

$$A = \pi d_{\mathrm{i}} \times L_{\mathrm{ch}} \tag{6.8}$$

$$A = \pi d_{\mathrm{i}} \times \frac{V \times 4}{\pi d_{\mathrm{i}}^2} = \frac{V \times 4}{d_{\mathrm{i}}} \tag{6.9}$$

$$y = kx \tag{6.10}$$

$$A \propto \frac{1}{d_{\mathrm{i}}} \tag{6.11}$$

Observing and comparing the plots in Figure 6.13, it could be noted that, for the 36-inch pipeline, the black line almost overlaps the blue line while for greater diameters the disparity between the two lines increases. This behaviour is present since the final temperature of the charging stage is greater for larger diameter systems, causing a greater temperature drop during the first hold stage as the temperature of air return back to that of the surrounding sea water. The 84-inch diameter pipeline suffers from a 10-bar pressure drop during the first hold stage, greater than what is experienced for smaller diameters. The lack of heat transfer for larger diameter pipelines also effects the final volume, where the final volume of the charging stage is greater for larger diameter pipelines.

The effect of the rate of heat transfer also influences the polytropic index of the system, as the greater the pipeline diameter the greater is the polytropic index, shifting the system towards non-isothermal conditions as indicated by Table 6.13. It can thus be concluded that smaller diameters allow for greater heat transfer, shifting the thermodynamic behaviour of the HPES accumulator towards isothermal behaviour while greater diameters shift the system towards a polytropic one.

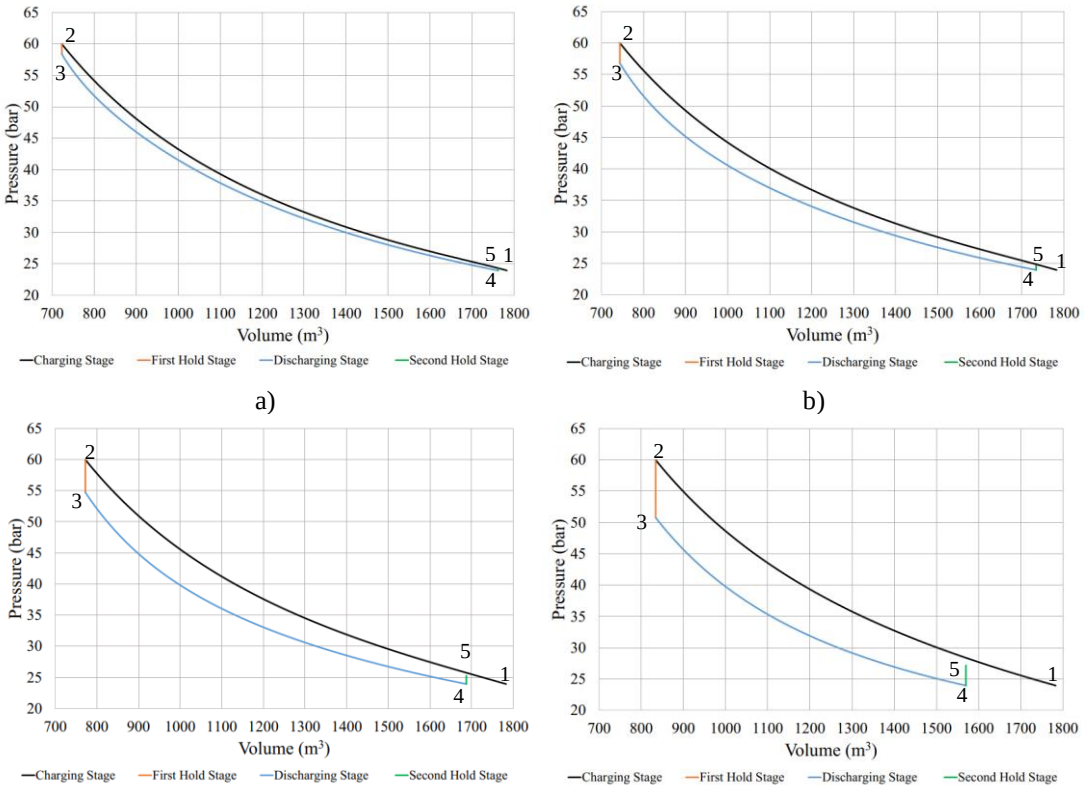

Figure 6.13-Pressure (bar) against Volume (m^3) for diameters of a) 36-inch, b) 48-inch, c) 60-inch and d) 84-inch pipeline for the whole cycle (1-2 charging stage, 2-3 first hold stage, 3-4 discharging stage, 4-5 second hold stage)

Table 6.13- Polytropic index for both the charging and discharging stages with the respective pipeline diameters

Pipeline Diameter (inch)	Polytropic Index	
	Charging Stage	Discharging Stage
36	1.016	0.999
48	1.049	1.019
60	1.096	1.056
84	1.207	1.187

6.5.1.1 Influence of Accumulator Diameter at Different Charging/Discharging Durations

The effect of the charging and discharging power was studied with respect to the greatest diameter under study, retaining the same accumulator volume. This was carried out since the CEF was found to be much less for 84-inch diameter pipeline than that of 36-inch diameter for the previous study (refer to section 6.5.1). Decreasing the charging and discharging power from 250 kW to 83 kW while maintaining the remaining parameters constant, the CEF increases both for 36- and 84-inch pipelines, as exhibited in Figure 6.14. Although the CEF in both cases increases, at no point does the CEF of the 84-inch pipeline system reaches that of the 36-inch. Hence, the 84-inch pipeline system would never be as thermally efficient as the 36-inch. Smaller charging and discharging power allow for heat to dissipate into the surrounding sea water, leading to the higher CEF estimates.

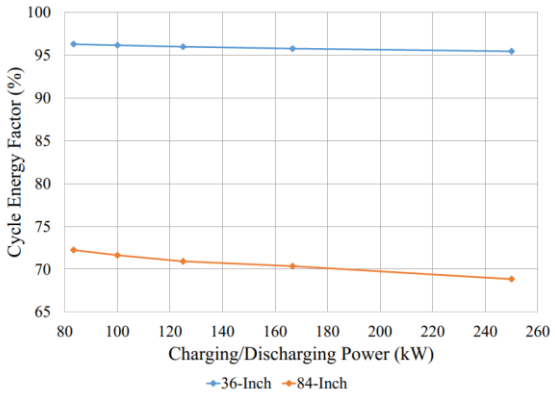

Figure 6.14- Cycle Energy Factor (%) against Charging/Discharging Power (kW) for 36-inch and 84-inch diameter pipelines

Table 6.14 shows that for lower powers the RMS is less than that for greater powers but relatively greater than the temperature of the surrounding sea water for the 84-inch pipeline. For a power of 83 kW, the degree of isothermal for the 36-inch pipeline resulted to be of 3.68 K and 3.58 K for the charging and discharging stages, being much less than that obtained for the 84-inch pipeline.

Table 6.14- Root mean square (K) for the 84-inch diameter pipeline and the different stages power (kW)

Charging/Discharging Stages Power (kW)	Root Mean Square (K)	
	Charging Stage	Discharging Stage
250	29.38	22.71
167	28.17	22.18
125	27.27	21.75
100	26.56	21.40
83	25.98	21.09

6.5.2 Inner Liner Influence

To protect the steel pipeline for corrosion, an inner protective liner is introduced having the parameters discussed in section 5.1. It is expected that the inner liner influences the CEF and the system thermal performance since the high-density polyethylene (HDPE) has different parameters than the steel outer pipeline, hindering the heat flow from the gas to the surrounding sea water and vice versa.

The influence of the inner liner was studied for different power of the charging and discharging stages, varying from 500 kW to 83 kW. It is observed from Table 6.15 that the liner has a negative impact on the CEF. The reduction in the CEF is however dependent on the power. For a power of 500 kW the CEF is only 90.27%, while for the longest power of 83 kW the CEF is of 95.71%. Hence, smaller charging power result in greater CEF values, a difference greater than 5%. Meanwhile, the system without the liner also experiences a CEF increase with smaller charging power but between the CEF of 500 kW and 83 kW the difference is less than 2%. The system

with the liner would require 167 kW to attain a CEF similar to that of 500 kW when no liner is present.

Table 6.15- Charging and discharging stages powers from 500 kW to 83 kW and the respective cycle energy factor for the system with/without inner liner along with the percentage change

Hydraulic Power (kW)	Cycle Energy Factor (%)		
	With Inner Liner	Without Inner Liner	Percentage Change
500	90.27	94.30	-4.27
250	93.18	95.07	-1.99
167	94.33	95.47	-1.19
125	94.99	95.75	-0.79
100	95.41	95.95	-0.56
83	95.71	96.11	-0.42

The charging and discharging stage power greatly influence the heat transfer as has been established. For the charging stage having a power of 500 kW, the maximum temperature was of 296.13 K while for a power of 83 kW the maximum temperature was of 288.82 K. A similar behaviour was observed for the minimum discharging temperature, since greater power led to lower temperatures, as presented in Table 6.16. The RMS reduces with lower power, both for charging and discharging, as presented in Table 6.16. Hence, in the presence of the inner liner the system deviates further away from being isothermal, irrespective of the power.

Table 6.16- Charging and discharging stages power at 500 kW and 83 kW with the respective maximum charging and minimum discharging temperatures along with the root mean square for both stages

Charging and Discharging Stages Power (kW)	Temperature (K)		Root Mean Square (K)	
	Maximum Charging	Minimum Discharging	Charging Stage	Discharging Stage
500	296.13	272.65	9.02	8.67
83	288.82	277.91	4.04	3.94

Plotting the four stages on a pressure against volume plot for the 500 kW and 83 kW (Figure 6.15it is evident that the area enclosed between the blue and black line is greater for the 500 kW power. The pressure drop during the first hold stage is the greatest for a charging power of 500 kW rather than of 83 kW, as could be observed from Figure 6.15a and b, respectively. Such behaviour is present since the final temperature during the charging stage is the greatest for 83 kW charging power. Moreover, the final volume after both charging and discharging stages is influenced since the desired pressure is reached at a greater volume during charging and at a smaller volume during discharging for greater power. Hence, the thermal behaviour of the system including the inner liner is greatly influenced by the charging and discharging power.

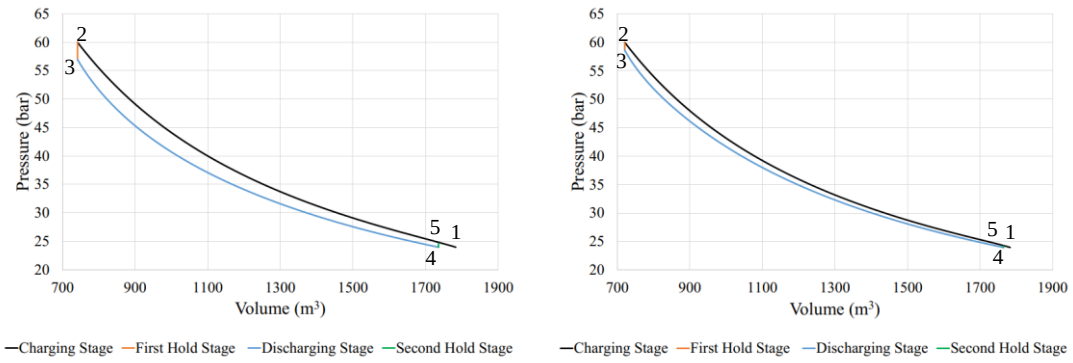

a) b)

Figure 6.15- Pressure (bar) against Volume (m^3) for a) 2 hours and b) 12 hours of charging and discharging stages (1-2 charging stage, 2-3 first hold stage, 3-4 discharging stage, 4-5 second hold stage)

6.5.3 Influence of the Pipeline Inspection Gauge

After independently studying the influence of the inner liner on the system, the next step was to study the influence of the pipeline inspection gauge (PIG) on the system. A fraction of the pump power is utilised to overcome the friction between the PIG and the outer pipeline, while the remaining power is utilised to pressurise the air. The effect of the PIG was studied by varying the charging and discharging stage power while also varying friction coefficient, stated in section 5.1, by $\pm$ 25% and $\pm$ 50%.

6.5.3.1 Variation of Charging and Discharging Power

The charging and discharging stage power was varied from 500 kW to 83 kW. Analysing the CEF of the system with and without the PIG from the results presented in Table 6.17, it is evident that the presence of the PIG effects the CEF of the system. Yet the change is only marginal. This is a result that comparatively large compressed air pressures are considered. Irrespective of the charging and discharging power, the presence of the PIG estimated to reduce the CEF by less than 1% in all cases. Hence, the PIG does not impact the system performance, as opposed to what has been observed for the inner liner.

Table 6.17- Charging and discharging power from 500 kW to 83 kW along with the cycle energy factor for the system with/without pipeline inspection gauge and the percentage change between the system with the pipeline inspection gauge to that without

Hydraulic Power (kW)	Cycle Energy Factor (%)		
	With Pipeline Inspection Gauge	Without Pipeline Inspection Gauge	Percentage Change
500	93.59	94.30	-0.75
250	94.35	95.07	-0.76
167	94.76	95.47	-0.74
125	95.03	95.75	-0.75
100	95.23	95.95	-0.75
83	95.39	96.10	-0.74

Irrespective of the charging and discharging stage duration stated by the user in equation 3.2, the code takes longer to reach the desired pressure. In the presence of the PIG, the duration of the charging stage results to be of 2.173 hours while without the PIG the code takes 2.165 hours, for a pump hydraulic power of 500 kW. Such an occurrence takes place since a fraction of the pump work is utilised to overcome the PIG friction. Moreover, since the remaining pump work is utilised to pressurise the gas, it causes the desired pressure of 60 bar to be reached at a slower rate than that without a PIG. Consequently, allowing time for the generated heat to be dissipated and achieving a final lower temperature. A similar behaviour was present during the discharging stage, as the system with the PIG required 2.052 hours to discharge while the system without the PIG required 2.048 hours for a recovery turbine power of 500 kW. The studied behaviour was present irrespective of the charging and discharging power.

6.5.3.2 Influence of the Pipeline Inspection Gauge Friction Coefficient

The value of the friction coefficient was studied by varying the values of the static and kinetic friction from literature by $\pm$50 % and $\pm$ 25 % (Table 6.18). The power of the charging/discharging stages was set at 250 kW. All the other parameters were also kept constant. This study was carried out to ensure whether the selected values of the static and kinetic friction have an impact on the system performance. It was found that a variation from -50% to +50% in the nominal static and kinetic friction coefficients only results in a CEF change of less than 1%. Thus, the coefficient of friction has a minimal influence over the system performance.

Table 6.18 – Friction coefficient percentage with the respective friction coefficient for both static and kinetic conditions along with the cycle energy factor

Sensitivity of the Friction Coefficient (%)	**Friction Coefficient**		**Cycle Energy Factor (%)**
	Static	**Kinetic**	
-50	0.300	0.250	94.72
-25	0.450	0.375	94.54
0	0.600	0.500	94.35
+25	0.750	0.625	94.16
+50	0.900	0.750	93.95

During the charging stage, the greater the value of the coefficient of friction, the greater the amount of pump energy utilised to move the PIG rather than to be stored. The same happens during discharging, that is the greater the value of the coefficient of friction the greater amount of stored energy is exhausted in moving the PIG rather than as useful energy (refer to Table 6.19). Moreover, greater values of the coefficient of friction prolong the charging stage duration, therefore allowing heat to escape at each

increment allowing for more energy to be stored as presented in Table 6.19. It could be concluded that the PIG friction coefficient value leads to minimal effect on the overall system performance but causes less energy to be recovered from that stored.

Table 6.19 – Friction coefficient percentage with the respective energy stored and recovered

Sensitivity of the Friction Coefficient (%)	Energy Stored (MWh)	Energy Recovered (MWh)
-50	0.9975	0.9448
-25	0.9984	0.9440
0	0.9994	0.9430
+25	1.0004	0.9420
+50	1.0015	0.9409

6.5.4 Combined Influence of the Inner Liner and the Pipeline Inspection Gauge

The final numerical study on air-based HPES system involved an investigation of the combined influence of the inner liner and the pipeline inspection gauge. Studying the combined effect of the inner liner along with the PIG provides a better understanding of the proposed system when utilising air as the compressible gas. Moreover, this study provides a baseline study to which the carbon dioxide-based system could be compared to.

6.5.4.1 Different Charging and Discharging Stage Power

In section 6.5.2 and 6.5.3 it was observed that the presence of the inner liner and the PIG independently effect the maximum achievable CEF of the accumulator, undoubtedly the inner liner showing the greatest impact. Observing the combined system CEF for the different power, it could be noted that the CEF is much less than when the inner liner and PIG are not present. For a power of 500 kW the system suffers from a 4 % decrease in the CEF while for a power of 83 kW the system suffers from a decrease of less than 1%, as presented in Table 6.20. Therefore, the influence of the inner liner and PIG becomes almost negligible for lower power.

Table 6.20 – Charging and discharging stages power from 500 kW to 83 kW and the respective cycle energy factor for the system with/without inner liner and pipeline inspection gauge

Hydraulic Power (kW)	Cycle Energy Factor (%)		
	With Inner Liner and PIG	Without Inner Liner and PIG	Percentage Difference
500	90.04	94.30	-4.52
250	92.94	95.07	-2.24
167	94.09	95.47	-1.45
125	94.74	95.75	-1.05
100	95.17	95.95	-0.81
83	95.47	96.11	-0.67

As already noted in section 6.5.2, the inner liner highly influences the heat transfer from the air to the surrounding sea water and vice versa due to the lower thermal conductivity. Such influence is also present when analysing the combined system, as presented in Table 6.20. Moreover, in the presence of the inner liner and the PIG, the maximum and minimum air temperatures are more towards the temperature of the surrounding sea water for lower charging and discharging powers.

The maximum temperature of the charging stage occurs at the final timestep of the stage, therefore resulting to be the initial temperature of the first hold stage. Observing the maximum temperature of the charging stage from Table 6.21 and the pressure drop experienced for the first hold stage, present in Figure 6.16, it is evident that lower charging powers result in lower pressure drops. This occurs as a result of the temperature of air being closer to that of the surrounding sea water.

Table 6.21- Maximum charging temperature and minimum discharging temperature during the different charging and discharging stage powers

Charging/Discharging Stage Power (kW)	Temperature (K)	
	Maximum Charging	Minimum Discharging
500	296.127	272.646
250	292.251	275.312
167	290.694	276.455
125	289.815	277.124
100	289.234	277.574
83	288.815	277.905

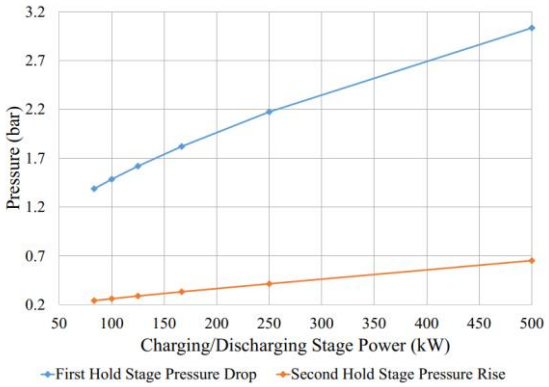

Figure 6.16 – Pressure (bar) against Charging/Discharging Stages Power (kW) for both first and second hold stages

During the discharging stage, the minimum temperature occurs towards the mid points of the stage duration while towards the end of the stage the temperature starts to increase towards the temperature of the surrounding sea water, as observed in section 6.3.3. Non the less the temperature of air would still be less than that of the surrounding sea water towards the end of the discharging stage but closer to the sea water

temperature at lower discharging power. Similarly, to the charging stage, the lower the discharging power the less the pressure increase during the second hold stage as exhibited in Figure 6.16.

6.5.4.2 Pipeline Inspection Gauge Friction Coefficient Influence

The value of static and kinetic coefficient of friction between the PIG disc and HDPE inner liner, stated in section 5.1, was varied from – 50 % to + 50 % in increments of 25 %, as presented in Table 6.22. This was carried out to study the influence of the coefficient of friction over the system performance. Observing the CEF for the different values of the coefficient of friction it is evident that between the CEF at -50% and +50% there is less than 0.3% difference. Hence, indicating that the value of the coefficient of friction has a minimal effect over the system performance.

Similar to what has been observed in section 0, the energy stored increases the greater the value of the coefficient of friction while the energy extracted decreases for greater coefficient of friction. Hence, the value of the coefficient of friction has minimal effect over the system performance, especially in the scenario of the inner liner being present since it mainly hinders the system thermal performance.

Table 6.22 – Friction coefficient percentage with the respective friction coefficient for both static and kinetic conditions along with the cycle nergy factor

Sensitivity of the Friction Coefficient (%)	Friction Coefficient		Cycle Energy Factor (%)
	Static	Kinetic	
-50	0.10	0.06	93.0606
-25	0.15	0.09	93.0014
0	0.20	0.12	92.9419
+25	0.25	0.15	92.8800
+50	0.30	0.18	92.8205

6.5.5 Conclusions from the Study for Air-based HPES Systems

From this study the following conclusions could be drawn;

1. Lower charging and discharging power lead to a greater CEF value while the system approaches more isothermal behaviour.
2. Keeping the accumulator volume constant, while increasing its diameter to results in a reduction on the CEF. This is due to the decrease in the effected contact area in direct contact with the surrounding sea water.
3. The presence of the PIG does not hinder the system heat transfer but still effects the system CEF. However, this effect is only marginal. The combination of the HDPE inner liner along with the PIG does not cause any significant changes apart from those already observed in the independent systems.

7 Carbon Dioxide-Based HPES System

This section verifies the CO_2-based HPES code C^2O_2 while studying the proposed accumulator system under different conditions. For the following studies, irrespective of the pipeline inspection gauge being present or not, the sea water is set to fill the accumulator horizontally as illustrated in Figure 6.1.

7.1 Verification

Initially the CO_2-based HPES code had to be verified similarly to what was carried out for the air-based HPES system in section 6.1. The verification process was carried out to ensure that the code yields realistic results. Since the code for the CO_2 system is different than that of air, the verification process is different. It was divided into three sections; 1) varying the incremental time step size (Δt), 2) the acceptable minimal value of the specific internal energy (u_{dif}) and 3) the incremental temperature size (T_{inc}). Due to the nature of the code, the Δt directly influences the numerical error of CO_2 in its gaseous state while the u_{dif} and the T_{inc} influences the numerical error of CO_2 as a mixture of liquid and vapour (gaseous). For the code verification, the system did not include the inner liner nor the PIG. Moreover, the system was subjected to a pump hydraulic and recovery turbine power of 250 kW while having a duration of 4 hours for both hold stages. The surrounding sea water temperature was set to 283 K.

7.1.1 Determination of the Optimal Time Step

The incremental time step size was varied from 5 seconds down to 0.2 seconds as presented in Table 7.1, while the code was set to run up to a charging pressure of 44.8 bar. This pressure is relatively close to the liquifying pressure at 283 K. The stated pressure ensures that the gas does not liquify as the temperature of the gas reverts back to that of the surrounding. When setting the incremental time step size to 5 seconds the code failed to yield results and an error was noted, while for the remaining time step sizes the code yielded a result.

Table 7.1- Simulation number with the incremental time step size, cycle energy factor and the simulation time

No.	Time step size (s)	Cycle Energy Factor (%)	Simulation time (s)
1	5	-	-
2	3	94.0600	14.1
3	1	94.0512	42.1
4	0.8	94.0493	53.4
5	0.4	94.0433	105.4
6	0.2	94.0432	206.4

Table 7.1 indicates that the finer the size of the incremental time step the greater is the simulation duration. Furthermore, it could be noted from Table 7.1 and Figure 7.1 that the gradual reduction in the time step leads to a convergence in the CEF estimate. The degree to which the thermodynamic process exhibits an isothermal behaviour was analysed for each stage and for each incremental time step size, as presented in Table 7.2. It is noted that the predicted RMS values are relatively low, even for a large time step of 3 seconds.

The pressure values for each time step obtained for the Δt between 0.4 and 3 seconds were compared to those of 0.2 seconds while utilising equation 6.2. The maximum, minimum and average values for the percentage difference in the pressure at a given time step with respect to a time step of 0.2 seconds were computed. The results are presented in Table 7.3.

From Table 7.3 it is evident that irrespective of the incremental time step size, the resulting difference with respect to 0.2 seconds is always less than $\pm$ 1% for both the charging and discharging stages. From the verification study of the incremental time step size during the gaseous state, it could therefore be concluded that the incremental time step size led to a minimal effect in the results. Since the time step size also does not greatly affect the simulation duration, an incremental time step size of 0.4 seconds was selected for subsequent simulations.

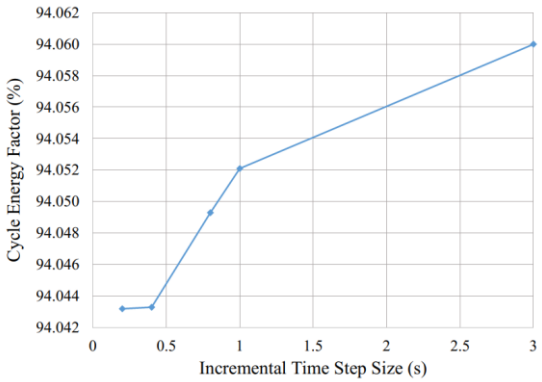

Figure 7.1- Cycle Energy Factor (%) against Incremental Time Step Size (s)

Table 7.2- Root mean square for the four stages of the whole cycle with respect to time step size (s)

Time step size (s)	Charging Stage	First Hold Stage	Discharging Stage	Second Hold Stage
3	2.3528	0.8403	2.8292	0.6051
1	2.3535	0.8402	2.8301	0.6050
0.8	2.3536	0.8402	2.8307	0.6050
0.4	2.3538	0.8402	2.8304	0.6049
0.2	2.3539	0.8402	2.8306	0.6049

Table 7.3- Pressure percentage difference of the remaining time step size with respect to 0.2 seconds results

Charging Stage			
	Maximum (%)	**Minimum (%)**	**Average (%)**
0.4-0.2	0.0002	0.0000	0.0002
0.8-0.2	0.0023	0.0000	0.0005
1-0.2	0.0010	0.0000	0.0006
3-0.2	0.0034	-0.0005	0.0021
Discharging Stage			
	Maximum (%)	**Minimum (%)**	**Average (%)**
0.4-0.2	0.0199	0.0001	0.0004
0.8-0.2	0.0035	-0.0023	0.0029
1-0.2	0.0023	-0.0035	0.0015
3-0.2	0.0035	-0.0023	0.0010

7.1.2 Acceptable Minimal Value for the Specific Internal Energy

This section presents the numerical analysis of the dependence of the prediction in the CEF and storage capacity to parameter u_{dif}, which is the acceptable minimal value between the specific internal energy calculated from equation 3.86 and 3.87, as presented by equation 3.89 (flow charts presented in Figure 4.30 and Figure 4.31). For all the values studied for the u_{dif} the incremental temperature size, T_{inc}, was set constant to 0.000001 K while u_{dif} was varied from 1% to 0.00001%, as exhibited by Table 7.4.

Setting the acceptable u_{dif} between 1 % to 0.01 % for the flow chart presented by Figure 4.30 and Figure 4.31, does not manage to capture any changes within the system hence yielding same results for the CEF, energy stored and energy recovered. Further refinement of u_{dif} to 0.001 % manage to capture a change in the CEF, energy stored and recovered. Moreover, decreasing the allowable u_{dif} value to 0.0001% and 0.00001% it is evident that the value of the CEF reduces further to a single value, similarly for the energy stored and recovered. Convergence to a single CEF value is also evident in Figure 7.2.

Table 7.4- The cycle energy factor, energy stored and recovered with the respective simulation time for the different difference of the specific internal energy

Difference of the Specific Internal Energy (%)	**Cycle Energy Factor (%)**	**Energy Stored (MWh)**	**Energy Recovered (MWh)**	**Simulation Time (s)**
1	96.3113	1.5023	1.4468	179.49
0.1	96.3113	1.5023	1.4468	178.32
0.01	96.3113	1.5023	1.4468	179.08
0.001	90.4656	1.5162	1.3717	15214.89
0.0001	86.6819	1.5454	1.3396	14498.63
0.00001	86.3990	1.5487	1.3381	24607.20

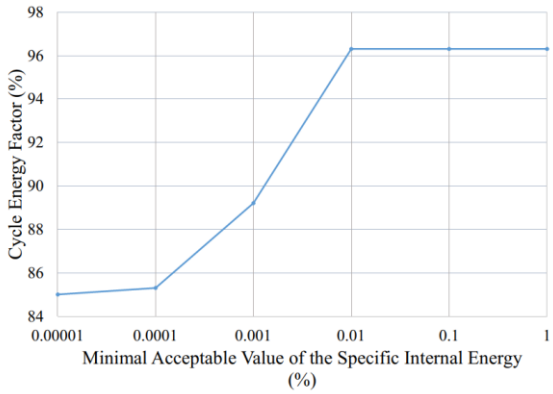

Figure 7.2- Cycle Energy Factor (%) against Minimal Acceptable Value of the Specific Internal Energy (u_{dif}, %)

The results for u_{dif} at 1 %, 0.001 %, 0.0001% and 0.00001 % were plotted on a pressure enthalpy chart as presented in Figure 7.3a, b, c and d respectively. The value of u_{dif} influences the CO_2 within the liquid-vapour dome, being presented by the black lines. According to the graph presented in Figure 7.3a, the fluid experiences no changes as it is being compressed and expanded within the liquid-vapour dome. Furthermore, the CO_2 should experience a temperature and pressure drop during the first hold stage since its temperature is greater than that of the surrounding sea water but such behaviour is not evident in Figure 7.3a. Therefore, this highlights that the value of 1% is not refined enough to capture the behaviour in the dome.

For u_{dif} of 0.001%, 0.0001% and 0.00001% the code manages to capture a change in pressure and temperature within the dome, as depicted by Figure 7.3b, c and d. In the case of u_{dif} equal to 0.0001% and 0.00001% the pressure change within the dome is greater than that of 0.001% due to the finer scales. Hence, from this study it could be concluded that the finer the value of u_{dif} to be satisfied, the greater the probability that the code captures the change between the two equations within the liquid-vapour dome.

The112ffectt of u_{dif} is further clarified by observing the temperature at a dryness fraction less than 1 during the charging stage as presented in Figure 7.4. Observing Figure 7.4 it could be noted that for u_{dif} limit of 0.001% and a dryness fraction greater than 0.6, no change in temperature is captured. Figure 7.3a indicates that for u_{dif} of 1%, the temperature remains constant within the dome while for a difference of 0.001% the CO_2 experiences a change in temperature within the dome. Since for a difference of 0.001% the scale is not well refined it does not capture the same changes as those captured by 0.0001% and 0.00001%. The results obtained for u_{dif} of 0.0001% and 0.00001% show minimal changes between one another, although the latter takes

longer to compute. Hence u_{dif} limit is set at 0.0001% to obtain results with a great accuracy and within a reasonable time frame.

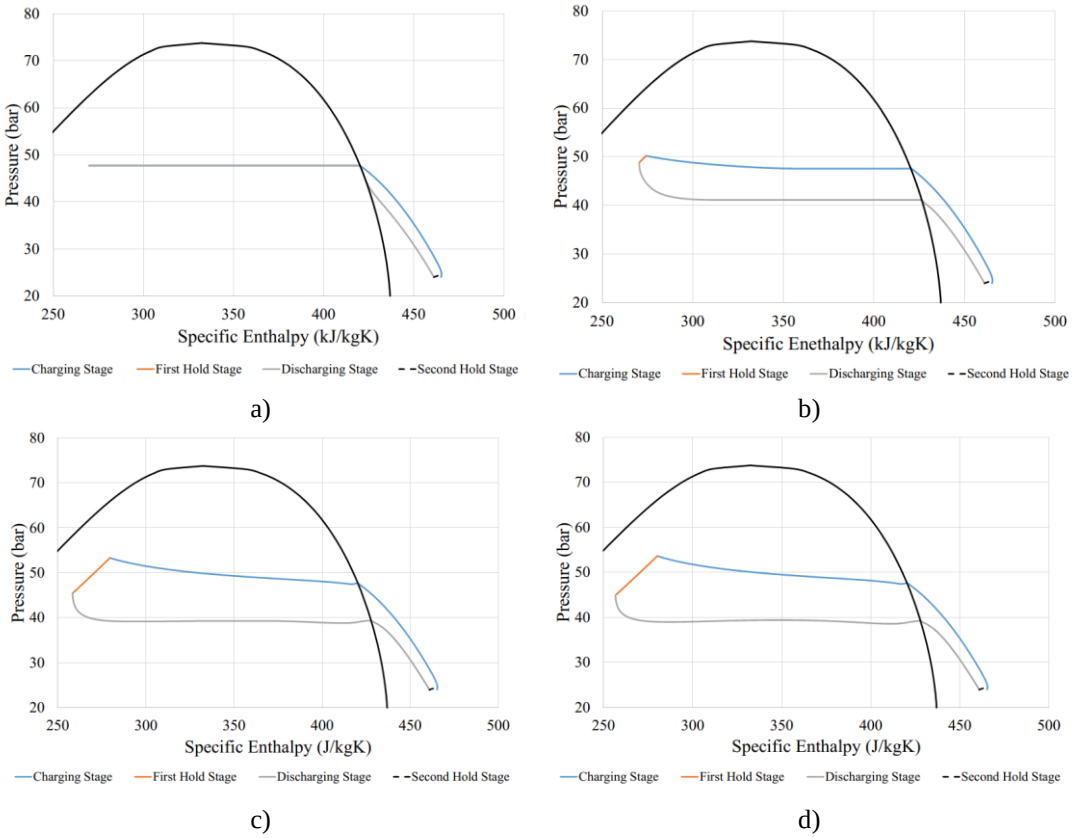

Figure 7.3- Pressure (bar) against Specific Enthalpy (J/kgK) for a) 1 %, b) 0.001%, c) 0.0001% and d) 0.00001% while the black solid lines indicate the liquid vapour dome of CO_2

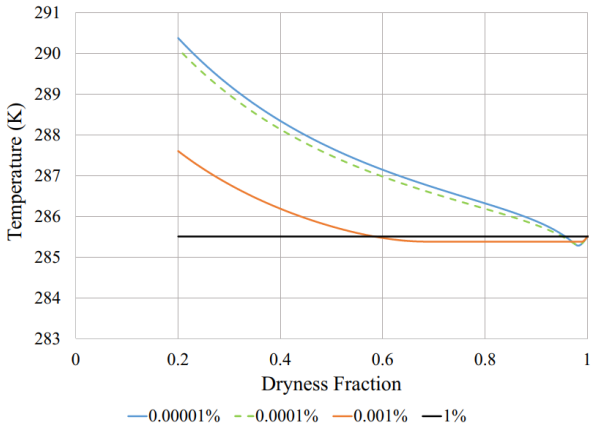

Figure 7.4- Temperature (K) against Dryness Fraction for $\boldsymbol{u_{\text{dif}}}$ of 1%, 0.001%, 0.0001% and 0.00001% during the charging stage

7.1.3 Incremental Temperature Size

If the result from equation 3.89 does not satisfy the statement derived from section 7.1.2 then the temperature is increased or decreased by the incremental temperature size, T_{inc}. To determine a reasonable value for the incremental temperature size its value was varied from 0.1 down to 0.000001 K, as presented in Table 7.5. For an incremental temperature size of 0.1, 0.01 and 0.001 K the code does not manage to

yield any results because the increment is large enough causing the condition of u_{dif} to not be satisfied. On the other hand, for an incremental temperature size of 0.0001 to 0.000001 K the code managed to yield results while converging to a single point for the CEF, energy stored and energy recovered as exhibited in Table 7.5. A finer incremental temperature size results in a simulation time to increase from 353.65 s up to 14498.63 s (equivalent of 4.03 hours).

Table 7.5- The cycle energy factor, energy stored and recovered with the respective simulation time for the different incremental temperature size

Incremental Temperature size (K)	Cycle Energy Factor (%)	Energy Stored (MWh)	Energy Recovered (MWh)	Simulation Time (s)
0.1	-	-	-	-
0.01	-	-	-	-
0.001	-	-	-	-
0.0001	86.5104	1.5481	1.3393	353.65
0.00001	86.6659	1.5457	1.3396	1692.63
0.000001	86.6819	1.5454	1.3396	14498.63

Assuming that a finer T_{inc} value for the temperature yields results with a greater accuracy, the results of greater incremental size could be compared to those of finer size. Since the T_{inc} is mainly applied during the charging stage, first hold stage and discharging stage it is best to analyse the results within these 3 stages. The finer the value of the T_{inc}, the less the difference with respect to the data of 0.000001 K. This is noted from Table 7.6 for the charging stage, where the difference is always less than 2.5% for the RMS. Moreover, the remaining results of Table 7.6 for a T_{inc} of 0.0001 and 0.000001 K deviate by less than 1 % from the values of T_{inc} of 0.000001 K.

Similar to the charging stage, during the discharging the finer the value of T_{inc}, the less the difference with respect to the results of 0.000001 K, as presented in Table 7.7. Therefore, provided these results it would be best to apply an incremental temperature size of 0.00001 K since results are obtained with great accuracy and within a reasonable timeframe.

Table 7.6- Comparing the difference of the results for the incremental temperature size at 0.0001 K and 0.00001 K to 0.000001 K for the final temperature, root mean square, final pressure and final volume during the charging stage

Incremental Temperature size (K)	Final Temperature (%)	RMS (%)	Final Pressure (%)	Final Volume
0.0001	0.072	2.192	0.501	-0.304
0.00001	0.006	0.147	0.039	-0.025

Table 7.7- Comparing the difference of the results for the incremental temperature size at 0.0001 K and 0.00001 K to 0.000001 K for the final temperature, degree of isothermal, final pressure and final volume during the discharging stage

Incremental Temperature size (K)	Final Temperature (%)	Minimum Temperature (%)	Degree of Isothermal (%)	Final Pressure (%)	Final Volume (%)
0.0001	-0.005	-0.045	0.750	-0.000	-0.009
0.00001	0.000	-0.006	0.088	0.000	-0.001

7.1.4 Conclusions from the Numerical Verification Study

From the verification process it could be concluded that a value for the incremental time step equal to 0.4 s would result in minimal numerical errors. The result of the equation 3.89 should be less than 0.0001% and the incremental temperature size should be of 0.00001 K. Simulating the system under the verified parameters led to the graph presented in Figure 7.5. Figure 7.5 also indicates the isotherm lines from 273 K to 293 K and it could be noted that the saturation pressure is sensitive to the temperature.

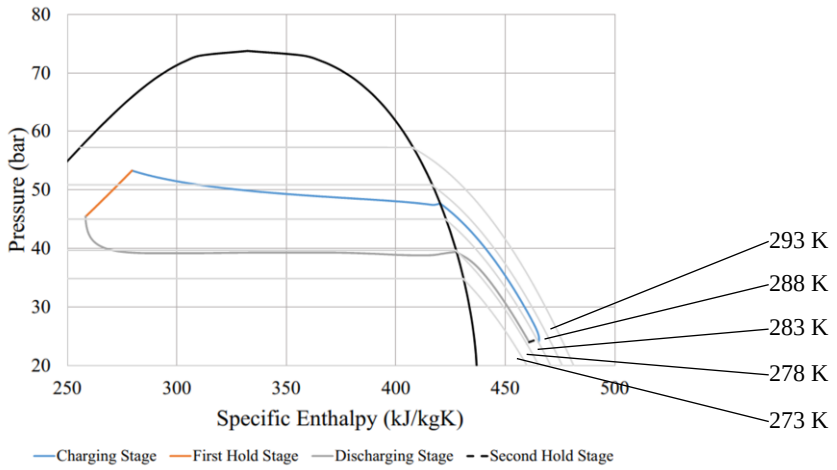

Figure 7.5- Pressure (bar) against Specific Enthalpy (kJ/kgK) for the system understudy while the black solid lines indicate the liquid vapour dome of CO_2

7.2 Initial System Observation of the Time Response Characteristics for Carbon Dioxide

Prior to studying the influence of different parameters on the system, a basic understanding of the baseline system for CO_2 is necessary. The baseline system utilises the same dimensions as those of the air based HPES system while the pump power and recovery turbine power were set to 250 kW. Moreover, the system was set to have 4 hours for both hold stages and having the surrounding sea water at 283 K. The system is charged up until the dryness fraction of 0.2 or the desired pressure of 60 bar is reached. On the other hand, during the discharging stage, the system is discharged to the initial system pressure of 24 bar. The system studied in this section will be referred to as the baseline study for CO_2 in the following sections.

7.2.1 Charging Stage

Compressing the CO_2 to a smaller volume during the charging stage causes the pressure of the gas to increase while also exhibiting two phases where initially it is in complete gaseous state and eventually co-exists with its liquid constituent. At the initial conditions of 24 bar and 283 K CO_2 exists in its gaseous state, as can be noted Figure 7.6a on the right-hand side while liquification of the gas during compression occurs at a pressure of 47.65 bar, temperature of 285.46 K and volume of 650.88 m^3. The desired dryness fraction of 0.2 is reached at a pressure of 53.34 bar, temperature of 290.13K and volume of 205.39 m^3. Moreover, plotting the pressure against volume for the charging stage, as carried out for air in section 6.3.1, the plot for air follows a smoother path than that of CO_2, comparing Figure 7.6b to Figure 6.3b. From Figure 7.6b between 600 m^3 and 800 m^3, it could be observed that when the gas starts to liquify it experiences a temperature and pressure drop due to a sudden increase in the convective heat transfer coefficient which is predicted by Thome et al. [90] (refer to section 3.2.2.2).

In accordance with fundamental theory of ideal thermodynamics cycle for refrigeration systems, the evaporator and condenser do not exhibit any change in the pressure and temperature within the liquid-vapour dome (refer to Figure 7.7, solid lines). [112] On the other hand, for a real scenario, the gas does experience a change in pressure and temperature within the dome. The real process is depicted by the dotted line in Figure 7.7. Hence, the mentioned argument provides a foundation that a change in pressure and temperature within the dome, as exhibited by the simulation in Figure 7.6a, likely to reflect a real scenario.

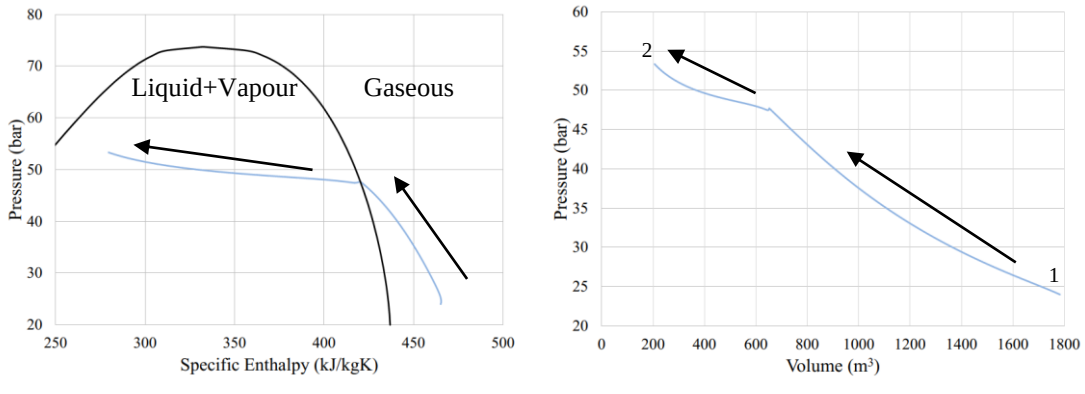

a) b)

Figure 7.6- a) Pressure (bar) against Specific Enthalpy (kJ/kgK) and b) Pressure (bar) against Volume (m^3) (process 1-2) for the charging stage along with arrows indicating direction while the black solid lines indicate the liquid vapour dome of CO_2

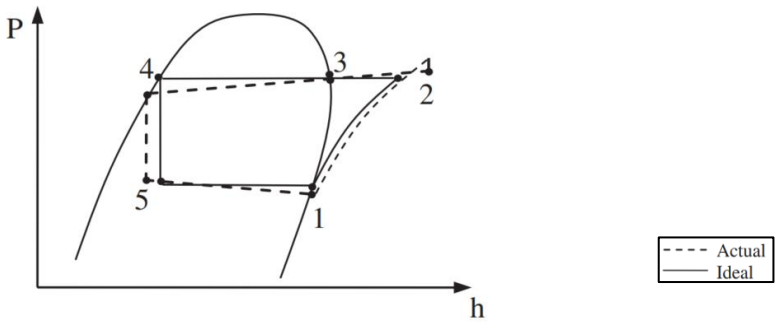

Figure 7.7- Actual and ideal refrigeration cycle on a pressure against enthalpy chart [112]

7.2.2 First Hold Stage

The heat gained from the gas compression is allowed to be dissipated to the surrounding sea water during the first hold stage. Figure 7.8a indicates that as heat energy is lost to the surrounding, the pressure of the CO_2 suffers from a drop due to both parameters being directly correlated within the liquid-vapour dome. Initially the temperature of the gas is much greater than that of the surrounding sea water, causing a steep temperature and pressure drop during the first hour of the hold stage as exhibited in Figure 7.8b and c, respectively.

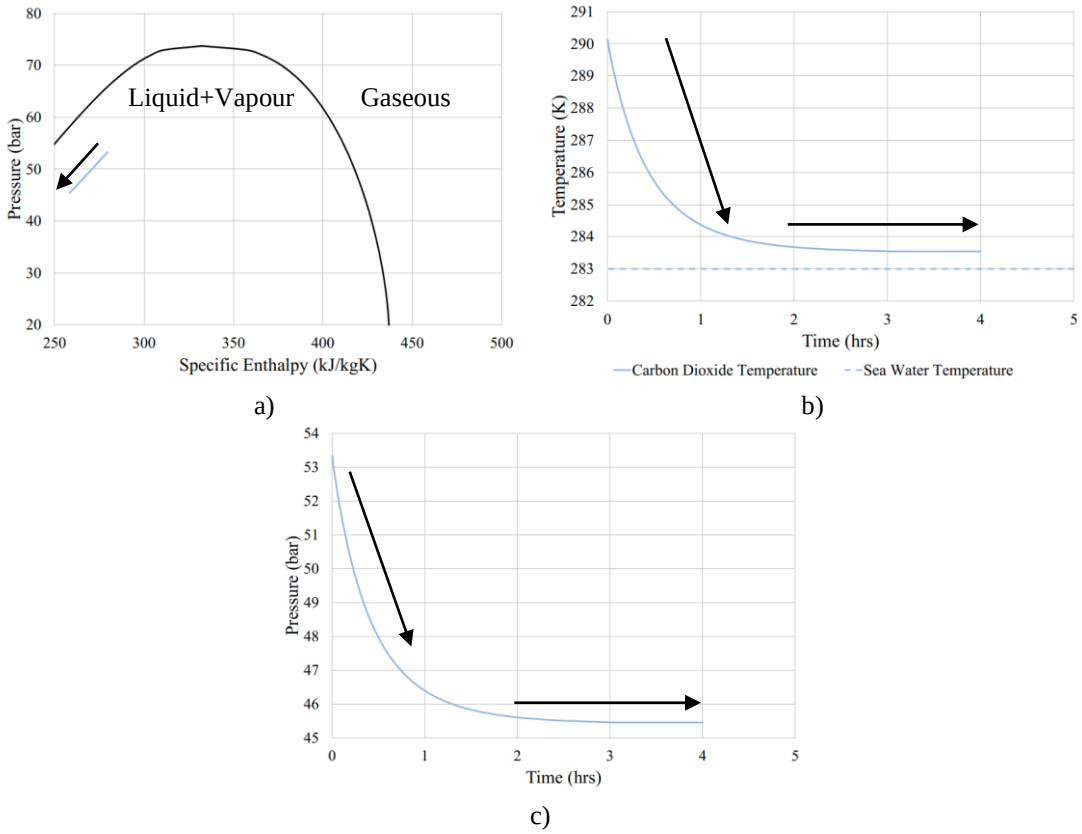

Figure 7.8- a) Pressure (bar) against Enthalpy (kJ/kgK), b) Temperature (K) and c) Pressure (bar) against Time (hrs) for the first hold stage with arrows indicating direction while the black solid lines indicate the liquid vapour dome of CO_2

After the first hour or so the temperature of the gas almost reaches the temperature of the surrounding sea water at 283 K while constantly getting closer for the remaining

of the 4 hour hold stage duration. From Figure 7.8b it is evident that the temperature of the gas is never equal to 283 K while the final temperature is of 283.54 K. During the hold stage the gas suffers from a temperature drop of 6.58 K which results in a pressure drop of 7.87 bar, more than 1 bar of pressure drop for each 1 K drop.

7.2.3 Discharging Stage

Observing Figure 7.9a it could be noted that during the discharging stage the system goes through 3 main parts; 1) an initial sudden temperature drop as the volume of the system starts to expand, due to the lack of heat transfer from the surrounding sea water to the CO_2, 2) for the second part, as the volume continuous to expand, the fluid suffers from a continuous fluctuation in temperature and pressure while the CO_2 experiences phase change to the gaseous state and 3) in the final part, the CO_2 returns back to a complete gaseous state while it experiences minimal temperature change. During expansion, the CO_2 exhibits almost a constant pressure as the dryness fraction increases, as presented in Figure 7.9a and b.

7.2.4 Second Hold Stage

After the discharging stage, the gas is allowed to settle for another hold stage. During the second hold stage the CO_2 is in its gaseous state and absorbs thermal energy from the surrounding sea water since the temperature of the gas is initially at 279.31 K, less than the surrounding. Due to the temperature being less than that of the surrounding, the gas experiences a temperature, pressure and a specific enthalpy rise, as exhibited in Figure 7.10a. The gas initially absorbs energy from the surrounding at a faster rate as presented in Figure 7.10b such that within the first hour the temperature of the gas is close to that of the surrounding. Due to the temperature increase at constant volume the pressure of the gas also increases, Figure 7.10c.

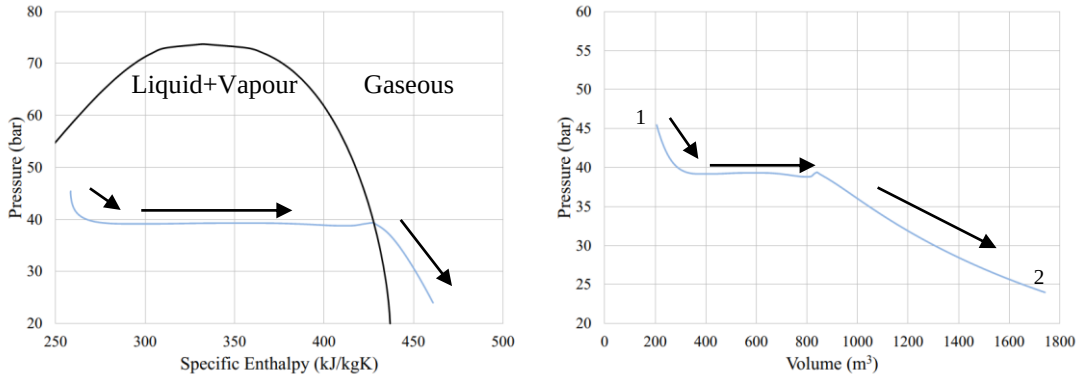

a) b)

Figure 7.9- a) Pressure (bar) against Specific Enthalpy (kJ/kgK) and b) Pressure (bar) against Volume (m^3) for the discharging stage with arrows indicating direction while the black solid lines indicate the liquid vapour dome of CO_2

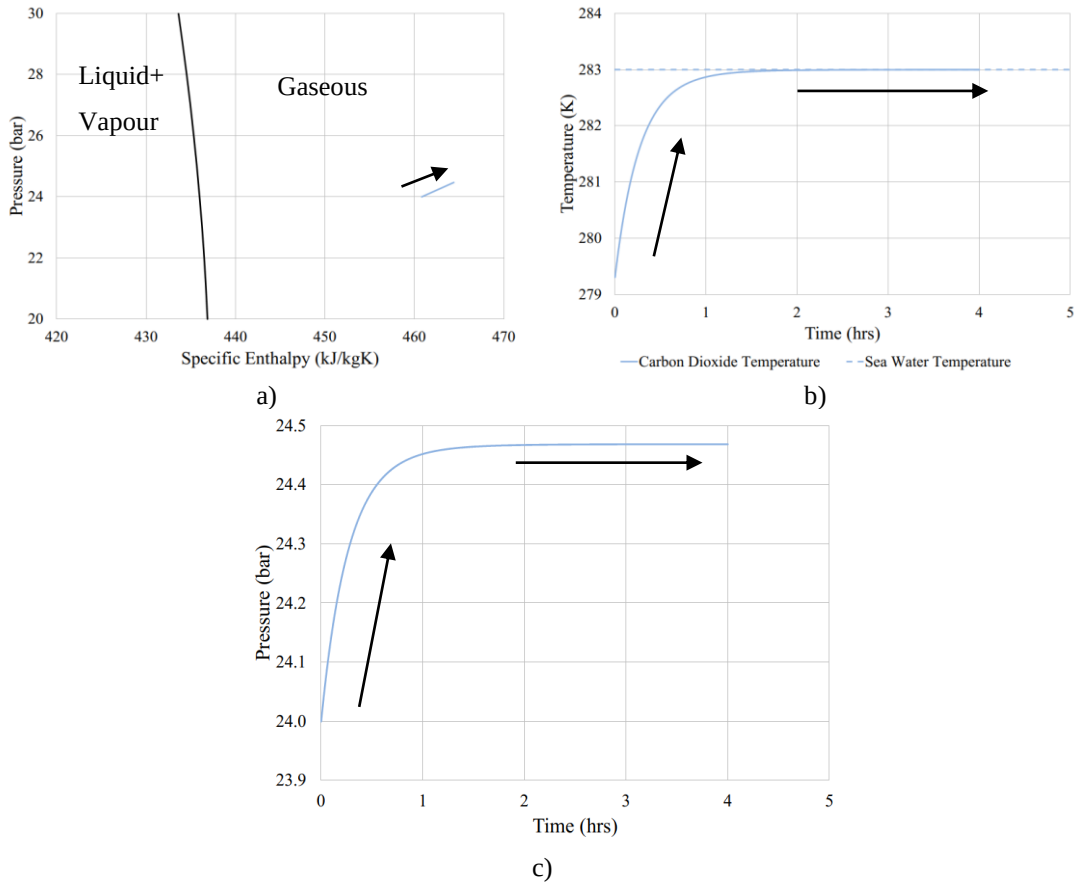

Figure 7.10- a) Pressure (bar) against Specific Enthalpy (kJ/kgK), b) Temperature (K) and c) Pressure (bar) against Time (hrs) for the second hold stage with arrows indicating direction while the black solid lines indicate the liquid vapour dome of CO_2

7.2.5 Remarks

Dedicated physical experiments on CO_2-charged accumulators in controlled subsea environments would be essential to confirm the validity of the predictions in sections 7.2.1 to 7.2.4. Such work was beyond the scope of the present study given time constraints.

7.3 Initial Parametric Code Analysis

Initially analysing the code, a series of parametric simulations were considered to analyse the code results under different conditions such as; 1) high convective heat transfer coefficient and no-heat transfer, 2) variation of the charging and discharging power, 3) liquid-vapour state internal convective heat transfer coefficient, 4) hold stages internal convective heat transfer coefficient and 5) hold stages duration.

7.3.1 High Convective Heat Transfer Coefficient and No-heat Transfer Study

An adiabatic CO_2-charged accumulator was simulated by switching off the heat transfer equations. An isothermal system was then modelled by prescribing an unrealistically high convective heat transfer coefficient (100,000 W/m^2K) for both

inside and outside. Similar to the air-based HPES system, the CO_2-based HPES system managed to obtain a CEF close 100% for both adiabatic and isothermal conditions (Table 7.8). A CEF close to 100% during the adiabatic process implies that no heat is lost or gained. On the other hand, for the isothermal system it indicates that the heat was completely lost to the surrounding sea water during charging while fully recovered from the sea water during the discharging. Table 7.8 indicates that the energy extracted is similar to that stored for both cases.

Table 7.8- Cycle energy factor, energy stored and recovered for the adiabatic and isothermal system

	Cycle Energy Factor (%)	**Energy Stored (MWhr)**	**Energy Recovered (MWhr)**
No Heat Transfer	100.00	0.96	0.96
High Convective Heat Transfer Coefficient	99.33	1.45	1.44

Analysing the process of the CO_2 system having no heat transfer on a pressure-enthalpy chart, presented by Figure 7.11a, the following observations could be noted;

1. The process deviates away from the liquid-vapour dome, that is, the CO_2 remains gaseous. Figure 7.11a also indicates that during compression and expansions the gas suffers from a pressure and temperature rise, similar to what is observed during the compression of a refrigerant.
2. CO_2 follows the same path for the charging and discharging stages, highlighting that no energy is lost or gained.

It is shown that when a high value for the convective heat transfer coefficient is prescribed, the code predicts a thermodynamic process that is very close to isothermal conditions. As shown in Figure 7.11b, it is evident that both the charging and discharging stages closely follow the isotherm line at 283 K.

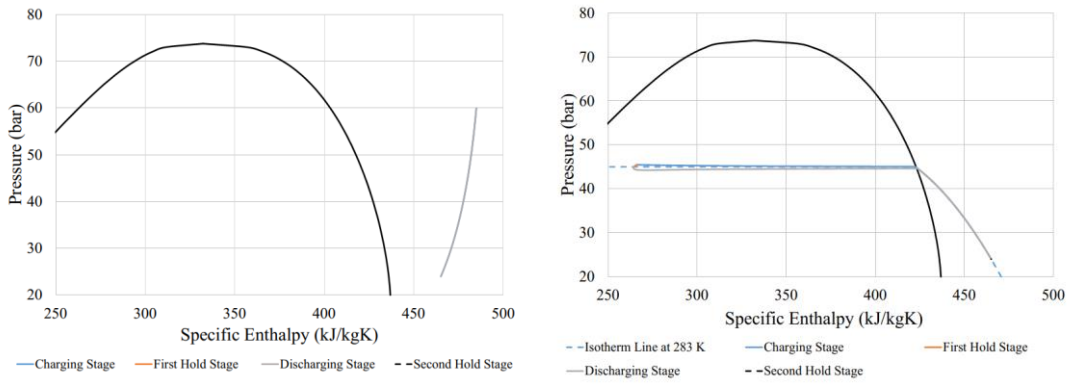

`a) b)

Figure 7.11- Pressure (bar) against Specific Enthalpy (kJ/kgK) for a) no heat transfer (adiabatic process) b) high convective heat transfer coefficient value (isothermal process)

The temperature for the adiabatic process increases significantly as initially the temperature is at 283 K and increases up to 334.19 K during charging. On the other hand, the temperature for the isothermal process is initially at 283 K and experience a slight increase during charging resulting in a final temperature of 283.64 K. Similar behaviour was noted during the discharging stage, where in the case of the adiabatic process the temperature of the gas returns back to 283 K while for the isothermal process only exhibits a minor deviation from 283 K. Such results provide confidence that the code is providing credible results.

7.3.2 Variation of the Charging and Discharging Power

The system hydraulic power was varied to the powers stated within Table 7.9. Lower power resulted in greater CEF, presented in Table 7.9, while resulting in lower final charging temperature and higher final discharging temperature. This indicates that greater power results in less thermal energy dissipation and absorption during charging and discharging, respectively. This is similar to what is presented in 6.4.1.

Plotting the results of the different powers on a pressure against enthalpy graphs it provides insights on the carbon dioxide behaviour throughout the whole cycle, presented in Figure 7.12. From Figure 7.12a it is evident that initially all the three cycles start off from the same point but as different levels of power are applied through the pump, the cycles start to deviate away from one another. The system becomes less isothermal for higher power, where for the power of 250 kW the temperature of the CO_2 deviates further away from the isotherm of the surrounding sea water during the charging stage, Figure 7.12a.

Due to the final temperature being greater for a hydraulic power of 250 kW, the CO_2 experiences a greater temperature and pressure drop during the first hold stage as exhibited in Figure 7.12b. Irrespective of the pump power and the final temperature of the gas after the charging stage, the final temperature after the 4 hour hold stage duration returns relatively close to 283 K, as presented in Figure 7.12b.

Table 7.9- Cycle energy factor and final temperature during charging and discharging stages for the different power

Hydraulic Power (kW)	Cycle Energy Factor (%)	Final Temperature (K)	
		Charging	Discharging
250	86.67	290.13	279.31
125	91.36	286.88	279.99
83	93.12	285.69	280.30

The system is allowed to expand and a result of the expansion the gas experience a temperature and pressure drop, which are directly correlated within the liquid-vapour dome. From Figure 7.12c, it is evident that the greater the power of the recovery turbine, the greater the temperature drop. Moreover, Figure 7.12c indicates that the final points of the three test cases are close to one another. Finally, during the second hold stage the CO_2 is allowed to absorb thermal energy from the surrounding sea water due to the lower temperature, causing for the pressure to increase as presented by Figure 7.12d.

The power of the pump greatly influences its flow rate, as presented by Figure 7.13, which is directly correlated to the rate at which heat is dissipated or absorbed from the surrounding sea water. Hence, the previous observations are reasonable since high power results in a larger sea water flow rate which consequently lead to greater temperature during charging and lower temperatures during discharging, as observed from Figure 7.12.

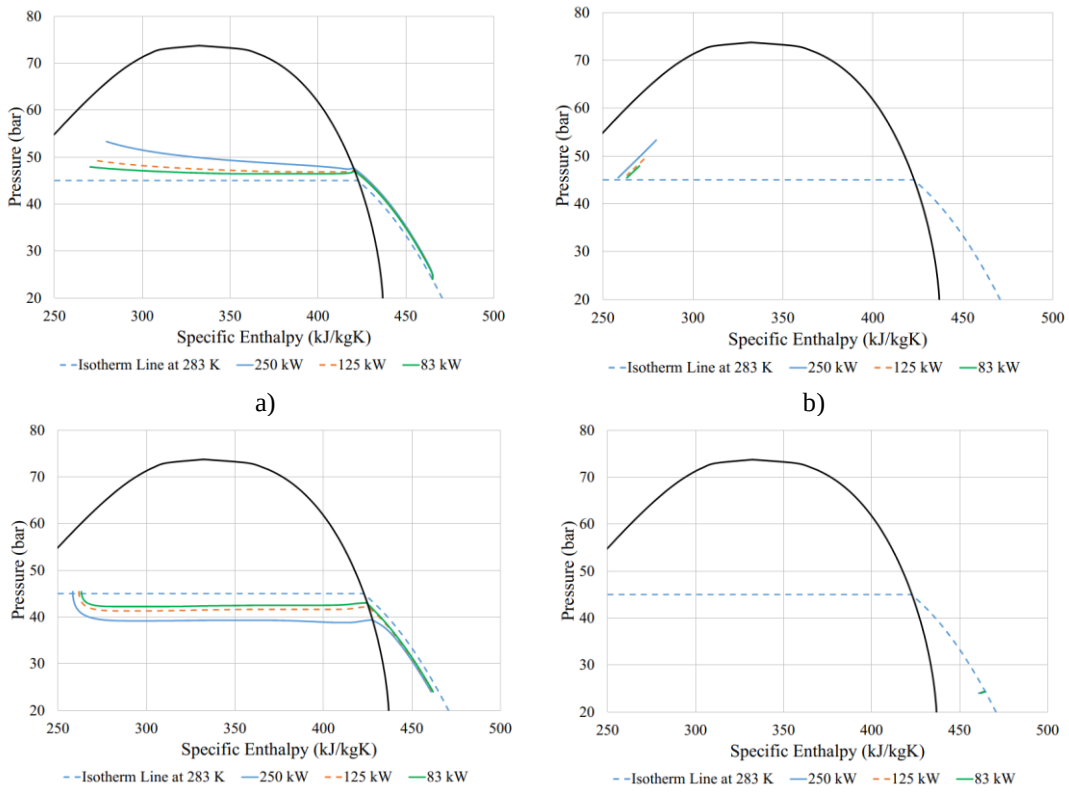

Figure 7.12- Pressure (bar) against Specific Enthalpy (kJ/kgK) a) charging stage, b) first hold stage, c) discharging stage and d) second hold stage for the different hydraulic power

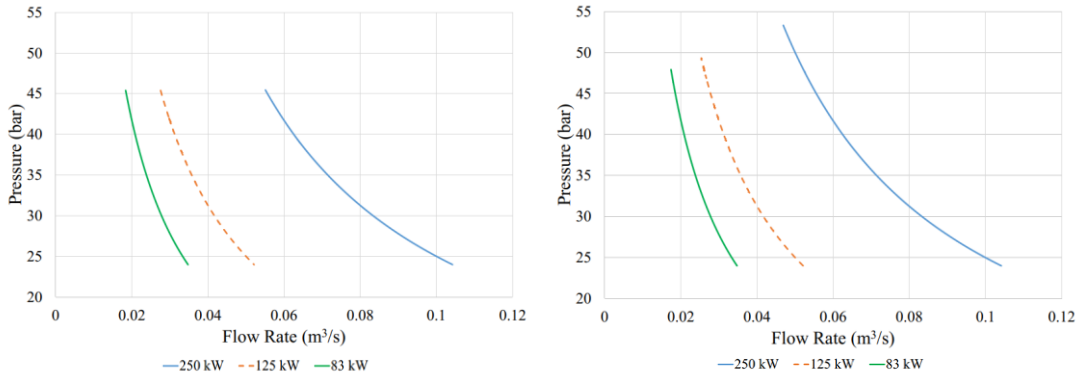

Figure 7.13- Pressure (bar) against Flow Rate (m^3/s) for a) charging stage and b) discharging stage

7.3.3 Liquid-Vapour State Influence of Convective Heat Transfer Coefficient

Section 3.2.2.2 states that the models applied to calculate the internal convective heat transfer coefficient (h_{in}) during the two-phase flow were intentionally developed for a continuous flow system. Since the system under study is non-flow, then to study the influence of the uncertainty in the h_{in}, the calculated values from the Thome et al. [90] and Fang [89] model were varied at $\pm$ 25 %, $\pm$ 50 % and 100 %, as indicated in Table 7.10.

Initially observing the cycle energy factor for the different percentage uncertainty, it could be noted that the CEF is the least for a variation of -50% while the greatest for a variation of +100%. Moreover, observing the RMS of the system, it could be noted that an uncertainty of -50% results in the system being less isothermal than in the case of greater positive uncertainty. The mentioned system behaviour is present irrespective of the charging or discharging stage. Due to the system being less isothermal at the negative percentage uncertainty, the heat transfer is limited, hence the final temperature at -50 % is the greatest for the charging and least for the discharging stage.

Table 7.10- Cycle energy factor, root mean square and final temperature for the different percentage sensitivity of the calculated internal convective heat transfer coefficient

Sensitivity in the Internal Convective Heat Transfer Coefficient (%)	Cycle Energy Factor (%)	Root Mean Square (K)		Final Temperature (K)	
		Charging	Discharging	Charging	Discharging
- 50	78.44	3.65	9.35	291.70	279.19
- 25	84.83	3.39	5.38	290.67	279.27
0	86.67	3.26	4.39	290.13	279.31
+ 25	87.48	3.18	4.01	289.80	279.33
+ 50	87.90	3.13	3.83	289.57	279.34
+ 100	88.35	3.06	3.66	289.29	279.36

The pressure results for the different h_{in} values were plotted against the specific enthalpy for the charging and discharging stages, presented by Figure 7.14a and b,

respectively. Figure 7.14 only considers the liquid-vapour dome since the uncertainty is only applicable within the two-phase regime. A variation of -50 % causes the system to experience greater temperature change from that of the surrounding sea water for both charging and discharging stages (Figure 7.14). Hence, this study concludes that the value of the convective heat transfer coefficient during the liquid-vapour phase change greatly influence the system efficiency, temperature and pressure. Therefore, further studies and experimentation regarding the convective heat transfer coefficient is a must.

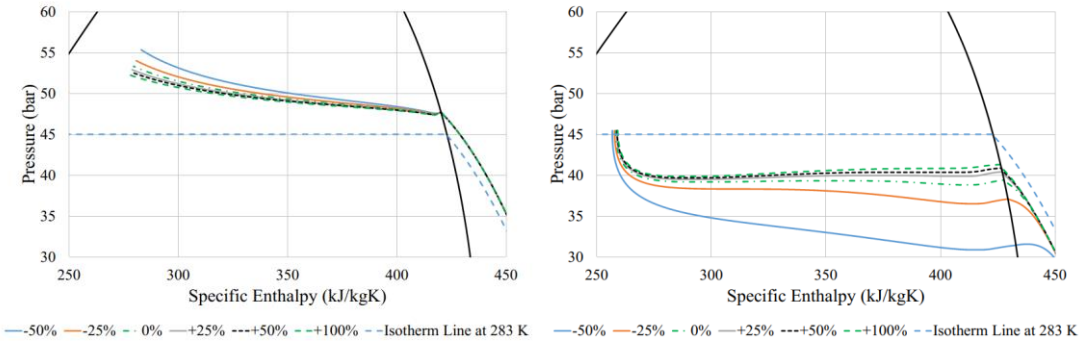

a) b)

Figure 7.14- Pressure (bar) against Specific Enthalpy (kJ/kgK) for a) charging stage and b) discharging stage for the different uncertainty

7.3.4 Influence of the Heat Transfer Coefficient During the Hold Stages

The internal convective heat transfer coefficient during the first and second hold stages were set constant to 10 $W.m^{-2}K^{-1}$ for the gaseous state and 1000 $W.m^{-2}K^{-}1$ for the liquid-vapour state. To evaluate the effect of these constants, the values were varied to the uncertainties of $\pm$ 50 % and $\pm$ 25 % of the initially stated values, as presented in Table 7.11, while the remaining properties were maintained constant. Analysing and comparing the CEF for the uncertainties of the two extremes, at -50 % and +50 % from Table 7.11, the CEF varies by less than 0.01 %. The final temperature for the first and second hold stages experiences minor variation for the different h_{in} values under study, as could be observed from Table 7.11.

Table 7.11- Cycle energy factor and the final temperature for the first and second hold stages as a result of the sensitivity in the internal convective heat transfer coefficient for both hold stages (gaseous or liquid phase)

Sensitivity in the Internal Convective Heat Transfer Coefficient (%)	Convective Heat Transfer Coefficient ($W.m^{-2}K^{-1}$)	Cycle Energy Factor (%)	Final Temperature (K)	
			First Hold Stage	Second Hold Stage
- 50	5/500	86.6749	283.6085	282.9953
-25	7.5/750	86.6679	283.5658	282.9988
0	10/1000	86.6659	283.5444	282.9993
+25	12.5/1250	86.6641	283.5316	282.9995
+50	15/1500	86.6624	283.5230	282.9995

Irrespective of the convective heat transfer coefficient value, after the 4 hour hold duration, the temperature of the CO_2 returns close to 283 K, while observing the rate at which this occurs from Figure 7.15. For both the hold stages, the temperature of the gas after 2 hours for a percentage variation of -25% to +50% remains relatively unchanged to one another. To conclude, the convective heat transfer coefficient for the hold stages has minimal effect on the final temperature for a hold stage duration equal to 4 hours or greater. In the case of the hold stage being less than 4 hours, than the final temperature is affected by the coefficient, as demonstrated by Figure 7.15 and noted in section 6.4.3 for air.

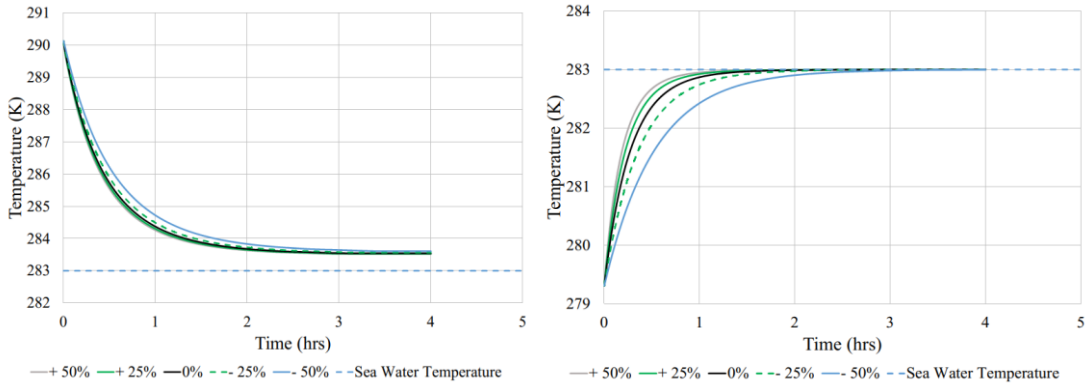

Figure 7.15- Temperature (K) against Time (hrs) a) charging stage and b) discharging stage

7.3.5 Influence of the Hold Stages Duration

The system hold stage duration was varied by - 50% to + 50% in increments of 25 % from the 4-hour duration, as presented by Table 7.12, while maintaining the remaining system parameters constant. Observing the system CEF, it is evident that for shorter durations the system CEF is greater than for longer ones. The CEF is greater in such instance since for shorter hold durations the system does not completely dissipate the thermal energy during the first hold stage, as could be observed from Table 7.12 and the final temperature after the first hold stage. Therefore, higher thermal energy after the first hold stage yields more energy to be extracted during discharging stage.

Table 7.12- Cycle energy factor and the final temperature (K) for the first and second hold stage for the different durations

Sensitivity of the Hold Stage Duration (%)	Charging/ Discharging Duration (hrs)	Cycle Energy Factor (%)	Final Temperature (K)	
			First Hold Stage	Second Hold Stage
- 50	2	86.6874	283.6803	282.9889
- 25	3	86.6660	283.5497	282.9978
0	4	86.6659	283.5444	282.9993
+25	5	86.6659	283.5444	282.9997
+50	6	86.6659	283.5444	282.9998

Similarly, observing the final temperature after the second hold stage, it is evident that for shorter hold durations, the temperature of the gas does not return back to that of the surrounding sea water. It could be concluded that the duration of the hold stages minimally influences the final temperature within the stated ranges.

7.3.6 Remarks

The following observations were noted from the analysis of sections 7.3.1 to 7.3.5; 1) high heat transfer coefficient for the charging and discharging stages lead the system to exhibit isothermal behaviour as the cycle approached very closely the isotherm of the surrounding sea water temperature; 2) no heat transfer between the gas and the surrounding leads the code to predict adiabatic behaviour, similar to what is observed in the compressor of a refrigeration cycle; 3) lower charging and discharging power lead to higher CEF as more time is allowed for the CO_2 to exchange heat with the surrounding sea water; 4) when studying the different uncertainty of the convective heat transfer coefficient for the two-phase region, it resulted that smaller uncertainties lead to greater RMS values; 5) lower hold stage convective heat transfer coefficients cause the system to dissipate heat at a slower rate, and 6) Shorter hold stage durations influence the dissipation of thermal energy as shorter durations do not dissipate the same amount of thermal energy to the surrounding sea water as much as longer durations.

7.4 Influence of Mechanical Design of System Performance

Further numerical investigation were conducted to understand the influence of the following mechanical design parameter in the performance of the CO_2-based HPES systems; 1) influence of the sea water temperature, 2) influence of the initial pre-charge pressure, 3) influence of the final dryness fraction, 4) influence of the accumulator pipeline length-to-diameter ratio, 5) inner liner effect, 6) pipeline inspection gauge influence and 7) combined influence of the inner liner and pipeline inspection gauge

7.4.1 Influence of the Sea Water Temperature

The surrounding sea water and the initial system temperature was varied from 273 K to 293 K, presented in Table 7.13,while maintaining the system parameters constant. Evaluating the obtained results for the different temperatures in Table 7.13, it is evident that higher temperatures caused greater CEF values.

At an initial temperature of 273 K the system manages to store less energy than at 288 K but more than at 293 K, for the same constant pump power of 250 kW. For all the

temperatures, the systems start off at the same initial pressure of 24 bar, but the pressure of liquification for the CO_2 is temperature dependent. Therefore, the liquification of CO_2 at lower temperatures occurs at a lower pressure which reduces the area under the graph and consequently the energy stored. The effect of the charging and discharging temperature over the area under the graph of a pressure against volume plot could be observed through Figure 7.16. On the other hand, for an initial temperature of 293 K the gas does not manage to liquify.

Table 7.13- Sea water temperature with the respective system cycle energy factor, energy stored, energy recovered and pressure drop during first hold stage

Sea Water Temperature (K)	Cycle Energy Factor (%)	Energy Stored (MWhr)	Energy Recovered (MWhr)	Pressure Drop for First Hold Stage (bar)
273	82.88	1.31	1.09	6.84
278	85.40	1.43	1.22	7.12
283	86.67	1.55	1.34	7.88
288	87.33	1.64	1.43	8.62
293	93.11	1.31	1.22	2.45

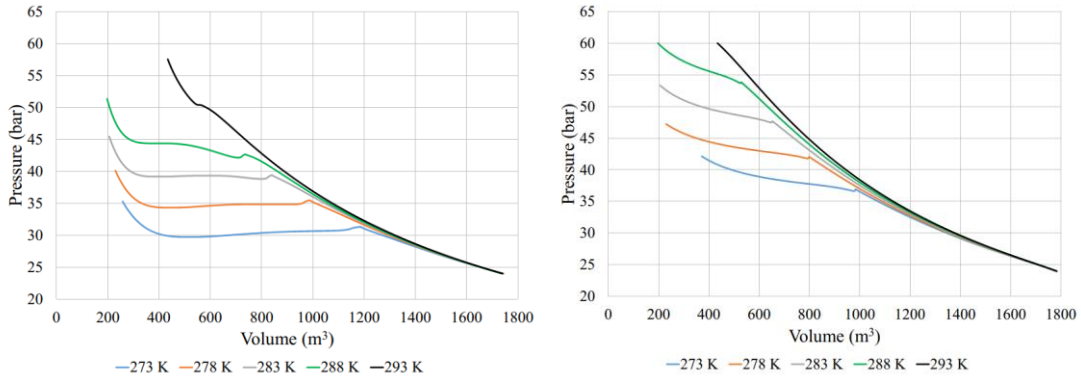

Figure 7.16- Pressure (bar) against Volume (m^3) a) charging stage and b) discharging stage for the different temperatures

Observing Figure 7.17a it is evident that for a temperature of 293 K the gas does not manage to liquify since the liquification of CO_2 at 293 K occurs at a greater pressure than 60 bar, which is the peak working pressure of the HPES accumulator under study. Since the gas at 293 K does not liquify, the energy stored is less than for the remaining temperatures of this study. However, the CEF of the system operating in a sea water temperature of 293 K is higher. Consequently, as the final temperature of the gas returns back to that of the surrounding sea water, the temperature drop is partially experienced in the gaseous state and within the liquid-vapour state. This result in a smaller pressure drop during the first hold stage whilst compared to those experienced at lower temperatures, as exhibited in Table 7.13. Although the CEF is the greatest for

a temperature of 293 K, more energy is extracted during the discharging stage at a temperature of 278 K to 288 K. Figure 7.17b indicates that all of the discharging stages are initiated in the liquid-vapour state.

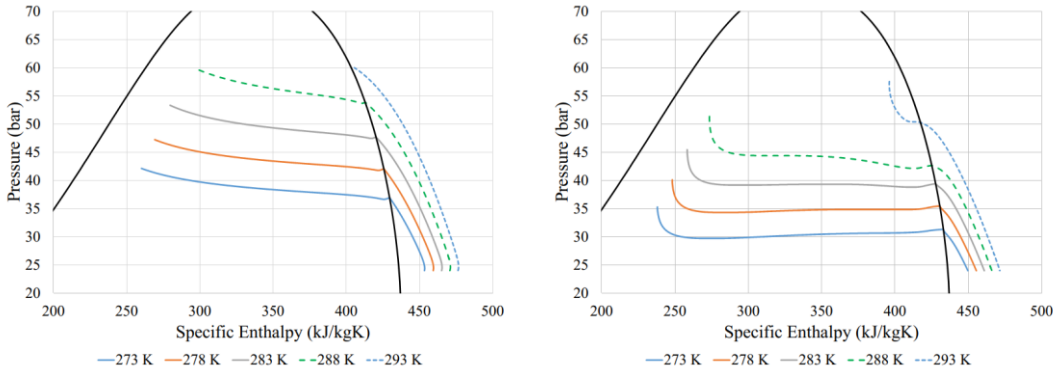

Figure 7.17- Pressure (bar) against Specific Enthalpy (kJ/kgK) a) charging stage and b) discharging stage for the different sea water temperatures

7.4.2 Influence of the Initial Pre-Charge Pressure

Simulations were conducted for the CO_2-based HPES operating at three different initial (pre-charge) pressures; 1) 24 bar, 2) 28 bar and c) 32 bar. For this study, the temperature of the surrounding sea water was maintained at 283 K, the pump and recovery turbine power were set to 250 kW and the dimensions of the system were constant throughout for each simulation. It is predicted that for an initial pressure of 32 bar the system stores more energy than for an initial pressure of 24 bar, as presented in Table 7.14. Moreover, for an initial pressure of 32 bar the CEF of the system is around 1.1 % greater than that of an initial pressure of 24 bar. It is important to mention that the final discharge pressure is equal to the pre-charge pressure, thus this was also varied during this study.

Table 7.14- Cycle energy factor, energy stored and energy recovered for the different initial pre-charge pressures

Pre-Charge Pressure (bar)	Cycle Energy Factor (%)	Energy Stored (MWhr)	Energy Recovered (MWhr)
24	86.67	1.5457	1.3396
28	87.34	1.5509	1.3337
32	87.68	1.6446	1.4419

The equation to calculate the pump flow rate is dependent on two factors; a) the pump power, which is set to constant at 250 kW and b) the pressure to overcome, as presented by equation 3.2. It is evident that, for a given power, greater pump pressure results in lower flow rate as exhibited by Figure 7.18a, thus for an initial pressure of 32 bar, the charging stage exhibits lower pressures than for 24 and 28 bar. A lower pump flow rate allows more time for heat generated during compression to be dissipated to the

surrounding sea water, hence a greater initial chamber pressure results in the final temperature to be less than for smaller initial pressure, as shown in Figure 7.18b. Moreover, the final pressure is also influenced due to lower flow rate for greater pre-charge pressures. From this study it could be concluded that operating the system at a greater pressure than 24 bar yields to higher energy storage capacity. However, the CO_2 takes longer to reach the desired dryness fraction of 0.2 due to lower flow rates.

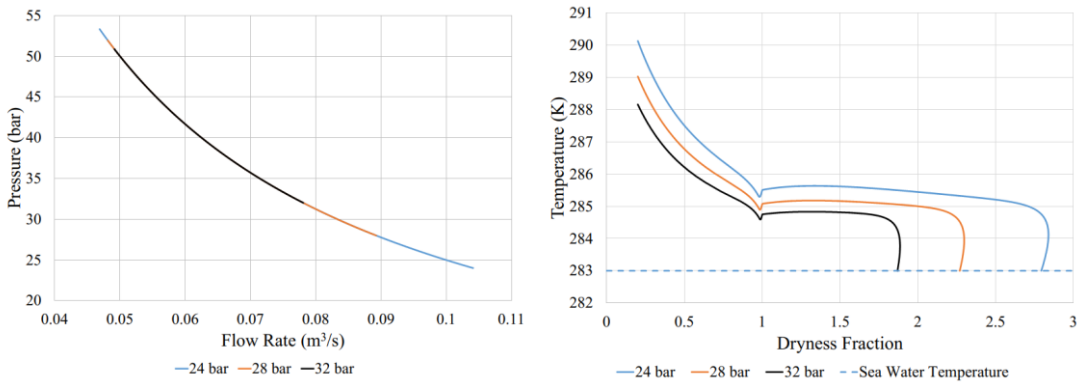

a) b)

Figure 7.18- a) Pressure (bar) against Flow Rate (m^3/s) and b) Temperature (K) against Dryness Fraction for the different initial pressures during the charging stage

7.4.3 Influence of the Final Dryness Fraction at the Full Charged State

To study the effect of the dryness fraction over the system performance, the dryness fraction, x, was varied from 0.2 to 1 as indicated in Table 7.15. For this study, the remaining system parameters were retained fixed, equal to those of the CO_2 baseline study (section 7.2). It is important to mention that the pump power during the charging stage was assumed to be constant at 250 kW.

Table 7.15- Cycle Energy Factor, energy stored, energy recovered and charging duration for the different dryness fraction limit

Dryness Fraction	Cycle Energy Factor (%)	Energy Stored (MWhr)	Energy Recovered (MWhr)	Charging Duration (hrs)
0.2	86.67	1.55	1.34	6.71
0.4	88.43	1.41	1.24	6.13
0.8	91.56	1.12	1.02	4.89
1	93.50	0.97	0.90	4.25

It is evident that the dryness fraction greatly influences the system CEF, as well as the energy stored and recovered. For a dryness fraction of 0.2, the system manages to store 1.55 MWhr whilst for a dryness fraction of 1 the system only manages to store 0.97 MWhr. Although for a dryness fraction of 0.2 the system stores more energy than at a dryness fraction of 1 for the same mass of steel and initial volume, the system obviously takes longer to charge up to a dryness fraction of 0.2. The system having the limit of x equal to 0.2 manages to recover more energy than is stored for the limit of

x equal to 1, irrespective of the latter having a greater CEF. From the predicted pressure enthalpy plots for the different values of x (Figure 7.19), it is evident that the final pressure of the charging stage is dependent on the dryness fraction limit. Consequently, the final temperature of the charging stage is also affected, resulting in greater temperature drop during the first hold stage for smaller dryness fraction values.

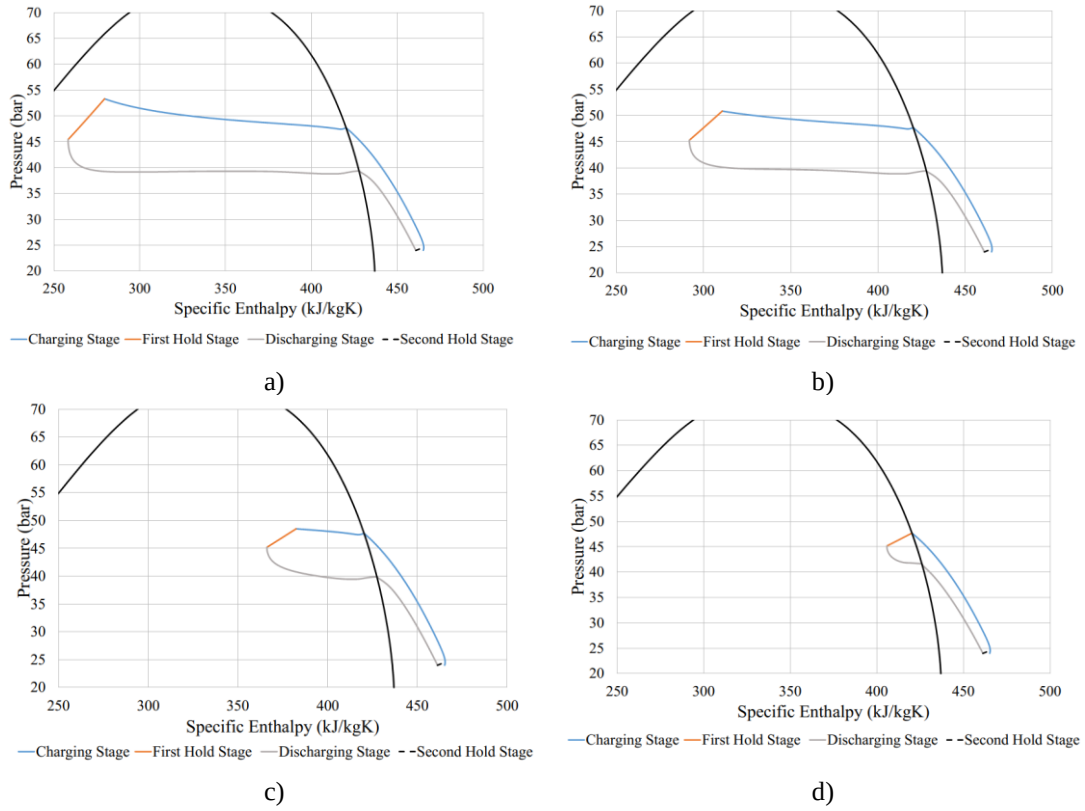

Figure 7.19- Pressure (bar) against Specific Enthalpy (kJ/kgK) at dryness fraction of a) 0.2, b) 0.4, c) 0.8 and d) 1

7.4.4 Influence of the Accumulator Pipeline Length-to-Diameter Ratio

To study the influence of the system dimensions over the energy stored and recovered, the pipeline diameter was varied from 36-inch to 84-inch while maintaining a constant internal volume and system parameters, similar to what was performed in section 6.5.1. Analysing the CEF from Table 7.16, it is evident that the CEF is greatly influenced by the system diameter. The decay in the CEF at greater diameters could be observed by comparing the area under the graph of Figure 7.20a and b. Energy stored increased from the 36-inch system to the 60-inch while decreases drastically at 84-inch.

Table 7.16-Cycle energy factor, energy stored and energy recovered for the different diameters under study

System Diameter (inch)	Internal Length-to-Diameter Ratio	Cycle Energy Factor (%)	Energy Stored (MWhr)	Energy Recovered (MWhr)
36	3286	86.7	1.55	1.34
48	1347	79.1	1.60	1.26
60	700	70.0	1.68	1.18
84	252	68.3	1.13	0.77

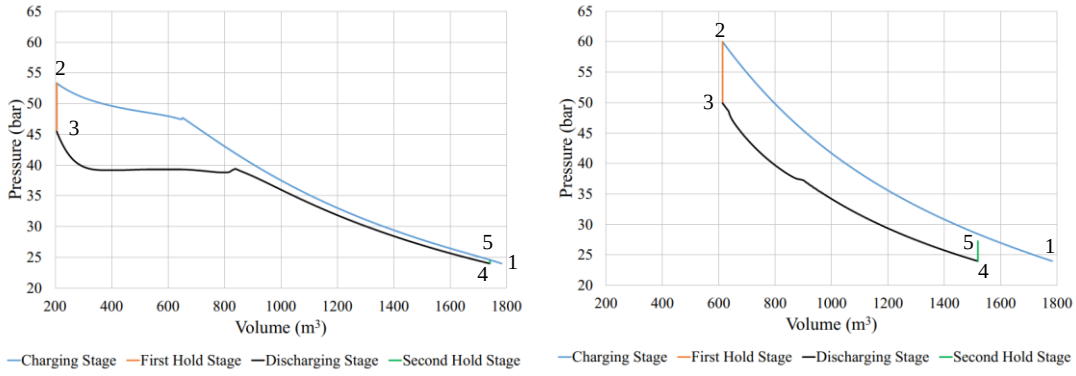

Figure 7.20- Pressure (bar) against Volume (m^3) a) 36-inch and b) 84-inch pipeline for the whole cycle (1-2 charging stage, 2-3 first hold stage, 3-4 discharging stage, 4-5 second hold stage)

The system at 60-inch manages to store more energy than at 36-inch since the final temperature and pressure is much greater than the latter, as presented in Table 7.17, while in both cases the gas liquifies up to a dryness fraction of 0.2. The 84-inch system does not manage to liquify before the charging stage is terminated as it stops at the 60 bar limit. Moreover, for the 84-inch diameter pipeline the final temperature is much greater than that of the surrounding at 309.67 K. The final temperature and the RMS indicate that greater system diameters hinder heat transfer, therefore the system becoming less isothermal.

Table 7.17- Limit reached, final pressure and final temperature for the charging stage and different diameters along with the root mean square

System Diameter (inch)	Limit Reached	Final Pressure (bar)	Final Temperature (K)	Root Mean Square (K)
36	$x = 0.2$	53.34	290.13	3.26
48	$x = 0.2$	56.24	292.36	5.51
60	$x = 0.2$	59.52	294.79	9.29
84	60 bar	60.00	309.67	18.32

Table 7.18 indicates that the greatest pressure drop during the first hold stage occurs for the system having a diameter of 60-inch, irrespective of the highest temperature occurring for the 84-inch diameter pipeline. Carbon dioxide experiences a 22 K temperature drop during the first hold stage for the system having the 84-inch diameter pipeline while in the case of the 60-inch diameter pipeline the system experience around 10 K temperature drop. Therefore, larger diameters dissipate more thermal energy to the surrounding during the first hold stage. It could be concluded that CO_2 small is more susceptible to temperature change within the liquid vapour dome.

During the discharging stage, the largest diameter pipeline experiences the greatest temperature drop while the desired pressure of 24 bar is reached at a smaller volume,

as presented in Table 7.19. Similar behaviour to the charging stage is experienced during the discharging, where the RMS is greater for larger system diameters, presented in Table 7.19.

Table 7.18- Pressure drop and final temperature for the different accumulator diameters after the first hold stage

System Diameter (inch)	Pressure Drop (bar)	Final Temperature (K)
36	7.88	283.54
48	10.59	283.71
60	13.59	283.96
84	10.08	287.55

Table 7.19- Minimum temperature, final volume and the root mean square for the discharging stage of the different diameters

System Diameter (inch)	Minimum Temperature (K)	Final Volume (m^3)	Root Mean Square (K)
36	277.28	1740.89	4.39
48	274.04	1686.25	7.42
60	268.21	1607.29	10.61
84	261.54	1518.88	12.26

It was noted that the larger the diameter, the greater the pressure increase during the final stage as exhibited in Table 7.20. This occurs since the final temperature of the discharging stage being much less than that of the surrounding sea water, at a volume smaller than that initially prescribed, while the temperature of the gas returns back to that of surrounding sea water. From Table 7.20 it is also evident that for greater diameters the final temperature is not equal to 283 K, but is still relatively close. Therefore, a larger diameter has a negative effect on the thermal performance of the accumulator, leading to a lower amount of energy being recovered and a lower CEF.

7.4.5 Inner Liner Influence

As already highlighted earlier in section 2.7, the inner liner is introduced into the system to mitigate corrosion issues induced by liquid CO_2. The influence of the liner on the thermal performance of CO_2-based accumulators is now studied using the code. The following are varied; a) the charging and discharging power, b) sea water temperature, c) initial (pre-charge) pressure, d) hold stage duration and e) uncertainty in the convective heat transfer coefficient of the two-phase region. The results for the system integrating a liner were compared against a standard system (no liner)

Table 7.20- Pressure increase and final temperature for the different system diameters after the second hold stage

System Diameter (inch)	Pressure Increase (bar)	Final Temperature (K)
36	0.47	283.00
48	1.11	283.00
60	2.09	282.99
84	3.26	282.86

Prior to understanding the influence of the different parameters on the system including the inner liner, it requires to be compared to an equivalent system without the liner. The equivalent system utilises a hydraulic pump and recovery turbine power of 250 kW while having both hold stages set to 4 hours. The CEF is greatly influenced by the inner liner as it experiences around 7% drop while comparing the system with the liner to that without from Table 7.21. Moreover, the system with the liner stores less energy and consequently less energy is recovered. Less energy is stored for the inner liner system since the charging stage is terminated at the 60 bar pressure limit and not the x of 0.2. Therefore, the area under the graph is less for the system including the liner.

Table 7.21- Cycle energy factor, energy stored and recovered for the accumulator with and without the inner liner

	Limit Reached	**Cycle Energy Factor (%)**	**Energy Stored (MWhr)**	**Energy Recovered (MWhr)**
No Inner Liner	x = 0.2	86.67	1.55	1.34
Inner Liner	60 bar	79.10	1.26	1.00

7.4.5.1 Influence of the Charging and Discharging Power

As has been observed in section 7.3.2, lower charging power result in greater CEF, this behaviour is also present with the introduction of the inner liner, as presented by Table 7.22. It is important to mention that, irrespective of the system power, the system CEF is never equal to or greater than that without the inner liner. Hence, the inner liner hinders the system performance considerably. Due to the inner liner, irrespective of the pump power, the code terminates the computation due to the prescribed working pressure limit of 60 bar and not the limit of x at 0.2. Moreover, from Table 7.22 it could be concluded that lower power leads to a higher storage capacity, and consequently more energy available for recovery.

Table 7.22- Cycle energy factor, energy stored and energy recovered for the stated hydraulic power

Hydraulic Power (kW)	**Cycle Energy Factor (%)**	**Energy Stored (MWhr)**	**Energy Recovered (MWhr)**
250	79.10	1.26	1.00
125	83.67	1.32	1.11
83	83.80	1.44	1.20

Analysing the extent to which the thermodynamic processes deviate from isothermal conditions for the systems during the charging and discharging stages, it is evident that the greater the power, the more the system deviates away from being isothermal (refer to Table 7.23). An issue arises when analysing the RMS for the charging stage when having a power of 125 kW and 83 kW, since for the latter the RMS is greater than that

of 125 kW. This occurs due to more data points being utilised for the RMS calculation leading to a greater temperature for 83 kW than 125 kW.

Table 7.23- Degree of isothermal and final temperature for the charging and discharging stages whilst considering the different powers

Hydraulic Power (kW)	Root Mean Square (K)		Final Temperature (K)	
	Charging Stage	Discharging Stage	Charging Stage	Discharging Stage
250	5.54	11.16	295.13	276.84
125	4.89	7.20	295.13	279.04
83	4.98	6.14	295.13	279.61

The final temperature for the charging stage is the same for all powers, as exhibited in Table 7.23, since the charging stage is terminated at 60 bar which occurs at the same temperature within and towards the liquid-vapour dome. Moreover, the final temperature during the discharging stage is less the greater the power since not enough time is allowed for the CO_2 to absorb heat from the surrounding.

Analysing Figure 7.21 the following observations could be drawn; 1) during the charging stage and the pump hydraulic power of 250 kW, the CO_2 does not manage to liquify and follows along the saturated vapour line; 2) for all the different power, during the charging stage it is evident that the temperature and pressure significantly deviate away from the 283 K isotherm; 3) due to the final charging volume being smaller for lower power, the temperature and pressure drop experienced by the CO_2 during the first hold stage is lower; 4) during the discharging stage, the highest temperature and pressure drop is experienced by the greatest power under study (the blue solid line) and 5) during the second hold stage, irrespective of the power all the systems experience a similar pressure increase while being greater for higher power.

Comparing the analysed results within this section to those in section 7.3.2, it could be concluded that the inner liner hinders the heat flow such that charging is terminated at 60 bar rather than at a dryness fraction of 0.2 for a power of 250 kW. Moreover, in the presence of the inner liner, the temperature of the gas does not return back to that of the surrounding sea water after the first hold stage. Comparing the results of the discharging stage when the liner is present to when its not from Figure 7.21c to Figure 7.12c, respectively. It is evident that in the presence of the inner liner, the CO_2 suffers from a greater temperature and pressure drop irrespective the pump power. Due to the greater temperature drops experienced during the discharging stage in the presence of the inner liner, the CO_2 experience a greater temperature gain during the second hold stage.

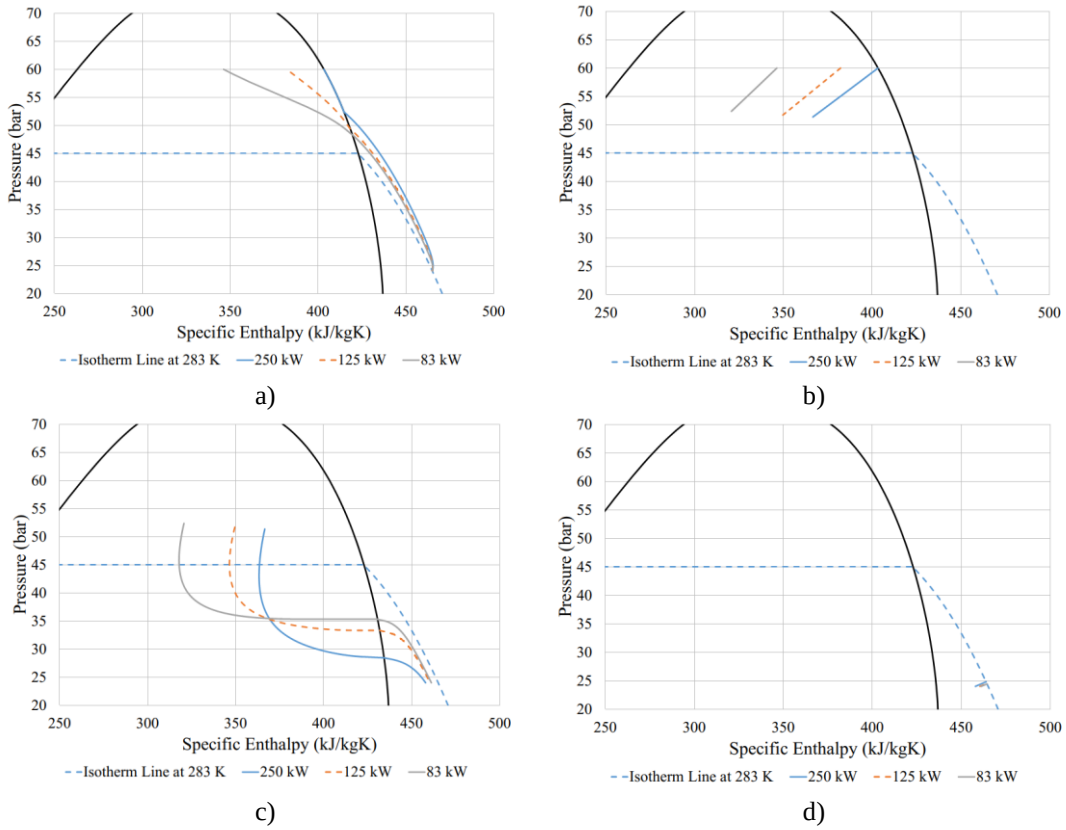

Figure 7.21- Pressure (bar) against Specific Enthalpy (kJ/kgK) a) charging stage, b) first hold stage, c) discharging stage and d) second hold stage for the different charging/discharging power

7.4.5.2 Influence of the Sea Water Temperature

The behaviour of the CO_2 system with the liner was subjected to different sea water temperatures and studied using the same approach as for section 7.4.1. The CEF is predicted to significantly increase at higher temperatures, as presented by the blue line in Figure 7.22. For a temperature of 293 K the CEF is equal to approximately 90%. Moreover, it is seen that although lower sea temperatures result in marginally higher storage capacities for a given accumulator volume, the recoverable energy is lower due to the smaller CEF values.

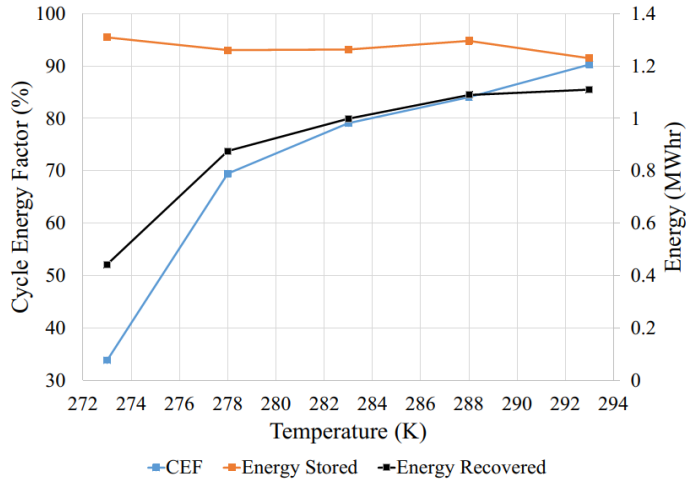

Figure 7.22- Cycle Energy Factor (%) and Energy (MWhr) against Temperature (K)

The following observations for the charging stage (Figure 7.23a) could be drawn;

1. At 273 and 278 K, CO_2 manages to liquify but the charging stage is terminated due to the 60 bar limit being reached.
2. At 283 K the process starts in gaseous state and as it gets compressed the CO_2 follows the saturated line up to the 60 bar limit.
3. Both at 288 K and 293 K the CO_2 does not liquify and the charging stage terminates at 60 bar in the gaseous state.

The following observations for the discharging stage (Figure 7.23b) could be drawn:

1. At 273 K the CO_2 does not manage to return to the gaseous state before reaching the initial pressure of 24 bar, therefore less energy is recovered from that stored. Such behaviour was not exhibited in section 7.4.1, for the system without the inner liner.
2. For the remaining liquified temperatures, the CO_2 manages to return to the gaseous state.
3. At 293 K the CO_2 does not liquify at any point and manage to return to the initial pressure.

Comparing Figure 7.23b to a it is evident that at higher temperatures, the CO_2 pressure drop during the first hold stage is much less than for lower temperatures. For 273 K the CO_2 experience around 15 bar pressure drop while at 288K the gas experiences a drop of around 5 bar. Since for a water temperature of 293 K the CO_2 is completely outside the liquid-vapour dome, the CO_2 experience less than 5 bar pressure drop. This is due to the inherent thermal properties of CO_2, for which a small temperature change within the liquid-vapour phase is linked to a high-pressure variation.

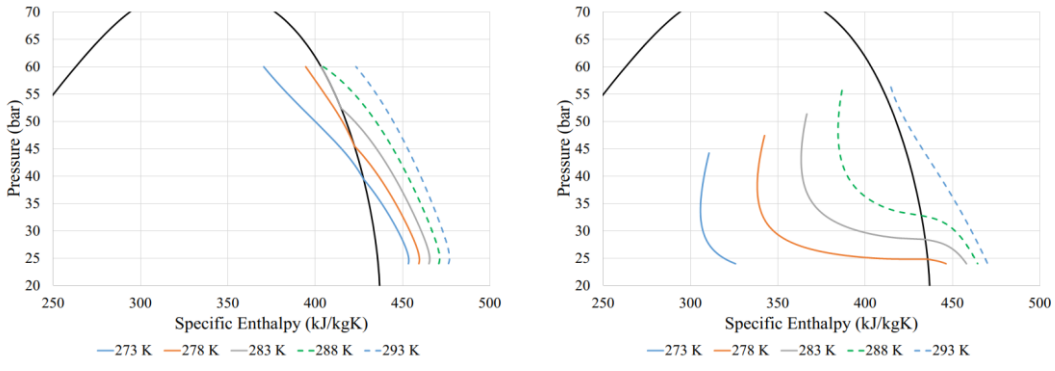

Figure 7.23- Pressure (bar) against Specific Enthalpy (J/kgK) for a) charging stage and b) discharging stage for the different sea water temperatures

7.4.5.3 Influence of the Initial Pre-Charge Pressure

The system initial pre-charge pressure was varied to 24 bar, 28 bar and 32 bar. Initially observing the CEF of the system, it is evident that for higher initial pre-charge pressure the system CEF reduces significantly (Table 7.24). On the other hand, the energy stored during the charging stage increases as the initial pressure increases, while the energy recovered reduces sufficiently at higher pressures. The mentioned observations were not noted for the system without the inner liner, but in the case of no inner liner the charging stage was terminated at a dryness fraction of 0.2 and not due to the 60 bar limit, as has been observed in the presence of the liner.

Table 7.24- Cycle energy factor, energy stored and recovered for the different initial pressures

Pre-Charge Pressure (bar)	Cycle Energy Factor (%)	Energy Stored (MWhr)	Energy Recovered (MWhr)
24	79.10	1.26	1.00
28	77.50	1.28	0.99
32	56.65	1.29	0.73

Analysing the plot for the pressure against the specific enthalpy during charging from Figure 7.24a, it is evident that for an initial pressure of 24 bar and 28 bar the system does not manage to liquify. On the other hand, for an initial pressure of 32 bar the gas manages to liquify, as exhibited in Figure 7.24a. Due to the initial pressure being different to one another, this greatly influences the flow rate which consequently effect the final volume of the charging stage. Hence, the final volume for lower pre-charge pressures is smaller than for higher pressures.

The three different systems suffer from a temperature drop which contributes to a pressure drop during the first hold stage. Irrespective whether the last point of the charging stage was at the liquid state or not, the CO_2 manages to liquify during the first hold stage, as presented by Figure 7.24b. After the first hold stage, Figure 7.24b, the final pressure and temperature are approximately equivalent to one another, irrespective of the initial pressure. Observing Figure 7.24c, it is noticeable that as the CO_2 discharges back to the initial pressure of 24 bar and 28 bar, the stage is terminated in the gaseous state, while for the 32 bar, it is terminated in the liquid-vapour state. For the second hold stage, Figure 7.24d, the gas of the initial pressure of 32 bar suffers the largest pressure increase as its temperature returns back to the surrounding sea water.

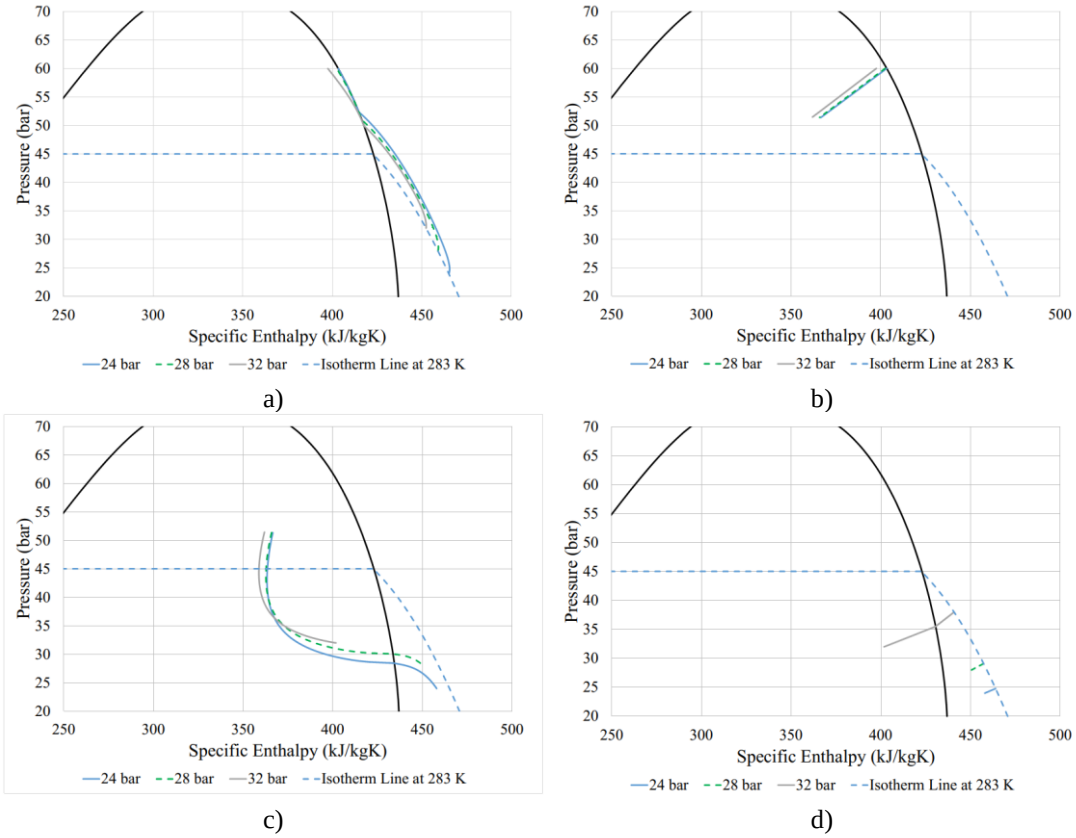

Figure 7.24- Pressure (bar) against Specific Enthalpy (kJ/kgK) a) charging stage, b) first hold stage, c) discharging stage and d) second hold stage for the different initial pressures

7.4.5.4 Hold Stage Duration

The baseline duration of the hold storage was that of 4 hours. To study the effect of the hold duration in the presence of the inner liner, the duration was varied to ± 25 % (-25 % = 3 hours, + 25 % = 5 hours) and ± 50 % (-50 % = 2 hours, + 50 % = 6 hours). Figure 7.25 indicates that the CEF of the system for longer durations reduces drastically due to the final temperature after the hold stage being less than in the case of shorter durations, as will be discussed.

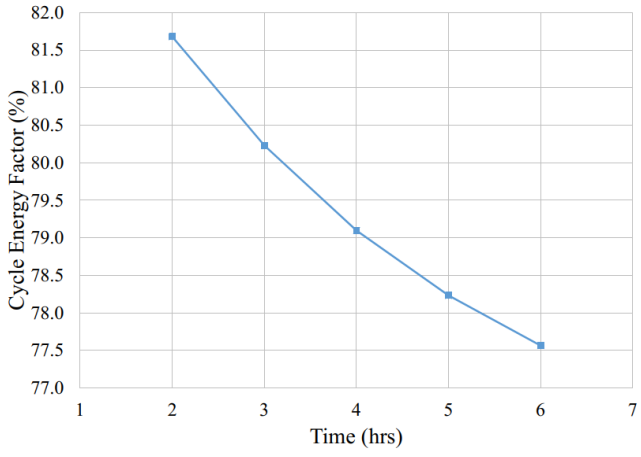

Figure 7.25-Cycle energy factor (%) against Time (hrs) for the different hold stage duration

The temperature drop experienced during the first hold stage is dependent on the duration allowed for the heat to be dissipated to the surrounding sea water. The mentioned behaviour could also be observed from Table 7.25, where for longer hold durations, the CO_2 experience the greatest temperature drop. Consequently, as a result of the temperature drop the CO_2 also experience a significant pressure drop. Hence, longer hold stage durations lead to greater percentage of the thermal energy to be lost to the surrounding sea water. The CO_2 experiences a significant temperature increase irrespective of the duration during the second hold stage. In contrast to what have been experienced during the first hold stage, the pressure change during the second hold stage is not as significant. Table 7.25 evidently proves that in the liquid-vapour state CO_2 is more susceptible to temperature than in the gaseous state.

Irrespective of the hold stage duration, the CO_2 does not manage to reach the temperature of the surrounding sea water during the first hold stage, Figure 7.26a. The accumulator not including the inner liner experiences a sudden initial temperature drop towards that of the surrounding, which is not exhibited in the presence of the inner liner. During the second hold stage the gas manage to almost return to the temperature of the surrounding sea water, irrespective of the duration, as presented by Figure 7.26b.

Table 7.25- Pressure and temperature drop during the first hold stage and increase during the second hold stage for the different hold durations (hrs)

Hold Stage Duration (hrs)	First Hold Stage		Second Hold Stage	
	Pressure Drop (bar)	Temperature Drop (K)	Pressure Increase (bar)	Temperature Increase (K)
2	5.48	4.08	0.77	5.84
3	7.27	5.48	0.78	6.03
4	8.63	6.57	0.79	6.15
5	9.65	7.40	0.81	6.25
6	10.42	8.04	0.82	6.32

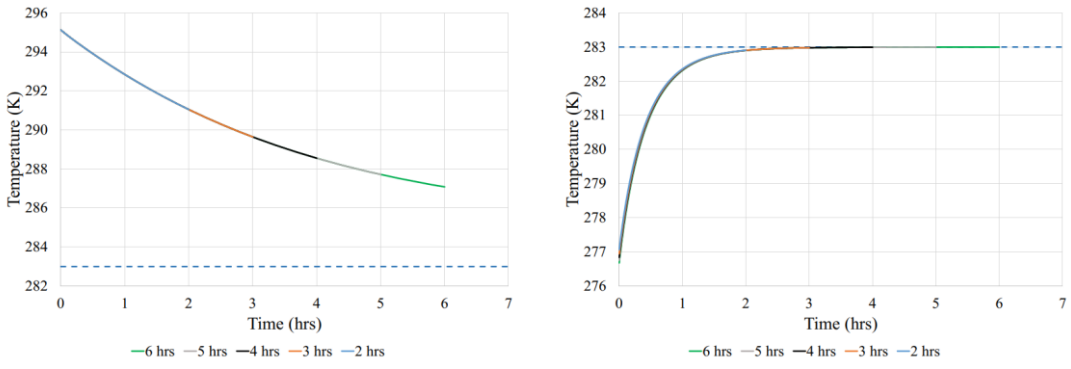

a) b)

Figure 7.26- Temperature (K) against Time (hrs) for the different hold stage durations of the a) first hold stage and b) second hold stage

7.4.5.5 Liquid-Vapour State Convective Heat Transfer Coefficient

The result of the internal convective heat transfer coefficient (h_{in}) for liquified CO_2, calculated from Thome and Fang equation presented in section 3.2.2.2, was varied to $\pm$ 25 %, $\pm$ 50 % and 100 %. Variation of the h_{in} led to less than 2 % difference between the two extremes for the CEF as dictated in Table 7.26. The RMS and the final temperature exhibit no change for the charging stage since the CO_2 does not liquify. On the other hand, during the discharging stage, the RMS decreases for higher variations while the final temperature gets closer to that of the surrounding, although the change is minimal. The RMS reduces at higher uncertainties due to the system convective heat transfer coefficient increasing which resulting in greater heat transfer.

Table 7.26- Cycle energy factor, root mean square and final temperature for the charging and discharging stages while considering the different sensitivities in the internal convective heat transfer coefficient

Sensitivity in the Internal Convective Heat Transfer Coefficient (%)	Cycle Energy Factor (%)	Root Mean Square (K)		Final Temperature (K)	
		Charging	Discharging	Charging	Discharging
- 50	77.17	5.54	12.64	295.13	276.01
-25	78.53	5.54	11.61	295.13	276.65
0	79.10	5.54	11.16	295.13	276.84
+25	79.41	5.54	10.91	295.13	276.93
+50	79.60	5.54	10.76	295.13	276.98
+100	79.83	5.54	10.57	295.13	277.04

Figure 7.27a indicate that the charging stage is not influenced by the variation of h_{in} because CO_2 does not enter the liquid vapour dome. The effect of the percentage variation is taken into effect during the discharging stage since the CO_2 is within the vapour dome. As the fluid discharges at lower percentage uncertainties it suffers from lower pressures and temperatures within the dome due to the system having lower heat transfer, dissimilar to what is observed at higher uncertainties. The mentioned observations for the discharging stage could be noted from Figure 7.27b.

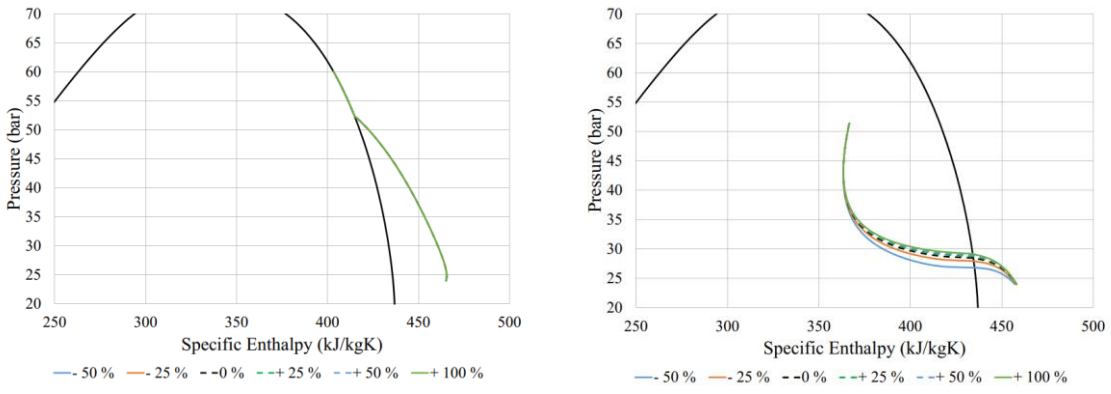

a) b)

Figure 7.27- Pressure (bar) against Specific enthalpy for the different uncertainties, a) charging stage and b) discharging stage

7.4.6 Influence of the Pipeline Inspection Gauge

The aim of this study is to understand the influence of the PIG friction while having CO_2 as the compressible fluid. Initially comparing the system CEF including the friction to that without from Table 7.27, it is evident that the CEF reduces with the presence of friction with a small margin of less than 1%. Although the CEF is smaller for a system including friction, the energy stored is greater than that of the system without. On the other hand, less energy is recovered during the discharging while including friction since a margin of the energy stored is utilised to overcome the friction.

Table 7.27- Cycle energy factor, energy stored and recovered for the systems with/without pipeline inspection gauge

System Type	Cycle Energy Factor (%)	Energy Stored (MWhr)	Energy Recovered (MWhr)
Without PIG	86.67	1.5457	1.3396
With PIG	85.99	1.5509	1.3337

Analysing Figure 7.28 for the four stages and for the systems with and without the PIG, it is evident that the PIG friction minimally influences the system due to both cases overlapping one another. Hence, it can be concluded that the system performance experience minimal effect by the introduction of the PIG friction.

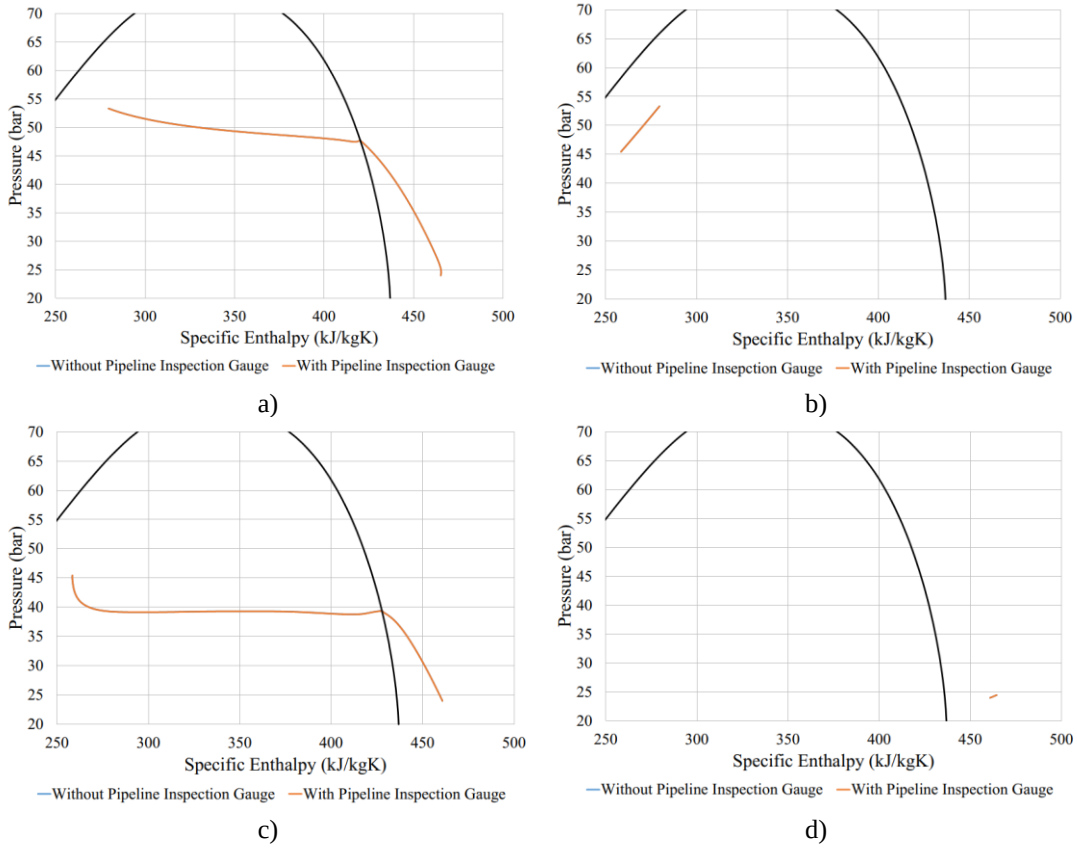

Figure 7.28- Pressure (bar) against Specific Enthalpy (kJ/kgK) for a) charging stage, b) first hold stage, c) discharging stage and d) second hold stage while having systems with and without the pipeline inspection gauge

7.4.7 Inner Liner and Pipeline Inspection Gauge

The initial proposed system included a combined system having the inner liner and the PIG working within a single system while having carbon dioxide as the compressible fluid. The combined effect is studied by carrying the following studies; 1) varying the charging and discharging power and 2) varying the final dryness fraction.

7.4.7.1 Variation of Charging and Discharging Power

Varying the power of the pump to 250 kW, 125 kW and 83kW led to the same observations as those noted for the system not including the PIG in section 7.4.5.1, while comparing Table 7.28 to Table 7.22. Comparing the results for the CEF of the two mentioned tables and the different power, it is evident that the introduction of the PIG causes no major change in the system CEF (less than 1% change). Moreover, the introduction of the PIG does not affect the energy stored and recovered.

Table 7.28- Cycle energy factor, energy stored and recovered for the stated power

Hydraulic Power (kW)	Cycle Energy Factor (%)	Energy Stored (MWhr)	Energy Recovered (MWhr)
250	78.87	1.2648	0.9975
125	83.44	1.3244	1.1050
83	83.57	1.4379	1.2017

Analysis of the RMS and the final temperature from Table 7.29 results to the same behaviour when the PIG was not present, section 7.4.5.1. The results of the RMS and final temperature do not vary between those including the PIG and not as could be deduced by comparing the results of Table 7.29 to Table 7.23. Such behaviour is exhibited by the system because the PIG does not hinder the thermal properties of the system, unlike the inner liner.

Table 7.29- Root mean square and final temperature for the charging and discharging stages whilst considering the different hydraulic pump power

Hydraulic Power (kW)	Root Mean Square (K)		Final Temperature (K)	
	Charging Stage	Discharging Stage	Charging Stage	Discharging Stage
250	5.54	11.18	295.13	276.82
125	4.89	7.21	295.13	279.04
83	4.99	6.15	295.13	279.61

7.4.7.2 Influence of the Final Dryness Fraction at the Full Charged State

In section 7.4.3 the effect of the final dryness fraction, x, was studied by considering different values between 0.2 and 1, while maintaining the system parameters constant. In the presence of the inner liner, the CO_2 does not liquify and stops at the limit of 60 bar while following the vapour saturated line. Therefore, varying the limit of the x between 0.2 to 0.8 causes no changes, as could be noted from Table 7.30. The limit of

the x is taken into effect for a fraction of 1. For this value, the CEF increases from 78.87 % to 84.90 % while suffering a decrease in the energy stored and recovered, as presented in Table 7.30. Longer charging durations are required for the limit to be reached for lower dryness fraction.

Table 7.30- Cycle energy factor, energy stored, energy recovered and charging duration for the different dryness fraction limit

Dryness Fraction	Cycle Energy Factor (%)	Energy Stored (MWhr)	Energy Recovered (MWhr)	Charging Duration (hrs)
0.2	78.87	1.26	1.00	5.51
0.4	78.87	1.26	1.00	5.51
0.8	78.87	1.26	1.00	5.51
1	84.90	1.09	0.93	4.78

The path followed on a pressure against specific enthalpy for a whole cycle is the same for final x equal to 0.2, 0.4 and 0.8 but for a dryness fraction of 1 it varies, presented in Figure 7.29. It could be observed that for a dryness fraction of 1 the charging stage is terminated immediately as soon as the CO_2 reaches the saturated liquid line at a lower pressure than in the case of a x equal to 0.2. Due to the charging stage being terminated at a lower pressure, the magnitude of the pressure drop experienced during the first hold stage is less. Moreover, during the discharging stage the CO_2 experience lower temperatures within the dome for the limit of the dryness fraction of 0.2.

Therefore, it could be concluded that the dryness fraction limit between 0.2 to 0.8 does not influence the system performance, which is not the case for a limit of 1. For a limit of x equal to 1 the area under the graph is reduced than for lower limits, causing for less energy to be stored but greater CEF is attained while the system is charged at a shorter duration.

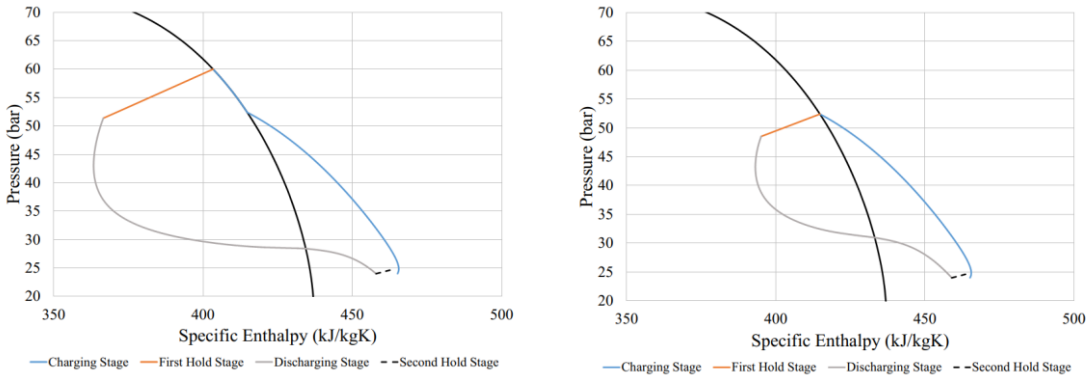

a) b)

Figure 7.29- Pressure (bar) against Specific Enthalpy (kJ/kgK) for final dryness fraction limit of a) 0.2 and b) 1

8 Comparison of the Performance Characteristics of the Air-based and CO2-based HPES Systems

This chapter is intended to use the salient results from Chapter 6 and 7 to directly compare the performance characteristics of air-based and CO_2-based accumulators. It is assumed that both accumulators have the same volume and peak operations of 1782.72 m^3 and 60 bar, respectively. The pre-charge pressure is also the same for both cases and equal to 24 bar. The comparison is also restricted to a pump and turbine power of 250 kW. The hold is also set to 4 hours. The CO_2 dryness fraction, x, at the end of the charging stage is not allowed to be less than 0.2. The sea water temperature is assumed to be equal to 283 K in both cases. Two scenarios for each accumulator compressible fluid are assumed: 1) basic accumulator with no internal protective liner and PIG and (2) accumulator equipped with both internal liner and PIG.

Figure 8.1, compares the CEF estimates for the air- and CO_2-based accumulators. It is evident that the accumulators using air as the compressible fluid are more thermally efficient, with the CEF values being >90%. The introduction of the inner liner and PIG to overcome engineering challenges related to corrosion, diffusion of the compressible fluid into the injected sea water and seabed undulations has a negative impact of the CEF for both accumulator types. Yet the percentage reduction in the CEF resulting from the use of a liner and the PIG is larger for CO_2-based system than for air (7.81 versus 2.13)

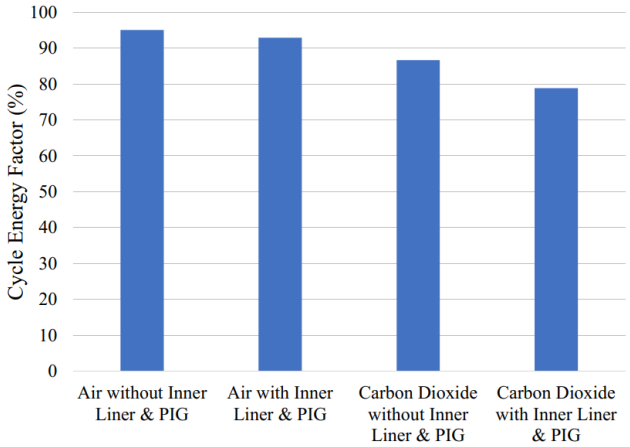

Figure 8.1-Cycle Energy Factor (%) for the systems with/without inner liner and pipeline inspection gauge, having air and carbon dioxide as the compressible fluid while the system operates at 250 kW for both charging/discharging stages and 4 hours for both hold stages

Although CO_2 use in lieu of air results in a lower CEF, irrespective of the inner liner and PIG being present or not, the energy storage capacity is still higher. This may be noted in Figure 8.2. When air is utilised without the inner liner and PIG, the code

estimates that the accumulator stores 1 MWhr whilst for CO_2 it estimates that it stores 1.55 MWhr. Thus, the same volume and mass of steel manage to store more energy at a lower pressure for CO_2 based HPES system rather than that of air. Similarly, the accumulators with the inner liner and PIG, resulted in 0.99 MWhr to be stored while for CO_2 1.26 MWhr are stored.

Analysing the energy recovered from Figure 8.2, it is evident that utilising CO_2 without the inner liner and PIG results in the greatest amount of energy recovered out of the four accumulators, followed by the accumulator utilising CO_2 with the inner liner and PIG. Further analysis of Figure 8.2 indicate that the greatest difference between the energy recovered to that stored occurs for CO_2 while the inner liner along with the PIG are present. The least energy difference between recovered and stored is present in the first accumulator for air. This analysis concludes that the presence of the inner liner and PIG result in the greatest energy loss during the first hold stage. Irrespective of the degree of the energy lost for CO_2, more energy is extracted than that for air.

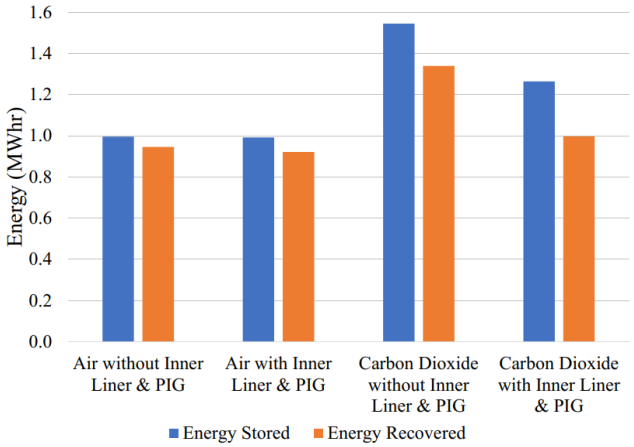

Figure 8.2- Energy Stored and Recovered (MWhr) for the systems with/without inner liner and pipeline inspection gauge, having air and carbon dioxide as the compressible gas while the system operates at 250 kW for both charging/discharging stages and 4 hours for both hold stages

Due to the nature of the different fluids and accumulators under study, the final temperature of the charging stage is greatly affected as could be observed from Table 8.1. For the two fluids when the inner liner and PIG are not present, the final temperatures are relatively close to one another, differentiating by only 0.5 K. On the other hand, in the presence of the inner liner and PIG, the CO_2 temperature is greater than that of air by 3 K. Moreover, during the first hold stage, almost all the systems temperatures return back to that of the surrounding sea water at 283 K except that of CO_2 with the inner liner and PIG as it retains most of its temperature. Such instance occurs because the final volume of the CO_2 system is less than that of air, hindering the contact area of the gas to that of surrounding wall.

The minimum discharging temperature is also influenced by the structure of accumulator and the compressible fluid. Table 8.1 indicates that the introduction of the inner liner and PIG hinder heat flow since it results in lower temperatures during discharging, irrespective of the fluid. The lowest temperature during the discharging stage occurs for CO_2 with inner liner and PIG. During the second hold stage, the fluid experiences a temperature rise due to the final temperature of the fluid after the discharging stage being less than that of the surrounding. For all the accumulators, except the last one presented in Table 8.1, the temperature rise is relatively close to one another. The pressure rise for all the accumulators is always less than 1 bar for all the accumulators under study.

Table 8.1- Charging stage final temperature, pressure and temperature drop during the first hold stage and minimum discharging temperature for the accumulators utilising air and carbon dioxide with/without inner liner and pipeline inspection gauge along with the pressure and temperature rise during the second hold stage

	Charging Stage Final Temperature (K)	**Pressure and Temperature Drop During First Hold Stage (bar & K)**	**Minimum Discharging Temperature (K)**	**Pressure and Temperature Rise During Second Hold Stage (bar & K)**
Air without Inner Liner & PIG	289.66	1.59 & 6.66	277.26	0.28 & 3.12
Air with Inner Liner & PIG	292.25	2.16 & 9.23	275.31	0.41 & 4.52
Carbon Dioxide without Inner Liner & PIG	290.13	7.87 & 6.58	277.28	0.47 & 3.69
Carbon Dioxide with Inner Liner & PIG	295.13	8.63 & 6.57	265.66	0.80 & 6.17

Another quantification of the temperature introduced through this study is the root mean square (equation 6.1), introduced in Chapter 6. Throughout the charging stage, the accumulator utilising CO_2 without the inner liner and PIG yielded the least RMS as exhibited in Figure 8.3. This indicates that the temperature of CO_2 deviated from the surrounding sea water by a smaller magnitude than for the remaining accumulators for the whole stage of charging. Similarly, was observed for the discharging stage. The greatest deviation of the gas from the surrounding sea water temperature occurs for the discharging stage when CO_2 is utilised while including the inner liner and PIG.

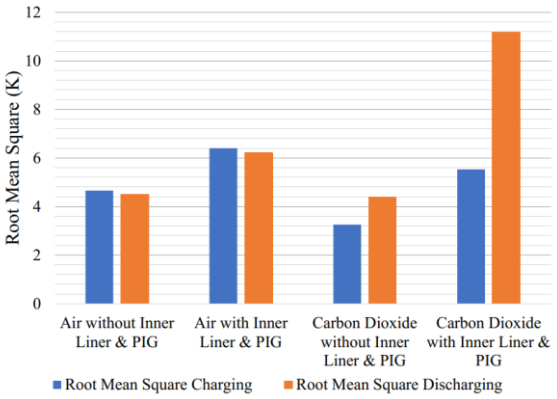

Figure 8.3- Root mean square for charging and discharging stages for the systems with/without inner liner and pipeline inspection gauge, having air and carbon dioxide as the compressible gas while the system operates at 250 kW for both charging/discharging stages and 4 hours for both hold stages

A trend is visible for the two fluids as air yields a higher RMS for charging than discharging, vice versa to what is observed for CO_2. It is also evident for the charging stage, the accumulators utilising CO_2 yielded lower RMS values compared to when air is the compressible fluid. Similar behaviour was present during the discharging stage except for the system utilising CO_2 and including the inner liner and PIG.

Operating with CO_2 as the compressible gas results in the greatest amount of energy to be recovered per unit accumulator volume, irrespective whether the inner liner and PIG are present or not. This may be noted from Figure 8.4a. Similar behavior is present for the energy recovered per unit mass of steel of the outer pipeline, see Figure 8.4b. However, when the inner liner and PIG are introduced, the increase in recoverable energy per unit volume of steel from an accumulator operating with CO_2 is only being predicted to be marginally larger than that for the equivalent system operating with air.

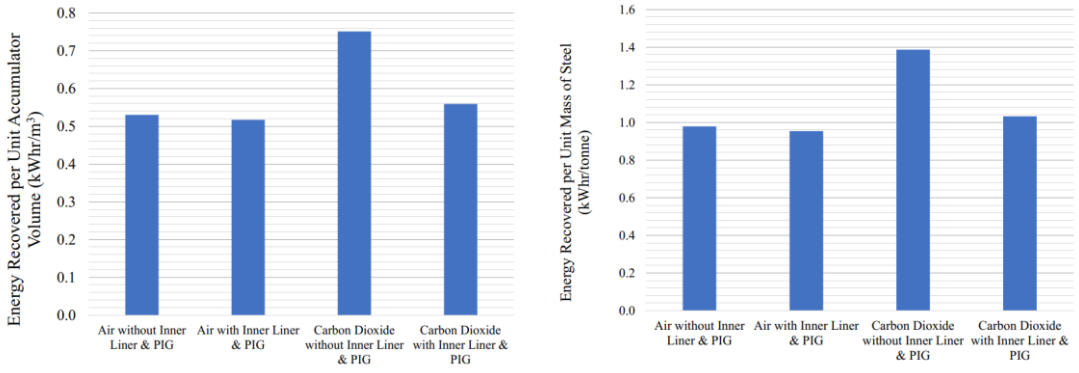

a) b)

Figure 8.4- a) Energy recovered per unit accumulator volume (kWhr/m^3) and b) Energy recovered per unit mass of steel (kWhr/tonne) for the systems with/without inner liner and pipeline inspection gauge, having air and carbon dioxide as the compressible gas while the system operates at 250 kW for both charging/discharging stages and 4 hours for both hold stages

9 Conclusions and Suggestions for Further Work

This study provided a preliminary understanding of the expected transient thermal behaviour of an HPES system consisting of a subsea pipeline to act as the accumulator for storing energy in the form of a compressible fluid. The numerical modelling compared the thermal behaviour of the subsea accumulator utilising CO_2 instead of air, while introducing an inner polymeric liner and a PIG to mitigate issues related to corrosion and dissolution of the gas being compressed into the sea water. The study was mainly divided into three main parts; 1) the influence of air as the compressible gas within the accumulator, 2) the influence of CO_2 as the compressible fluid and 3) comparison of the observations of CO_2 to those obtained for air.

Part 1: The following are the main conclusions drawn from the studies investigating the HPES accumulator operating with air as the compressible fluid:

i. When the inner liner and pipeline inspection gauge are not present, the charging and discharging power minimally influence the cycle energy factor and the final temperature for both charging and discharging stages. In contrast, when the inner liner and PIG are both present the charging and discharging power greatly influences the system CEF and final temperature for both stages.
ii. Large accumulator diameters hinder the thermal behaviour of the system such that for an accumulator diameter of 84-inch the CEF is never similar nor close to that of the 36-inch pipeline, irrespective of the charging and discharging power.
iii. The CEF is considerably influenced by the accumulator length-to-diameter ratio. A larger ratio allows the system to thermodynamically approach the ideal isothermal scenario, thus resulting in a higher CEF.
iv. The internal convective heat transfer coefficient, h_{in}, value during the first and second hold stages minimally influences the final temperature of both hold stages for a duration of 4 hours or greater. On the other hand, for shorter durations the value of h_{in} considerably influences the final temperature.

Part 2: The following are the main conclusions drawn from the studies for the HPES accumulator using carbon dioxide in lieu of air:

i. As the CO_2 is compressed into the liquid-vapour dome it experiences a pressure and temperature change within the dome, thus moving vertically within the dome. A similar behaviour is exhibited during expansion.

ii. When the inner liner and PIG are not present, decreasing the charging and discharging power results in the CO_2 to closely follow the isotherm of the surrounding sea water.

iii. When the inner liner and PIG are both present, the CO_2 manages to liquify for a charging power lower than 250 kW while for a charging power equal to 250 kW it does not liquify and closely follow the saturated vapour line of the liquid-vapour dome.

iv. Increasing the pre-charge pressure from 24 bar to 32 bar yields greater energy storage and recovery for an accumulator without the inner liner, while in the presence of the inner liner the contrary is observed.

v. The pressure of CO_2 is more susceptible to temperature change within the liquid-vapour dome than in complete gaseous phase, such that for 1 K of temperature change it experiences a pressure change greater than 1 bar.

Part 3: Comparing the results from air-based and CO_2-based HPES system, the following conclusions could be drawn:

i. Both fluids are thermally influenced by the presence of the inner liner, however the impact is much more prominent in the case where CO_2 is used as the compressible fluid.

ii. The simulations indicate that the accumulator length-to-diameter ratio has a significant influence on the round-trip thermal efficiency, such that accumulators with smaller ratios deviate further away from isothermal behaviour.

iii. The influence of the PIG on the CEF is only marginal for both accumulators under study.

iv. The transient numerical modelling indicated that the achievable storage capacity of CO_2-based accumulator is around 0.55 MWhr higher than that of air-based system when no inner liner and PIG are included while the charging and discharging powers are both set to 250 kW. This difference is reduced to 0.27 MWhr when the liner and PIG are included while maintain the same power.

v. For a unit of accumulator volume and a unit mass of steel, more energy is recovered when CO_2 is utilised irrespective of the inner liner and PIG being present.

Although having its limitations, the presented study provides motivation to explore the potential CO_2-based accumulators for storing energy in a subsea environment in further detail. To address the limitations of this study, the following further work is being proposed:

i. Conduct finite element analysis (FEA) for the PIG friction with the pipeline and the inner liner for better determination of the friction behaviour on the system.

ii. Carry out computational fluid dynamics (CFD) study of the CO_2-based accumulator when transitioning from the gaseous state to the two-phase state and vice versa to further model the heat transfer phenomena more comprehensively.

iii. Validate the in-house developed code using measurements from a prototype accumulator submerged in sea water.

iv. Study the influence of the contact area of the accumulator with the seabed to examine how this influences the thermal behaviour of the system.

v. Analyse the effect of different mediums which could be utilised as the non-corrosive protective liner for liquefied CO_2 while considering their cost. Consequently, study the influence of the newly proposed non-corrosive protective liner on the isothermal behaviour of the system.

10 References

[1] United Nations, “Sustainable Development Goals: Teaching Guide and Resaurces,” United Nations, [Online]. Available: https://www.un.org/en/sustainable-development-goals. [Accessed 28 July 2022].

[2] United States Environment Protection Agency, “Greenhouse Gas Emissions,” United States Environment Protection Agency, 16 May 2022. [Online]. Available: https://www.epa.gov/ghgemissions/overview-greenhouse-gases#:~:text=Carbon%20dioxide%20(CO2)%20is,gas%20emissions%20from%20human%20activities.. [Accessed 28 July 2022].

[3] J. Jaeger, “Explaining the Exponential Growth of Renewable Energy,” World Resource Institute, 20 September 2021. [Online]. Available: https://www.wri.org/insights/growth-renewable-energy-sector-explained. [Accessed 28 July 2022].

[4] M. Y. Worku, “Recent Advances in Energy Storage Systems for Renewable Source Grid Integration: A Comprehensive Review,” *Sustainability,* vol. 14, pp. 1-18, 2022.

[5] M. S. Guney and Y. Tepe, “Classification and Assessment of Energy Storage Systems,” *Renewable and Sustainable Energy Reviews,* vol. 75, pp. 1187-1197, 2017.

[6] M. Arbabzadeh, R. Sioshansi, J. X. Johnsons and G. A. Koleian, “The Role of Energy Storage in Deep Decarbonization of Electricity Production,” *Nature Communications,* vol. 10, pp. 1-19, 2019.

[7] A. N. Abdalla, M. S. Nazir, H. Tao, S. Cao, R. Ji, M. Jiang and L. Yao, “Integration of Energy Storage System and Renewable Energy Sources Based on Artificial Intelligence: An Overview,” *Journal of Energy Storage,* vol. 40, pp. 1-13, 2021.

[8] Storm 4, “The Energy Storage Technologies Fighting Climate Change,” Storm 4, 22 March 2022. [Online]. Available: https://storm4.com/storm4-voice/energy-storage/energy-storage-technology-climate-change/. [Accessed 4 August 2022].

[9] L. Li, W. Liang, H. Lian, J. Yang and M. Dusseault, “Compressed Air Energy Storage: Characteristics, Basic Principles, and Geological Considerations,” *Advances in Geo-Energy Research ,* vol. 2, no. 2, pp. 135-147, 2018.

[10] M. Killer, M. Farrokhseresht and N. G. Paterakis, “Implementation of Large-scale Li-ion Battery Energy Storage Systems within the EMEA Region,” *Applied Energy,* vol. 260, pp. 1-17, 2020.

[11] United Nations, “Fact sheet: People and Oceans,” *The Ocean Conference,* pp. 1-7, 2017.

[12] M. Aneke and M. Wang, “Energy Storage Technologies and Real Life Applications- A State of the Art Review,” *Applied Energy,* vol. 179, pp. 350-377, 2016.

[13] S. Øvergaard, “Issue Paper: Definition of Primary and Secondary Energy,” in *Prepared as input to Chapter 3: Standard International Energy Classification (SIEC) in the International Recommendtion on Energy Statistics (IRES),* 2008, pp. 1-7.

[14] E. M. Gouda, Y. Fan, M. Benaoucha, T. Neu and L. Luo, “Review on Liquid Piston Technology for Compressed Air Energy Storage,” *Journal of Energy Storage,* vol. 43, pp. 1-61, 2021.

[15] Y. Zhang, K. Yang, H. Hong, X. Zhong and J. Xu, “Thermodynamic Analysis of a Novel Energy Storage System with Carbon Dioxide as Working Fluid,” *Renewable Energy,* vol. 99, pp. 682-697, 2016.

[16] J. Wang, K. Lu, l. Ma, J. Wang, M. Dooner, S. Miao, J. Li and D. Wang, “Overview of Compressed Air Energy Storage and Technology Development,” *Energies,* vol. 10, pp. 1-22, 2017.

[17] A. Abuheiba, M. R. Ally, B. Smith and A. Momen, “Increasing Compressed Gas Energy Storage Density Using CO2-N2 Gas Mixture,” *Energies* , vol. 13, pp. 1-13, 2020.

[18] “Fact Sheet | Energy Storage (2019),” Environmental and Energy Study Institute , 2019 February 2019. [Online]. Available: https://www.eesi.org/papers/view/energy-storage-2019. [Accessed 20 December 2021].

[19] U.S. Department of Energy, “Electricity Storage Technology Review,” pp. 1-61, 2020.

[20] M. M. Rahman, A. O. Oni, E. Gemechu and A. Kumar, “Assessment of Energy Storage Technologies: A Review,” *Energy Conversion and Management,* vol. 223, pp. 1-28, 2020.

[21] M. Müller, L. Viernstein, C. N. Truong, A. Eiting, H. C. Hesse, R. Witzmann and A. Jossen, “Evaluation of Grid-Level Adaptability for Stationary Battery Energy Storage System Application in Eruope,” *Journal of Energy Storage,* vol. 9, pp. 1-11, 2017.

[22] B. K. Sovacool, “When Subterranean Slavery Supports Sustainability Transitions? Power, Patriarchy and Child Labor in Artisanal Congolese Cobalt Mining,” *The Extractive Industries and Society* , vol. 8, pp. 271-293, 2021.

[23] J. F. Weaver, “Regulator Says Lithium-ion Batteries Create "Unacceptable Risks",” PV Magazine, 08 August 2019. [Online]. Available: https://pv-magazine-usa.com/2019/08/08/lithium-ion-not-prudent-and-create-unacceptable-risks/. [Accessed 16 September 2022].

[24] M. Bonvento and C. J. Cox, “Lithium Ion Battery Fires: A Threat to Container Shipping,” Maritime Logistics Professional, 12 August 2020. [Online]. Available: https://www.maritimeprofessional.com/news/lithium-battery-fires-threat-container-360275. [Accessed 16 September 2022].

[25] Y. A. Gandomi, D. S. Aaron, J. R. Houser, M. C. Daugherty, J. T. Clement, A. M. Pezeshki, T. Y. Ertugrul, D. P. Moseley and M. M. Mench, “Critical

Review—Experimental Diagnostics and Material Characterization Techniques Used on Redox Flow Batteries," *Journal of The Electrochemical Society,* vol. 165, pp. 970-1010, 2018.

[26] M. Budt, D. Wolf, R. Span and J. Yan, "A Review on Compressed Air Energy Storage: Basic Principles, Past Milestones and Recent Developments," *Applied Energy,* vol. 170, pp. 250-268, 2016.

[27] S. Rehman, L. Al-Hadhrami and M. M. Alam, "Pumped Hydro Energy Storage System: A Technological Review," *Renewable and Sustainable Energy Reviews,* vol. 44, pp. 586-598, 2015.

[28] L. F. Cabeza, "Using Molten Salts and Other Liquid Sensible Storage Media in Thermal Energy Storage (TES) Systems," in *Advances in Thermal Energy Storage Systems Methods and Applications*, Cambridge, Woodhead Publishing, 2015, pp. 49-61.

[29] R. Morgan, S. Nelmes, E. Gibson and G. Brett, "Liquid Air Energy Storage – Analysis and First Results from a Pilot Scale," *Applied Energy,* vol. 137, pp. 845-853, 2015.

[30] M. J. Palys and P. Daoutidis, "Using Hydrogen and Ammonia for Renewable Energy Storage: A Geographical Comprehensive Techno-Economic Study," *Computers and Chemical Engineering*, vol. 136, pp. 1-13, 2020.

[31] A. G. Olabi, C. Onumaegbu, T. Wilberforce, M. Ramadan, M. A. Abdelkareem, Alami and A. H. Al, "Critical Review of Energy Storage Systems," *Energy,* vol. 214, pp. 1-22, 2021.

[32] L. Wagner, "Overview of Energy Storage Methods," Mora Associates, Clean Energy and Clean Technology, 2007.

[33] H. Liu, Q. He, A. Borgia, L. Pan and C. M. Oldebburg, "Thermodynamic Analysis of a Compressed Carbon Dioxide Energy Storage System Using Two Saline Aquifers at Different Depths as Storage Reservoirs," *Energy Conversion and Management,* vol. 127, pp. 149-159, 2016.

[34] O. A. V, J. D. McTigue, P. Farres-Antunez, A. Tafone, A. Romagnoli, Y. Li, W.-D. Steinmann, L. Wang, H. Chen and C. N. Markides, "Progress and

Prospects of Thermo-Mechanical Energy Stroage- A critical Review," *Progress in Energy,* vol. 3, pp. 1-44, 2021.

[35] M. Raju and S. K. Khaitan, "Modeling and Simulation of Compressed Air Storage in Caverns: A Case Study of the Huntorf Plant," *Applied Energy,* vol. 89, pp. 474-487, 2012.

[36] X. Luo, J. Wang, M. Dooner and C. Jonathan, "Overview of Current Development in Electrical Energy Storage Technologies and the Application Potential in Power System Operation," *Applied Energy,* vol. 137, pp. 511-536, 2015.

[37] F. A. Tiano and G. Rizzo, "Use of an Under-Water Compressed Air Energy Storage (UWCAES) to Fully Power the Sicily Region (Italy) with Renewable Energy: A Case Study," *Frontiers in Mechanical Engineering,* vol. 7, pp. 1-16, 2021.

[38] C. Cutajar, "Loads and Motion Analyss of a Floating Offshore Wind Turbine with Integrated Hydro-pneumatic Energy Storage," *M. Sc. Thesis, Department of Mechanical Enegineering, University of Malta, Malta,* pp. 1-150, 2019.

[39] A. Pimm and S. D. Garvey, "Chapter 7-Underwater Compressed Air Energy Storage," in *Storing Energy,* Elsevier, 2016, pp. 135-154.

[40] A. J. Pimm, S. D. Garvey and M. Jong, "Design and Testing of Energy Bags for Underwater Compressed Air Energy Storage," *Energy,* vol. 66, pp. 496-508, 2014.

[41] O. Sampedro. Egoi, A. Dazin, G. Caignaert and F. Colas, "Modeling of Hydro-Pneumatic Energy Storage Using Pump Turbines," *International Seminar on Hydropower Plant,* vol. 17, pp. 117-128, 2013.

[42] A. Odukomaiya, A. Abu-Heiba, S. Graham and A. Momen, "Experimental and Analytical Evaluation of a Hydro-Pneumatic Compressed-Air Ground-Level Integrated Diverse Energy Storage (GLIDES) System," *Applied Energy,* vol. 221, pp. 75-85, 2018.

[43] A. Oddukomaiya, A. M. Momen, A. Abu-Heiba, K. Gluesenkamp, O. Abdelaziz and S. Graham, “Transiet Thermofluids Analysis of a Ground-Level Integrated Diverse Energy Storage (GLIDES) System,” *IMECE,* pp. 13-19, 2015.

[44] C. Qin and E. Loth, “Liquid piston compression efficiency with droplet heat transfer,” *Applied Energy,* vol. 114, pp. 539-550, 2014.

[45] S. Lemofouet and A. Rufer, “A Hybrid Energy Storage System Based on,” *IEEE Transactions on Industrial Electronics,* vol. 53, pp. 1105-1115, 2006.

[46] DNV.GL, “Living The Future Today,” in *A Broader View Electrifying the Future*, 2014, pp. 44-56.

[47] D. Buhagiar, T. Sant and R. Farrugia, “Hydro-Pneumatic Energy Storage,” *Encyclopedia of Energy Storage,* pp. 1-18, 2021.

[48] M. Puchta, J. Bard, C. Dick, D. Hau, B. Krautkremer, F. Thalemann and H. Hahn, “Development and Testing of a Novel Offshore Pumped Storage Concept for Storing Energy a Sea-StEnSea,” *Journal of energy Storage,* vol. 14, pp. 271-275, 2017.

[49] B. Ernst, J. Bard, M. Puchta and C. Dick, “Deep Sea Pumped Storage,” Energy System Integration Group, 26 November 2019. [Online]. Available: https://www.esig.energy/deep-sea-pumped-storage/. [Accessed 11 August 2022].

[50] D. Buhagiar, T. Sant, R. N. Farrugia, L. Aquilina, D. Farrugia and F. M. Strati, “Small-scale Experimental Testing of a Novel Marine Floating Platform with Integrated Hydro-Pneumatic Energy Storage,” *Journal of Energy Storage,* vol. 24, pp. 1-13, 2019.

[51] L. Aquilina, “Open-Field Measurements and Analysis of a Solar-Driven Hydro-Pneumatic Energy Storage System,” *M.S. Thesis, Department of Mechanical Engineering, Malta Univ., Malta,* pp. 1-150, 2018.

[52] D. Buhagiar, “Modeling and Analysis of Hydraulic Wind Turbines with Integrated Energy Storage,” *Ph.D dissertation, Department of Mechanical Engineering, University of Malta, Malta,* pp. 1-274, 2016.

[53] O. O'Callaghan and P. Donnellan, “Liquid Air Energy Storage System: A Review,” *Renewable and Sustainable Energy Reviews,* vol. 146, pp. 1-12, 2021.

[54] P. Maina and Z. Huan, “A Review of Carbon Dioxide as a Refrigerant in Refrigeration Technology,” *South African Journal of Science,* vol. 111, pp. 1-10, 2015.

[55] G. Lorntzen, “Revival of Carbon Dioxide as a Refrigerant,” vol. 17, pp. 1-10, 1994.

[56] M. Bazzanella. Alexis, S. Schiebahn, S. Luhr and L. Zhao, “Carbon Dioxide,” *Ullmann's- Encyclopedia of Industrial Chemistry,* pp. 1-43, 2014.

[57] C.-H. Son and S.-J. Park, “An Experimental Study on Heat Transfer and Pressure Drop Charateristics of Carbon Dioxide During Gas Cooling Process in a Horizontal Tube,” *International Journal of Refrigeration ,* vol. 29, pp. 539-546, 2006.

[58] S. Sawalha, “Carbon Dioxide in Supermarket Refrigeration,” *Doctoral Thesis, Department of Eergy Technology, Royal Institute of Technology, Stockholm, Sweden,* pp. 1-163, 2008.

[59] Chemicalogic, “Mollier Charts,” Chemicalogic, [Online]. Available: http://www.chemicalogic.com/Pages/DownloadMollierCharts.html . [Accessed 20 December 2021].

[60] Ohio, “Thermodynamic Properties of R744 (Carbon Dioxide - CO2),” Ohio, [Online]. Available: https://www.ohio.edu/mechanical/thermo/property_tables/CO2/ph_CO2.html. [Accessed 17 May 2022].

[61] Q. He, H. Liu, Y. Hao, Y. Liu and W. Liu, “Thermodynamic Analysis of a Novel Supercritical Compressed Carbon Dioxide Energy Storage System

Through Advanced Exergy Analysis," *Renewable Energy,* vol. 127, pp. 835-849, 2018.

[62] A. H. Alami, A. A. Hawili, R. Hassan, M. Al-Hemyari and K. Aokal, "Experimental Study of Carbon Dioxide as Working Fluid in a Closed-Loop Compressed Gas Energy Storage System," *Renewable Energy,* vol. 134, pp. 603-611, 2019.

[63] Energy Dome, "Energy Dome CO2 Battery," Energy Dome, 2021. [Online]. Available: https://energydome.com/co2-battery/. [Accessed 20 December 2021].

[64] S. Li, Z. Zeng, M. A. Harris, L. J. Sánchez and H. Cong, "CO2 Corrosion of Low Carbon Steel Under the Joint Effects of Time-Temperature-Salt Concentration," *Frontiers in Materials,* pp. 1-17, 2019.

[65] F. Spritzler, "Carbonated (Sparkling) Water: Good or Bad?," Helthline, 3 November 2019. [Online]. Available: https://www.healthline.com/nutrition/carbonated-water-good-or-bad. [Accessed 20 December 2021].

[66] B. J. Usman and S. A. Ali, "Carbon Dioxide Corrosion Inhibitors: A review," *Arabian Journal of Science and Engineering,* vol. 43, pp. 1-22, 2017.

[67] H. M. A. El-Lateef, V. M. Abbosv, L. I. Aliyeva and T. A. Ismayilov, "Corrosion Protection of Steel Pipelines Against CO2 Corrosion - A Review," *Chemistry,* vol. 02, no. 02, pp. 52-63, 2012.

[68] S. Paul, R. Shpherd and P. Woolin, "Selection of Materials forHigh Pressure CO2 Transport," The Welding Institute, June 2012. [Online]. Available: https://www.twi-global.com/technical-knowledge/published-papers/selection-of-materials-for-high-pressure-co2-transport. [Accessed 20 December 2021].

[69] A. K. Dey, "What is Cladded Pipe? Difference between Clad and Lined Pipe," What is Piping, 17 December 2020. [Online]. Available: https://whatispiping.com/cladded-pipe/. [Accessed 11 August 2022].

[70] Hard Hat Engineer, “What is Lined and Clad Pipe? Difference Between Lined and Clad Pipes,” Hard Hat Engineer, 17 May 2018. [Online]. Available: https://hardhatengineer.com/what-is-lined-and-clad-pipe-difference-between-line-and-clad-pipes/. [Accessed 11 August 2022].

[71] C. Liu, Y. Cao, H. Tian and S. Ma, “A Novel Method for Analyzing the Driving Force of the Bi-Directional Pig Based on the Four-Element Model,” *International Journal of Pressure Vessels and Piping,* vol. 190, pp. 1-11, 2021.

[72] X. Zhu, S. Zhang, X. Li, D. Wang and D. Yu, “Numerical Simulation of Contact Force on Bi-Directional PIG in Gas Pipeline: At the Early Stage of Pigging,” *Journal of Natural Gas Science and Engineering,* vol. 23, pp. 127-138, 2015.

[73] A. d. Heijer, “Frictional Behaviour of Pigs in Motion,” *M.Sc Thesis, Department of Mechanical Engineering, Unversity of Delft, Delft,* pp. 1-139, 2016.

[74] A. Kumar, “Pipeline Pigging: Pig Types, Pig Launcher, and Receiver,” What is Piping, [Online]. Available: https://whatispiping.com/pipeline-pigging/. [Accessed 20 December 2021].

[75] The Piping Engineering Resource, “Pipeline Pigging - Purpose, Pig Types and PRocedure,” The Piping Engineering Resource, 26 December 2019. [Online]. Available: https://www.piping-world.com/pipeline-pigging-types-procedure. [Accessed 12 August 2022].

[76] A. F. O'Donoghue, “On the Steady State Motion of Coneventional Pipeline Pigs Using Incompressible Drive Media,” *PhD Thesis, School of Mechanical Engineering, Cranfield University , Bedforshire, England,* pp. 1-247, 1996.

[77] J. Jiang, H. Zhang, J. Beilei, F. Yi, F. Yan and X. Liu, “Numerical Investigation on Sealing Performance of Drainage Pipeline Inspection Gauge Crossing Pipeline Elbows,” *Energy Science and Engineering,* pp. 1858-1871, 2021.

[78] J. T. Cie´sli´nski, S. Smolen and D. Sawicka, “Free Convection Heat Transfer from Horizontal Cylinders,” *Energies,* vol. 14, no. 559, pp. 1-22, 2021.

[79] International Towing Tank Conference, “Fresh Water and Seawater Properties,” *Internation Towing Tank Conference,* pp. 1-45, 2011.

[80] G. Kishor, M. H. Nayar, Sharqway and J. H. Lienhard V, “Seawater Thermophysical Properties Library,” 21 December 2016. [Online]. Available: http://web.mit.edu/seawater/. [Accessed 10 January 2022].

[81] T. Neu, C. Solliec and B. Santos Piccoli, “Experimental Study of Convective Heat Transfer During Liquid Piston Compressions Applied to near Isothermal Underwater Compressed-Air Energy Storage,” *Journal of Energy Storage,* vol. 32, pp. 1-16, 2020.

[82] T. Neu and A. Subrenat, “Experimental Investigation of Internal Air Flow During Slow Piston Compression Into Isothermal Compressed Air Energy Storage,” *Journal of Energy Storage,* vol. 38, pp. 1-10, 2021.

[83] F. P. Incropera and D. P. Deqitt, Fundamental of Heat and Mass Transfer, Seventh Edition, United States of America: John Wiley and Sons, 2011.

[84] Y. Elsadi, “Thermal Analysis of an Offshore Hydro-Pneumatic Energy Storage System,” *M. S. Thesis, Department of Engineering, University of Malta, Malta,* pp. 1-190, 2020.

[85] P. Stephen, “B. Fundamental of Heat Transfer,” in *VDI Heat Atlas, Second Edition,* Dusseldorf, Germany, Springer, 2010, pp. 17-29.

[86] M. A. Boles and Y. A. Cengel, Thermodynamics: An Engineering Approach, Eight Edition, United States: Mc Graw Hill, 2015.

[87] The Engineering ToolBox, “The Engineering ToolBox,” The Engineering ToolBox, 2003. [Online]. Available: https://www.engineeringtoolbox.com/gas-critical-temperature-pressure-d_161.html. [Accessed 02 05 2022].

[88] Concoa, “Air Description (Air),” Concoa, [Online]. Available: https://www.concoa.com/air_properties.html. [Accessed 02 May 2022].

[89] X. Fang, “A New Correlation of Flow Boiling Heat Transfer Coefficients for Carbon Dioxide,” *International Journal of Heat and Mass Transfer,* vol. 64, pp. 802-807, 2013.

[90] J. R. Thome, J. E. Hajal and A. Cavaillini, “Condensation in Horizontal Tubes, part 2: New Heat Transfer Model Based on Flow Regimes,” *Internation Journal of Heat and Mass Transfer ,* vol. 46, pp. 3365-3387, 2003.

[91] J. E. Hajal, J. R. Thome and A. Cavallini, “Condensation in Horizontal Tubes, Part 1: Two-Phase Flow Pattern Map,” *Internation Journal of Heat and Mass Transfer,* vol. 46, pp. 3349-3363, 2003.

[92] Engineers Edge, “Convective Heat Transfer Coefficients Table Chart,” Engineers Edge, [Online]. Available: https://www.engineersedge.com/heat_transfer/convective_heat_transfer_coefficients__13378.htm . [Accessed 02 February 2022].

[93] CoolProp, “Welcome to CoolProp,” CoolProp, [Online]. Available: http://www.coolprop.org/. [Accessed 09 August 2022].

[94] Geek for Geeks, “Python Language advantages and applications,” Geek for Geeks, 30 June 2021. [Online]. Available: https://www.geeksforgeeks.org/python-language-advantages-applications/. [Accessed 05 May 2022].

[95] C. Cutajar, T. Sant, R. N. Farrugie and D. Buhagiar, “Design Optimastion of Pressure Vessel Bundles for Offshore Hydro-Pneumatic Energy Storage Using a Smart Design Software,” *IX International Conference on Computational Methods in Marine Engineering ,* vol. 9, pp. 1-12, 2021.

[96] C. Cutajar, T. Sant, R. N. Farrugia and D. Buhagiar, “A Software Tool for the Design and Operational Analysis of Pressure Vessels used in Offshore Hydro-pneumatic Energy Storage,” *Journal of Energy Storage,* vol. 40, pp. 1-12, 2021.

[97] N. Bouchonneau, F. Grosjean and V. Sauvant-Moynot, “Thermal Insulation Material for Subsea Pipelines: Benefits of Instrumented Full-Scale Testing to Predict the Long-Term Thermomechanical Behaviour,” *Offshore Technology Conference,* pp. 1-13, 2007.

[98] Pipe Flow, “Pipe Roughness,” Pipe Flow, [Online]. Available: https://www.pipeflow.com/pipe-pressure-drop-calculations/pipe-roughness. [Accessed 10 January 2022].

[99] J. Schmitz, “High Density Polyethylene Liners for High Temperature and Gaseous Applications,” *Corrosion Conference & Exhibition,* vol. 13, pp. 1-9, 2010.

[100] Vinidex, “Polyethylene Properties,” Vinidex, [Online]. Available: https://www.vinidex.com.au/technical-resources/material-properties/polyethylene-properties/. [Accessed 2 February 2022].

[101] Mat Web, “Overview of Materials for High Density Polyetyhlene (HDPE), Injection Molded,” Mat Web, [Online]. Available: https://www.matweb.com/search/datasheet_print.aspx?matguid=fce23f90005d4fbe8e12a1bce53ebdc8. [Accessed 2 February 2022].

[102] Mat Web, “Overview of Materials for High Density Polyethylene (HDPE), Extruded,” Mat Web, [Online]. Available: https://www.matweb.com/search/DataSheet.aspx?MatGUID=482765fad3b443169ec28fb6f9606660&ckck=1. [Accessed 02 February 2022].

[103] Mat Web, “Overview of Materials of High Density Polyethylene (HDPE), Ultra High Molecular Weight,” Mat Web, [Online]. Available: https://www.matweb.com/search/datasheet_print.aspx?matguid=f9470672aa5549cb9c7b157677d02062. [Accessed 02 February 2022].

[104] P. Association, “Polyethylene & HDPE PE100 Pipe : Properties and Types,” PE100+ Association, 29 May 2018. [Online]. Available: https://www.pe100plus.com/PE-Pipes/Technical-guidance/Trenchless/Methods/PE-Pipe-i1341.html.. [Accessed 11 February 2022].

[105] R. Feistel, “Thermodynamic Properties of Seawater- Appendix to EOLSS Article 02-03-07,” *Encyclopedia of Life Support Systems,* pp. 1-38, 2015.

[106] D.-H. Cho, B. Bhushan and J. Dyess, “Mechanism of Static and Kinetic Friction of Polypropylene, Polyethylene Terephthalate and High-desnity Polyethylene Pairs During Sliding,” *TribologyInternational,* vol. 94, pp. 165-175, 2016.

[107] Vinessmann, “How Much CO2 Does a Tree Absorb,” Vinessmann, [Online]. Available: https://www.viessmann.co.uk/heating-advice/how-much-co2-does-tree-absorb#:~:text=A%20typical%20tree%20can%20absorb,around%20a%20tonne%20of%20CO2... [Accessed 04 August 2022].

[108] Carbon Pirates, “How Much Carbon Does One Tree Absorb?,” Carbon Pirates, 24 August 2019. [Online]. Available: https://www.carbonpirates.com/blog/how-much-carbon-do-trees-absorb/. [Accessed 04 August 2022].

[109] I. H. Bell, J. Wronski, S. Quoilin and V. Lemort, “Pure and Pseudo-pure Fluid Thermophysical Property Evaluation and the Open-Source Thermophysical Property Library CoolProp,” *Industrial and Engineering Chemistry Research* , vol. 53, pp. 2498-2508, 2014.

[110] T. D. Eastop and A. McConkey, Applied Thermodynamics for Engineering Technologies, New Delhi, India: Pearson Eductation Ltd., 2009.

[111] X. Wang and Z. Xu, “Study of Polytropic Exponent Based on High Pressure Switching Expansion Reduction,” *Journal of Thermal Science,* vol. 20, no. 5, pp. 435-441, 2011.

[112] A. Sencan, R. Selbas, O. Kizilkan and S. A. Kalogirou, “Thermodynamic Analysis of Subcooling and Superheating Effects of Alternative Refrigerant for vapour Compression Refrigeration Cycles,” *Internation Journal of Energy Research* , vol. 30, pp. 323-347, 2006.